Stress in a crystal palace: Using experimental micro-sensors to investigate light stress in Antarctic sea-ice diatoms

Fraser Kennedy, M.AntSci., B.MarSci., Dip.Screen.

Institute for Marine and Antarctic Studies

University of Tasmania

This dissertation is submitted for the degree of

Doctor of Philosophy

June 2019

For Madeleine and Harriet. Open your mind and you will find things that you don't know exist.

Follow your curiosity, look closer, and you may discover.

Acknowledgements

The unfaltering support of my family who are always happy to receive me despite my monosyllabic transitory nature. Also my parents who are ever-present despite any storm; it is appreciated. My two supervisors, Andrew McMinn and Andrew Martin, I am extremely grateful for your guidance and words of advice. Over the years you have inspired and encouraged my development while maintaining the humour that has kept me going. Andrew, you have taught me a considerable amount about science and the scientific process and have always been able to provide valuable advice and direction, I simply thank you. Thanks also to John Bowman, Richard Wilson, Ken Ryan, Mini-loader, Sahan Jayasinghe, Emiliano Cimoili, Vanessa Lucieer, Jenna Patterson, Richard Coleman, Big Nev, Toby Bolton, Kazuhiro Yoshida, Gustaaf Hallegraeff and all others that I have forgotton to mention. For funding, I thank the Antarctic Gateway Partnership, New Zealand Antarctic Research Institute and the Trans-Antarctic Association.

Declaration

This thesis contains no material which has been accepted for a degree or diploma by the University or any other institution, except by way of background information and duly acknowledged in the thesis, and to the best of my knowledge and belief no material previously published or written by another person except where due acknowledgement is made in the text of the thesis, nor does the thesis contain any material that infringes copyright.

Fraser Kennedy

June 2019

Authority of Access

Fraser Kennedy

June 2019

Statement of Co-Authorship

This thesis has been written as a series of manuscripts, as a result there is some repetition of general methods and background information. The following people contributed to the publication of the following manuscripts:

Chapter 2 - has been published as : **Kennedy F**, Martin A ,Bowman JP, Wilson R, and McMinn, A. 2019. Dark Metabolism: A Molecular Insight into how the Antarctic sea-ice diatom *Fragilariopsis cylindrus* survives long-term darkness. *New Phytologist* : nph.15843. https://doi.org/10.1111/nph.15843.

- **Fraser Kennedy** (90%)
- Andrew Martin (3%)
- John Bowman (1%)
- Richard Wilson (4%)
- Andrew McMinn (2%)

Chapter 3 - is currently in review as: **Kennedy F**, Martin A, McMinn, A. 2019. Rapid changes in spectral composition after darkness influences nitric oxide, glucose and hydrogen peroxide production in *Fragilariopsis cylindrus. Journal of Experimental Marine Biology and Ecology.*

- **Fraser Kennedy** (97%)
- Andrew Martin (2%)
- Andrew McMinn (1%)

Chapter 4 - is currently in review as: **Kennedy F**, Martin A, McMinn, A. 2019. An insight into the production of nitric oxide in the Antarctic sea-ice diatom *Fragilariopsis cylindrus* using microelectrodes. *Peer J - Environmental Science*

- **Fraser Kennedy** (97%)
- Andrew Martin (2%)
- Andrew McMinn (1%)

Chapter 5 - is currently in preparation for publication as: **Kennedy F**, Martin A, Ryan K, Castrisios K, Higginson N, McMinn, A. 2019. Rapid transition in snow thickness causes physiological stress in fast-ice communities in McMurdo Sound, Antarctica. *Scientific Reports*

- **Fraser Kennedy** (80%)
- Andrew Martin (10%)
- Ken Ryan (6%)
- Katerina Castrisios (2%)
- Neville Higginson (1%)
- Andrew McMinn (1%)

Details of authors roles

Andrew Martin and Andrew McMinn contributed to project development, refinement and document preparation. John Bowman provided technical advice. Richard Wilson analysed proteomic samples and provide technical assistance. Ken Ryan contributed to the filed campaign and provided advice. Katerina Castrisios and Neville Higginson contributed to field assistance.

I the undersigned agree with the above stated proportion of work undertaken for each of the above published (or submitted) peer-reviewed manuscripts contributing to this thesis:

Prof. Andrew McMinn

Primary Supervisor

University of Tasmania

Prof. Craig Johnson

Head, Ecology & Biodiversity Centre, IMAS

University of Tasmania

Abstract

Antarctic sea-ice provides a highly structured yet dynamic environment for a diverse range of microbes. Ice-associated microalage, which survive in some of the most extreme environments on earth, contribute significantly to primary production in the Southern Ocean. Because the sea-ice matrix is highly spatially and temporally variable, microalgae must adapt to ranging physio-chemical gradients and significant variation in solar irradiance. Light is the most influential driver of algal community dynamics, but due to variation in ice and snow thickness, light is both transient and inconstant. The ability of photoautotrophs to adapt to this ephemeral habitat requires highly efficient metabolic machinery to rapidly adapt to periods of high irradiance and extended periods of darkness. This thesis pairs microelectrodes, microfluidics and experimental sea-ice tanks with molecular mechanisms to investigate the physiological response of the model sea-ice diatom *Fragilariopsis cylindrus* to the complex variation in irradiance. Specifically, I examine how the three main seasonal changes in incident irradiance (darkness, sub-saturating and saturating) influences diatom physiology and how microelectrodes can be used to sense light-induced stress.

In the first part of the thesis, I focus on proteomics, the molecular plasticity that enables *F. cylindrus* to survive during extended darkness (Chapter 2). This is the first study to quantitatively analyse the whole cell proteome of a sea-ice diatom during prolonged darkness prior to re-illumination. I describe how this diatom utilises ancient alternative metabolic mechanisms to sustain essential metabolic processes in the dark to retain functionality of the photosynthetic apparatus. Chapter 3 details how *F. cylindrus* responds to modification in light intensity and spectral composition

upon illumination after long-term darkness. I illustrate how extracellular production of hydrogen peroxide (H_2O_2), nitric oxide (NO) and glucose are produced in response to variation in spectral quality. I also examine the influence that exposure to different wavelength of light has on the physiology of *F. cylindrus* and demonstrate that the detection of extracellular products can be directly attributed to the photophysiological state of the cell. I suggest that the metabolic overflow of H_2O_2, NO and glucose is a useful proxy for the *in situ* detection of phototrophic stress of bottom-ice microbial communities. One of these metabolites, NO, is under-reported in microalgal research and has not been studied in ice-associated diatoms. In chapter 4, I investigate the mechanisms that enables NO production in *F. cylindrus*, and show that NO is nitrite-dependent; most likely via a nitrate reductase enzyme. Interestingly, NO production was abolished upon exposure to light, but could be induced in the light when normal photosynthetic electron flow was disrupted. Finally, the thesis applies the laboratory findings to an Antarctic field experiment, whereby *in vivo* extracellular metabolites produced by an under-ice microbial community were measured in response to rapid transitions in snow thickness. The results presented in chapter 5 illustrate that rapid changes in transmitted irradiance can impose a strong selective pressure on sea-ice taxa. The presence of a thin layer of snow (10 cm) positively influenced the under-ice algal biomass, whereas a rapid shift from thick snow (30 cm) to no snow caused significant oxidative stress in the under-ice community. I illustrate, for the first time, that extracellular 'stress' metabolites produced following environmental forcing can be measured *in vivo* and directly attributed to habitat modification.

The results presented in this thesis provide a unique insight into plasticity of ice-associated diatoms with respect their capacity to survive long periods of darkness and to adapt to changes in irradiance. The production of extracellular metabolites was successfully measured using microelectrodes in both the laboratory and the field. The results indicate that under conditions of saturating irradiance that cause stress or disrupt normal photosynthetic electron flow, increased production of metabolites can be attributed to photophysiological state of the cell. The ability to measure *in vivo* overflow metabolism may provide an effective tool for real-time measurement of under-ice phototrophic health during periods of environmental change.

Table of contents

List of figures

List of tables

Chapter 1

Introduction and overview

1.1 Antarctic sea-ice

The annual formation of sea-ice is the most significant environmental change that occurs in the Southern Ocean. At its greatest extent, sea-ice doubles the total area of the Antarctic continent each year (~19 million km^2) and is the most important habitat for primary production in coastal regions. The ice matrix is characterised by vertical extremes in light, temperature, salinity and nutrients that challenge the very existence of biological colonisation. During ice formation, a diverse microbial consortia are initially scavenged from the water column and incorporated within the ice. However, the extreme environmental pressure experienced upon incorporation, influences the life strategies of the micro-organisms, selecting for a unique consortia that possesses high metabolic plasticity (Martin et al., 2011). While these communities are diverse comprising viruses, bacteria and protozoa, the microalgal fraction typically dominates. These ice-associated phototrophic taxa, generally comprising pennate diatoms, contribute significantly to the overall Antarctic primary production. Estimates range between 60-70 TG C yr^{-1} for sea-ice algae and 1300 Tg C yr^{-1} for oceanic phytoplankton (Arrigo, 2014; Arrigo et al., 2008). Importantly, primary production is spatially and temporally variable, largely due to the strong physiochemical gradients within the ice and seasonal variation in solar irradiance. The light required for photosynthesis is the single most influential driver of ice-associated algal communities (Arrigo, 2014; Peters and Thomas,

1996), however ice and snow typically attenuate surface irradiance from ~1500 μmol photon m^{-2} s^{-1} to ~5 μmol photon m^{-2} s^{-1} during the summer months (McMinn et al., 2010). At the onset of the polar winter, light drops to below detectable limits for up to four months of the year and sea-ice algae must rely on their capacity to modify metabolic output and survive on stored energy resources (Kennedy et al., 2019; McMinn and Martin, 2013; Peters and Thomas, 1996). The extreme transience of light in this environment has forced many diatom species to evolve mechanisms that enable rapid adjustment of their photosynthetic apparatus to either increase photon capture in low light, or minimise damage from excess irradiance. However, high inter-annual variability and the increased occurrence of extreme climatic events in this region will influence both the timing and magnitude of light transmission and subsequently the development of *in situ* microbial communities (Deppeler and Davidson, 2017).

Current climate models predict that the Antarctic ecosystem will undergo extensive cumulative environmental change as a result of continued anthropogenic-driven forcing (Bracegirdle et al., 2008; Turner et al., 2008). Projections indicate that less ice will form in warmer water during winter and melt earlier in spring/summer. Currently (June, 2019), the total extent of sea-ice encompassing the Antarctic continent is the lowest on record (~11 million km^2) with ice presently forming late in the season (Figure 1.1). These alterations in sea-ice environmental dynamics are likely to impact phototrophic organisms that are associated with the sea ice-matrix. Whether theses changes will positively or negatively impact ice-associated primary production is currently unknown. Sea-ice microalgae are fundamental drivers of the Antarctic marine food-web and any significant disruption in primary production is likely to impact trophodynamics. Furthermore, climate predications anticipate an enhanced poleward shift in storm events resulting in higher winds, wave magnitude and precipitation (Bracegirdle et al., 2008; Massom and Stammerjohn, 2010). Increased wind and wave action will intensify the fragmentation of existing sea-ice floes, accelerating ice melt leading to alterations in productivity. Increased precipitation in the form of rain will enhance light transmission, whereas precipitation in the form of snow will both decrease the quantity and alter the spectral composition of the irradiance reaching bottom-ice communities (Massom et al., 2001; Meiners et al., 2017). The overall predicted increase in harmful irradiance could lead to

photodamage in sea-ice algae and may even stall *in situ* primary production (Campbell et al., 2015; Juhl and Krembs, 2010). The timing and magnitude of changes in irradiance is critical in determining the capacity for algal adaptation (Juhl and Krembs, 2010). On the scale of hours to days, bottom-ice algae can efficiently photoacclimate to increased irradiance by modifying their light harvesting pigments and reaction centres (Katayama et al., 2011; Kuczynska et al., 2015). Adaptation on the scale of minutes to hours is limited by their photophysiological state (Juhl and Krembs, 2010; Petrou et al., 2010). The failure to quickly acclimate can rapidly lead to photoinhibition and photodamage if available photo-protection mechanisms cannot efficiently dissipate excess excitation energy (Ruban et al., 2004). An understanding of how rapid shifts in irradiance will impact sea-ice algae communities, and the ability to efficiently measure *in situ* metabolic status, is clearly needed.

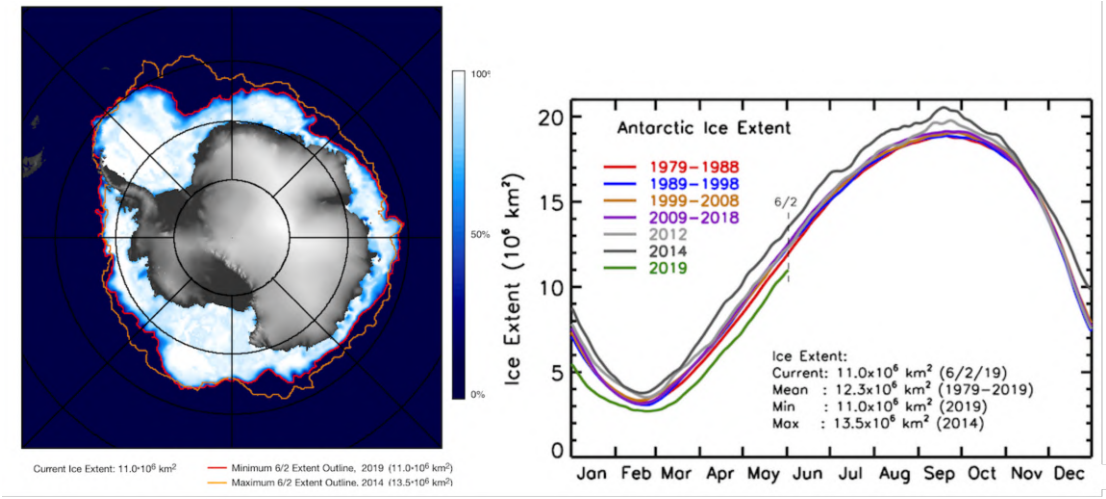

Figure 1.1: **a)** A map of the current Antarctic sea-ice extent as of the 2 June 2019; figure shows the maximum (2014 - in orange) and minimum (2019 - in red) sea-ice extents (10^6 km^2) during the period from November 1978 to the present. **b)** The daily Antarctic sea-ice magnitude given as ten year averages between 1979 and 2018. Yearly averages are also shown for 2012, 2014, and 2019. The figure also displays the current sea-ice extent, historical mean, minimum, and maximum values in km^2. Modified from Comiso et al. (2019).

Environment perturbation can influence multiple aspects of phototrophic metabolism and cause significant stress that manifests first in the photosynthetic apparatus. While photosynthesis primarily serves to capture and convert light into cellular energy, it can also function as an efficient monitoring system for environmental change. During events of ecosystem flux, alteration in the

photosynthetic redox status and balance of photon capture to assimilation all act as molecular messengers that activate metabolic and photosynthetic adjustment. By measuring fluctuations in both the rate of, and products relating to photosynthesis, a real-time indication of microalgal health can be obtained that mirrors the *in situ* status of ice-associated microbes. The development of micrometer-sized microsensors has enabled fine-scale chemical gradients to be measured in microbial mats and attributed to meaningful biological processes. Leland Clark (1955) originally developed a method to detected dissolved oxygen in liquids using an electrical current (aptly named the Clarke electrode). Pamatmat (1968) firstly used this electrode to study the physiology of microbial biofilm's in benthic substrates, however problems were established with the electrodes sensitivity and aspects of its design. Revsbecht and Ward (1983) developed a more robust Clarke-type oxygen electrode that could be used in almost all liquids, introducing a range of possible applications across multiple habitats. Additional Clarke-type electrodes were quickly established that could measure a whole suite of chemical molecules. In the sea-ice environment, McMinn and Ashworth (2007) pioneered the use of oxygen microelectrodes to study ice-associated algal productivity. However, since McMinn (1997) the deployment of microelectrodes that detect other chemical biosignatures in sea-ice has been limited. Furthermore, there have been no reports of studies using microsensors to examine the sea-ice microbial response to environmental change. In this thesis I will examine how changes in incident irradiance influence diatom physiology and emphasise how microelectrodes can be used to detect light-induced stress. Specifically, I detail the use of four microsensors: oxygen, nitric oxide, glucose and hydrogen peroxide.

1.2 Thesis aims and structure

In this thesis I examine the physiological responses of an Antarctic sea-ice diatom to large-scale variations in the quantity and quality of irradiance, specifically focusing on detecting photosynthetically-derived extracellular "stress" metabolites using microelectrodes. I examine the influence of light during three main seasonal transitions (darkness, sub-saturating and saturating) and will highlight the importance of light as a regulator of stress in ice-associated diatoms.

The specific aims of this thesis are to:

1. Determine how Antarctic sea-ice diatoms are able to survive extended periods of darkness and recover upon illumination;

2. Investigate if exposure to variation in the magnitude and spectral quality of light upon illumination causes photophysiological stress;

3. Determine if light-induced photophysiological stress can be measured extracellularly using microelectrodes;

4. Investigate if ice-associated phototrophic stress can be measured *in situ* with microsensors when exposed to rapid changes in irradiance.

I begin this thesis in the dark - sea-ice diatoms are annually exposed to four months of darkness and the specific molecular mechanisms that enable long-term dark survival is unknown. In Chapter 2, I use whole cell proteomics to quantitatively investigate metabolic changes that occur during sustained darkness and during recovery upon illumination. An abbreviated version of Chapter 2 has been published as:

- **Kennedy F**, Martin A, Bowman JP, Wilson R, and McMinn, A. 2019. Dark Metabolism: A Molecular insight into how the Antarctic sea-ice diatom *Fragilariopsis cylindrus* survives long-term darkness. *New Phytologist* : nph.15843. https://doi.org/10.1111/nph.15843.

Following the polar winter, light condition upon illumination is critical in determining under-ice algal productivity. Climate models predict cumulative degree of environmental changes that will influence both the quantity and quality of irradiance reaching ice-associated taxa during key transition events. Chapter 3 investigates the influence of variation in irradiance upon illumination after darkness has on the photophysiology of *F. cylindrus* and if light-induced stress can be detected using microsensors.

Chapter 3 is currently in review with Journal of Experimental Marine Biology and Ecology as:

- **Kennedy F**, Martin A, McMinn, A. 2019. Rapid changes in spectral composition after darkness influences nitric oxide, glucose and hydrogen peroxide production in *Fragilariopsis cylindrus. Journal of Experimental Marine Biology and Ecology*

Chapter 4 further explores the results obtained in Chapter 3 with respect to the production of nitric oxide (NO). I investigate the mechanisms that induced NO production in *F. cylindrus* in response to saturating irradiance. This is the first study to examine the production of NO in a polar ice-associated diatom. I highlight that variation in abiotic parameters can influence the production of NO in *F. cylindrus* as a "stress signal" molecule which may exert a metabolic influence for physiological adaptation. Chapter 4 is currently in review with Peer J Environmental Science as:

- **Kennedy F**, Martin A, McMinn, A. 2019. An insight into the production of nitric oxide in the Antarctic sea-ice diatom *Fragilariopsis cylindrus* using microelectrodes. *Peer J - Environmental Science*

Chapter 5 explores the response of a shade-adapted fast-ice algal community exposed to rapid changes in light. The previous findings are essentially applied in the field; and extracellular metabolites are measured during an Antarctic habitat manipulation experiment. Snow thickness was modified and its influence on under-ice microbial stress during rapid transitions is investigated. Chapter 5 is currently in preparation for submission to *Scientific Reports* as:

- **Kennedy F**, Martin A, Ryan K, Castrisios K, Higginson N, McMinn, A. 2019. Rapid transition in snow thickness causes physiological stress in fast-ice communities in McMurdo Sound, Antarctica. *Scientific Reports*

Finally, chapter 6 concludes the thesis with a summary of the major findings. In the appendices, my contributions to additional published research during the courses of my candidature has been included.

Chapter 2

Dark metabolism: a molecular insight into how the Antarctic diatom *Fragilariopsis cylindrus* survives the dark

---

2.1 Introduction

Primary production within Antarctic sea-ice is spatially and temporally variable, largely due to strong physiochemical gradients within the ice and seasonal variation in solar irradiance. The light required for photosynthesis is the single most influential driver of ice-associated microbial communities (Arrigo, 2014; Peters and Thomas, 1996), however ice typically attenuates surface irradiance from ~1500 μmol photon m^{-2} s^{-1} to ~5 μmol photon $m^{-2}s^{-1}$ during the summer months (McMinn et al., 2010). Ecological success of phototrophs relies on metabolic plasticity with respect to the pigment-protein complexes of the photosynthetic apparatus. Ice-associated algae must minimise damage from excess light or increase photon capture in low light by modifying the specific ratio of these complex types.

The light harvesting antenna in diatoms is large, and although it shares a high homology to the light harvesting complexes of higher plants and green algae, it differs with respect to pigment

composition and excitation absorption properties (Giovagnetti and Ruban, 2017; Ishihara et al., 2015; Taddei et al., 2016; Wilhelm et al., 2014). It is comprised largely of the pigments chlorophyll *a, c*, and fucoxanthin, which are bound to fucoxanthin chlorophyll a/c binding proteins (FCPs). The addition of fucoxanthin allows diatoms to absorb more of the electromagnetic spectrum, particularly the blue-green wavelengths that dominate aquatic environments (Bertrand, 2010). Diatom genomes encode three variations of FCP, each with its own evolutionary origin and differing with respect to functionality and thylakoid interaction (Büchel, 2003; Ishihara et al., 2015; Lepetit et al., 2012; Nymark et al., 2013). The three clades of FCP are i) LHCF – those associated with all chlorophyll *c* containing algae that fulfils the primary role in light harvesting, ii) LHCR – those of distinct red algal origin, tightly associated with the photosystem I (PSI) antenna, iii) LHCx – those related to the ancient Li818 light inducible proteins of green algae that are mainly ultilised during periods of stress (Gundermann et al., 2013; Wilhelm et al., 2014). Variation in the type of FCP accompanying the photosystem is biologically relevant because irradiance directly influences clade expression (Lepetit et al., 2010). Collectively, the FCP's have led to the success of diatoms in ecosystems characterised by variable irradiance, especially low light conditions (Kuczynska et al., 2015; Morgan-Kiss et al., 2016; Nagao et al., 2013).

With the onset of the polar winter, light drops to below detectable limits for up to four months (McMinn and Martin, 2013; Palmisano and Sullivan, 1983; Peters and Thomas, 1996). To retain viability, polar phototrophs use strategies that modify physiology and metabolic output to maintain DNA integrity. Some taxa form cysts or resting stages while others are facultatively heterotrophic and/or survive on stored energy reserves. Cyst and spore formation is relatively common in the Arctic, but does not appear to be a mainstream strategy among Antarctic taxa (McMinn and Martin, 2013; Taylor and McMinn, 2002). Heterotrophic uptake of organic substrates has been previously reported as a potential mechanism to supplement energy requirements (Laybourn-Parry et al., 2005; Palmisano and Sullivan, 1983; Rivkin and Putt, 1987), however the energy obtained is unlikely to be sufficient to enable long-term dark survival. Studies have also shown that the uptake and metabolism of exogenous supplied organic substrates to be irregular or ineffective (Bunt and Lee, 1972; Horner and Alexander, 1972). Sea-ice diatoms may exploit currently unknown metabolic

pathways that sustain essential metabolic processes and the components required to maintain viability. The ability to rapidly regulate metabolic output in response to any given light regime would confer a competitive advantage and ensure rapid recovery of the photosynthetic machinery upon re-illumination. Maintenance metabolism may help to explain why many sea-ice diatoms are able to rapidly resume photosynthesis and grow quickly after extended darkness (McMinn et al., 2010; Nymark et al., 2013; Peters and Thomas, 1996; Reeves et al., 2011; Wulff et al., 2008). Despite studies indicating strong downregulation of photophysiological processes during prolonged darkness (Martin et al., 2012; Peters and Thomas, 1996; Popels et al., 2007; Reeves et al., 2011; Wulff et al., 2008), a certain level of functionality and structural arrangement must be retained in the dark. This infers that cells are actively maintaining some degree of photosynthetic capacity and sustaining constituents of the photosynthetic apparatus in the dark. The question remains as to how cells are able to sustain metabolism in the absence of a primary energy source. It is widely known that diatoms are able to use stored energy reserves in the form of lipids and carbohydrates during periods of low cellular energetics (Antia, 1976; Bunt and Lee, 1972; Martin et al., 2012; Mock et al., 2017; Raven and Beardall, 2011; Smayda and Mitchell-Innes, 1974; Zhang et al., 1995) and that the rate of consumption is low. Cells might also switch to alternative unconventional metabolic pathways, or amplify the regulatory flexibility of existing pathways to enhance metabolic possibilities (Allen et al., 2011). For example, some marine algae use alternative electron donors and utilise fermentative metabolism under dark anoxic conditions (Catalanotti et al., 2013; Fernie et al., 2004; Kamp et al., 2015, 2013; Yang et al., 2015). Considering the complex genomic origins of sea-ice diatoms where alternative metabolic routes may have been acquired by the procurement of genes via horizontal gene transfer, endosymbiosis and duplication events, adjustment of metabolism via alternative routes is possible (Medlin, 2016; Sims et al., 2006; Tirichine and Bowler, 2011). Evidence of diatoms acquiring genes from various sources is illustrated in the functional differentiation of genes encoding isozymes of conserved metabolic functions (Bowler et al., 2008; Falciatore and Bowler, 2002; Mock et al., 2017; Smith et al., 2012). Smith et al. (2012), showed that 31% of the genes in diatoms are unique to that particular species; an observation attributed to the complex evolutionary adjustments of the genome. Some species have re-targeted select nuclear encoded genes to discrete organelles resulting in isozymes that target multiple subcellular

locations (Kroth et al., 2008; Smith et al., 2012). For example, diatoms have approximately twice as many enzymes involved in glycolysis than green algae. A high number of isozymes can amplify regulatory flexibility and enhance the functional possibilities of metabolic processes.

The psychrophilic pennate diatom *Fragilariopsis cylindrus* is prominently ice-associated and as a result has evolved specialised survival mechanisms. Therefore, it is a useful indicator species for investigations into adaptation and acclimation to the polar sea-ice habitat (Mock et al., 2017). A number of studies have described the effect of darkness on the survivability of Antarctic phytoplankton and sea-ice algae (Baldisserotto et al., 2005; Bunt and Lee, 1972; Palmisano and Sullivan, 1983; Reeves et al., 2011), but most research has focused on physiological adaptation rather than the biochemical and molecular drivers behind dark-induced metabolism. Recent advances in functional genomics has made it possible to examine the molecular processes enabling dark survival (Bai et al., 2016; Mock et al., 2017; Nymark et al., 2013). In this study, I aim to gain a comprehensive insight into how *F. cylindrus* can survive extended periods of darkness by examining the expression profile of the proteome. These results provide the first insight into the molecular basis for dark survival.

2.2 Materials and Methods

2.2.1 Algal culture

A monoculture of *F. cylindrus* was isolated from Antarctic pack ice in 2015 (Davis station, East Antarctica). This culture was taxonomically identified using the descriptions found in Scott and Marchant (2005) and confirmed by 18S rRNA sequencing (Appendix A, Chapter A). The culture was maintained in exponential growth phase in L_1 media (Guillard and Hargraves, 1993) under cool white fluorescent light (50 μmol photon m^{-2} s^{-1}, 12:12 L/D cycle) at 2°C ± 1°C in a batch system and bubbled with filtered air. Cultures were then divided into six Erlenmeyer flasks (and amended with double concentrated L_1 media (Table 2.1). Flasks were divided into two treatments: 1) continuous light (50 μmol photon m^{-2} s^{-1}), n=3 and 2) continuous dark, n=3 (Figure 2.1). Cells were kept in their respective treatment for a total of 120 days, with sub-sampling on days 0, 0.5 (12 hours), 1,

3, 7, 21, 30, 60, 120. Following 120 days, dark cells were re-exposed to 50 μmol photon m^{-2} s^{-1} of white light for 24 hours to examine cell recovery.

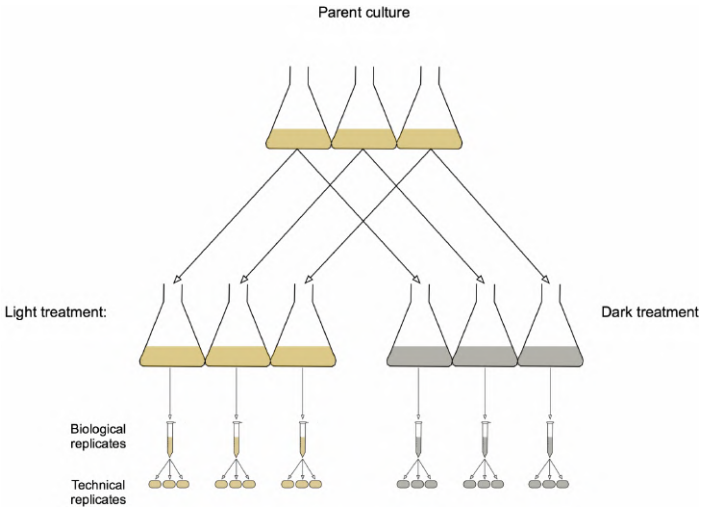

Figure 2.1: Graphical representation of the experimental design.

Table 2.1: Concentrations of the growth media nutrients used.

Component	**Concentration in Final media (M)**
$NaNO_3$	1.76E-03
$NaH_2PO_4.H_2O$	7.24E-05
$Na_2SIO_3.9H_2O$	2.12E-04
$Na_2EDTA.2H_2O$	2.34E-05
$FeCl_2.6H_2O$	2.34E-05
$MnCl_2.H_2O$	1.82E-06
$ZnSO_4.7H_2O$	1.60E-07
$COCl_2.6H_2O$	1.00E-07
$CuSO_4.5H_2O$	2.00E-08
$Na_2MoO_4.2H_2O$	1.64E-07
H_2SeO_3	2.00E-08
$NiSO_4.6H_2O$	2.00E-08
Thiamine.HCl	5.92E-07
Biotin	4.10E-09
Cyanocobalamin	4.78E-09

2.2.2 DNA extraction

DNA was extracted using the boiling method developed by Liu et al. (2014). Firstly, the sample was heated to 95°C for 10 minute in sterile 10 mM Tris pH 8.1 using 0.5 cm^2 of *F. cylindrus* embedded on filter. Filter material was vortexed 1 minute to free as much cells from the filter. After heating, the extract was cooled on ice and spun for 1 minute on a microfuge. A PCR reaction was set up using MyTaq (Bioline Australia), 1 μL of template DNA, 1 μM of each primer (18S rRNA) Euk 4F 5' CTG GTT GAT CCT GCC AG 3' and Euk 516R 5' ACC AGA CTT GCC CTC C 3'.

The thermocycling conditions used were initial denaturation at 98°C for 30 seconds and 32 cycles of: 95°C for 30 s, 59°C for 30 seconds, and 72°C for 45 seconds, followed by a final extension of 10 minute at 72 °C. Thermocycler model used was a Peltier PTC200. Sequencing used the ABI BigDye cycle terminator kit 3.1 and ABI 3730 xl automated sequencer (performed at Macrogen, Seoul, South Korea). Sequences were manually checked and ambiguous nucleotide positions near the primer regions were removed. The sequences were subsequently compared to the NCBI database and the closest sequences were downloaded (Appendix A - Chapter A) (https://nph.onlinelibrary.wiley.com/doi/10.1111/nph.15843).

2.2.3 Proteomic sample preparation, lysis and digestion

Sub-samples (100 mL) were withdrawn from each replicate and centrifuged at 10,000 x g for 2 minute at 2°C. The supernatant was then removed, and the resulting pellets were placed in 1 mL centrifuge tubes and spun again at 2°C for 1 minute at 10,000 × g. The supernatant was discarded, and the resulting pellets were washed with 1 mL of ice-cold phosphate buffered saline (pH 7.3) and spun at 2°C for 10 minute. This step was repeated twice. The pellets were finally plunged into liquid nitrogen and stored at -80°C for approximately 1 month before analysis.

The algal cell extracts were thawed on ice followed by the addition of 500 μL of ice-cold HPLC grade water. Extracts were then sonicated on ice for 2 minute in a 100 W, 20 KHz sonicator with a titanium microtip then plunged into liquid nitrogen. The extracts were then thawed on ice before 0.1 g of

combusted quartz glass beads were added. Sample were beaten for 2 minute at 2°C, and then plunged in liquid nitrogen. This was repeated twice. Un-lysed cells and debris were subsequently collected by centrifugation at 15,000 × g for 30 minute at 2°C. The resulting whole cell lysates were removed and spun again at 15,000 x g for 15 minute to isolate any insoluble components. The supernatant was aspirated, and protein concentrations were calculated using a Pierce Coomassie Protein Assay Kit (Thermo Scientific). Samples were normalised by taking approximately equal amounts of protein (100 μg) for each trypsin digest and analysing the same amount of each digest by LC/MS. Any remaining variation in overall signal is compensated for by the normalisation of peptide intensities across samples.

Protein solutions were added to -20°C absolute ethanol at a ratio of 1:9, mixed and kept at -20°C for 60 minute. Samples were then centrifuged at 18,000 × g for 10 minute to concentrate precipitated protein. The supernatant was removed, and the resulting pellets washed with -20°C absolute ethanol. This step was then repeated. Samples were spun again at 18,000 × g for 10 min; the supernatant was aspirated and the remaining pellet was left to air dry to eliminate any ethanol residue.

Protein samples were trypsin-digested using standard procedures (Wilson et al., 2010) and analyzed by nanoLC-MS/MS using an LTQ-Orbitrap XL and Ultimate 3000 nanoHPLC system (ThermoFisher Scientific, MA, USA). Tryptic peptides (~1 μg) were loaded onto a 20 mm x 75 mm PepMap 100 trapping column (3 mm C18) at 5 mL/minute, using 98% water, 2% acetonitrile and 0.05%TFA. Peptides were separated at 0.3 mL/minute on a 250 mm x 75 mm PepMap 100 RSLC column (2 mm C18) at 40°C from 97% mobile phase A (0.1% formic acid in water) to 50% mobile phase B (0.08% formic acid in 80% acetonitrile and 20 % water) by elution with 3-10% B over 10 minute, 10-40% B over 120 minute, 40-50% B over 10 minute, holding at 95% B for 10 minute then re-equilibration in 3% B for 15 minute. Solid phase peptide extracts were injected once and dissolved phase extracts were injected twice to achieve equivalent analysis time. The LTQ-Orbitrap was controlled using Xcalibur 2.1 software in data-dependent mode as described in Wilson et al. (2016).

MS/MS spectra were searched against the *F. cylindrus* database (Joint Genome Institute, *F. cylindrus* CCMP 1102 (https://genome.jgi.doe.gov/Fracy1/Fracy1.home.html) using the Andromeda search engine in MaxQuant, version 1.5.1.2 (http://maxquant.org/). Default settings for protein identification by LTQ-Orbitrap MS/MS and label-free quantitation (LFQ) included a maximum of two missed cleavages, mass error tolerances of 20 ppm then 4.5 ppm for initial and main peptide searches, respectively; 0.5 Da tolerance for fragment ions, variable methionine oxidation and fixed cysteine carbamidomethylation. The false discovery rate (FDR) for both peptide-spectrum matching and protein identification was set to 0.01. Proteins only identified by site, reverse sequences, contaminants and proteins identified on the basis of a single matching peptide were excluded. Peptide LFQ values, normalized according to the MaxLFQ algorithm using a minimum peptide ratio count of two (Cox et al., 2014), were first $\log_2$-transformed and proteins identified in fewer than two biological replicates and five time points were excluded. After imputation of remaining missing values with random intensity values for low-abundance proteins, mean LFQ values (dark vs light) were compared using a moderated t-test. Protein abundance changes are expressed throughout on a $\log_2$ scale, where positive values represent increased abundance in dark-induced cells, and negative values indicate reduced abundance. Proteins with a FDR of less than 2% and mean $\log_2$ LFQ differences >/<0.5 (~1.4-fold on the linear scale) were considered significant.

The mass spectrometry proteomics data have been deposited to the ProteomeXchange Consortium via the PRIDE partner repository (Vizcaíno et al., 2016) with the dataset identifier PXD007098.

2.2.4 Pulse amplitude modulated fluorometry (PAM)

Chlorophyll *a* fluorescence was measured using a pulse-amplitude-modulated fluorometer (Water-PAM, Walz, Effeltrich, Germany) with an internal actinic light source centered on 660 nm. All samples were dark-acclimated for 30 minute prior to measurement. Rapid light curves (RLC) were obtained under software control (WinControl, Walz). Measurements were taken on days 0, 0.5, 1, 3, 7 ,14, 21, 30, 60, 90, 120 and recovery was assessed at 1, 2, 4, 8 and 24 hours.

Maximum quantum yield in the dark-acclimated state, F_v/F_m, was obtained from the first value of the RLC when the irradiance was 0 μmol photon m^{-2} s^{-1}. Samples were exposed to a weak measuring light (<1 μmol photon m^{-2} s^{-1}), which induces fluorescence without stimulating photosynthesis and allows minimal fluorescence (F_o in the dark, F in the light). A second light source, a saturating pulse (>1800 μmol photon m^{-2} s^{-1} for 0.6 s), was used to close all reaction centres and measure maximum fluorescence (F_m in the dark $F_{m'}$ in the light). RLCs were comprised of a series of nine saturation pulses followed by exposure to a sequence of increasing actinic light of 10s duration. The effective quantum yield, $\Delta F/F_m$, was obtained after exposure to each actinic light level, which here was 12, 36, 53, 82, 121, 185, 277, 393 and 545 μmol photon m^{-2} s^{-1}. The relative photosynthetic electron transport rate (rETR) was calculated as the product of the effective quantum yield of PSII and quantum flux density of photosynthetically active radiation (PAR). The rETR data generated by the rapid light curves were fitted to the exponential function of Platt and Jassby (1976) using a multiple non-linear regression. In this case rETR was substituted for photosynthesis (P) in their P vs I (Irradiance) relationship and the photosynthetic efficiency (α) is subsequently referred to as the initial slope of the rETR vs E curve.

$$rETR = rETR_{max} \times \left[1 - e\left(\frac{-\alpha E_d}{rETR_{max}}\right)\right] e\left(\frac{\beta E_d}{rETR_{max}}\right) \tag{2.1}$$

As photoinhibition did not occur in the light curves, the function reduces to:

$$rETR = rETR_{max} \times \left[1 - e\left(\frac{-\alpha E_d}{rETR_{max}}\right)\right] \tag{2.2}$$

Non-photochemical fluorescence quenching (NPQ) was calculated using the Stern-Volmer quenching parameter described in Kramer et al. (2004).

2.2.5 Adenosine -5 Triphosphate

Determination of ATP concentration in cell extracts was performed through the bioluminescence of ATP with recombinant firefly luciferase and D-luciferin (Molecular Probes, USA) as per the manufactures instructions. Luminescence of samples and standards was read on a microplate reader

(BMG FLUOstar OPTIMA). Standard curves were conducted with each assay and the concentration of cellular ATP was normalised to cell concentration.

2.2.6 Chlorophyll a analysis

Chlorophyll *a* (chl*a*) concentration was determined in triplicate using the acidification protocol as described by Evans et al. (1987). Briefly, 20 mL sub-samples were filtered onto 25 mm GF/F filters and extracted in 10 mL of methanol in the dark at 4°C for 12 hours. Chl*a* extracts were subsequently measured on a Turner fluorometer (10AU Turner designs, USA).

2.3 Results

One of two treatments were assigned to cultures of *F. cylindrus*, 1) continuous light, and 2) continuous dark. Cells were kept in these respective treatments for a total of 120 days, with sub-sampling on days 0, 0.5 (12 hours), 1, 3, 7, 21, 30, 60, 120. Following 120 days, dark cells were re-exposed to white light for 24 hours to examine cell recovery. The proteomic profiles of dark cells were compared with those in constant light and this comparison revealed two key functional differences: 1) widespread downregulation of proteins associated with photosynthesis and carbon fixation, and 2) upregulation of respiratory processes of glycolysis, Entner-Doudoroff and the tricarboxylic acid cycle.

Proteins that became more abundant in the dark compared to continuous light conditions were classified according to their KOG functional group (euKaryotic Orthologous Groups). These groupings were categorised according to the length of dark exposure: A) early (before 30 days) and B) late (30 days and after) (Figure 2.2). During the first 21 days of darkness (early) a higher proportion of upregulated proteins were linked to carbohydrate transport and metabolism (19%), translation, ribosomal structure and biogenesis (18%), lipid transport and metabolism (11%). Following 30 days of dark exposure (late), the percentage of proteins in those KOG classes decreased; carbohydrate transport and metabolism (10%), translation, ribosomal structure and biogenesis (12%), lipid transport and metabolism (4%). Increases in proteins classified in amino acid transport and

metabolism (20%), protein turnover, posttranslational modification (24%) and energy production and conversion (14%) were observed after 30 days of dark exposure.

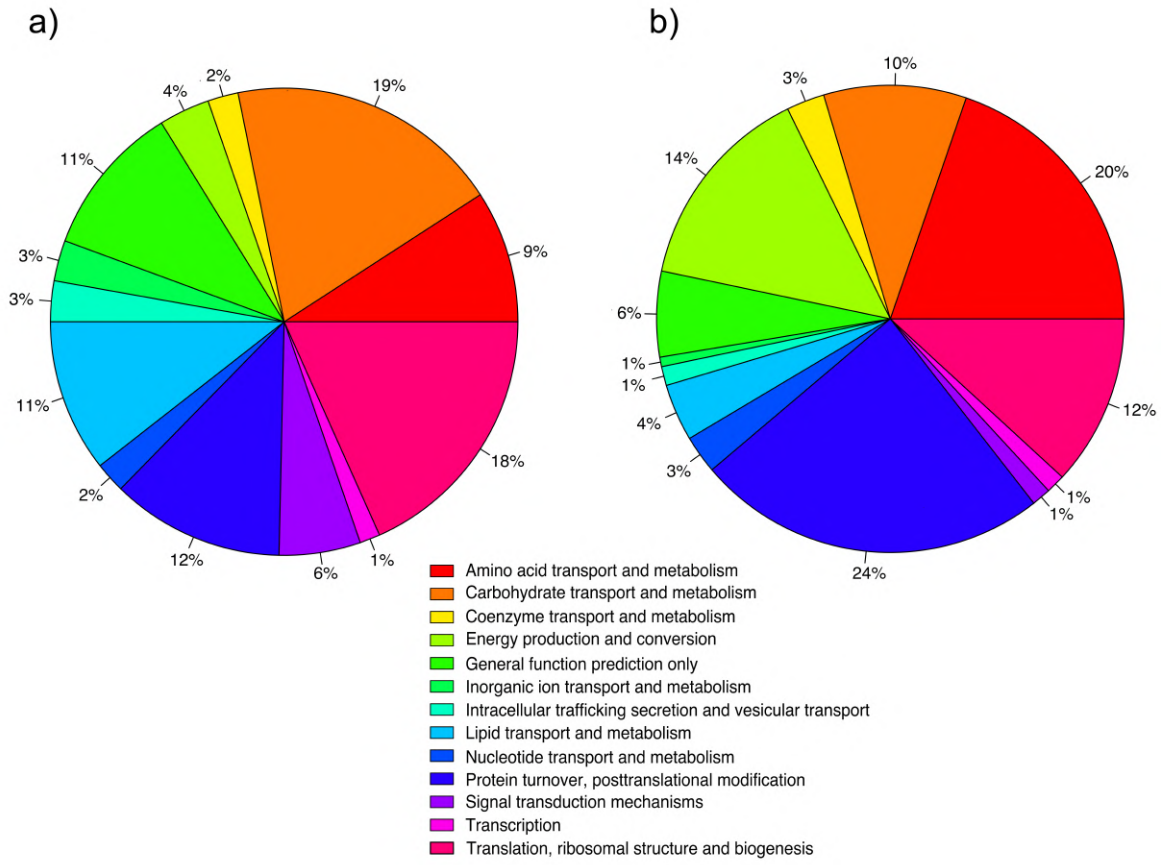

Figure 2.2: Representation of the percentage of upregulated ($\log_2$ >0.5 fold) proteins in the dark classified according to their respective KOG category. These are split into two groups that correspond to the mean expression of proteins in each KOG category conferring to the length of dark exposure: a) early – mean expression of proteins until 30 days of darkness and, b) late – mean expression of proteins following 30 days of darkness.

2.3.1 Cell numbers and chlorophyll concentration

Cell concentration decreased in both treatments until day 21, when stabilisation in cell numbers was observed (Figure 2.3a). Cells in the constant light increased from day 30, which may indicate a degree of active growth. While proteomic samples were normalized for any changes in biomass, some minor variations in protein expressions may be present.

Following three days of darkness, chl*a* concentration declined from a mean of 18.63 μg L^{-1} to 12.74 μg L^{-1} (Figure 2.3b). This increased to 17.34 μg L^{-1} on day 7 and remained relatively unchanged until day 60. Thereafter chl*a* decreased from 17.58 μg L^{-1} to 14.72 μg L^{-1} by day 120 of darkness. Chl*a* concentration did not differ significantly between light and dark for the first 21 days, after which chl*a* concentration in the light increased from 19.03 μg L^{-1} on day 21 to 28.71 μg L^{-1} on day 60. Re-exposure of dark treated cells to light failed to alter chl*a* concentration.

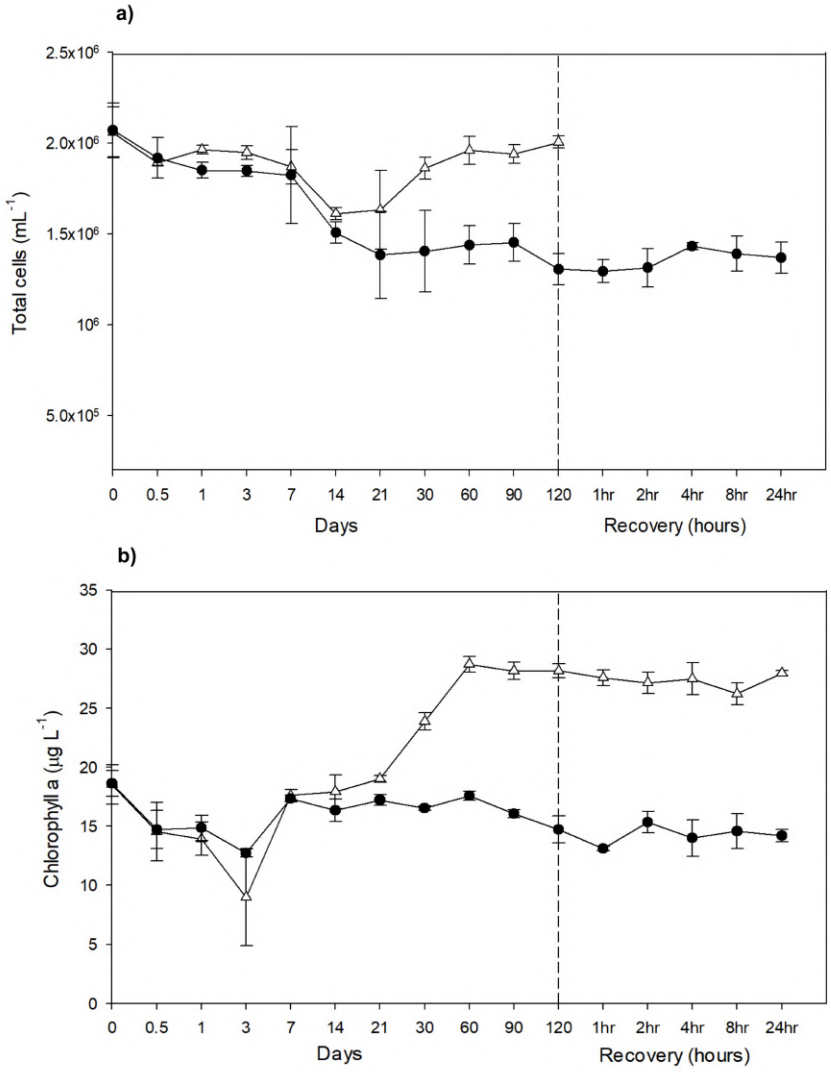

Figure 2.3: **a)** Growth curves of *F. cylindrus* (cells mL^{-1}) and **b)** Chlorophyll *a* concentration (μg L^{-1}) of dark (closed circles) and light (open triangles) treated cells. Points after the dashed line represent the re-illumination of dark treated cells for 24 hours at 50 μmol photon m^{-2} s^{-1}. Error bars represents the standard deviation of the mean.

2.3.2 Light harvesting and the photosynthetic pathway

Proteins from the three-major light harvesting complex (LHC) clades (LHCF, LHCR and LHCx) were mostly downregulated within the initial 12 hours of darkness (Figure 2.3). Following this, there was limited change in the expression of these proteins in the dark when compared to the light during the first 21 days. After 30 days, downregulation of the majority of LHC proteins across all clades was observed. In addition, oxygen evolving complex 1, photosystem II 12kDa protein and chlorophyll a/b binding protein Fc17531 were also downregulated. There was no change in the expression of ATP synthase subunits following 12 hours. Widespread up-regulation of light harvesting proteins after 120 days of dark exposure compared to continuous light was observed except for those classified in the photo-protective clade (LHCx), which remained downregulated. This was also reflected in proteins involved in the photosynthetic chain: ferredoxin (log2 +1.1-fold), flavodoxin (log2 +1.91 fold), plastocyanin (log2 +1.3-fold) and photosystem II 12kDa protein (log2 +0.5-fold). These were all highly expressed in the dark at 120 days. Re-illumination of dark cells for 24 hours induced significant expression of proteins in the primary light harvesting clades LHC and LHCF, as well as the red-algal-like LHCR clade. In contrast, proteins of the photo-protective LHCx clade were either downregulated or remained unchanged.

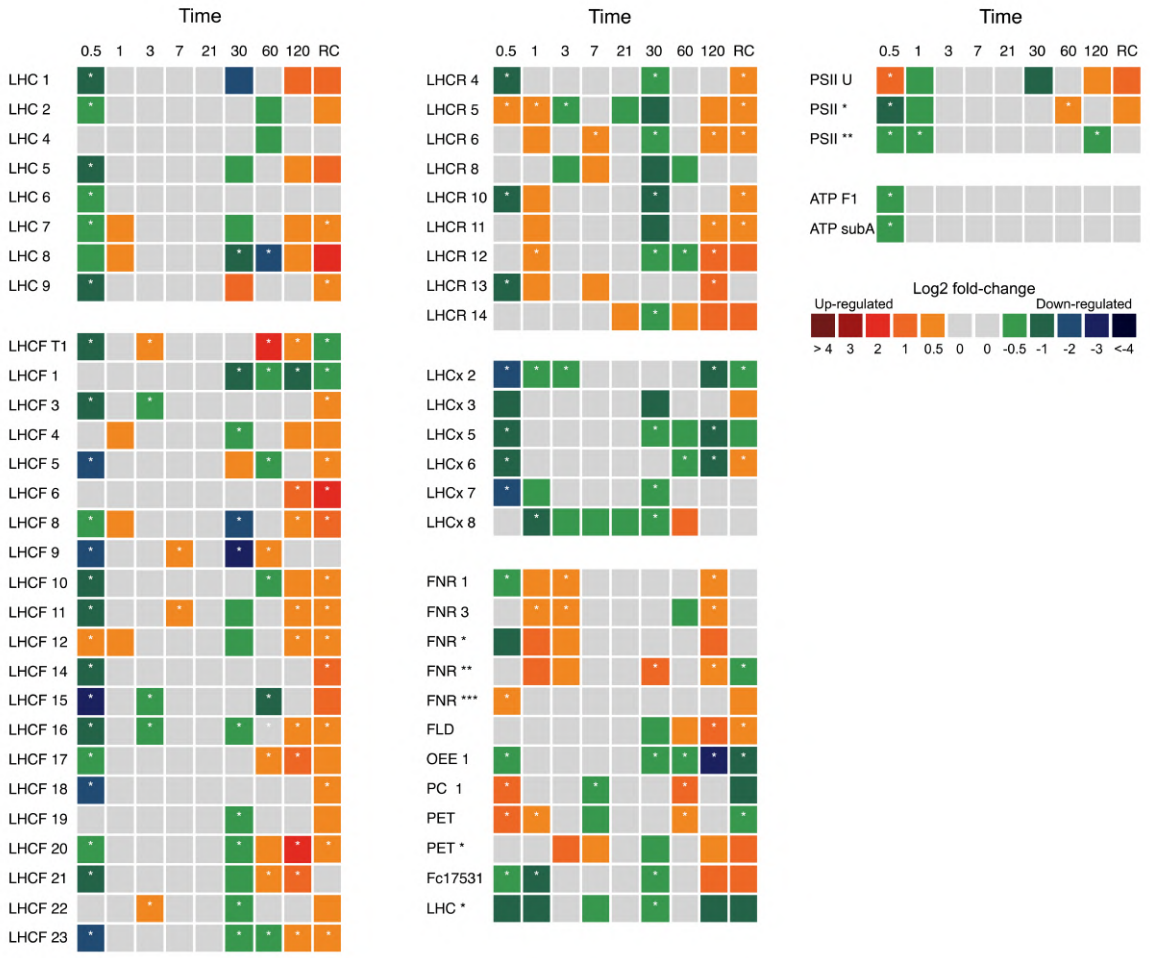

Figure 2.4: Matrix of photosynthesis-associated proteins in dark treated cells when compared to continuous light. Proteins are grouped by relative function and the corresponding clade; antenna proteins (LHCF – major light harvesting, LHCR – red-algal linage, LHCx – photoprotective or LHC – clade unknown) or those involved in oxygenic photosynthesis. Each box represents the relative expression of the proteins indicated, after the duration of dark exposure in days as indicated, with the exception of RC which denotes the dark recovery phase where dark treated cells were re-exposed to white light (50 μmol photon m^{-2} s^{-1}) for 24 hours. The colours represent the protein abundance change (difference in mean $\log_2$ LFQ values, dark vs light). White stars (*) inside boxes represent a significant expression (FDR<2% and $\log_2$ LFQ difference >/<0.5). All expressed proteins have been normalised to relative cell abundance. Abbreviations correspond to the proteins described in Appendix B -Chapter B

The maximum quantum yield (F_v/F_m) of photosystem II (PS_{II}) was similar in both dark and light treated cells over 120 days (Figure 2.5a). In the light, F_v/F_m declined from a pre-incubation mean of 0.585 to a mean of 0.388 on day 120. A similar pattern was observed in the dark, F_v/F_m declined from a mean of 0.577 to 0.461 on day 120. The maximum electron transfer rate ($rETR_{max}$) was

significantly higher ($p<0.05$) in the light than the dark at all time points except day 14. Within 1 hour of dark cells being re-illuminated, the $rETR_{max}$ and F_v/F_m rapidly increased and continued to increase until the final assessment at 24 hours where it was well above the pre-incubation levels.

Non-photochemical quenching (NPQ), which is important to dissipate adverse effects of high light intensities, was, considerably lower in the dark (Figure 2.5b). However, after an initial sharp decline, NPQ in the dark treatment increased from 0.14 on day 1 to 0.41 on day 120. Following re-illumination, NPQ of dark cells continued to increase with increasing light exposure. The photosynthetic parameter alpha (α) was significantly higher in the dark than the light over the course of the experiment (Figure 2.5c) indicating that structural breakdown between the antenna and photosystem II did not occur in the dark. Upon re-illumination of dark treated cells with 50 μmol m^{-2} s^{-1} of white light, α was reduced to pre-incubation levels.

Cellular ATP concentration decreased to undetectable levels after 21 days of dark exposure (Figure 2.5d) and remained at low levels until re-illumination occurred. As ATP concentration is highly unlikely to be zero, the observed concentration may not be attributed to the cells current physiology but is more likely a limitation of the assay where ATP concentration is below the detection limit. Within one hour of re-illumination, cellular ATP concentrations returned to pre-incubation levels. ATP in light treated cell increased from a low of 0.018 pmol $cell^{-1}$ after 12 hours to a high of 0.080 pmol $cell^{-1}$ after 14 days and remained at that level until day 120.

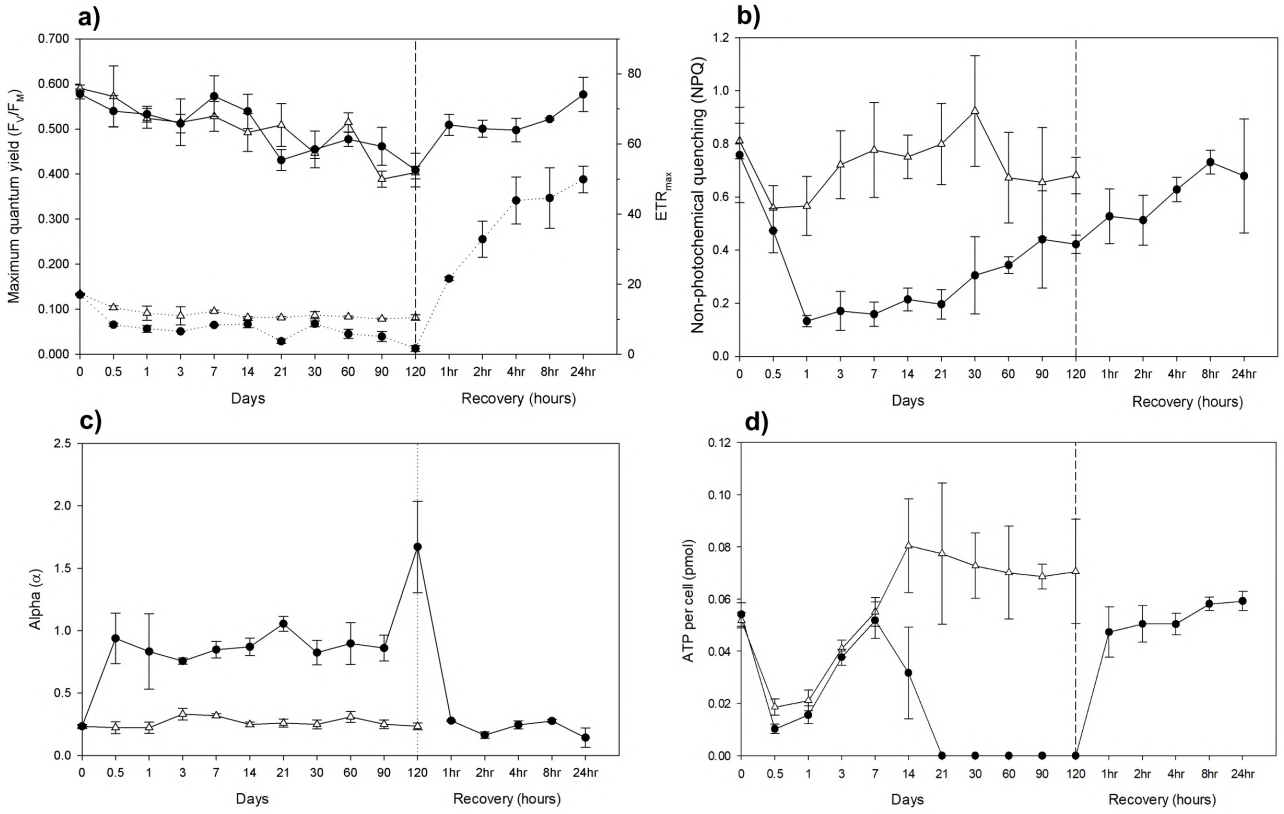

Figure 2.5: **a)** Maximum quantum yield (F_v/F_m) and relative maximum electron transfer rate ($rETR_{max}$) (dotted lines),**b)** Non-photochemical quenching (NPQ), **c)** Photosynthetic parameter alpha (α), **d)** ATP concentration per cell (pmol), of dark (closed circles) and light (open triangles) treated cells. Points after the dashed line represent the re-illumination of dark treated cells for 24 hours at 50 μmol photon m^{-2} s^{-1}. Error bars represent the standard deviation of the mean.

Pigments

While a number of proteins of the tetrapyrrole/chlorophyll biosynthetic pathway were significantly affected in dark treated cells, their expression changes were not co-ordinated. The degree of expression changes and the specific roles of components in the pathway are shown in Figure 2.6. Three days of darkness resulted in the sporadic upregulation of a number of proteins in the pathway, appearing to coincide with a decline in chl*a* concentration (Figure 2.2b). Limited change in expression was observed between days 7 and 21 of dark exposure. Subsequently, four out of nine enzymes in the pathway were significantly upregulated from day 30 to day 120 compared to the light. Two proteins of the pathway remained either unchanged or downregulated throughout the entire experimental period (porphobilinogen synthase (JGI|187290) and Mg-protoporphyrin

IX methyltransferase (JGI|268444)). It remains unclear as to the exact reason for the contrasting expression of this pathway in the dark when compared to the light.

Providing essential precursors for the synthesis of chlorophyll, carotenoids and tocopherols, the methylerythritol phosphate (MEP) and the mevalonate pathways (MVA) are closely associated. Contrasting protein expression was observed in the MEP pathway (Figure 2.6), where geranylgeranyl reductase (JGI|179770) was heavily upregulated towards the latter part of dark exposure. Geranylgeranyl reductase provides phytol for both chlorophyll and tocopherol synthesis. Interestingly its upregulation coincided with the upregulation of a protein involved in the key methylation step of tocopherol synthesis (2-methyl-6-phytyl 1,4-benzo-quinone/2-methyl-6-solanyl 1,4-benzoquinone methyltransferase (MPBQ/MSBQ - JGI|197116) (Figure 2.6). Proteins of the cytosolic MVA pathway were largely upregulated; particularly the ATP-dependant enzymes mevalonate kinase (JGI|188664) and mevalonate diphosphate decarboxylase (JGI|198850) (Figure 2.6).

Proteins of the carotenoid biosynthetic pathway were not coordinately expressed in the dark when compared to the light (Figure 2.7). Phytoene desaturase (JGI|213515, JGI|270748) and β-carotene desaturase (JGI|229199) were predominately downregulated, whereas two violaxanthin de-epoxidases, which are important in the generation of non-photochemical quenching (also called diadinoxanthin de-epoxidase), were upregulated but at different times.

Figure 2.6: Expression of proteins involved in the pathways of tetrapyyrole synthesis, methylerythritol pathway (MEP) and the mevalonate pathway (MVA) in the dark when compared to the light. Each box represents the relative expression of the proteins indicated, after the duration of dark exposure in days as indicated, with the exception of RC which denotes the dark recovery phase where dark treated cells were re-exposed to white light (50 μmol photon m^{-2} s^{-1}) for 24 hours. The colours represent the protein abundance change (difference in mean $\log_2$ LFQ values, dark vs light) on the scale shown. White stars (*) inside boxes represent a significant expression (FDR<2% and $\log_2$ LFQ difference >/<0.5). All expressed proteins have been normalised to relative cell abundance.

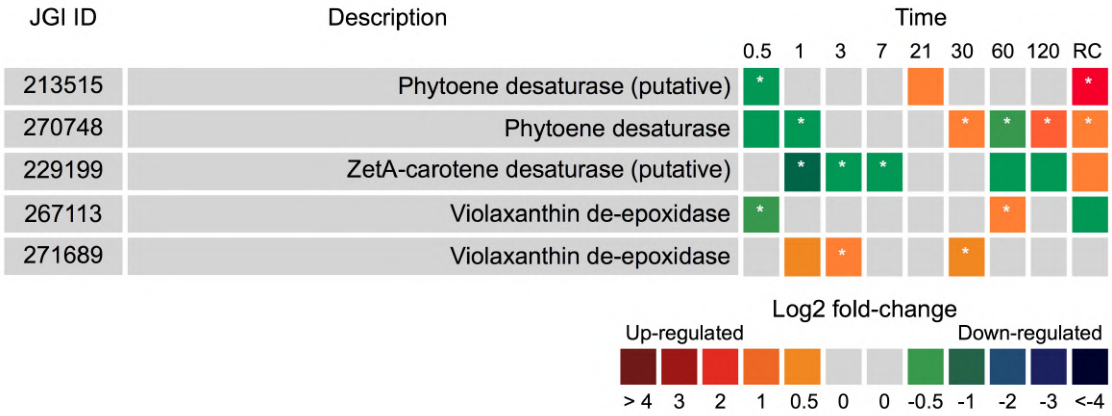

Figure 2.7: Expression of proteins involved in the biosynthesis of carotenoids in the dark when compared to the light. Each box represents the relative expression of the proteins indicated, after the duration of dark exposure in days as indicated, with the exception of RC which denotes the dark recovery phase where dark treated cells were re-exposed to white light (50 μmol photon m^{-2} s^{-1}) for 24 hours. The colours represent the protein abundance change (difference in mean $\log_2$ LFQ values, dark vs light) on the scale shown. White stars (*) inside boxes represent a significant expression (FDR<2% and $\log_2$ LFQ difference >/<0.5). All expressed proteins have been normalised to relative cell abundance.

Calvin Cycle

The majority of proteins involved in the Calvin cycle were downregulated in response to extended darkness when compared to the light (Figure 2.8). This was not surprising as the three main functional proteins involved: ribulose-1,5 bisphosphate carboxylase/oxygenase (RUBISCO, JGI|274497), fructose-1,6- bisphosphatase (FBPase, JGI|1739843, JGI|158118, JGI|212570) and sedoheptulose 1,7-bisphophate (SBPase, JGI|271643) are activated by photosynthesis-associated reactions. All proteins of the Calvin cycle were observed; widespread downregulation occurred on days 7, 30, 60 and 120. Re-illumination for 24 hours failed to alter the expression of most Calvin cycle proteins.

Figure 2.8: Expression of proteins involved in the Calvin cycle in the dark when compared to the light. JGI ID corresponds to the Joint Genome Institute identification number of that particular protein. Each box represents the relative expression of the proteins indicated, after the duration of dark exposure in days as indicated, with the exception of RC which denotes the dark recovery phase where dark treated cells were re-exposed to white light (50 μmol photon m^{-2} s^{-1}) for 24 hours. The colours represent the protein abundance change (difference in mean $\log_2$ LFQ values, dark vs light) on the scale shown. White stars (*) inside boxes represent a significant expression (FDR<2% and $\log_2$ LFQ difference >/<0.5). All expressed proteins have been normalised to relative cell abundance.

2.3.3 Respiratory metabolism

Glycolysis and the Entner-Doudoroff pathway

Glycolysis occurs in two phases; the upper (preparatory) and lower (pay-off) phases. Conventionally, the upper-phase begins in the chloroplast and completes in the cytosol. However, all chloroplast and cytosol-targeted glycolytic proteins were downregulated during prolonged darkness, particularly from day 30 (Figure 2.9). After 30 days of darkness, a number of lower-phase glycolytic proteins, thought to be mitochondrial targeted, were upregulated. This coincided with the unexpected expression of proteins involved in a mitochondrial Entner-Doudoroff pathway (EDP) (Figure 2.9).

A number of glycolysis proteins can also function in reverse for gluconeogenesis to form glucose from pyruvate. The use of this pathway during darkness seems unlikely as the specific enzymes of the pathway were downregulated, specifically two pyruvate carboxylase (PEP) and three phosphoenolpyruvate carboxylase (PEPCK) isozymes.

The anabolic pentose phosphate pathway runs parallel to that of glycolysis. In response to dark exposure, the proteins involved in the pentose phosphate pathway were heavily downregulated compared to the light (Figure 2.9).

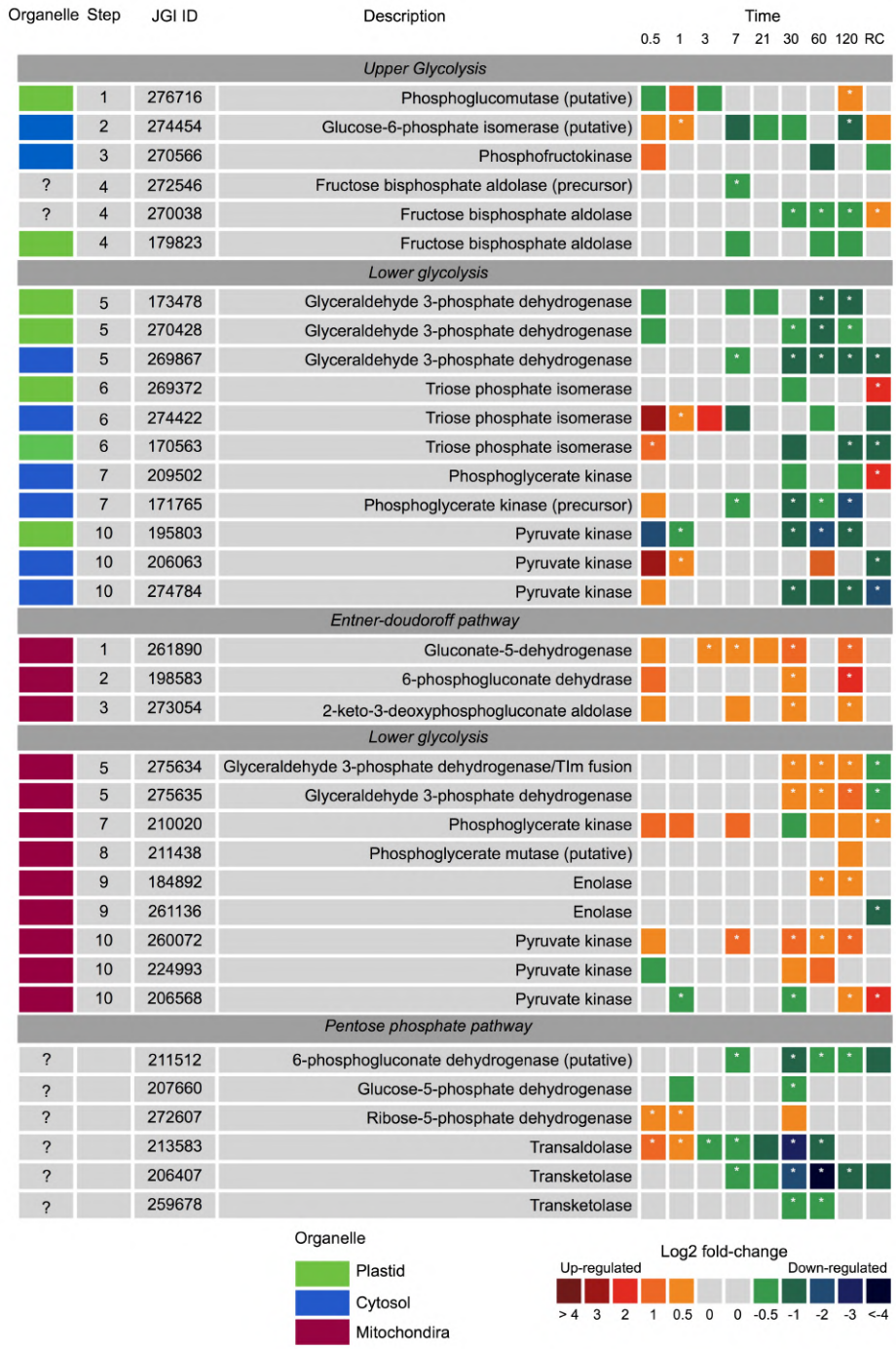

Figure 2.9: Expression of proteins involved in glycolysis, Entner-doudoroff and pentose phosphate pathways in the dark when compared to continuous light. JGI ID corresponds to the Joint Genome Institute identification number of that particular protein. Organelle indicates the proteins suggested cellular location. Each box represents the relative expression of the proteins indicated, after the duration of dark exposure in days as indicated, with the exception of RC which denotes the dark recovery phase where dark treated cells were re-exposed to white light (50 μmol photon m^{-2} s^{-1}) for 24 hours. The colours represent the protein abundance change (difference in mean $\log_2$ LFQ values, dark vs light) on the scale shown. White stars (*) inside boxes represent a significant expression (FDR<2% and $\log_2$ LFQ difference >/<0.5). All expressed proteins have been normalised to relative cell abundance.

Tricarboxylic acid cycle (TCA), pyruvate and mitochondrial electron transport chain

The TCA cycle is located in the mitochondrial matrix where it catalyses the complete aerobic oxidation of pyruvate to form CO_2, ATP, NADH, and carbon skeletons for biosynthetic processes. The TCA cycle was widely upregulated in the dark compared to the light, especially on days 30, 60 and 120. The eight main TCA cycle reactions are summarised in Figure 2.10.

Imperative for TCA cycle function is a source of pyruvate. Proteins of the 2-oxoacid dehydrogenase multienzyme family involved in the production of pyruvate were upregulated in the dark (Figure 2.10). These comprise the pyruvate dehydrogenase complex (PDHC), oxoglutarate dehydrogenase complex (ODHC), and the branched-chain 2-oxoacid dehydrogenase (BCODH).

Although specifically unrelated to the TCA cycle, L-lactate dehydrogenase (JGI|274468) was also heavily upregulated in the dark from day 30 to day 120. This protein catalyzes the reversible conversion of lactate into pyruvate. Similarly, malic enzyme (JGI|173391) which also forms pyruvate (from malate, reversible), was heavily upregulated in the dark from day 30 (Figure 2.10). Methylmalonyl-CoA mutase (JGI|273786) was highly upregulated throughout dark exposure (Figure 2.10). This mitochondrial enzyme forms succinyl-CoA for use in the TCA cycle via the breakdown of odd-chain fatty acids, or branched chain amino acids.

Utilising precursors of the TCA cycle to generate energy across the mitochondrial membrane are the series of enzyme complexes of the electron transport chain (mETC). Complexes I, II and V but not III and IV were observed. These enzyme complexes were primarily upregulated towards the latter half of dark exposure when compared to the light (Figure 2.11a).

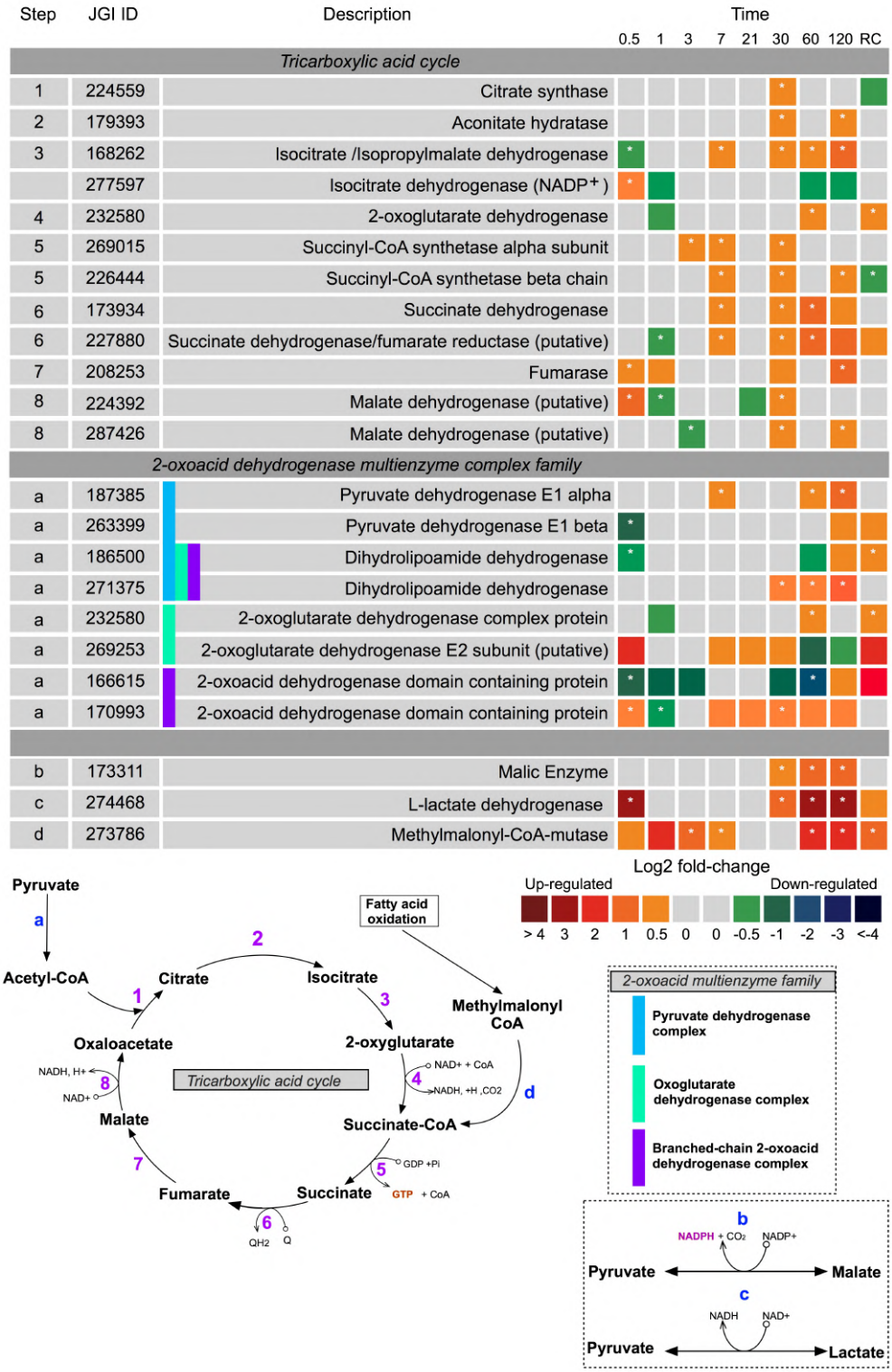

Figure 2.10: Expression of proteins involved tricarboxylic acid pathway and pyruvate metabolism in the dark when compared to the light. Steps corresponds to the stage in which a protein appears in the biosynthetic pathway. JGI ID corresponds to the Joint Genome Institute identification number of that particular protein. Each box represents the relative expression of the proteins indicated, after the duration of dark exposure in days as indicated, with the exception of RC which denotes the dark recovery phase where dark treated cells were re-exposed to white light (50 μmol photon m^{-2} s^{-1}) for 24 hours. The colours represent the protein abundance change (difference in mean $\log_2$ LFQ values, dark vs light) on the scale shown. White stars (*) inside boxes represent a significant expression (FDR<2% and $\log_2$ LFQ difference >/<0.5). All expressed proteins have been normalised to relative cell abundance.

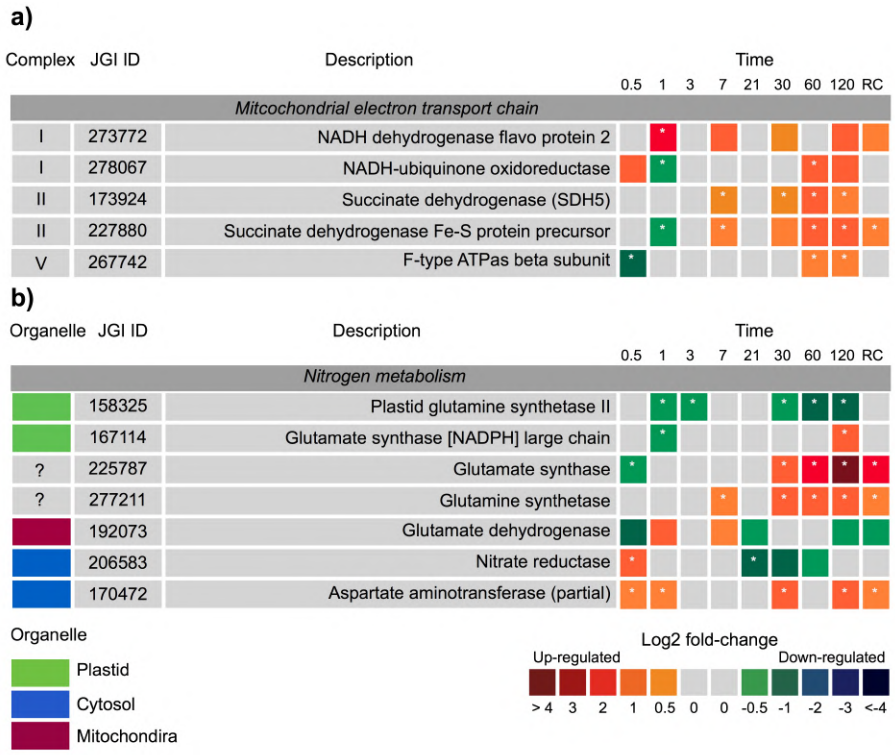

Figure 2.11: Expression of proteins involved in a) the mitochondrial electron transport chain and b) nitrogen metabolism in the dark when compared to the light. Complex refers to the denoted protein complex number of the transport chain, whereas organelle indicates the proteins suggested cellular location. JGI ID corresponds to the Joint Genome Institute identification number of that particular protein. Each box represents the relative expression of the proteins indicated, after the duration of dark exposure in days as indicated, with the exception of RC which denotes the dark recovery phase where dark treated cells were re-exposed to white light (50 μmol photon m^{-2} s^{-1}) for 24 hours. The colours represent the protein abundance change (difference in mean $\log_2$ LFQ values, dark vs light) on the scale shown. White stars (*) inside boxes represent a significant expression (FDR<2% and $\log_2$ LFQ difference >/<0.5). All expressed proteins have been normalised to relative cell abundance.

2.3.4 Urea cycle and nitrogen metabolism

Proteins of the urea cycle were significantly upregulated in the dark when compared to the light but were not all co-ordinately expressed. Argininosuccinate synthase (JGI|207847 and JGI|213508) and argininosuccinate lyase (JGI|215156) were the only proteins in the cycle to be significantly downregulated from day 30 of dark exposure (Figure 2.12). All other proteins were predominately upregulated, primarily on day 0.5 and from day 30 to day 120.

Several auxiliary pathways of the urea cycle were observed in the dark. Firstly, two precursors involved in the formation of proline were predominantly upregulated (ornithine transaminase (JGI|269005) and pyrroline-5-carboxylate reductase (JGI|191403)). Secondly, two proteins essential in the production of polyamines were also upregulated (Fig.2.12), including a putative putrescine-forming ornithine decarboxylase (JGI|227544) and spermidine forming spermidine synthase (JGI|278171).

The glutamate cycle (or GS/GOGAT cycle) plays a central role in the recycling and assimilation of nitrogen (Fig.2.11b). Two glutamine synthase proteins were observed in the experiments; a plastid located glutamine synthase II (GSII) (JGI|158325) and glutamine synthase (GS) (JGI|277211). The former was consistently downregulated under dark conditions, while the latter was heavily upregulated from day 30. GS expression coincided with significant upregulation of a glutamate synthase (GOGAT) on day 30 (JGI|225787) and a cytoplasmic aspartate aminotransferase (AST) (JGI|170472); both are involved in the primary assimilation of ammonium. Nitrate reductase (JGI|206583) which assimilates nitrate was downregulated from day 21 (dark).

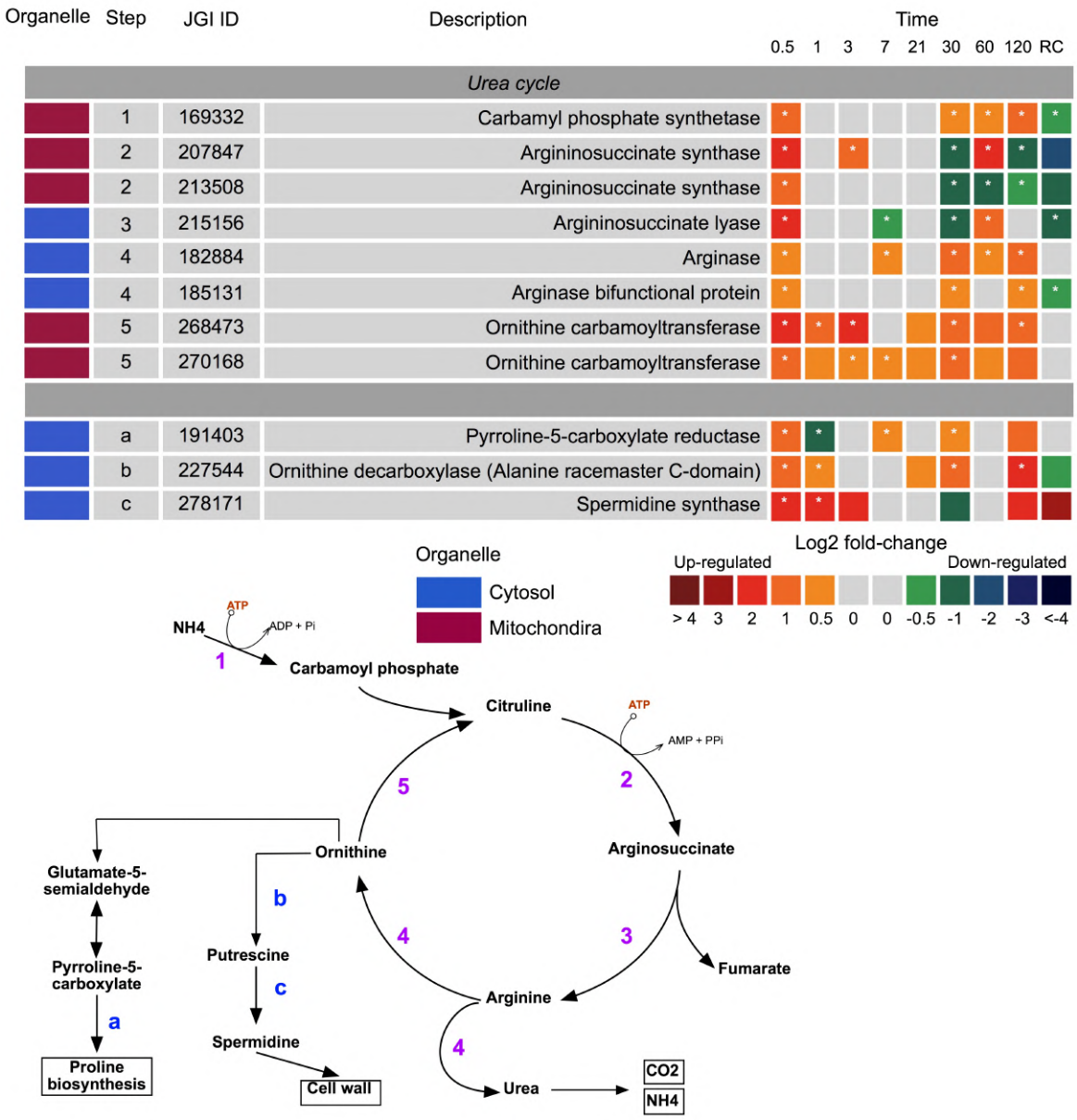

Figure 2.12: Expression of proteins involved in the urea cycle and auxillaries in the dark when compared to the light. JGI ID corresponds to the Joint Genome Institute identification number of that particular protein. Each box represents the relative expression of the proteins indicated, after the duration of dark exposure in days as indicated, with the exception of RC which denotes the dark recovery phase where dark treated cells were re-exposed to white light (50 μmol photon m^{-2} s^{-1}) for 24 hours. The colours represent the protein abundance change (difference in mean $\log_2$ LFQ values, dark vs light) on the scale shown. White stars (*) inside boxes represent a significant expression (FDR<2% and $\log_2$ LFQ difference >/<0.5). All expressed proteins have been normalised to relative cell abundance.

2.3.5 Fatty-acid biosynthesis and B-oxidation

Proteins involved in the synthesis of fatty acids were predominantly downregulated in the dark compared to the light (Figure 2.13). UDP-sulfoquinovose synthase (putative: JGI|268690), which forms the important thylakoid lipid SQDG, was upregulated in the dark from 12 hours. The hydrophobic molecule carrier protein lipocalin (JGI|268796) was also upregulated in the dark from day 3. A number of proteins involved in fatty acid β-oxidation were upregulated toward the latter part of the dark incubation (Figure 2.13).

2.3.6 Transcription, translation and proteolysis

Ribosomal proteins were largely downregulated following 12 hours of darkness (Figure 2.14). After day 1, these ribosomal proteins were strongly upregulated compared to continuous light. Subsequently, there was limited change in the expression of these proteins until day 60 when a number of ribosomal 40S subunit proteins were significantly upregulated. In contrast, following 120 days of dark exposure, most ribosomal proteins were downregulated. Re-illumination of dark cells for 24 hours failed to alter the expression of many ribosomal proteins.

The down-regulation of most ribosomal proteins on day 120 of dark exposure coincided with the up-regulation of a number of serine and cysteine protease's, in addition to ubiquitin-containing proteins and proteasome subunits (Figure 2.15). Dark proteolytic subunits that are ATP-dependant were predominately downregulated.

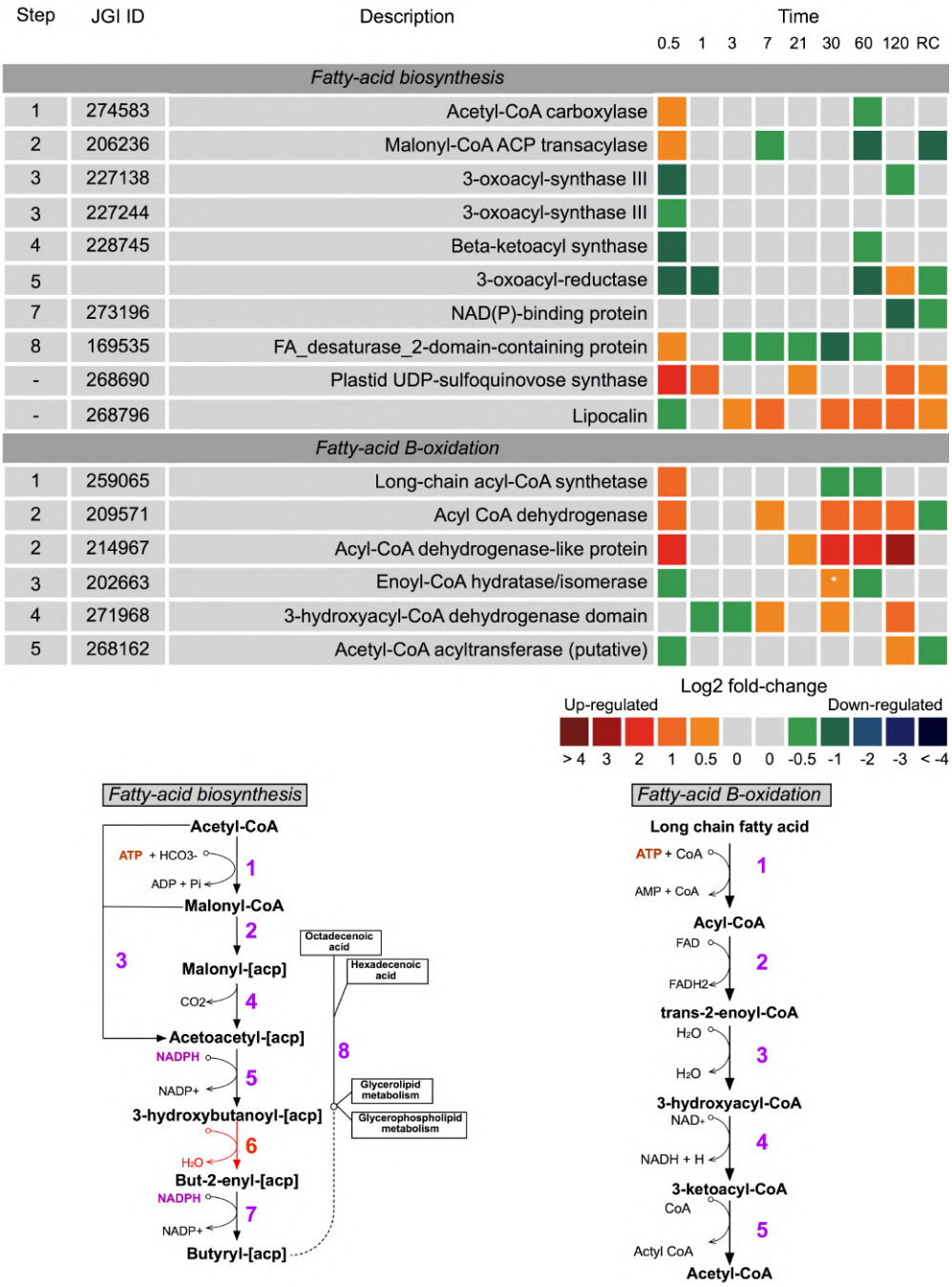

Figure 2.13: Expression of proteins involved in the biosynthesis or β-oxidation of fatty-acids in the dark when compared to the light. JGI ID corresponds to the Joint Genome Institute identification number of that particular protein. Each box represents the relative expression of the proteins indicated, after the duration of dark exposure in days as indicated, with the exception of RC which denotes the dark recovery phase where dark treated cells were re-exposed to white light (50 μmol photon m^{-2} s^{-1}) for 24 hours. The colours represent the protein abundance change (difference in mean $\log_2$ LFQ values, dark vs light) on the scale shown. White stars (*) inside boxes represent a significant expression (FDR<2% and $\log_2$ LFQ difference >/<0.5). All expressed proteins have been normalised to relative cell abundance.

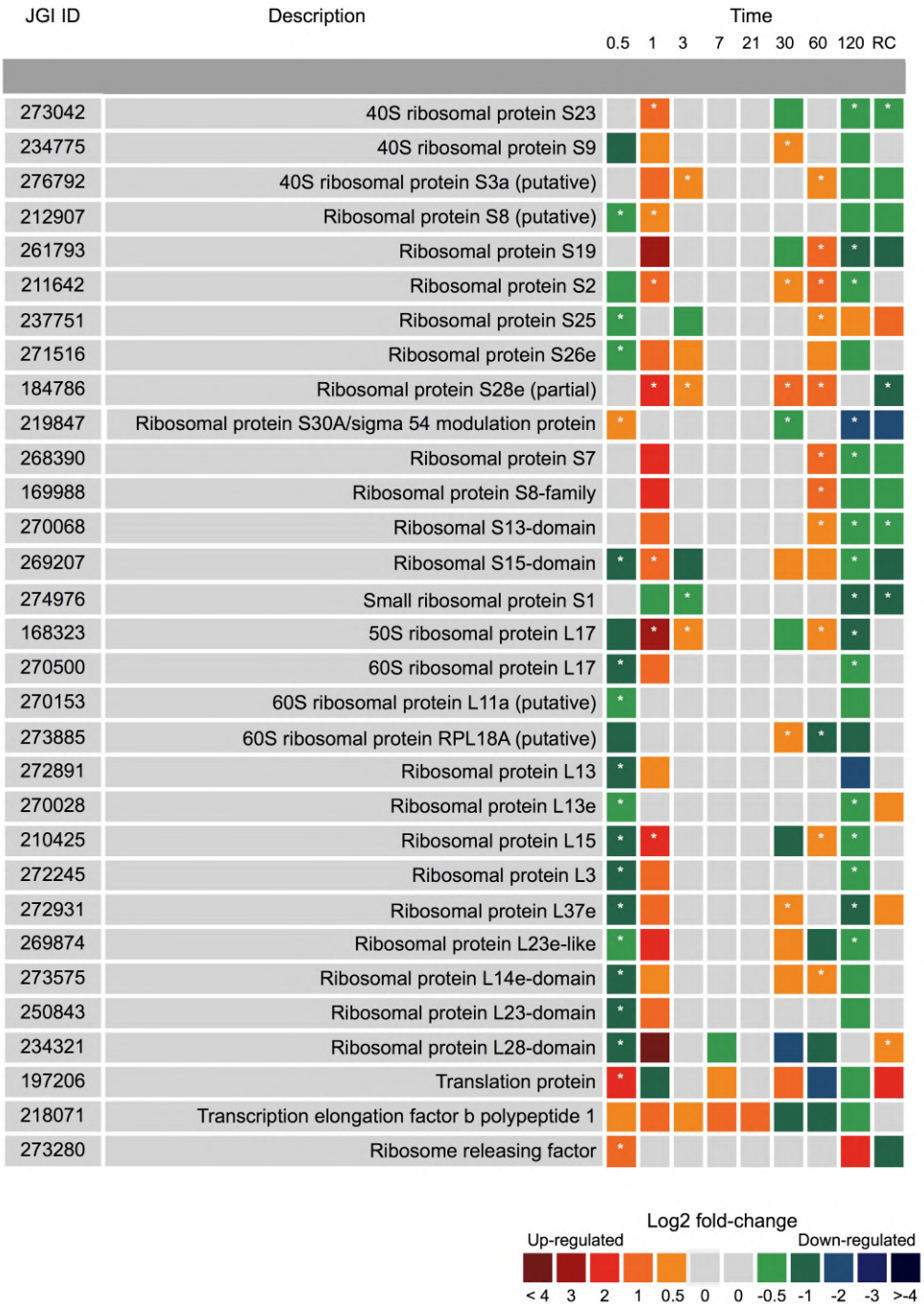

Figure 2.14: Expression of proteins involved in transcription and translation the dark when compared to the light. JGI ID corresponds to the Joint Genome Institute identification number of that particular protein. Each box represents the relative expression of the proteins indicated, after the duration of dark exposure in days as indicated, with the exception of RC which denotes the dark recovery phase where dark treated cells were re-exposed to white light (50 μmol photon m^{-2} s^{-1}) for 24 hours. The colours represent the protein abundance change (difference in mean $\log_2$ LFQ values, dark vs light) the scale shown. White stars (*) inside boxes represent a significant expression (FDR<2% and $\log_2$ LFQ difference >/<0.5). All expressed proteins have been normalised to relative cell abundance.

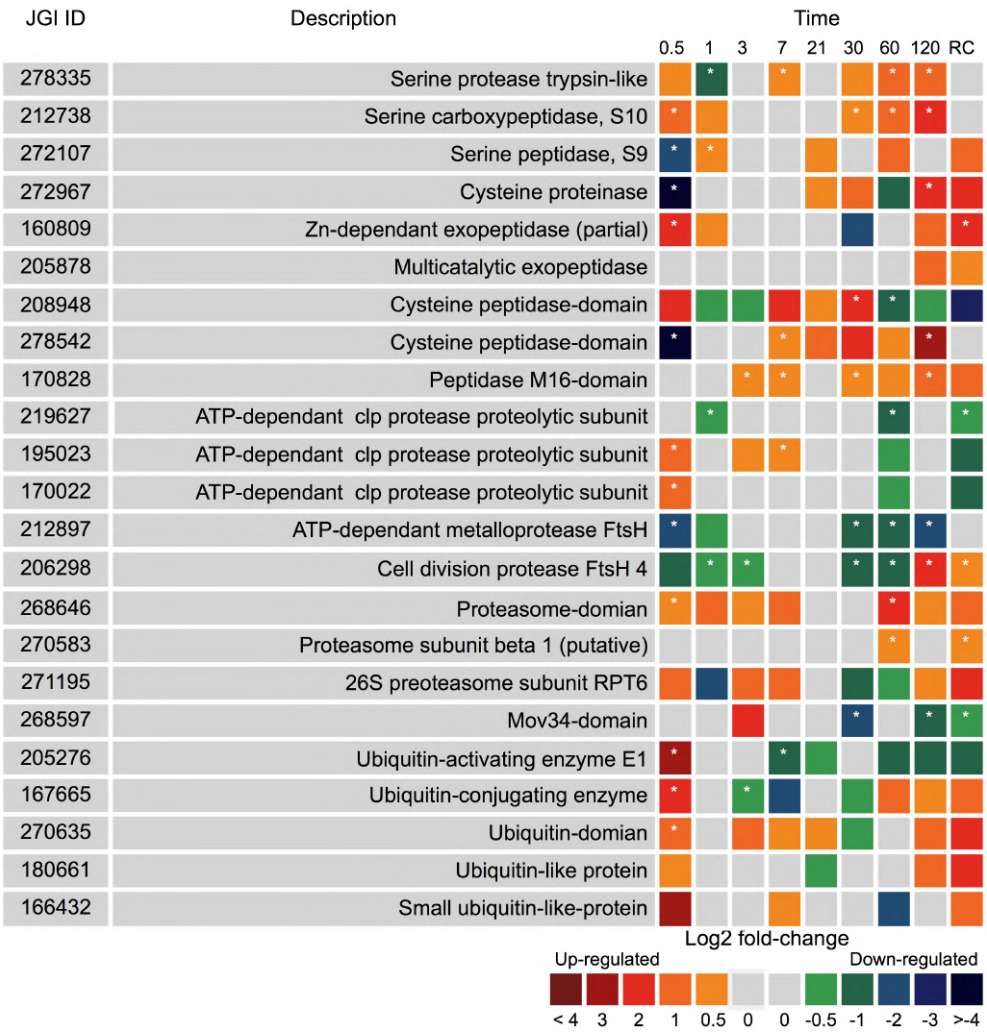

Figure 2.15: Expression of proteins involved in proteolysis the dark when compared to the light. JGI ID corresponds to the Joint Genome Institute identification number of that particular protein. Each box represents the relative expression of the proteins indicated, after the duration of dark exposure in days as indicated, with the exception of RC which denotes the dark recovery phase where dark treated cells were re-exposed to white light (50 μmol photon m^{-2} s^{-1}) for 24 hours. The colours represent the protein abundance change (difference in mean $\log_2$ LFQ values, dark vs light) the scale shown. White stars (*) inside boxes represent a significant expression (FDR<2% and $\log_2$ LFQ difference >/<0.5). All expressed proteins have been normalised to relative cell abundance.

2.4 Discussion

This is the first study to examine the proteome of a prominent sea-ice diatom in response to extended darkness. It has been successful in illustrating the capacity of *Fragilariopsis cylindrus* to survive four months of darkness and retain photosynthetic viability. Examination of the proteome

demonstrates the ability of the species to utilise cellular resources to sustain dark metabolism.

This study should be viewed with an understanding of the likely effect of constant light, which may influence the protein comparisons. Cells grown in constant light likely experienced oxidative stress which can affect consumption of photosystem products via the Calvin-Benson cycle. As a result, some protein expressions may be over or underestimated. Despite this caveat, this is the first study to examine the proteome of a sea-ice diatom over an extended period of darkness and a comparison with cells in constant light was a necessary limitation. This study is intended to provide a foundation for future studies on the long-term dark metabolism of sea-ice diatoms.

2.4.1 Light harvesting and photosynthetic pathway

A number of the proteins involved in light harvesting identified in this study were significantly altered in abundance during extended darkness. Within 12 hours, proteins from all clades of the light harvesting apparatus were downregulated, with the LHCx photoprotective clade being heavily downregulated. This finding is similar to that of Mock et al. (2017), who also observed the widespread reduction in the regulation of photosystem genes in the dark. Interestingly, these authors only observed this trend after 7 days; it remains unclear why photosynthetic proteins in this study were so rapidly downregulated. Within one hour of light re-exposure after 120 days of darkness, rETRmax exhibited higher levels following dark exposure than the pre-treatment, indicating that cells regained and even improved their photosynthetic performance upon re-illumination. A similar response in rETRmax following re-illumination was observed by Nymark et al. (2013) and this may illustrate that the photosynthetic apparatus of *F. cylindrus* does not degrade during extended darkness. This adaptive response has been noted in previous studies with polar diatoms, whereby the photosynthetic apparatus is maintained so that photosynthesis can resume rapidly upon return to favourable light conditions (Bunt and Lee, 1972; McMinn and Martin, 2013; Palmisano and Sullivan, 1982; Peters and Thomas, 1996; Schaub et al., 2017). Furthermore, if degradation of light-harvesting antenna complexes was occurring, a gradual reduction in the photosynthetic parameter α would be apparent, as resonance energy transfer between the antenna and photosystem II would become inefficient due to physical breakdown (Falkowski

and LaRoche, 1991; Nymark et al., 2013; Vernotte et al., 1992). This appears unlikely as α was maintained. Additionally, the widespread upregulation of LHCF and LHCR proteins at day 120 of dark exposure implies that cells were actively regulating and maintaining photosystem proteins.

To ensure photosystem functionality, continuous transport across multiple membranes needs to be protected and maintained. Any depletion in macromolecule transporters in thylakoid membranes would result in the degradation of the light harvesting complex. Diatom thylakoids are enriched with the anionic lipid sulfoquinovosyldiacylglycerol (SQDG), which accounts for over 40% of the total lipid content (Schaub et al., 2017). In this study, while speculative, an increased expression of a plastid UDP-sulfoquinovose synthase, which is essential for the production of SQDG, was observed in the dark. The potential function of SQDG in thylakoid membranes may be like that of higher plants and green algae where negatively charged lipids associate and interact with plastidic ATP synthase (Joshi et al., 2009; Pick et al., 1987). In addition, the outer lamellae of low-light adapted diatoms have been shown to be enriched in SQDG, ATP synthase and photosystem I (PSI) complexes (Pyszniak and Gibbs, 1992). This supports the concept that SQDG may act to help maintain thylakoid membrane integrity and protect the functionality of ATP synthase. Additionally, maintenance of chloroplasts in the dark may also involve the energisation of thylakoid membrane via chlororespiration. Chlororespiration has been shown to facilitate the maintenance of ATP synthase during prolonged darkness, enabling rapid ATP production upon re-illumination (Feild et al., 1998; Jakob et al., 1999; Lavaud et al., 2012, 2002; Nixon, 2000; Wilhelm et al., 2006). The de-epoxidation of diadinoxanthin is correlated with increased non-photochemical quenching (NPQ) of photosystem II fluorescence. NPQ increased from day 30 (dark), which is consistent with the results of Jakob et al. (2001), who showed that de-epoxidation of the xanthophyll cycle and subsequent increase in NPQ was highest during long-term dark exposure in *Phaeodactylum tricornatum*. Upon re-illumination, ATP concentration in dark exposed cells rapidly returned to pre-treatment levels within 1 hour and continued to increase over the next 24 hours. This not only infers active ATP synthase maintenance in the dark, but also indicates that cells may retain a fully functional light harvesting complex.

Diatoms contain two main pigment groups: chlorophyll *a* (chl*a*) and chlorophyll *c* (chl*c*). Chl*a*

is the main photochemical energy conversion pigment, whereas chl*c* is effectively an accessory antenna pigment. Chl*c* is synthesized in the same fashion as chl*a* but appears to diverge from that pathway (Hoober and Eggink, 2001; Kuczynska et al., 2015; Zapata et al., 2006). In addition to light harvesting, chl*c* has been postulated to help in the promotion and stablisation of the light harvesting complex assembly (Hoober et al., 2007). LHC of plants and algae usually contain an oxidized form of chlorophyll (*b* or *c*) in addition to chl*a*. This results in stronger connections between the pigments and the ligands of the apoproteins, thus stabilizing the structure and promoting the assembly within the chloroplast (Hoober et al., 2007; Zapata et al., 2006). It is tempting to speculate that the upregulation of protochlorophyllide oxidoreductase, thought to be the branching point, could indicate a diversion to chlorophyll *c* production. However more work needs to be conducted to substantiate this claim.

The precise function of tocopherols in photosynthetic organisms has yet to be determined but is likely to be similar to animals where they help maintain membrane integrity, act as antioxidants, and scavenge free radicals (Krieger-Liszkay and Trebst, 2006; Zhang and Bryant, 2014). Two mechanisms can provide the necessary phytyl-diphosphate (phytyl-PP) for tocopherol synthesis, either through the MEP pathway or via chlorophyll degradation (Tanaka et al., 1999). It appears that chlorophyll degradation was not substantial during extended darkness, as cellular chl*a* concentration remained constant from day 21 (dark). Upregulation of geranylgeranyl reductase of the MEP pathway forms the necessary phytyl-PP for both chlorophyll and tocopherol synthesis (von Wettstein et al., 1995)). Additionally, MPBQ/MSBQ MT was also upregulated, which catalyses the key methylation step in the production of tocopherols in the dark (Cheng, 2003; Mokrosnop, 2014). Tocopherols can stabilise membrane structure and integrity by scavenging reactive oxygen species (ROS), free radicals and block peroxidation of membrane lipids (Cheng, 2003; Krieger-Liszkay and Trebst, 2006; Mokrosnop, 2014). The primary source of ROS is as a by-product of photosynthesis, however in the dark it is via mitochondrial respiratory processes (Drábková et al., 2007; Nymark et al., 2009; Waring et al., 2010). Diatoms respond to oxidative stress by increasing the concentration of superoxide dismutase (SOD) (Wolfe-Simon et al., 2006), and catalase/hydroperoxidase

(CAT) enzymes (Graff van Creveld et al., 2016). Several putative SOD and CAT enzymes increased during prolonged darkness, which may indicate amplified oxidative stress.

2.4.2 Respiratory metabolism

Diatoms are unique in that they are the only photosynthetic organisms with a mitochondrial-targeted glycolytic pathway (Kroth et al., 2008; Smith et al., 2012). It is unknown if this is an ancient trait or one that has been recently acquired via gene transfer (Ginger et al., 2010). The observed downregulation of plastid/cytosolic-targeted glycolytic proteins in the dark and the up-regulation of mitochondrial lower phase proteins suggests significant metabolic plasticity. The physical association of glycolysis with the mitochondria negates the need to transport pyruvate and NADH into the organelle to supply the TCA cycle during dark respiration. Additionally, the recently discovered mitochondrial Entner-Doudoroff pathway (EDP) in diatoms can provide the necessary glyceraldehyde 3-phosphate for the lower phase and supplement pyruvate for the TCA cycle (Fabris et al., 2012). The EDP is considered to be an ancient form of glycolysis that is predominately restricted to prokaryotic lineages. EDP gene sets have are also been found in *Thalassiosira pseudonana* and *Phaeodactylum tricornutum*, seemingly obtained via horizontal gene transfer (Chen et al., 2016; Fabris et al., 2012). The regulation of the EDP has been hypothesised, like glycolysis, to be associated with the cellular energy status with pathway flux dependent on ATP concentration (Schuetz et al., 2007). Cellular ATP concentration declined to undetectable limits in the dark from day 21, likely triggering the cell to initiate glycolysis and the EDP. Upregulation here suggests that the EDP may be regulated by both cellular energetics and light modulation. A similar observation was noted by Fabris et al. (2012) in *P. tricornutum*, where gene transcripts for EDA increased in the dark. Although the EDP provides less energy per molecule of glucose than the conventional glycolytic route (with net yield of 1 ATP, 1 NADH and 1 NADPH and 2 pyruvate. Glycolysis: 2 ATP, 2 NADH and 1 pyruvate), it requires less resources to synthesise the necessary enzymes (Fabris et al., 2012; Wessely et al., 2011). Coordination of several metabolic routes derives from the necessity to conserve energy, and the move to energetic inefficiency is essentially a trade-off between the high operation costs of alternate catabolic processes and the low investment of enzyme synthesis. Additionally, the EDP may serve as a rapid by-pass to balance the production of NADPH/ATP and

increase pyruvate input into the TCA cycle (Kramer and Evans, 2011). Exactly why the ATP pool in the dark did not increase following the activation of respiratory pathways remains unclear. It may imply that the rate of consumption required to maintain essential metabolic processes are equal to, or exceed, that of production. This is highly likely if substrate level phosphorylation is the main ATP generating mechanism, as it produces less ATP than oxidative phosphorylation and is generally unable to replenish the ATP pool (Bottomley and Stewart, 1976).

The tricarboxylic acid cycle, pyruvate and the mitochondrial electron transport chain

TCA cycle proteins were coordinately expressed in the dark and predominantly upregulated from day 30. The delayed upregulation appears to correspond with the expression of the EDP and lower-phase mitochondrial glycolytic proteins. The cycle is also likely being sustained in the dark through the action of multiple anaplerotic enzymes which act to replenish TCA cycle intermediates. For example, malic enzyme to pyruvate, aspartate aminotransferase to 2-oxoglutarate and β-oxidation of fatty acids via succinyl-CoA. The TCA cycle is a series of catabolic reactions that support energy transduction, but it is also entangled in a broader network that augments multiple features of metabolism. For example, the TCA cycle has been shown to be tightly regulated with the urea cycle in diatoms (Allen et al., 2011). The urea cycle in this study did indeed appear to be coordinated with the TCA cycle and may serve as a center for the connection of carbon and nitrogen metabolism, both of which are critical in balancing the demand for cellular processes when carbon fixation is abolished. A key regulatory point for the TCA cycle flux, and crucial to its linkage with glycolysis, is the pyruvate dehydrogenase complex (PDHC) of the 2-oxoacid dehydrogenase multienzyme complex family (Tovar-Méndez et al., 2003), but may also be regulated by thioredoxin (Daloso et al., 2015). While it remains unclear in this study, it is probable that thioredoxin is not a major regulator. It is possible that the collective up-regulation of the PDHC may indicate amplified acetyl-CoA flux into the TCA cycle.

Coupled with the TCA cycle, the mitochondrial electron transport chain generates ATP in the absence of photosynthesis. The upregulation of complexes I, II and V, in the dark and the corresponding expression of proteins involved in both the TCA cycle and glycolysis indicate increased

oxidative phosphorylation. This is especially apparent from day 30 of dark exposure and may highlight a specific threshold in the capacity of cells to survive in the absence of photosynthesis without mobilizing reserves or inducing catabolism of non-essential metabolic components. Although when considering the observed ATP levels from day 21, any increase in abundance of oxidative phosphorylation processes must be viewed with caution as the protein abundance of oxidative phosphorylation process in cells exposed to constant light are not regulated when photo-phosphorylation is the primary energy generator. This may result in an overestimation in the abundance of dark oxidative phosphorylation proteins, exacerbating the expression of this pathway in the dark. Metabolic flux measurements would be useful to further explore dark respiratory processes.

Urea cycle and nitrogen metabolism

The main route of nitrogen assimilation in diatoms is via the reduction of nitrate by nitrate reductase (NR) in the cytosol. In this study, active uptake of nitrate in the dark is unlikely due to the energetic requirements for assimilation and downregulation of a NR enzyme. Instead, utilisation of other nitrogenous forms may be occurring. The use of NH_3/NH_4^+ formed through the catabolism of proteins and amino acids, is likely re-assimilated through GS/GOGAT enzymes. Significant expression of enzymes involved in the catabolism of proteins and amino acids suggests heightened NH_3/NH_4^+ formation. In addition, the downregulation of a plastid GSII and NADPH-GOGAT and up-regulation of GS/GOGAT with evidence for mitochondrial export, may infer heightened NH_3/NH_4^+ assimilation. Tight association between the mitochondria and GS/GOGAT is essential as it is dependent on the input of carbon skeletons in the form of 2-oxoglutarate derived from the TCA cycle.

Similarly associated with both pathways is the urea cycle, which in diatoms serves as a hub for recycling nitrogenous compounds (Allen et al., 2011; Prihoda et al., 2012). It is not clear why the cycle was not co-ordinately expressed in the dark, but this is consistent with other studies where alternative nitrogenous sources are available (Allen et al., 2011; Smith et al., 2016). The catabolism

of proteins into their amino acid constituents provides NH_4^+ and monomers for TCA oxidation.

The capacity for a phototroph to modify its metabolic activity to an obligatory light regime, enhances its survival and success in a transient environment. Sustaining essential metabolic processes in the dark is imperative so that photosynthesis can occur rapidly upon re-illumination. Maintenance metabolism (or the ability to live in the dark), may be one of the fundamental reasons why diatoms dominate Antarctic sea-ice ecosystems. The proteomic analysis of *F. cylindrus* during extended darkness has indicated that cells rapidly decrease the light harvesting complex and photosystems while maintaining their photosynthetic capacity. This appears to be mediated through mitochondrial respiratory processes of the Entner-doudorff pathway, glycolysis and TCA cycle, ensuring rapid recovery upon illumination. These results align with field studies where the ability of sea-ice diatoms to rapidly recover upon the return of light is well documented. While analysis of the proteome alone is still some way removed from actual proof of physiological function, it nonetheless provides a metabolic blueprint that establishes a valuable scaffold for future work to expand upon. Caveats of this study are acknowledged and in considering these, future work requires a mechanistic understanding of the processes that are primarily responsible for dark ATP generation and ATP synthase maintenance. This would benefit from a quantitative assessment of respiration and metabolic flux, along with the molecular and environmental drivers that enable activation of the Entner-Doudordoff and mitochondrial glycolysis pathways.

Chapter 3

Rapid changes in spectral composition after darkness influences nitric oxide, glucose and hydrogen peroxide production in *Fragilariopsis cylindrus*

3.1 Introduction

Microalgal taxa associated with the ice-water interface experience variation in both the quantity and quality of irradiance over multiple time scales. Annually, phototropic consortia are exposed to extended periods of darkness (Kennedy et al., 2019) and rapid bursts of high light intensities upon ice-breakup (Arrigo, 2014). High inter-annual variability and the increased occurrence of extreme climatic events in this region will have considerable impacts on both the timing and magnitude of light transmission (Deppeler and Davidson, 2017). Current climate models predict that increases in water temperature will lead to less ice formation in winter and speed up the melt process in spring/summer (Turner et al., 2008). Furthermore, these models anticipate an enhanced poleward shift in storm events that will result in higher winds, wave magnitude and precipitation (Bracegirdle et al., 2008; Massom and Stammerjohn, 2010). Increased wind and wave action will intensify the

fragmentation of existing sea-ice floes, accelerating ice melt leading to alterations in productivity. Increased precipitation in the form of rain will enhance light transmission, whereas precipitation in the form of snow will both decrease the quantity and alter the spectral distribution reaching bottom-ice communities (Massom et al., 2001; Meiners et al., 2017). It is unknown whether these changes will have a positive or negative effect on ice-associated primary production. The ability to measure photophysiology and the response of algal communities *in situ* under scenarios climatic change is needed. The objective of this study is to a) examine if exposure to variation in spectral composition after prolonged darkness alters photophysiology and b) determine if photophysiological stress can be measured by sensing extracellular metabolites with micro-electrodes.

3.2 Materials and Methods

3.2.1 Algal culture

A monoculture of *Fragilariopsis cylindrus* was isolated from Antarctic pack ice in 2015 (Davis station, East Antarctica), taxonomically identified according to descriptions by Scott and Marchant (2005) and confirmed via 18s rRNA sequencing (Appendix A - Chapter A). The culture was maintained axenically (as determiend by DAPI staining) in exponential growth phase in L_1 media (Guillard and Hargraves, 1993) under cool white fluorescent light (50 μmol photon m^{-2} s^{-1}, 16: 8L/D cycle) at 2°C ± 1°C.

3.2.2 Exposure to different spectral regimes after prolonged darkness

Microfluidics and the electrochemical detection of extracelullar metabolites

Microfludic devices were fabricated from optically clear acrylic and acrylic adhesive (ALINE Inc, USA). Each device comprised three micro-wells of 6.5 mm diameter; each well contained 110 μL (Figure 3.2a). The inlets and outlets of each device were fitted with a 0.45 um nylon membrane, limiting any cross contamination between wells. Cells of *F. cylindrus* were extracted from the master culture and concentrated to achieve a mean cell density of ~5.2 x 10^5 ± 7.2 x 10^4 cells mL^{-1}. These concentrated cells were then inoculated into each micro-well and sealed with a thin

membrane that allowed atmospheric gaseous exchange. Microfluidic devices were incubated in the dark for either, 0.5, 30 or 120 days (n =3). During the dark incubation, sterile L_1 media (Guillard and Hargraves, 1993) was continually passed through each of the chambers by a peristaltic pump at a flow rate of ~50 μL min^{-1}. The outflow media was not recirculated in order to avoid nutrient limitation.

Following the dark incubation period, microsensors were used to detect photosynthetically-derived extracellular metabolites. Sensors were inserted through the membrane using a motorized micromanipulator (Unisense, A/S, Aarhus, Denmark) to within ~50 μm of the base of each chamber (Figure 3.2b). The flow of media thorough the device was terminated before microsensor insertion. The sensors were initially left to equilibrate for 5 minutes. Data was then logged over 30 minutes during which time cells were exposed to a specific light spectra (photon flux of ~52 μmol photon m^{-2} s^{-1}). Illumination of different spectra was provided by a purpose built light box, where each micro-well of the microfluidic device was illuminated from below by a single LED controlled by a variable resistor (Figure 3.2b, 3.1a). Individual lightboxes were constructed for each of the four spectra: blue (467 nm), green (525 nm), red (660 nm) and white (Figure 3.1b). The LED's were calibrated with a RAMsES radiometer (TriOS optical systems, Germany) to ensure photon flux and spectral intensity was equal across micro-wells and LED colour (Figure 3.1b). Only one microsensor was placed in each well (Figure 3.2c); each treatment was replicated (n=3). To correct for any background electrochemical signals, controls were conducted without cells; these readings were subtracted from experimental traces. Electrochemical traces were also normalised to cell number or chlorophyll *a* concentration (chl*a*). Sensors were calibrated in filtered (0.2 μm) pre-chilled seawater (2°C) before use using the manufactures descriptions. Temperature was maintained at 2°C ± 0.5°C throughout the experiment.

Nitric oxide (NO) was measured electrochemically with a Clarke-type NO electrode (NO-100μm; Unisense, A/S, Aarhus, Denmark), connected to a picoammeter (Unisense).

Hydrogen Peroxide (H_2O_2) (ISO-HPO100) microsensors were obtained from World Precision Instruments (WPI, USA), and were connected to a WPI free radical analyser.

Glucose biosensors where obtained from Pinnacle Technology (Lawrence, KS, USA) and used

as previously described by McMinn and Lee (2018). The Pinnacle sensors were connected to a Unisense (Aarhus, Denmark) picoammeter by a custom made connector.

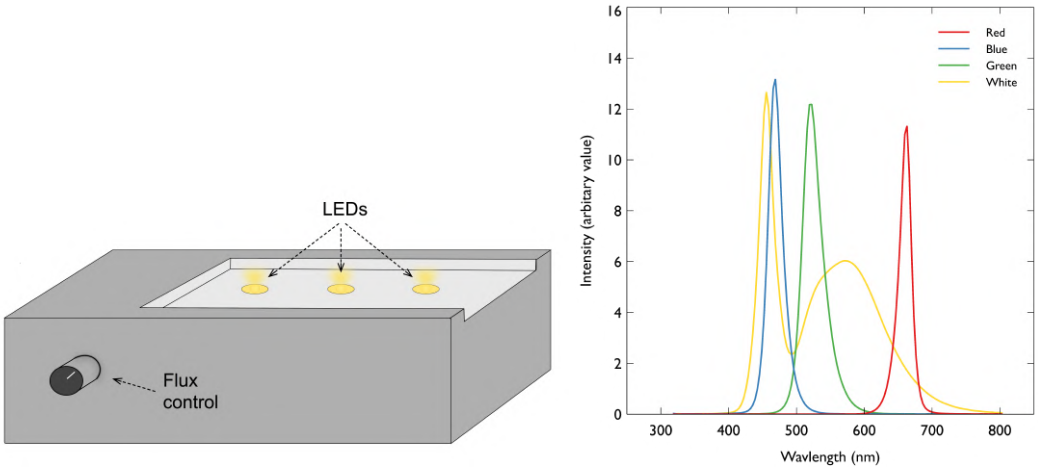

(a) **(b)**

Figure 3.1: **a)** schematic representation of a purpose-built light box that holds a microfluidic device. Illumination is provided underneath each micro-well via an individual LED; photon flux is controlled via a variable resistor. **b)** spectral profile of the each of the coloured LEDs.

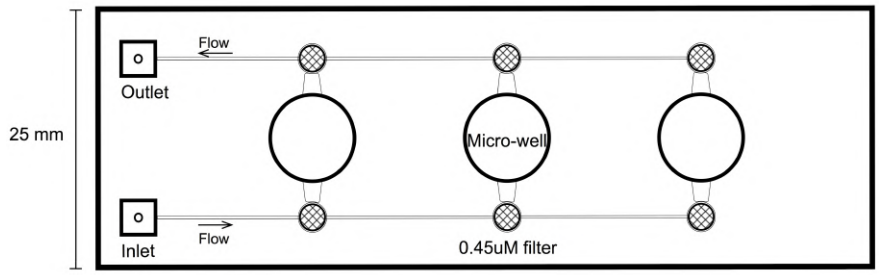

(a)

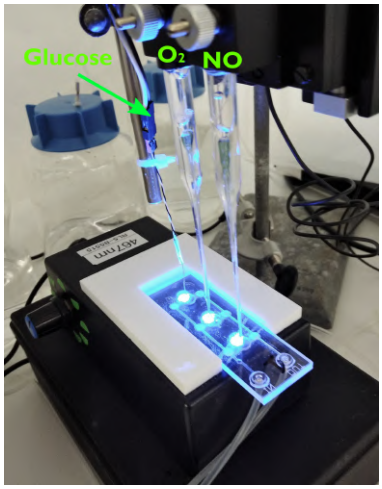

(b)

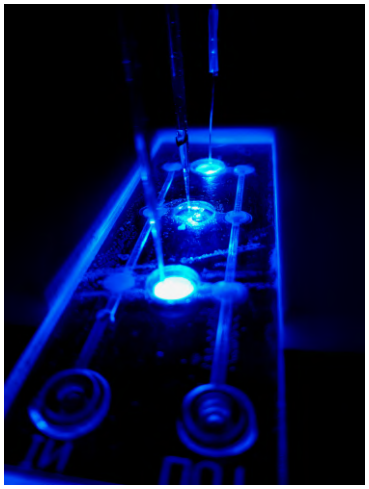

(c)

Figure 3.2: **a)** Schematic of the microfluidic devices. *F. cylindrus* cells were grown in the micro-wells displayed. L_1 media was circulated through the chambers at a flow rate of ~50 μL min^{-1}. **b)** photograph depicting how each microsensor was inserted through the microfluidic membrane into each well. **c)** microsensors embedded through the microfluidic membrane measuring metabolite concentration in the dark.

A separate experiment was conducted whereby the spectral flux was steadily increased to examine the influence on the production of extracellular metabolites. Cultures of *F. cylindrus* (1.2 x 10^6 ± 8.1 x 10^4 cells mL^{-1}) were inoculated into four 50 mL tissue culture flasks containing L_1 media and incubated at 2°C ± 0.5°C. Cultures were acclimated for 14 days and exposed to one of the following light regimes: 1) white, 2) blue, 3) red and 4) green (Figure 3.1b). The intensity of each light treatment was determined using a RAMSES radiometer (TriOS optical systems, Germany) and light boxes calibrated to ensure photon flux was consistent across the spectra (~21 μmol photon m^{-2} s^{-1} (16:8 L/D) cycle). Following the acclimation period, a subset of the algal culture was extracted and inoculated into microfluidic devices as previously described. Microsensors (glucose, NO, and H_2O_2) were inserted through the microfludic membrane and left in the dark for

10 minutes before the photon flux was increased (every 5 minutes) until the maximum output of the specific spectra achieved (white: 800 μmol photon m^{-2} s^{-1}, blue: 800 μmol photon m^{-2} s^{-1}, red: 633 μmol photon m^{-2} s^{-1} and green 400 μmol photon m^{-2} s^{-1}).

3.2.3 Rapid *ex situ* transition in spectral intensity using artificial sea-ice

Ice-tank

For microcosm studies, a custom-made sea-ice tank was engineered, with an inverted ice-water interface (Figure 3.3). This was designed to provide a practical means to allow discreet measurements of the algal biofilm with microsensors deployed vertically from above. Description of the inverted ice tank can be found in Cimoli et al. (2017). Briefly, ~35 litres of filtered seawater was incubated in the tank and frozen overnight (at -20°C) creating a ice surface measuring 850 cm x 850 cm. Hypersaline brine exuded from the matrix was removed via a vacuum pump before ~25 L of pre-chilled (-1.7°C) filtered seawater (35 ppt) was added on top of the formed ice, resulting in ~1 cm of seawater above the ice-water interface. The overlying seawater was amended with SiO_2 (0.102 mg L^{-1}), NH_4 (0.25 mg L^{-1}) and PO_4 (0.10 mg L^{-1}); based on ice-water interface nutrient concentrations measured in the field by Ryan and Martin 2009 (unpublished) (Table 3.1). Prior to ice formation, twelve cylinders measuring 1 cm x 1 cm were placed on the ice tanks glass surface and frozen in. The ice thickness and overlying seawater was calibrated to ensure the level of spectral irradiance reaching the algal biofilm was consistent. Following ice-formation, nine of the twelve cylinders were inoculated with a mean of 1.15 x 10^6 ± 1.02 x 10^4cells mL^{-1}; the remaining three cylinders did not contain cells and were used as a control. Cultures of *F. cylindrus* were pre-acclimated to the tank conditions by slowly decreasing the temperature of the algal culture in a refrigerated recirculating water-bath (to -1.7°C) over 24 hours. The cylinders containing *F. cylindrus* cells were exposed to a light regime of a mixed spectral composition for 14 days (16:8 L/D cycle) before sampling (Table 3.1). This light regime was established from field measurements conducted at Granite Harbour, Antarctica (77°S), by Ryan and Martin (2009) (unpublished). To achieve the specific light regimes, a light emitting diode (LED) array was engineered that incorporated hundreds of multiple coloured LED's (white, blue, red, green and UV (380 nm)). Each group of coloured LED'S were mounted on individual printed circuit boards (PCB) and connected to

a dedicated photon flux controller for each spectra. This enabled complete autonomy over the relative intensity of each wavelength of interest.

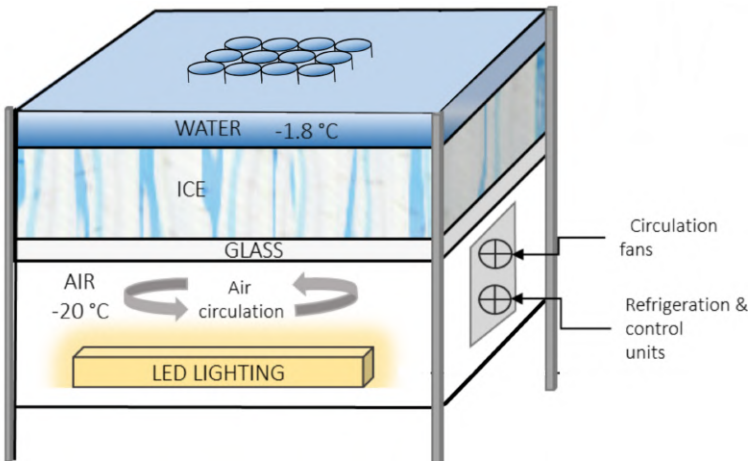

.

Figure 3.3: Graphical representation of the inverted sea-ice tank. Figure also displays the experimental chambers embedded in the ice matrix. Adapted with permission from Cimoli et al. (2017)

The spectral composition and intensity during the 14 day acclimation mimicked values measured at 1.5 m sea-ice depth (Figure 3.4b). After the 14 acclimation period an initial sample was taken (Time 0), then the irradiance was rapidly increased to mimic values obtained at 0.5 m ice-depth (Figure 3.4c). A schematic of the experimental design can be viewed in Figure 3.4a. Three randomly assigned cylinders containing an algal biofilm were measured at each time point; time 0 then 12 and 24 hours after the increase in illumination. Microsensors were orientated into the centre of each cylinder to within 50 μm of the algal biofilm by a motorised micro-manipulator (Unisense, A/S, Aarhus, Denmark). Glucose, NO and H_2O_2 concentrations were then measured over 5 minutes. Cells were also extracted for chlorophyll *a* (chl*a*), pulse amplitude modulated fluorometery (PAM), superoxide dismutase (SOD) and glutathione (GSH) analysis. During microsensor deployment, thick insulation (10 cm) was placed over the non-workable surface of the ice-tank to limit any variation in temperature during data collection.

Due to equipment constraints, each replicate cylinder could not be measured simultaneously leading to a time delay in data acquisition. However, the time taken to complete all measurement

was no more than 20 minutes and this did not appear to have any significantly influence on the dataset.

Table 3.1: Approximate physical parameters measured in sea-ice at Granite Harbour Antarctica (77°S), November 2009. The light levels are a percentage of the surface irradiance of 1634 μmol photon m^{-2} s^{-1}. This data was collected by Ryan and Martin (2009) (unpublished) and used with permission from the authors. The parameters used in this study are highlighted in yellow. The nutrient concentrations mimicked those found at the ice-water interface (3.1 m). The initial light regime used in the ice tank experiments mimicked that of 1.5 m depth before irradiance was rapidly increased to mimic 0.5 m depth.

Depth	Temperature	Salinity	SiO2 (mg L^{-1})	NH_4 (mg L^{-1})	PO_4 (mg L^{-1})	Blue	Green	Red	UV
0.5m	-6°C	149	-	-	-	3.4%	2.7%	0.4%	4.4%
1.5m	-5°C	124	0.55	0.549	0.032	2.1%	1.32%	0.1%	2.1%
3.1m	-1.8°C	35	0.102	0.245	0.0105	0.5%	0.2%	0.02%	0.3%

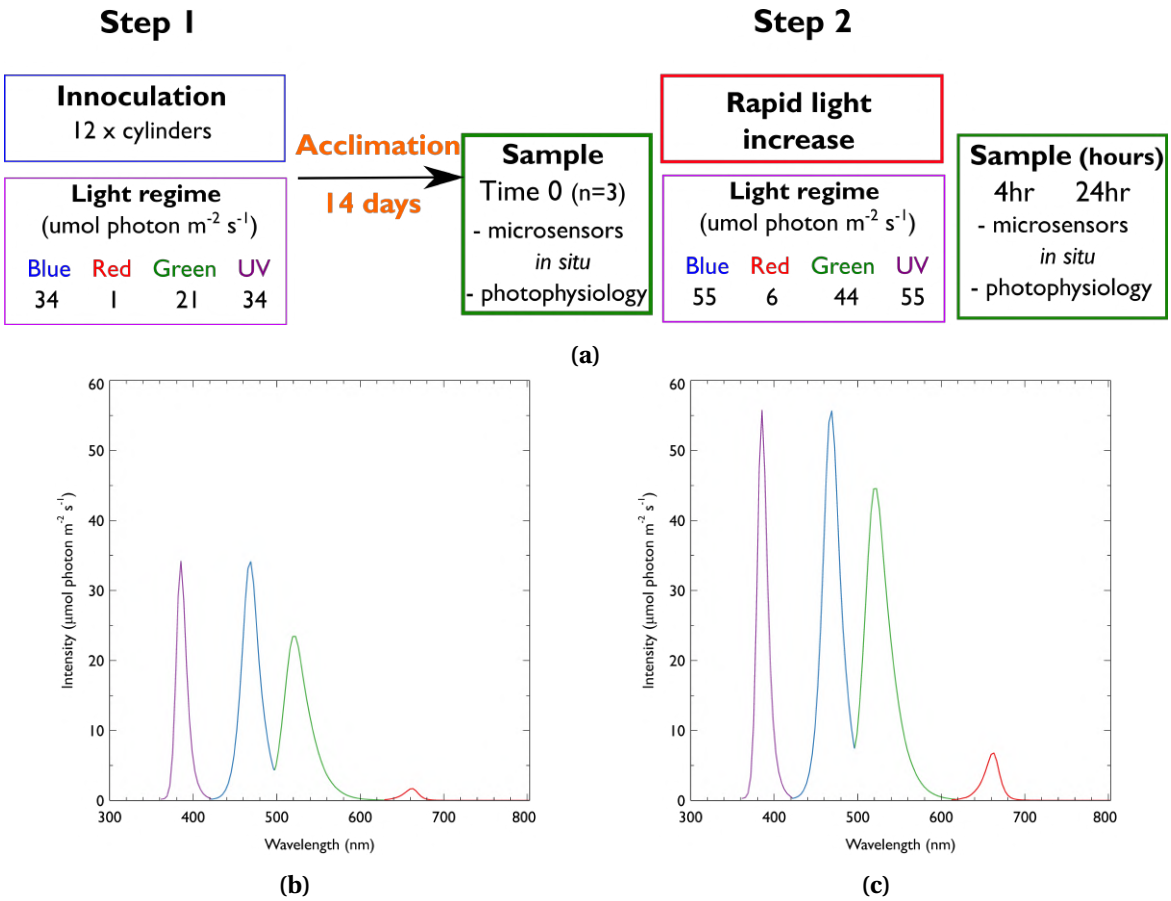

Figure 3.4: **a)** Schematic of the ice-tank experimental design. **b)** and **c)** The spectral composition and intensity of the LED array used during the ice-tank experiments. Spectral intensities are approximate values based on field measurements from Granite Harbour, Antarctica at **b)** 1.5m and **c)** 0.5 m sea-ice depth (Table 3.1).

3.2.4 Pulse amplitude modulated fluorometry (PAM)

Chlorophyll *a* fluorescence was measured using a pulse-amplitude-modulated fluorometer (Water-PAM, Walz, Effeltrich, Germany) with an internal actinic light source centered on 660 nm. All samples were dark-acclimated for 20 minutes prior to measurement. Rapid light curves (RLC) were obtained under software control (WinControl, Walz). Further details on the methods used herein are described in Chapter 2 - 1.2.4.

3.2.5 Glutathione (GSH) antioxidant assay

The detection and quantification of the reduced form of glutathione (GSH) was performed due to its role in the maintenance of cellular redox homeostasis. This assay was conducted on lysed cell extracts using the GSH-Glo (V6911 - Promega) luminescent assay kit, according to the manufactures instructions. The assay is based on the luminescent of recombinant firefly luciferase in the presences of gluthinone, catalysed by gluthinone S-transferase (GST). The intensity of luminescence is directly proportional to the amount of GSH present. Standard curves were conducted with each assay and the concentration of GSH was normalised to chlorophyll *a* content. Samples and standards were read on a microplate reader (BMG FLUOstar OPTIMA).

3.2.6 Superoxide dismutase enzymatic activity

The activity of the anti-oxidation enzyme superoxide dismutase (SOD) was measured spectrophotometrically using the method described by Nguyen-Deroche et al. (2012). Briefly, *F. cylindrus* cells were collected and spun in a refrigerated centrifuge at 1000 x g, 2°C. The resulting pellet was lysed in frozen phosphate buffered saline (Sigma Aldrich, pH 7) and the lysate centrifuged (10,000 x g, 15 minutes, 2°C). The supernatant was aspirated for the subsequent analysis. SOD activity was determined by measuring the inhibition of the photochemical reduction of nitroblue tetrazollium (NBT) at 560nm (Beauchamp and Fridovich, 1971). A unit of SOD (μg^{-1} total protein) is defined as the amount that caused 50% inhibition of the NBT reaction. Measurement of cellular protein content was necessary for the quantification of SOD; protein concentrations were calculated using a Pierce coomassie protein assay kit (ThermoFisher Scientific).

3.2.7 Statistical analysis

The production of extracellular metabolites by *F. cylindrus* with respect to changes in spectral composition over time, was assessed using two-way analysis of variance (ANOVA). If signification differences were observed, post-hoc Tukey pairwise multi-comparison tests were conducted. When appropriate, one-way ANOVA was also used. If significance was detected, Holm-Sidak

pairwise comparison tests were used to determine differences . Normality of data was assessed before each analysis and the data were transformed as appropriate.

3.3 Results

3.3.1 Exposure to increasing spectral intensity following darkness

The production of extracellular metabolites in *F. cylindrus* was measured following a defined period of darkness (0.5, 30 or 120 days), then illuminated with either white, blue, red or green light (~52 μmol photon m^{-1} s^{-1}).

A linear increase in the concentration of hydrogen peroxide (H_2O_2) was observed upon exposure to white or blue light (Figure 3.5a). The increase in H_2O_2 was only statistically significant following 120 days of darkness ($p<0.05$). H_2O_2 production correlated with the reduction in maximum quantum yield of PS_{II} (F_v/F_m) in white (mean; 0.29 ± 0.05 (120 days) and blue light (mean; 0.26 ± 0.04 (30 days), 0.10 ± 0.08 (120 days)) (Table 3.2). Furthermore, exposure to blue light after darkness caused a significant reduction in the maximum electron transfer rate ($rETR_{max}$) ($p<0.05$) and increased non-photochemical quenching (30 and 120 days). The production of nitric oxide (NO) was only apparent upon exposure to blue light (30 and 120 days) and not the other spectral regimes (Figure 3.5c). The exudation of glucose was observed, however there was no significant differences when comparing the treatments (Figure 3.5b). Furthermore, exposure to red or green light after darkness had no significant effect of the production of extracellular metabolites in *F. cylindrus*.

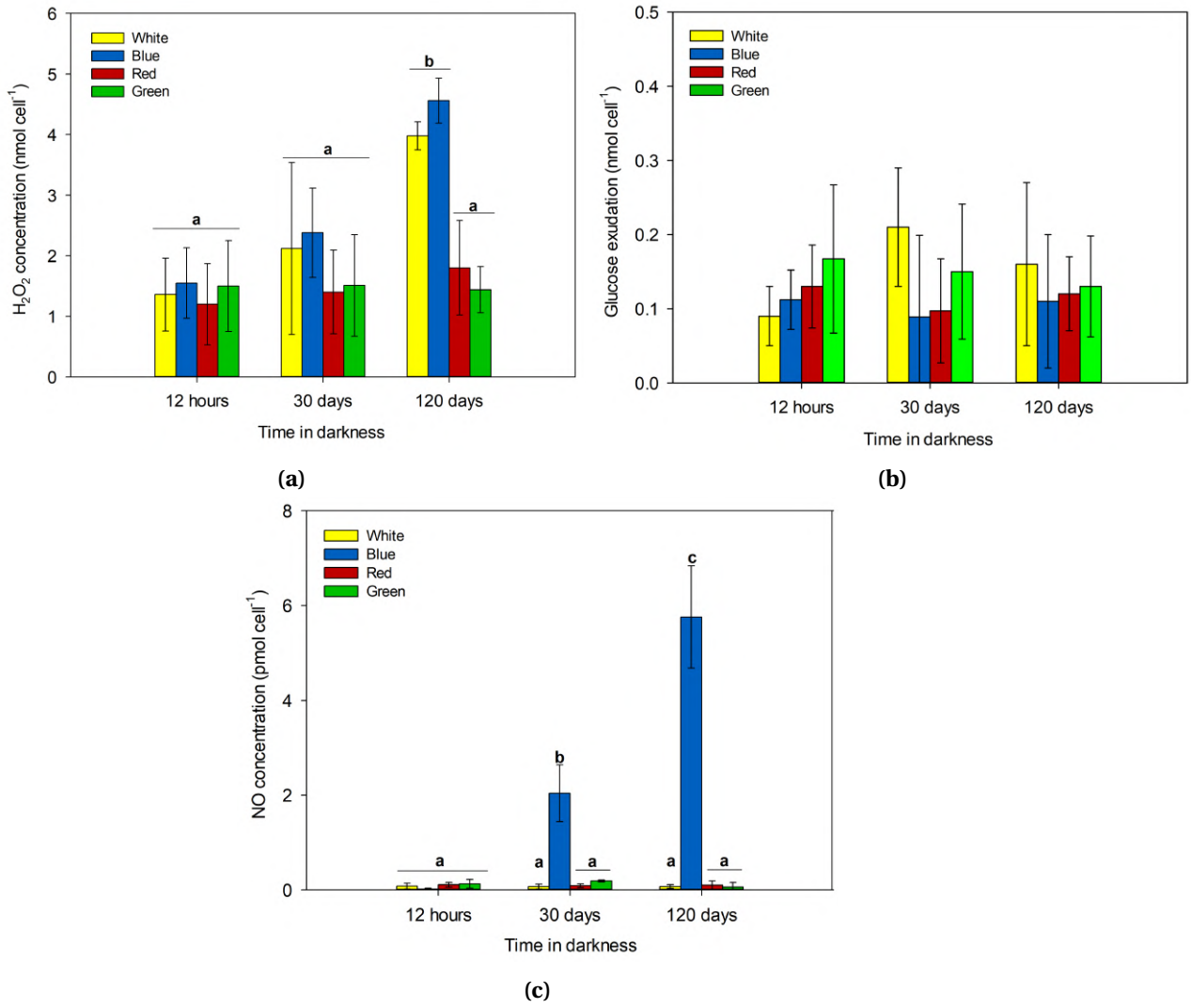

Figure 3.5: The production of the extracellular metabolites: **a)** H_2O_2 (nmol cell^{-1}), **b)** glucose (nmol cell^{-1}) and **c)** nitric oxide (NO) (pmol cell $^{-1}$) in *F. cylindrus* cells upon exposure to various spectra following darkness (0.5, 30 or 120 days). Cells contained in microfluidic devices were subjected to either: white, blue, red or green light for 30 minutes (photon flux ~52 μmol photon m^{-2} s^{-1}). Values are averages of n=3; errors are standard deviation of the mean. Values marked with same letters are not significantly different for the corresponding factor (Tukey's pairwise multi-comparison test; p>0.05).

Table 3.2: Photophysiological parameters of *F. cylindrus* following exposure to one of four light spectra (white, blue, red or green). Prior to illumination, cells were kept in complete darkness for either: 0.5, 30 or 120 days. Values are the mean of n=3; errors are standard deviation of the mean. Values marked with same letters are not significantly different for the corresponding factor (Tukey's pairwise multi-comparison test; p>0.05).

Spectrum	Darkness (days)	F_v/F_m	$rETR_{max}$	NPQ
White	0.5	0.50 ± 0.09^{a}	38 ± 1.01^{a}	0.36 ± 0.09^{a}
	30	0.43 ± 0.04^{a}	42 ± 2.13^{a}	0.33 ± 0.05^{a}
	120	0.32 ± 0.06^{a}	32 ± 0.08^{a}	$\mathbf{0.59 \pm 0.04^{b}}$
Blue				
	0.5	0.51 ± 0.05^{a}	35 ± 2.56^{a}	0.43 ± 0.09^{a}
	30	$\mathbf{0.26 \pm 0.04^{b}}$	$\mathbf{19 \pm 4.11^{b}}$	$\mathbf{0.72 \pm 0.10^{c}}$
	120	$\mathbf{0.10 \pm 0.08^{c}}$	$\mathbf{12 \pm 1.62^{b}}$	$\mathbf{0.97 \pm 0.17^{c}}$
Red				
	0.5	0.52 ± 0.10^{a}	28 ± 1.20^{a}	0.35 ± 0.07^{a}
	30	0.48 ± 0.07^{a}	31 ± 1.74^{a}	$\mathbf{0.53 \pm 0.01^{b}}$
	120	0.41 ± 0.02^{a}	38 ± 2.03^{a}	0.37 ± 0.09^{a}
Green				
	0.5	0.46 ± 0.04^{a}	$\mathbf{10 \pm 1.03^{b}}$	0.16 ± 0.08^{d}
	30	0.32 ± 0.08^{a}	$\mathbf{18 \pm 0.08^{b}}$	0.14 ± 0.03^{d}
	120	0.41 ± 0.06^{a}	$\mathbf{14 \pm 0.74^{b}}$	0.08 ± 0.02^{d}

3.3.2 The effect of a rapid transition in spectral intensity using a sea-ice tank

To determine if a rapid change in spectral intensity and quality influences the production of extracellular 'stress' metabolites, cultures of *F. cylindrus* were inoculated into an artificial sea-ice tank and acclimated to a spectral profile mimicking 1.5 m ice depth (Table 3.1). Following an acclimation period of 14 days, the photon flux was increased and the concentration of extracellular metabolites observed over a 24 hour period.

A significant increase in the concentration of H_2O_2 was observed 12 hours following exposure to heightened irradiance (Figure 3.6a). Unfortunately, additional H_2O_2 measurements could not be completed due to microsensor malfunction. A linear increase in glucose exudation was observed

over time (Figure 3.6b), with the highest amount of glucose observed after 24 hours (mean; 0.006 ± 0.0008 μmol mg^{-1} chl*a* L^{-1}). A large pulse of NO was recorded following 12 hours of increased irradiance (2.33 ± 1.39 nmol mg^{-1} chl*a* L^{-1}), but no subsequent production of NO was observed. The photosynthetic parameter, F_v/F_m declined from 0.36 ± 0.10 (Time 0) to 0.18 ± 0.06 (24 hours) ($p<0.05$) (Table 3.3). Conversely, an increase in NPQ was observed; 12 (0.83 ± 0.08) and 24 hours (0.91 ± 0.10) after increased illumination (Table 3.3).

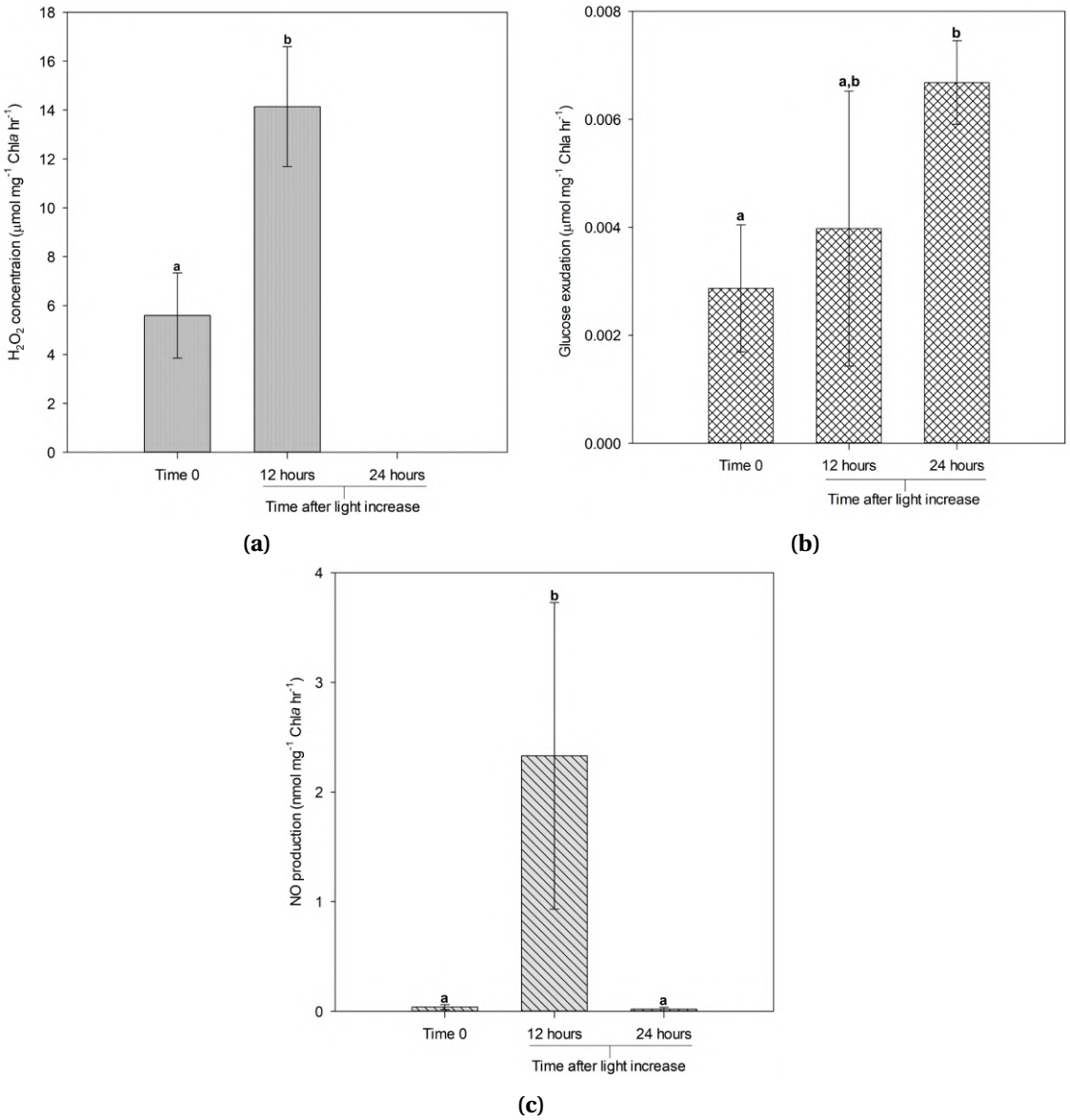

Figure 3.6: The production of extracellular, **a)** hydrogen peroxide (H_2O_2) (μmol mg^{-1} chl*a* L^{-1}), **b)** glucose (μmol mg^{-1} chl*a* L^{-1}) and **c)** nitric oxide(NO) (nmol mg^{-1} chl*a* L^{-1}) of *F. cylindrus* cells upon exposure to increased spectral irradiance over 24 hours. Time 0 denotes the photophysiological response prior to increasing the illumination. Whereas,12 and 24 hours represent the time prior to the light increase. Values are the average of n=3 and error is the standard deviation of the mean. Parameters marked with same letter are not significantly different (p> 0.05) (Holm-sidak pairwise multiple comparison).

Table 3.3: Photophysiological parameters of *F. cylindrus* exposed increased spectral intensity for 24 hours in an artificial ice-tank. Time 0 denotes the photophysiological response prior to increasing the illumination. Subsequent time points (12 and 24 hours) represent time after light increase. Values are the average of n=3 and error is the standard deviation of the mean. Parameters marked with same letter are not significantly different (p>0.05) (Holm-sidak pairwise multiple comparison).

Time (hrs)	F_vF_m	$rETR_{max}$	NPQ
Time 0	0.36 ± 0.10^{a}	24 ± 1.01^{a}	0.53 ± 0.10^{a}
12 hours	$\mathbf{0.24 \pm 0.08^{a,b}}$	$\mathbf{12 \pm 2.13^{b}}$	$\mathbf{0.83 \pm 0.08^{b}}$
24 hours	$\mathbf{0.18 \pm 0.06^{b}}$	$19 \pm 5.03^{a,b}$	$\mathbf{0.91 \pm 0.10^{b}}$

Anti-oxidation mechanisms were relatively high throughout the experiment, as observed by superoxide dismutase activity (SOD) (Figure 3.7a) and glutathione (GSH) concentration (Figure 3.7b). A statistically significant increase in SOD activity was observed at 12 hours (21.81 ± 3.48 (12 hours)), but decreased to 14.87 ± 0.87 after 24 hours. In contrast, GSH did not change within the first 12 hours of exposure but increased significantly after 24 hours (0.054 ± 0.0049) (p>0.05) (Figure 3.7b). The relationship between SOD activity and H_2O_2 production was examined using a Pearson correlation (Figure 3.7c). An increase SOD activity was correlated with that of H_2O_2 production (R^2 = 0.76, p = 0.024). It must be noted that due to H_2O_2 sensor malfunction at 24 hours, only SOD activity and H_2O_2 values from time 0 and 12 hours were used for the subsequent correlation.

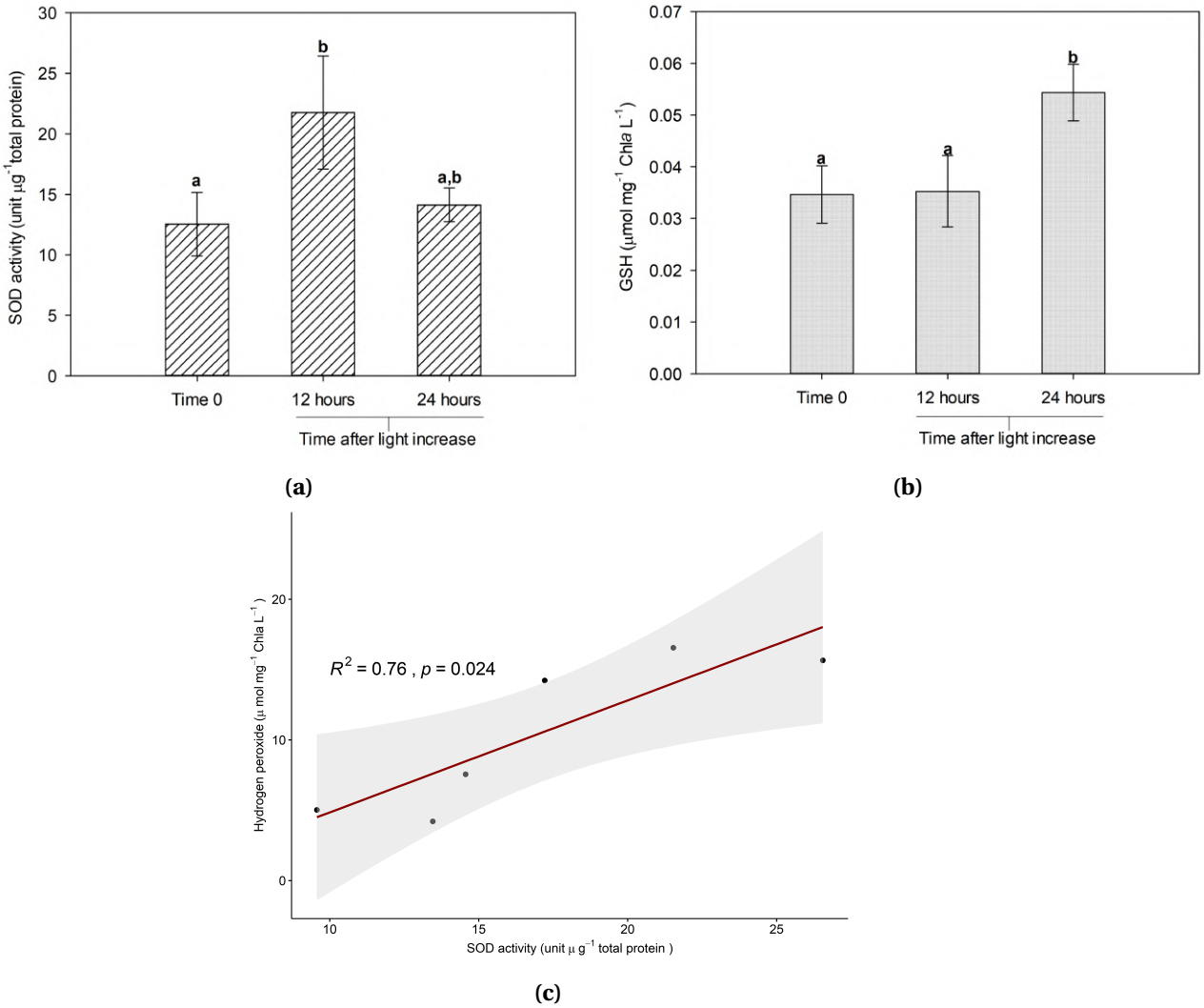

Figure 3.7: Anti-oxidation activity in *F. cylindrus* when exposed to increase spectral intensity over a 24 hour period in the ice tank. **a)** superoxide dismutase (SOD) activity (μg^{-1} of total protein) and, **b)** concentration of glutathione (GSH) mg^{-1} of chl*a*. **c)** Pearson correlation of hydrogen peroxide production and SOD activity. Values with the same letter are not significantly different (p>0.05) as determined using Holm-Sidak multiple pairwise comparison test.

To determine if excessive photon flux could induce the production of extracelluar metabolites, cells were exposed to incremental increases of either white, blue, red or green light. Extracellular metabolites were not significantly detected when cells were exposed to green or red light. However, there was a linear increase in the exudation of glucose in the blue and white light treatments (Figure 3.8a), with exposure to blue producing the highest concentration of glucose (0.96 ± 0.03 nmol $cell^{-1}$: 800 μmol photon m^{-2} s^{-1}). Furthermore, exposure to excessive levels of blue light

(>400 μmol photon m^{-2} s^{-1}) induced the production of nitric oxide (Figure 3.8b). To a lesser degree this was also apparent in high levels of white light (>650 μmol photon m^{-2} -s^{-1}). Interestingly, the concentration of H_2O_2 followed a similar trend to that of NO, whereby an increase in concentration was observed upon exposure to high levels of blue and white light (> 200 μmol photon m^{-2} -s^{-1}).

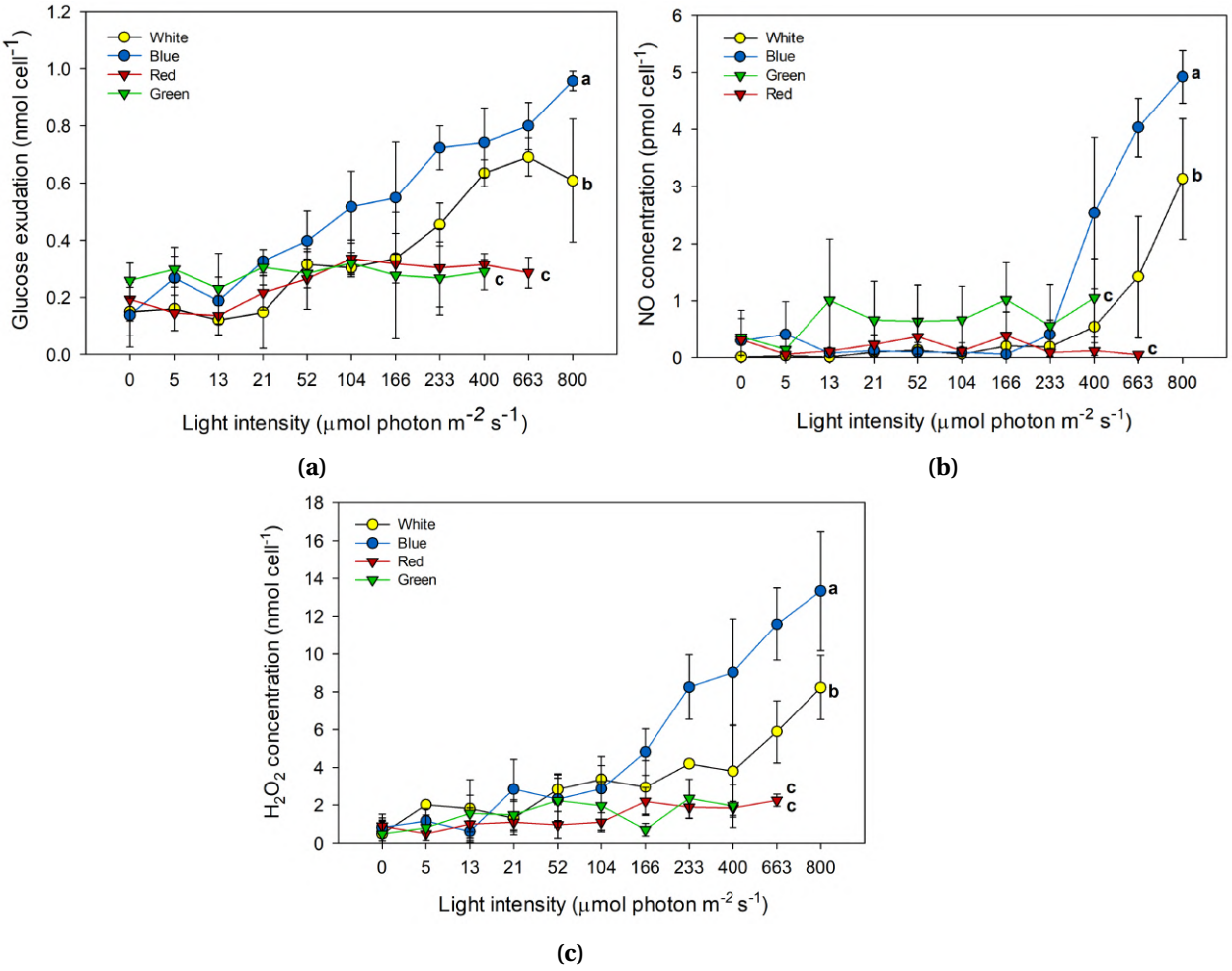

Figure 3.8: The production of extracellular metabolites **a)** glucose (nmol $cell^{-1}$, **b)** nitric oxide (NO - pmol $cell^{-1}$) and **c)** hydrogen peroxide (H_2O_2 - nmol $cell^{-1}$) when exposed to increasing light intensity (μmol photon m^{-2} s^{-1} of different spectra (white, blue, red or green). Values with the same letter are not significantly different (p>0.05) as determined using Tukey multiple pairwise comparison test.

3.4 Discussion

Sea ice is an unique habitat that supports complex microbial assemblages that are fundamental drivers of the Antarctic marine food-web. Future climate models suggest that the Antarctic ecosystem will experience dramatic cumulative environmental change. Any changes in ice thickness, precipitation and the timing of ice formation in winter and break-up in spring will lead to large scale fluctuations in the quantity and quality of light reaching ice-associated taxa (Massom and Stammerjohn, 2010). An understanding of how rapid shifts in irradiance will impact sea-ice algae communities, and the ability to efficiently measure *in situ* production, is clearly needed. Therefore, in this study I aimed to test the capability of certain microsensors to detect potential photosynthetically-derived extracellular "stress" metabolites. By focusing on key ecological transitions I have illustrated that the physiological response and severity of photo-stress is dependent on the wavelength upon re-illumination. The measurement of extracellular metabolites in response to rapid illumination was successful, and I propose that their production can be attributed to the photophysiological state of the cell.

3.4.1 Microfludics

The photophysiological response of *F. cylindrus* upon re-illumination after darkness varied according to the spectral composition of the incident irradiance. Exposure to blue light resulted in a significant impariment of both the photosynthetic efficiency of PS_{II} (F_v/F_m) and the electron transfer rate (ETR_{max}), whereas non-photochemical quenching (NPQ) was enhanced. Associated with the changes in photophysiology was the production of the extracellular metabolites hydrogen peroxide (H_2O_2) and nitric oxide (NO). Increased production of these molecules was also correlated with the length of darkness, which may suggest limited ability of *F. cylindrus* to chromatically adapt upon rapid re-illumination after lengthy dark periods. In chapter two, I illustrated the capacity of *F. cylindrus* to rapidly photosynthesise upon re-illumination with white light after 120 days of darkness. This result was also observed herein as was exposure to white light. However, re-illumination with blue light disrupted normal photosynthetic electron flow and caused

considerable stress. While the exact mechanisms for chromatic adaptation remain unclear, it is likely related to the diverse pigmentation of diatoms that allow absorption of proportionally more photons in the blue-green spectrum (Kuczynska et al., 2015). Furthermore, it has recently been shown that the nano-structure and optical properties of the diatom silica frustule can enhance blue light absorption, resulting in a higher proportion of energy reaching the light harvesting antenna (Yamanaka et al., 2008). Gosselin et al. (1990), also noted this phenomenon, whereby the frustules photonic structure of benthic pennate taxa enhanced the concentration of blue light by up to 120% of the down-welling irradiance. Studies have also shown that blue light improves both the growth and photosynthetic capacity of diatoms (Goessling et al., 2016; Voskresenskaya, 2003). Interestingly, the amplitude of NPQ also increased when cells were grown in blue light, suggesting that longer wavelengths can over stimulate the photosynthetic apparatus leading to early onset photoinhibition (Goessling et al., 2016, 2018; Holdsworth, 1985; Marchetti et al., 2013; Vogel and Sager, 1982). During periods of darkness, sea-ice diatoms enhance thylakoid membrane fluidity and densely pack photosynthetic pigments to maximise their photosynthetic capacity and increase the probability of light capture. It is likely that rapid exposure to blue light after darkness has resulted in the assimilation of excessive photons that cannot be efficiently processed, resulting in unsustainable levels of reactive oxygen species (ROS), and subsequently photoinhibition.

Under favourable illuminating conditions, cells are constantly producing reactive oxygen species (ROS) as a by-product of photosynthetic electron transport and metabolism. However these are readily detoxified by anti-oxidation mechanisms and rarely cause damage (Asada, 2006; Diaz and Plummer, 2018; Mallick and Mohn, 2000). Under saturating irradiance the photosynthetic electron transport chain becomes over reduced as consumption of the reducing equivalents cannot match their production (Masojídek et al., 2013; Schmitt et al., 2014). Electrons leak onto O_2 and significant amounts of damaging ROS are formed (O_2^-, H_2O_2, $^1O_2$). In this study, the increased production of H_2O_2 after darkness indicates that cells were experiencing elevated oxidative stress which may have been sufficient to impair photosynthesis. A large pulse in nitric oxide was also observed under blue light (30 and 120 days of darkness). The exact mechanisms behind NO production in microalgae remains unclear, but the majority of studies to date have indicated that production is likely a result

of nitrite consumption via the enzyme nitrate reductase in the absence of photosynthesis (Dolch et al., 2017; Mallick et al., 1999; Mur et al., 2013; Yamasaki et al., 1999). Previous studies have demonstrated that NO production does not occur during normal photosynthetic electron flow as the reduction of nitrite requires the reduced form of ferredoxin, created when water is oxidised at photosystem II (PS_{II}) to $NADP^+$ at photosystem I (PSI). Thus, when photosynthesis is operating normally, nitrite is rapidly assimilated and does not accumulate in the chloroplast. If the supply of reduced ferredoxin diminishes, such as during conditions that disrupt normal photosynthetic electron flow, nitrite accumulates, forcing nitrate reductase to convert nitrite to NO. Other studies have demonstrated that the enzymatic activity of nitrate reductase could be enhanced upon blue light exposure (Figueroa et al., 1995; Marchetti et al., 2013). In this study, the exposure to excess levels of blue light following prolonged darkness may have over stimulated the photosynthetic apparatus to such a degree that extreme levels of ROS are formed resulting in disruption of normal photosynthetic electron flow and photoinhibition.

The inability of cells to rapidly photo-adapt to different spectra is further illustrated when cells were acclimated to a specific spectrum prior to incremental increases in photon flux (Figure 3.8). When cells were acclimated to a particular spectrum for 14 days prior to increased photon flux, the production of H_2O_2 and NO was not observed. Exposure to blue light resulted in high production of 'stress' metabolites, but only under extreme illumination (NO: > 400 μmol photon m^{-2} s^{-1}; H_2O_2: > 200 μmol photon m^{-2} s^{-1}). Exposure to white light also resulted in increased production, but at higher intensities (NO: > 633 μmol photon m^{-2} s^{-1}; H_2O_2: > 233 μmol photon m^{-2} s^{-1}). Interestingly, the heightened glucose exudation was observed when exposed to incremental increases in both blue and white light. Previous studies have shown that the discharge of carbohydrate is common in microalgae biofilm's, where it is thought to function in cellular protection, mobility and assist in adhesion (Cooksey, 1995; Underwood and Paterson, 2003). It has been reported that up to 70% of the exuded carbohydrate can be composed of the monosaccharide glucose (Hama, 2001; McMinn and Lee, 2018). Furthermore, in environments frequently exposed to fluctuations in irradiance, the low molecular weight fraction (i.e glucose) of exuded sugars has been shown to be directly related to photosynthetic overflow (Underwood and Paterson, 2003). Perkins et al. (2001) and

McMinn and Lee (2018) demonstrated that exposure to excess illumination could increase the exudation of glucose in benthic diatoms. McMinn and Lee (2018) suggest that glucose production is correlated with the photophysiological state of the cell, and concluded that glucose exudation in benthic taxa is a direct result of photosynthetic overflow under saturating irradiance. In this study, I speculate that heightened glucose exudation in *F. cylindrus* can be attributed to the malfunction of normal photosynthetic flow as a direct result of excessive irradiance. The mechanistic drivers responsible for photosynthetic overflow in microalgae are not well understood, but it appears that under conditions of saturating irradiance, photosynthetic carbohydrate production exceeds that of consumption and carbon allocation which results in metabolic overflow. Furthermore, it appears that the cells light history can influence the degree of chromatic adaptation and the resulting photosynthetic response. This is the first study to measure photosynthetic carbohydrate overflow in a polar diatom with a biosensor. However, more work is necessary to determine the precise biochemical and physiological means of photosynthetic overflow.

3.4.2 Ice tank

In the ice tank experiment, I attempted to simulate an "*in situ*" scenario of a rapid light transition in irradiance as a result of ice break-up. Briefly, biofilms of *F. cylindrus* were acclimated to conditions found at the ice-water interface (1.5 m ice-depth), before rapidly increasing the irradiance to that found at 0.5 m depth. I acknowledge that this was an extreme scenario, but it was designed as a means to illicit a response in the production of 'stress' metabolites.

Rapid exposure to a broader spectrum resulted in similar observations with respect to the production of extracellular metabolites. It must be noted that prior to increasing the irradiance, the biofilm of *F. cylindrus* appeared to be moderately stressed, as observed by the reduced maximum quantum yield of PS_{II}. Also, relatively high levels of NPQ, H_2O_2, SOD activity and glutathione (GSH) were apparent. This suggests that biofilms of *F. cylindrus* were experiencing oxidative stress. It remains uncertain if this is a direct result of the boarder spectrum or a consequence of the physical attributes of sea-ice. Multiple abotic factors such as low temperature, high salinity and increased UV all contribute to enhanced ROS in sea-ice diatoms (Lyon and Mock, 2014; Lyon et al., 2011).

Nonetheless, 12 hours after the rapid increase in light, heightened production of H_2O_2, NO and SOD activity was observed. This appeared to be correlated with reductions in $F_v/F_{m,}$ $rETR_{max}$ and increased NPQ. Collectively, this indicates that cells were experiencing considerable oxidative stress as a direct result of the shift in irradiance. Furthermore, a positive correlation between SOD activity and H_2O_2 was observed, suggesting that H_2O_2 was indeed photochemically derived via detoxification of superoxide (O_2^-). Increased SOD activity and H_2O_2 production is characteristic of photosynthetic oxidative stress (Palenik et al., 1987; Schneider et al., 2016). Interestingly, 24 hours after increased illumination, SOD activity returned to a level observed prior to increased light. In a similar study, Janknegt et al. (2008) observed an large increase in SOD activity post-illumination followed by significant reduction within 24 hours. The rapid decrease in SOD activity, may in part, be explained by non-photochemical quenching (NPQ) which continued to increase over the duration of the experiment. NPQ is a product of the xanthophyll cycle that acts as a type of "safety valve" reducing the likelihood of photo-damage through the dissipation of excess excitation energy (Lavaud et al., 2002). NPQ in diatoms relies on the accessory pigments diadinoxanthin (DD) and diatoxanthin (DT). By increasing the ratio of DD+DT/Chl*a*, cells are able to diminish energy transfer and limit photodamage (Domingues et al., 2012). The reduced electron flow decreases the probability of superoxide formation in the photosystem and the cell decreases antioxidation mechanisms, like the detoxification of superoxide via SOD enzyme. Antioxidation mechanisms may be temporarily enhanced after rapid shifts in irradiance as a mechanism to reduce oxidative stress while cells are attempting to photoacclimate. The increase in NO, H_2O_2 and glucose is further evidence that under extreme light saturating scenarios, the production of these metabolites can be measured extracellularly and the physiological status of the photosynthetic apparatus inferred.

When cells of *F. cylindrus* emerge from long-term darkness, their photophysiological response differs depending on both the quantity and spectral quality of light on re-illumination. This may become pivotal under future scenarios which predict less ice will form in winter and melt faster in spring/summer. The timing, quality and quantity of sea-ice algal production during important transition events is imperative for efficient energy flow through the ecosystem. Rapid

transitions in irradiance can cause significant photoinhibition; if prolonged, early termination and alteration in the timing of bloom events occurs, this could cause a cascade of implications with respect to trophic dynamics. Therefore an effective system which can monitor the real-time *in situ* photophysiological performance of sea ice algae is imperative. The production of extracellular metabolites was successfully measured using micro-electrodes. The results indicate that stress or disruption of normal photosynthetic electron flow, increases the production of certain metabolites can be attributed to intracellular processes. Thus, the ability to measure *in situ* production of H_2O_2, NO and glucose may prove effective for use on deployable bioplatforms that provide a real-time physiological assessment of ice-associated microbial communities.

Chapter 4

The production and role of the metabolite nitric oxide in *Fragilariopsis cylindrus*

4.1 Introduction

Nitric oxide (NO) is a ubiquitous bioactive free-radical involved in many functions in both biotic and abiotic systems. The physiological importance of NO as a biological messenger was first established in animals, where it is used to transmit chemical signals in vascular, nervous and immune systems. Similarly in higher plants, NO can regulate aspects of growth, development, flowering, cell differentiation and influence physiology triggered by environmental stimuli. Research into the role of NO in marine algae has been relatively neglected in comparison to that of higher plants. This is surprising as marine algae are continually exposed to NO due to the increased photolysis of nitrate and nitrification processes that result in concentrations 10^4 higher in the marine environment than in the atmosphere (Kumar et al., 2015). The few studies to date have reported that some species of microalgae generate NO in the dark when supplied with nitrate (NO_3^-) or nitrite (NO_2^-). Other studies have shown that microalgae emit NO during the natural growth cycle (Estevez and Puntarulo, 2005; Zhang et al., 2006b). More recently, Vardi et al. (2006) found two diatom species that release NO as a stress-surveillance molecule when exposed to a diatom-derived aldehyde (2E, 4E/Z)-decadienal (DD). In a later study, Vardi (2008) illustrated that *Phaeodactylum tricortum*

increased the expression of a nitric oxide-associated protein (PtNOA), when exposed to DD, which resulted in increased NO production leading to decreased growth and photosynthetic efficiency. Despite these studies, an understanding of the precise mechanism behind NO synthesis in marine microalgae remains unclear. In animals, NO is primarily produced via nitric oxide synthase (NOS) from L-arginine. In photosynthetic organisms, NO production appears to be intimately linked to nitrogen metabolism where two different pathways appear to be a possibility; i) the oxidative pathway from L-arginine, ii) the reduction of nitrite. A number of studies in higher plants (Mur et al., 2013; Yamasaki et al., 1999) and algae (Dolch et al., 2017; Mallick et al., 1999; Sakihama et al., 2002), suggests a primary route via the reduction of nitrite by nitrate reductase (NR) using NADPH as a substrate, others have suggested an alternative pathway, namely L-arginine (Vardi et al., 2006). Despite the implications for marine diatoms, the role and means of production in this system remain unclear and ambiguous. Similar to higher plants and green algae, NO production is likely to be either nitrite or arginine-dependent via the nitric oxide synthase or nitrate reductase enzymatic pathway's (Figure 4.1. This is the first study endeavouring to resolve a basic mechanistic understanding of the role NO plays within an Antarctic sea-ice diatom. Specifically, I aim to determine: i) the primary enzymatic pathway that enables NO production in *Fragilariopsis cylindrus*, ii) if sea-ice associated abiotic factors influence NO production and, iii) if exogenous NO cause changes in photo-physiology.

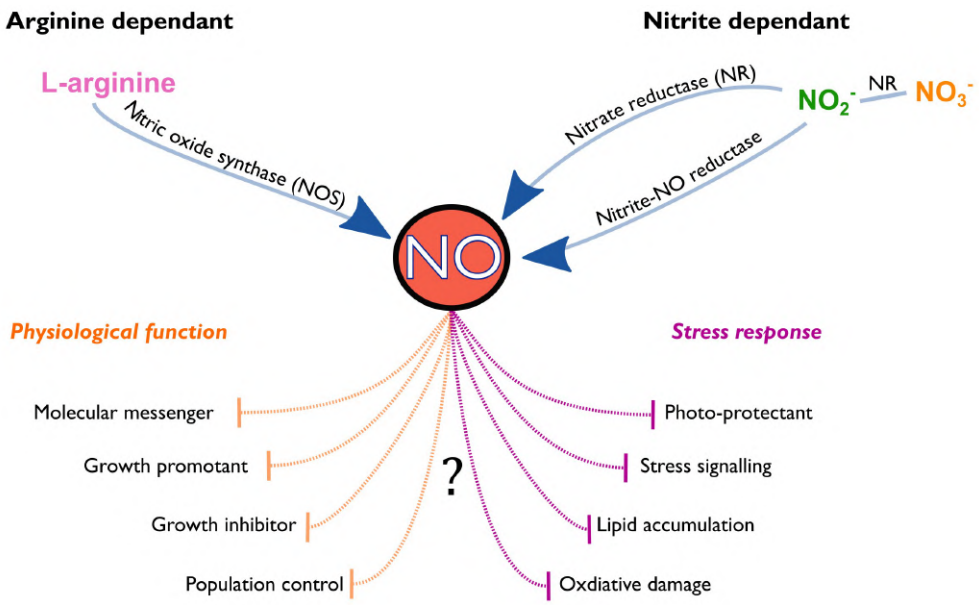

Figure 4.1: NO production in diatoms is likely to be either nitrite or arginine-dependent via the one of enzymatic pathway's described. The effect of NO on cellular biochemistry is unclear, but is likely that it is produced during periods of biotic and abiotic stress as a chemical cue to adjust aspect of cellular physiology.

4.2 Materials and Methods

4.2.1 Algal Culture

A monoculture of *Fragilariopsis cylindrus* was isolated from Antarctic pack ice in 2015 (Davis station, East Antarctica), and taxonomically identified according to descriptions by Scott and Marchant (2005) and confirmed via 18s rRNA sequencing (Appendix A, Chapter A). The culture was maintained axenically (as determined by DAPI staining) in exponential growth phase in L_1 media under cool white fluorescent light (50 μmol photon m^{-2} s^{-1}, 16:12 L/D cycle) at 2°C ± 1°C. Before experimentation, cultures were extracted and grown in modified L_1 media for seven days.

4.2.2 Microfluidics and the electrochemical detection of NO

Microfludic devices were fabricated from optically clear acrylic and acrylic adhesive (ALINE Inc (USA)). Each device had three micro-wells of 6.5mm diameter, which holds a volume of 110μL (Figure 4.2a). The inlets and outlets of each well were fitted with a 0.45 um nylon membrane,

limiting any cross contamination between wells. Cells of *F. cylindrus* were inoculated into each well before experimentation and sealed with a thin membrane that allowed gaseous atmospheric exchange. Exogenous NO concentration was measured electrochemically with a Clarke-type NO electrode (NO-100μm; Unisense, A/S, Aarhus, Denmark), connected to a picoammeter (Unisense). Microsensors were inserted through the membrane with a motorized micromanipulator and orientated to within ~50μm - 100μm of the base of each micro-well where the cells had settled (Figure 4.2b). The sensors were left to equilibrate for 20 minutes before logging NO production over 60 minutes in the dark. Microsensors were calibrated before use using the manufactures descriptions. NO production rate was calculated as nmol L^{-1} hr^{-1} using the relationship obtained from standard curves. Temperature was maintained at 2°C ± 0.5°C throughout the experiment.

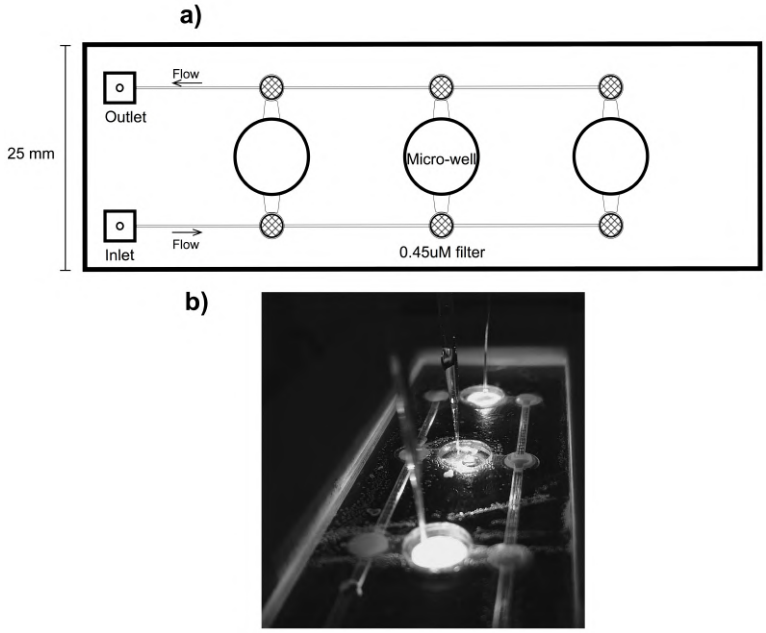

Figure 4.2: *a)* Schematic of a microfluidic device, cells were grown in the micro-wells displayed. Media was circulated through the chambers at a flow rate of ~100 μL min^{-1}. Electrochemical NO production was determined by inserting micro-sensors through a thin membrane covering each micro-well.

Light was provided by a purpose built light box, where each micro-well was illuminated from below by a single white LED controlled by a variable resistor (Figure 4.3). The LED's were calibrated with

a Li-COR PAR sensor to ensure the photon flux was equal in each micro-well. The spectral profile of the LEDs was also quantified to ensure consistency (Figure 4.3b).

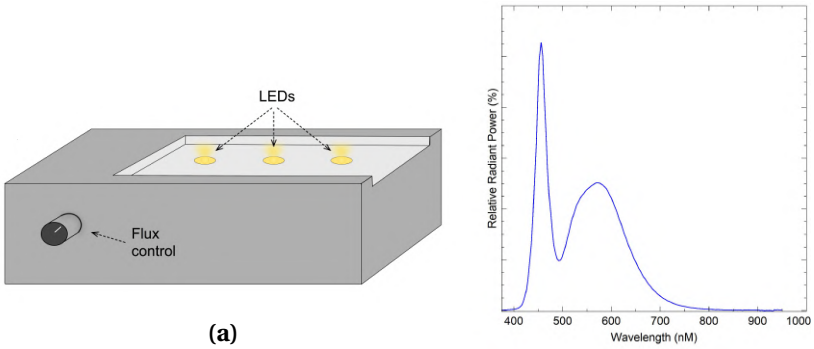

(a) **(b)**

Figure 4.3: **a)** schematic representation of a purpose build light box that holds a microfluidic device. Illumination is provided underneath each micro-well via an individual cool white LED; photon flux is controlled via a variable resistor. **b)** spectral profile of the cool white LEDs, showing the two peaks that are characteristic of white LEDS.

Determination of exogenous supplied nitrogen on NO production - microfludics

Cells in exponential growth phase (~2.76 x 10^6 cells mL^{-1} ± 0.32 x 10^6 cell mL^{-1} were inoculated into each of the three microfluidic wells and sealed. Devices were incubated at 2°C under 50 μmol photon m^{-2} s^{-1} (16L/8D) for 10 days. During this time nitrogen replete media flowed through the device at a rate of ~100 μL min^{-1} using a peristaltic pump. After 10 days, flow and light were turned off and the respective nitrogen treatments injected into micro-wells at the concentrations described in Table 4.1. Each microfluidic device contained three randomised nitrogen treatments or a control (filtered seawater injection). The treatments were repeated to n=3; a new sterile microfluidic device was used for each replicate.

Table 4.1: Treatments and concentrations used to determine the influence of exogenous supplied nitrogen on NO production. All chemicals were dissolved in filtered seawater (35ppt) before experimentation.

Treatment	Concentration
Filtered seawater (control)	35ppt
Sodium nitrite	5mM
Sodium nitrate	5mM
Sodium nitrite + sodium nitrate	5mM + 5mM
L-arginine	1mM
L-NAME + sodium nitrite	1mM + 5mM
L-NAME + L-arginine	1mM + 1mM

Chemicals

Nitrite was added as sodium nitrite ($NaNO_2^-$) and nitrate as sodium nitrate ($NaNO_3^-$). The nitric oxide synthase blocking agent Nω-Nitro-L-arginine methyl ester hydrochloride (L-NAME), the NO quencher bovine haemoglobin (Hb), L-arginine, $NaNO_2^-$ and $NaNO_3$ were all obtained from Sigma Aldrich. All chemicals were added to a filtered seawater (35 ppt) medium before being injected into each micro-well of the microfluidic experimental chamber.

4.2.3 Ice Tank

For microcosm studies, an inverted sea-ice tank was engineered, in which the ice-water interface was inverted (Figure 4.4). This was designed to provide a practical means to efficiently allow discreet measurements of the algal biofilm with micro-sensors from the surface. A description of the inverted ice tank can be found in Cimoli et al. (2017). Briefly, ~35 litres of filtered seawater was incubated in the tank and frozen overnight (at -20°C) creating a ice surface measuring 850 cm x 850 cm. Hypersaline brine exuded from the matrix was removed via a vacuum pump before ~25 L of pre-chilled (-1.7°C) filtered seawater (35 ppt) was added on top of the formed ice, resulting in ~1cm of seawater above the ice-water interface. Prior to ice formation, twelve cylinders measuring 1 cm x 1 cm where placed on the ice tanks glass surface. Each cylinder had a light-impermeable black film

Table 4.2: Treatments applied to the experimental chambers embedded with the ice matrix of the ice-tank. Each treatment was repeated and randomised to get n=3. Control = no chemical treatment applied. DCMU = addition of 20 mM of the photosynthetic inhibitor 3-(3,4-dichlorophenyl)-1,1-dimethylurea. DD = Addition of 50 μM of the aldehyde (2E,4E/Z)-decadienal.

Effect	Treatment		
Light	Control	DCMU	DD
Dark	Control	DCMU	DD
Light + nitrite	Control	DCMU	DD
Dark + nitrite	Control	DCMU	DD

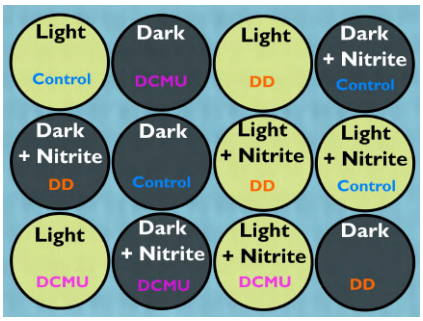

Figure 4.5: Representation of treatments randomly allocated chambers embedded into the ice matrix. DCMU = addition of 20 mM of the photosynthetic inhibitor 3-(3,4-dichlorophenyl)-1,1-dimethylurea. DD = a89of 50 μM of the aldehyde (2E,4E/Z)-decadienal.

attached to the outside of the chamber and a randomised treatment applied (Table 4.2). For the dark treatment, black light-impermeable tape was applied to the glass surface and the respective cylinder was placed on top and frozen into the ice matrix. The light treatment was applied directly to the glass and frozen in. Cultures of *F. cylindrus* were acclimated to the tank conditions by slowly decreasing the temperature (to -1.7°C) of the algal culture in a recirculating water-bath over 24 hours before inoculation. The ice thickness and overlying seawater was calibrated to ensure the level of PAR (measured using a Li-COR PAR sensor) reaching the algal biofilm was consistent (this ranged from ~96.3 μmol photon m^{-2} s^{-1} to 102 μmol photon m^{-2} s^{-1}).

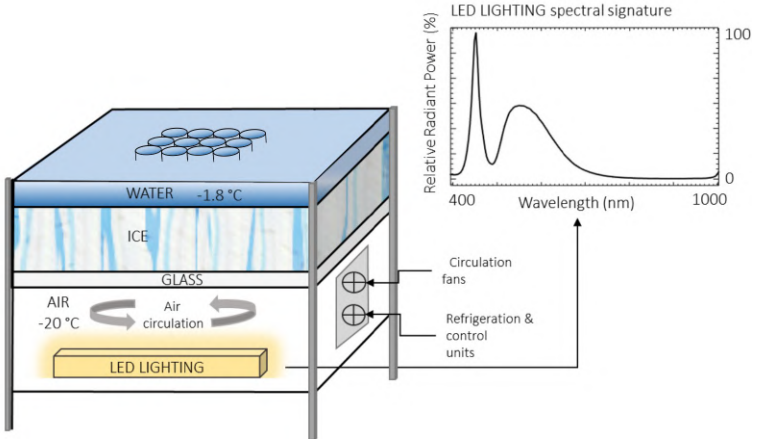

Figure 4.4: Graphical representation of the inverted sea-ice tank and the spectral signature of the LED lighting. Figure also displays the experimental chambers embedded in the ice matrix. Adapted with permission from Cimoli et al. (2017).

4.2.4 Temperature and salinity experiments

Salinity

Sodium chloride was added to modified L_1 media to produce four treatments (36 ppt, 38 ppt, 45 ppt and 55 ppt). Cultures of *F. cylindrus* (~2.50 x 10^6 cells mL^{-1} ± 0.5 x 10^6 cells mL^{-1}) in exponential growth phase (cultured at 2°C ± 1°C) were inoculated (5 mL) into 4 x 20 mL polycarbonate tubes containing 5 mL of L_1 media (salinity adjusted to their respective treatments). These cultures were acclimated for 5 days in the dark before NO production was measured. Experiments were conducted in the dark and repeated (n=3). Temperature was kept constant at 2°C ± 0.5°C.

Temperature

Experiments were conducted in 20 mL polycarbonate test-tubes contained in a temperature-gradient table as described in Boyd (2019). Constructed out of solid aluminium, the gradient table contained ten rows of four cylindrical chambers, in which 20 mL polycarbonate test tubes could be contained. At one end of the table cold water flowed through a hollow device, while at the other end warm water flowed through. This design resulted in a temperature gradient along the length of the table, so that each row of chamber could be adjusted to a specific temperature.

4.2.5 Pulse amplitude modulated fluorometry (PAM)

Chlorophyll *a* fluorescence of photosystem II was measured using a pulse-amplitude-modulated fluorometer (Water-PAM, Walz, Effeltrich, Germany) with an internal actinic light source centred on 660 nm. All samples were dark-acclimated for 30 minutes prior to measurement. Rapid light curves (RLC) were obtained under software control (WinControl 3, Walz). Maximum quantum yield in the dark-acclimated state, F_V/F_M, was obtained from the first value of the RLC when the irradiance was 0 μmol photon m^{-2} s^{-1}. A further description of the PAM methods used is described in Kennedy et al. (2012). The effective quantum yield ($\Delta F/F_{m'}$) was subsequently obtained after each exposure to increasing light at 31, 47, 71, 105, 162, 242, 346 and 483 μmol photon m^{-2} s^{-1}. The relative photosynthetic electron transport rate (rETR) was calculated as the product of the effective quantum yield of PSII and quantum flux density of photosynthetically active radiation (PAR). The

rETR data generated by the rapid light curves were fitted to the exponential function of Platt et al. (1980) using a multiple non-linear regression. In this case rETR was substituted for photosynthesis (P) in their P vs E relationship and the photosynthetic efficiency (α) is subsequently referred to as the initial slope of the rETR vs E curve (Equation 4.1).

$$rETR = rETR_{max} \times \left[1 - e\left(\frac{-\alpha E_d}{rETR_{max}}\right)\right] e\left(\frac{\beta E_d}{rETR_{max}}\right) \tag{4.1}$$

As photoinhibition did not occur in the light curves, the function reduces to:

$$rETR = rETR_{max} \times \left[1 - e\left(\frac{-\alpha E_d}{rETR_{max}}\right)\right] \tag{4.2}$$

Fluorescent induction curves were used to examine the effect of NO on PSII reaction centre kinetics and energy dissipation mechanisms. Firstly, cells were exposed to a brief pulse of far-red illumination (wavelength >680 nm) for 5 seconds to oxidise PSI and gain an estimate of F_o. Induction curves were initiated by first determining F_V/F_M through a saturation pulse, a delay of 30 seconds was used before the onset of actinic illumination (516 μmol photon m^{-2} s^{-1}). Another saturation pulse was performed at the onset of actinic illumination and every 20 seconds thereafter until the cessation of actinic light four minutes later. The final saturation pulse at four minutes was used to determine complementary quantum yields and photosynthetic quenching (qP).

qP was calculated as an estimate of the proportion of open PSII reaction centres, and as an indicator of quinone (Q_A and Q_B) redox state (it is assumed a linear relationship between fluorescence yield and percentage of Q_A exists) Equation: 4.3:

$$qP = \left(\frac{F'_m - F'}{F'_m - F_o}\right) \tag{4.3}$$

It should be noted that this model assumes that the antennae complexes for each reaction centre are not connected. Alternative methods for the calculation of qP based on the lake model which factors in reaction centre interconnectivity is described in Kramer et al. (2004). This model could not be used here due to the inability to reliably calculate F_o'.

Complementary quantum yields are calculated as described in Genty et al. (1996). These expressions are based on dividing absorbed excitation energy in PSII between three pathways:

$\Phi_{(II)}$ - photochemical conversion (Equation 4.4).

$\Phi_{(NPQ)}$ - regulated thermal energy dissipation (Equation 4.5).

$\Phi_{(NO)}$ - non-regulated heat dissipation and fluorescence emission (Equation 4.6).

Where,

$$\Phi_{(II)} = \left(\frac{F_{m'} - F}{F_{m'}}\right) = \frac{\Delta F}{F_{m'}} \tag{4.4}$$

$$\Phi_{(NPQ)} = \frac{F}{F_{m'}} - \frac{F}{F_m} \tag{4.5}$$

$$\Phi_{(NO)} = \frac{F}{F_m} \tag{4.6}$$

$\Phi_{(II)}$ refers to the fraction of energy that is photochemically converted in PSII, the remaining fraction (1- Φ_{II}) that does not get photochemically converted is the total yield of all non-photochemical excitation losses ($\Phi_{(loss)}$) (Equation 4.7) divided into two components Φ_{NPQ} and Φ_{NO} (Equation 4.8)

$$\Phi_{(loss)} = 1 - \Phi_{(II)} = \Phi_{(NO)} + \Phi_{(NPQ)} = \frac{F}{F_{m'}} \tag{4.7}$$

$\Phi_{(NO)}$ is the fraction of non-light induced energy dissipated as heat and fluorescence, due to closed PSII reaction centres. $\Phi_{(NPQ)}$ is the fraction of heat that is dissipated via the regulated photoprotective non-photochemical quenching (NPQ).

$$\Phi_{(II)} + = \Phi_{(NO)} + \Phi_{(NPQ)} = 1 \tag{4.8}$$

4.2.6 Adenosine -5 Triphosphate (ATP)

Determination of ATP concentration in cell extracts was performed through the bioluminescence of ATP with recombinant firefly luciferase and D-luciferin (Molecular Probes, USA) as per the manufactures instructions. Luminescence of samples and standards were read on a microplate reader

(BMG FLUOstar OPTIMA). Standard curves were conducted with each assay and the concentration of cellular ATP was normalised to cell concentration.

4.2.7 Statistical analysis

Data was analysed using Analysis of Variance (ANOVA) to determine the variation among treatments. If significant differences were detected, post-hoc Tukey multiple comparison tests were used to compare the experimental groups to the control. The software package XLSTAT (Addinsoft) and tests therein were used for all statistical analyses.

4.3 Results

4.3.1 Determination of exogenous supplied nitrogen on NO production

To determine the likely biochemical pathways of NO production in *F. cylindrus*, the effect of exogenous nitrogen on NO production in the dark was examined. Upon addition of NO_2^- (5 mM), NO production was significantly enhanced ($p<0.05$) compared to treatments without NO_2^- (Figure 4.6). Specifically, the sole addition of NO_2^- resulted in the highest observed NO production rate (mean of 26.01 nmol mg^{-1} chl*a* hr^{-1}; std ± 6.19) across all treatments. When NO_2^- (2.5 mM) was added in combination with NO_3^- (2.5 mM), NO production did not significantly differ to that of the sole NO_2^- addition (mean 2.40 nmol mg^{-1} *Chla* hr^{-1}; std ± 2.26). When the NOS inhibitor L-NAME was added with NO_2^- there was also no significant difference in NO production rate (mean 20.55 nmol mg^{-1} chl*a* hr^{-1}; std ± 4.41). The addition of NO_3^- (5 mM), L-arginine (1 mM) or L-NAME + L-arginine (1 mM + 1 mM) failed to induce significant NO production in *F. cylindrus*.

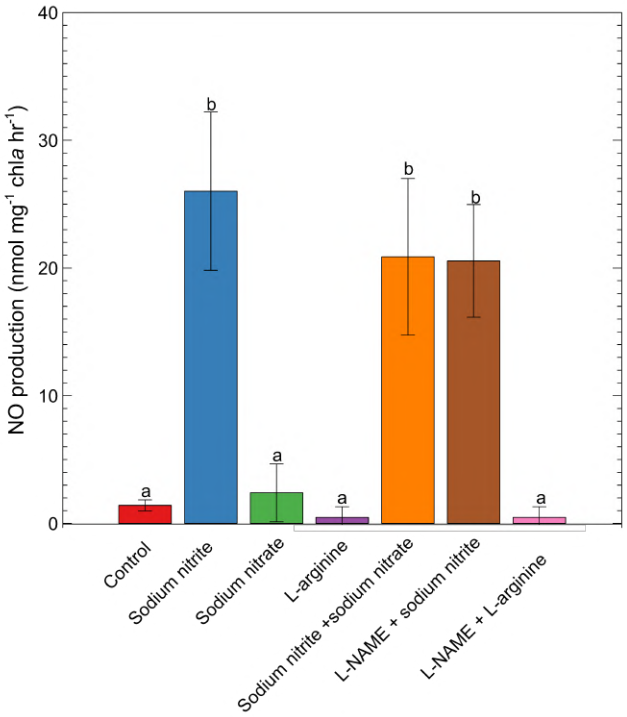

Figure 4.6: NO production of cells supplemented with the indicated nitrogen sources (nitrite, nitrate, L-arginine and the NOS blocking agent L-NAME). Cells (~10^6 mL^{-1}) were inoculated into separate microfluidic chambers and grown for 7 days with nitrogen replete media (flow rate of ~100 μL min^{-1}). Values with the same letter are not significantly different (p>0.05) as determined using Tukey multiple pairwise comparison test.

To confirm that the observed values were genuinely attributed to NO, an experiment was conducted in which the NO quencher bovine haemoglobin (Hb - 5 μM) was added following the addition of NO_2^- (5 mM) in the dark (Figure 4.7). The supplementation of NO_2^- resulted in a linear increase in the electrochemical signal, which was rapidly quenched following the addition of Hb. In comparison, NO_2^- and Hb failed to significantly alter the electrochemical signal in the control (no cells). These results confirm that the observed electrochemical signals can be ascribed to the production of NO and support a nitrite-dependent NO production mechanism in *F. cylindrus*.

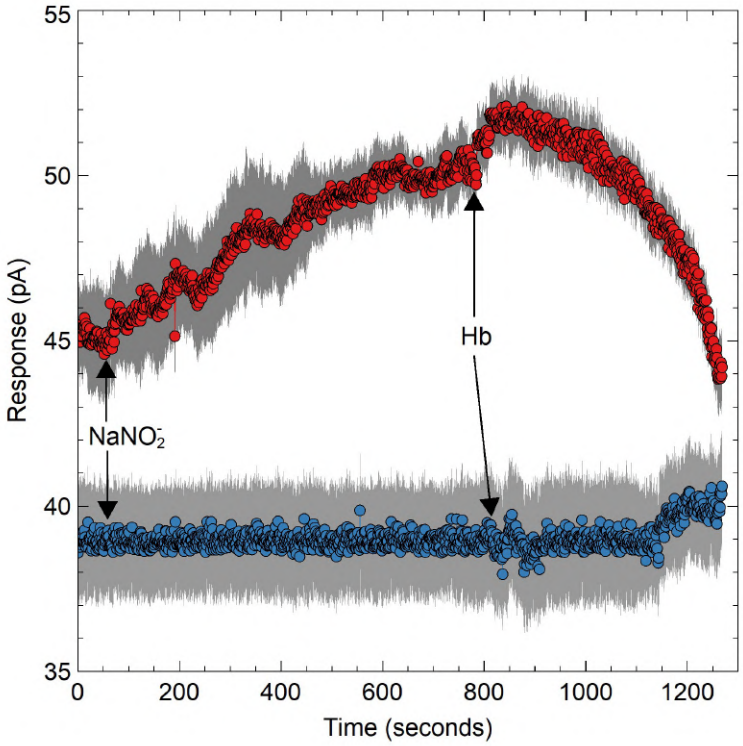

Figure 4.7: Electrochemical trace of NO in a cellular suspension of *F. cylindrus* following the addition of 5 mM NO_2^- in the dark, complete inhibition of the electrochemical trace was achieved with the NO quencher haemoglobin (Hb - 1 μM). Blue circles represent the control (no cells), where as the red circles represent the treatment with cells. Error is shown in grey as the standard deviation of the mean (n=3).

To test the hypothesis that nitrite-dependent NO production is inhibited during illumination, cells were exposed to light at 50 μmol photon m^{-2} s^{-1} following NO_2^- or NO_3^- addition in the dark (Figure 4.8). Supplementation of NO_2^- increased the production of NO (from ~38 pA to ~60 pA) which rapidly decreased at the onset of illumination. The addition of NO_3^- (5 mM) in a separate cellular suspension, resulted in a minor increase in NO which was also inhibited upon illumination. Both results suggest that light inhibits nitrite-dependent NO production in *F. cylindrus*.

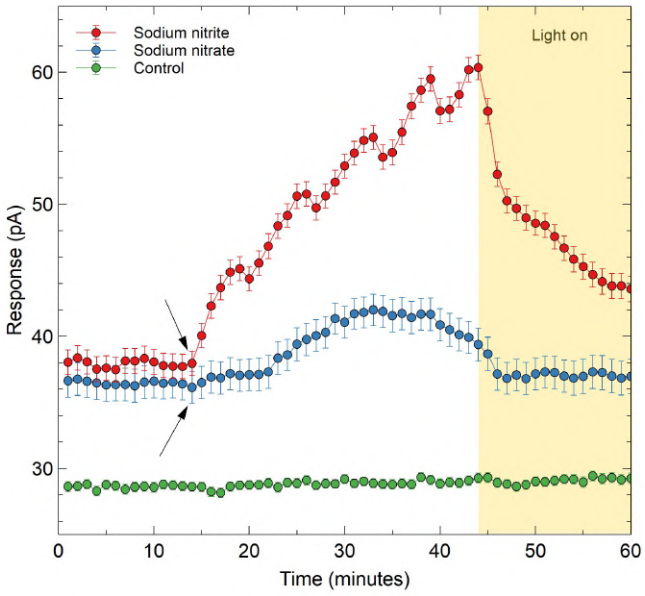

Figure 4.8: Electrochemical trace of NO (pA) of cells contained in microfludic chambers (~10^6 cells ml^{-1}). The arrows indicate when 5 mM NO_2^- or 5 mM NO_3^- was injected into each chamber in the dark, NO_2^- was also injected into the control. Cells were illuminated with 50 μmol photon m^{-2} s^{-1} after 45 minutes.

To determine if exposure to high light could induce NO production, cells were exposed to either low (50 μmol photon m^{-2} s^{-1}) or high light (933 μmol photon m^{-2} s^{-1}). Cells (~10^6) were cultured in microfluidic devices (n=3) in the dark for 10 days prior to light exposure. Illumination of cells with high light (933 μmol photon m^{-2} s^{-1}) resulted in a linear increase in the electrochemical trace (Figure 4.9), which rapidly dissipated following the addition of Hb (1 mM). Whereas, exposure to 50 μmol photon m^{-2} s^{-1} did not alter the electrochemical trace. This may suggest that exposure to such a high degree of light immediately after darkness may have disrupted normal photosynthetic electron flow, allowing for nitrite accumulation and NO production via nitrate reductase (NR). Therefore, nitrite-dependent NO production may be able to be detected under illuminated conditions, but only when the electron transport chain is inhibited.

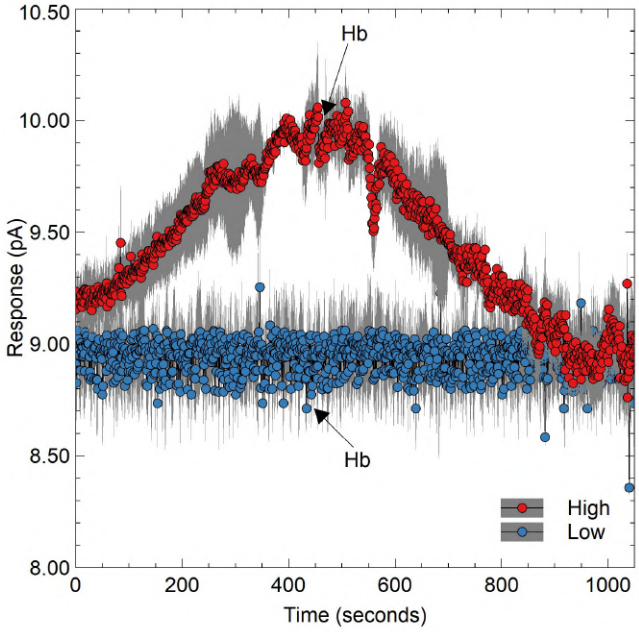

Figure 4.9: Electrochemical trace of NO production in cellular suspensions of *F. cylindrus* contained in microfluidic growth chambers under two illuminating conditions. Cells were incubated (in nitrogen replete L_1 media) in the dark for seven days prior to experimentation. Cells were then exposed to one of two treatments: i) high light (red circles - 933 μmol photon m^{-2} s^{-1}) or, 2) low light (blue circles - 50 μmol photon m^{-2} s^{-1}). The NO quencher haemoglobin (Hb - 1 μM) was added to ensure any increase in the electrochemical signal was indeed ascribed to NO. Error is shown in grey as the standard deviation of the mean (n=3).

To further explore the effect of light on NO production, the photosystem II inhibitor DCMU (10 μM) was added prior to illumination (with or without light) (Figure 4.10a). The addition of DCMU to illuminated cells with NO_2^- resulted in a similar level of NO production compared to those in the dark with NO_2^-. Without NO_2^-, illuminated DCMU treated cells produced minimal NO. This suggests that cells are unable to produce considerable amounts of NO when the photosynthetic apparatus is functioning optimally. No significant differences were observed between the light and dark treatments without the NO_2^-. Addition of the aldehyde decandinal (DD) resulted in a significant ($p < 0.05$) release of NO across all treatments, which is consistent with other studies using DD.

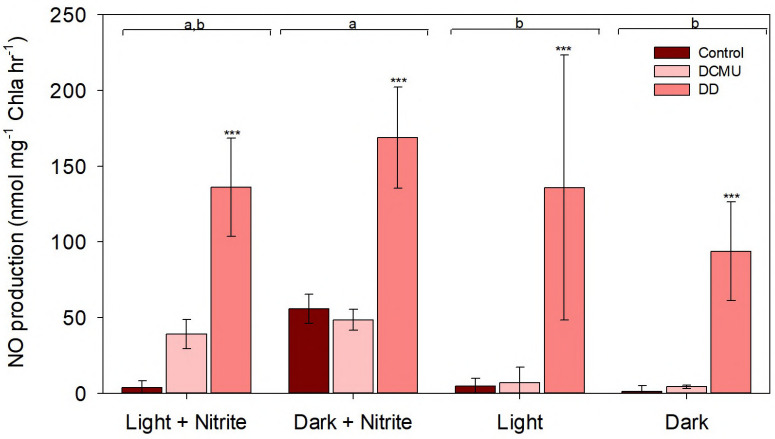

(a) Microfluidics

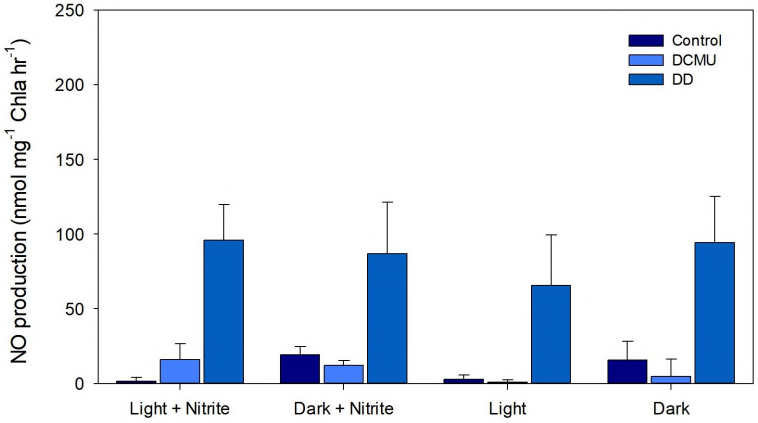

(b) Ice-tank

Figure 4.10: NO production in *F. cylindrus* cells when supplemented with or without NO_2^- (5 mM) and exposed to darkness or 50 μmol photon m^{-2} s^{-1} of white light for 60 minutes. Experiments were conducted in **a)** microfluidic growth chambers or **b)** cylinders embedded in an artificial ice-tank. Error is the standard deviation of the mean (n=3). Values with the same letter are not significantly different ($p > 0.05$) as determined using Tukey multiple pairwise comparison test. DCMU = addition of 20 mM 3-(3,4-dichlorophenyl)-1,1-dimethylurea. DD = addition of 50 μM of the aldehyde (2E,4E/Z)-decadienal.

This experiment was repeated in the ice-tank to explore if abiotic parameters associated with sea-ice had any influence on NO production (Figure 4.10b). The amount of NO observed was considerably less in the ice-tank compared to those in microfluidic devices across all treatments. Although the response to each nitrogen addition was similar. It remains unclear if this was a caveat of experiential design or one truly attributed the variation in abiotic parameters.

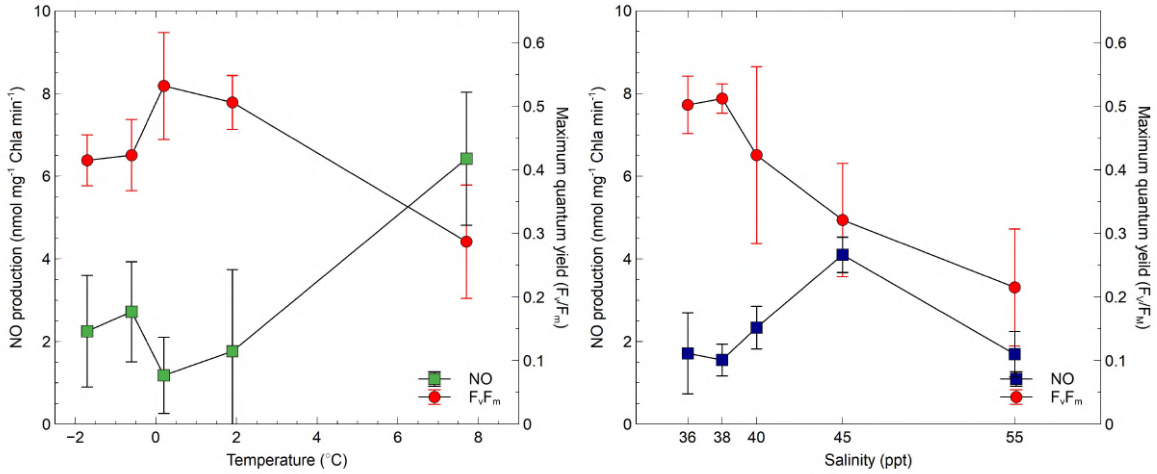

(a) Temperature **(b)** Salinity

Figure 4.11: NO production and maximum quantum yield (F_v/F_m) in cellular suspensions of *F. cylindrus* when exposed to variation in **a)** Temperature (-1.7°C, -0.6°C, 0.2°C, 1.9°C and 7.7°C) (salinity was 36 ppt for all treatments) and **b)** salinity (36 ppt, 38 ppt, 40 ppt, 45 ppt and 55 ppt) (temperature was maintained at 2°C ± 0.5°C). NO production rate was measured in the dark and normalised to chlorophyll *a* concentration.

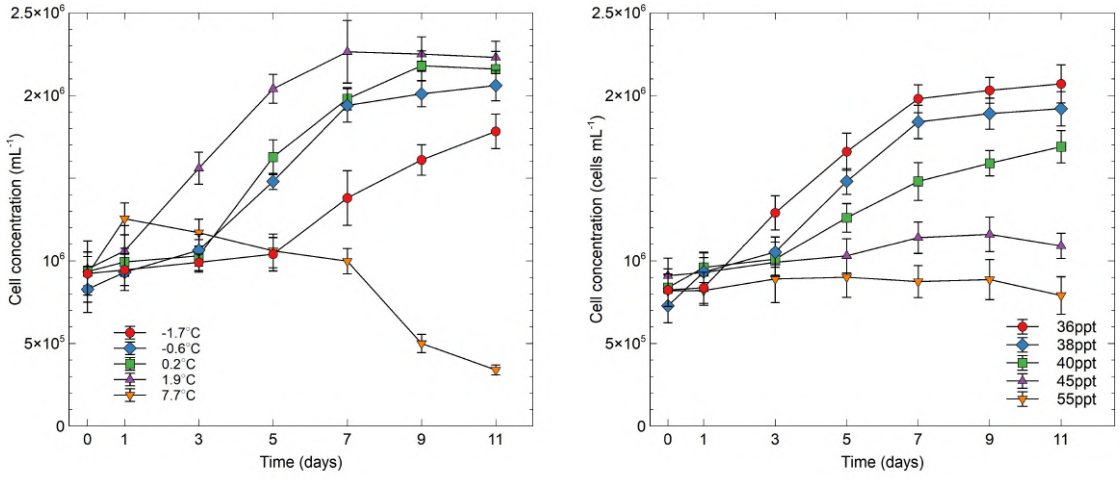

(a) Temperature **(b)** Salinity

Figure 4.12: Growth curves of *F. cylindrus* over 11 days when exposed to variations in **a)** temperature and **b)** salinity. Cultures were grown in 20 mL clear polycarbonate tubes under 50 μmol photon m^{-2} s^{-1} (16hr:8hr, light:dark cycle)

The concentration of NO increased when cultures of *F. cylindrus* were exposed to temperatures above 0°C (Figure 4.11a), although this was only significant at the highest temperature exposed (7.7°C (mean 6.42 nmol mg^{-1} chl*a* min^{-1} ± 1.61 nmol mg^{-1} Chl*a* min^{-1})). The maximum quan-

tum yield of PSII appeared to be inversely correlated with temperature (Figure 4.11a), with cells indicating heightened stress with increased temperature.

4.3.2 Physiological and photo-physiological implications of exogenously supplied NO

Cell concentration and ATP

When spiked with increasing concentrations of NO (from the NO donor SNAP; 0.5 mM, 5 mM and 10 mM) over 10 days, cellular growth stalled (Figure 4.13c). The addition of 10 mM and 5 mM SNAP resulted in the most pronounced inhibition of cell numbers, which were both significant after seven days of exposure ($p<0.05$ and $p<0.05$, respectively) (Figure 4.13c). The addition of 0.5 mM SNAP did not significantly influence cell numbers, compared to the control. The effect of 0.5 mM, and 5 mM SNAP on the Adenosine-triphosphate (ATP) level was not significant, whereas the addition of 10 mM resulted in lower ATP concentration per cell, which was significant on day 10 (Figure 4.13d).

Photophysiology

Figure 4.13a shows the influence of SNAP on the maximum quantum yield of PSII (F_v/F_m). Addition of 10 mM SNAP resulted in the most pronounced reduction of F_v/F_m from a mean of 0.602 to 0.392 and was significantly different to that of the control on days 5, 7 and 10 ($p<0.05$). This trend was also observed with the addition of 5 mM SNAP but this was only significant on day 5 ($p<0.05$) and day 10 ($p<0.05$).

When spiked with 5 mM and 10 mM SNAP, the maximum relative electron transfer rate ($rETR_{max}$) was heavily diminished (Figure4.13b), with 10 mM SNAP causing a significant reduction ($p<0.05$) in rETR over the ten days. This may indicate that high concentration of NO exerts a negative influence on the efficiency of electron transfer between photosystems.

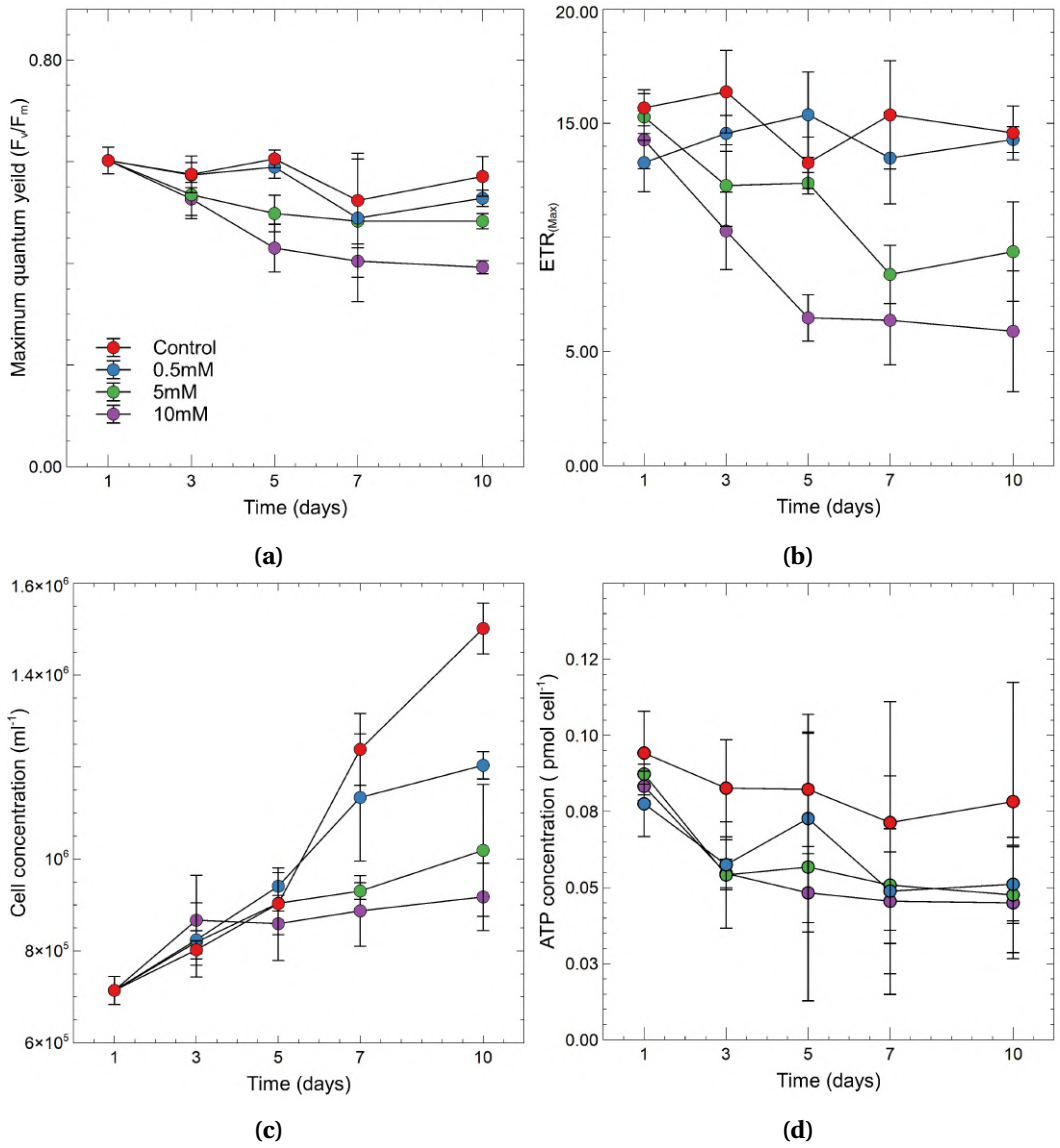

Figure 4.13: The effect of exogenously supplied NO (from SNAP) on *F. cylindrus* growth and photophysiology. Cultures were in exponential growth phase in L_1 media before SNAP was added at one of three concentrations: 0.5 mM, 5 mM and 10 mM. Its effect on **a)** maximum quantum yield (F_v/F_m) of PSII, **b)** maximum relative electron transfer rate ($rETR_{max}$) between PSII and PSI , **c)** growth rate (cells mL^{-1}) **d)** cellular ATP concentration (ρmol $cell^{-1}$) were examined over a period of ten days. Error is the standard deviation of the mean (n=3).

To further explore this result, fluorescent induction curves were conducted to examine the flux of excitation into photochemical or non-photochemical pathways. The addition of 5 mM and 10 mM SNAP significantly affected qP (Figure 4.14a). qP is the estimation of excitation energy used in photochemical reactions and is often used to describe the degree of "openness" of the

PSII reaction centres. More specifically, qP describes the oxidative state of the primary electron acceptor (Q_A) of PSII (Klughammer and Schreiber, 2008; Kramer et al., 2004). Thus, any reduction in qP can be attributed to the "closure" of reaction centres (or increased oxidation of Q_A) that results from a saturation of photosynthesis by light. Therefore, the observed decrease in qP from high concentrations of SNAP infers that NO can inhibit the electron transfer between Q_A and Q_B, and inhibit the charge recombination reactions of Q_A, causing a non-light induced closure of reaction centres. Moreover, when examining the quantum yield of all losses (the fraction of energy absorbed by PSII that is used photochemically and lost non-photochemically ($\Phi_{(loss)}$), the degree of energy shunted through regulated non-photochemical dissipation mechanisms ($\Phi_{(NPQ)}$) decreased with increased levels of SNAP (Figure 4.14b). Interestingly, the decrease of $\Phi_{(NPQ)}$ was inversely proportional to the increase in $\Phi_{(NO)}$, suggesting that high concentration of NO may influence the regulation of non-photochemical energy dissipation mechanism such as xanthophyll cycling and carotenoid dissipation.

4.3.3 A note on nitrite reductase (NiR)

Currently there are no identified NiR enzymes in the *F. cylindrus* genomic database. Consequently, a sequence alignment of a hypothetical protein (JGI|200565) to a number of nitrite reductase proteins in other diatoms was conducted (Table 4.3). The highest similarity was matched to a nitrite reductase protein in the oleaginous diatom *Fistulifera solaris* (Figure 4.15). Upon further inspection, this protein contained two major domains belonging to NiB and Rieske-NirD. NiB encodes a NADPH nitrite reductase large subunit and NirD a nitrite assimilation iron-sulfur binding cluster (Reiske) involved in the binding of ferredoxin.

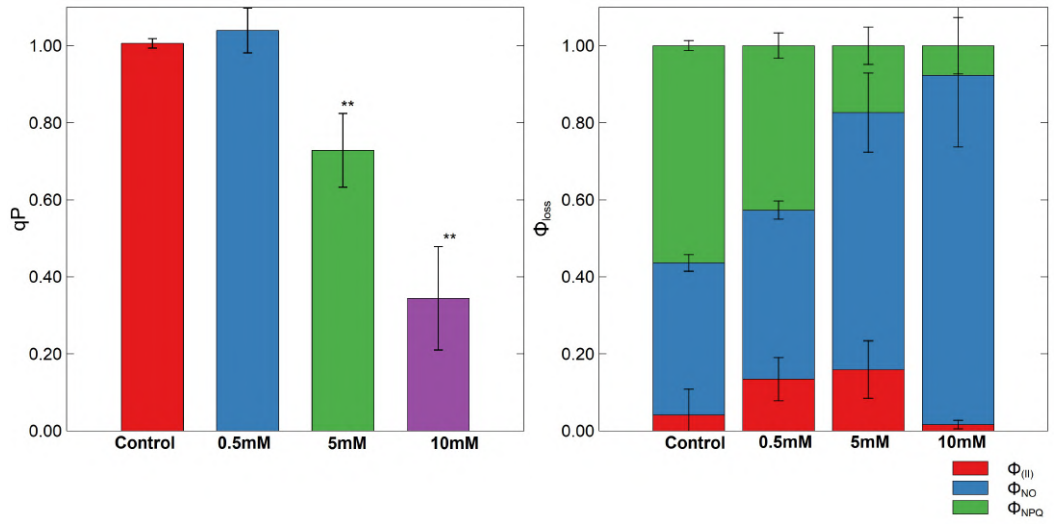

(a) **(b)**

Figure 4.14: **a)** Estimated proportion of open PSII reaction centres (qP) of cells exposed to increasing concentrations of the NO donor SNAP (0.5 mM, 5 mM and 10 mM). **b)** The fraction of energy absorbed by PSII that is used photochemically and lost non-photochemically. Collectively represented as the quantum yield of all losses ($\Phi_{(loss)}$), divided into three components: 1) photochemical conversion ($\Phi_{(II)}$), 2) energy loss to regulated non-photochemical dissipation via photoprotective mechanism ($\Phi_{(NPQ)}$) and 3) non-regulated energy dissipated in the form of heat and fluorescence ($\Phi_{(NO)}$), as determined by fluorescence induction curves where cells were exposed to actinic illumination of 516 μmol photon m^{-2} s^{-1} for 4 minutes. ** Represents a statistically significant difference ($p<0.05$).

Table 4.3: NCBI BLASTp amino acid similarity matches of a hypothetical protein (JGI protein Id|200565) to a number of nitrite reductase protein in other diatoms.

Description	**Max Score**	**Query Cover**	**E-value**	**Identified**	**Accession number**
hypothetical protein_JGI200565 [*Fragilariopsis cylindrus* CCMP1102]	2193	100%	0	100%	OEU06628.1
nitrite reductase (NADH) large subunit [*Fistulifera solaris*]	1576	98%	0	73%	GAX11222.1
nitrite reductase (NADH) large subunit [*Fistulifera solaris*]	1572	98%	0	73%	GAX13836.1
hypothetical protein THAOC_35252 [*Thalassiosira oceanic*a]	1514	100%	0	69%	EJK46104.1
NADPH nitrite reductase [*Thalassiosira pseudonana* CCMP1335]	1469	96%	0	69%	XP002287665.1
nitrite reductase (NAD(P)H) large subunit [*Ectocarpus siliculosus*]	1118	98%	0	55%	CBJ31380.1

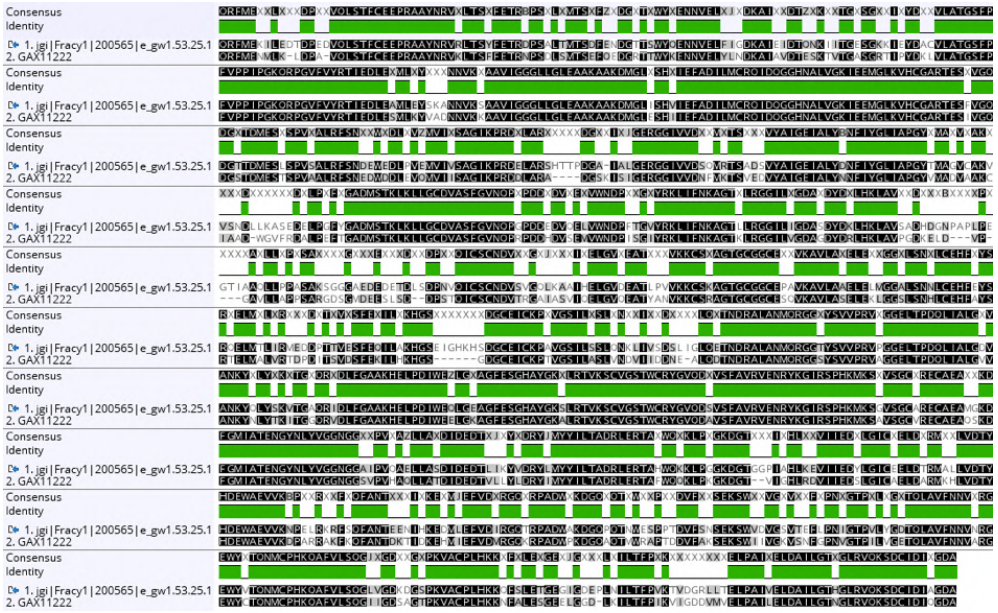

Figure 4.15: *F. cylindrus* amino acid sequence alignment of hypothetical protein (Joint Genome Institute protein Id|200565) matching highest similarity to a nitrite reductase protein in the oleaginous diatom *Fistulifera solaris* (BLASTp, Evalue < 0 ; similarity = 85.8%). Matching sequences are shown in green and the consensus in black, missing amino acids in grey. Alignment was conducted in Geneious (Biomatters limited).

4.4 Discussion

Results presented in the study have, for the first time, illustrated that NO production in *F. cylindrus* is nitrite-dependent; most likely via a NR mechanism. Moreover, no evidence was found to suggest that NO could be produced during normal illumination conditions, but only if the photosynthetic chain was inhibited. Also, it appears that extreme variation in environmental parameters can influence NO production where it may be used as a stress signalling molecule.

4.4.1 Biochemical mechanisms of NO production in *F. cylindrus*

There are two biochemical pathways of NO production reported to exist in marine microalgae: i) via nitric oxide synthase (NOS) using L-arginine as a substrate (Vardi et al., 2006), and, ii) via nitrate reductase using nitrite as a substrate (Dolch et al., 2017; Sakihama et al., 2002). Results presented here illustrate, for the first time, that NO production in *F. cylindrus* is nitrite-dependant via the enzymatic action of nitrate reductase (NR). Specifically, it was found that NO production increased when cells

were provided with nitrite in the dark. In contrast, it was not possible to induce any significant NO production when L-arginine was added. This suggests that a NOS-like mechanism is not present in *F. cylindrus*, or that the reaction does not use L-arginine as a substrate. Recently, Vardi et al. (2006) demonstrated that NO production in the marine diatoms *Phaeodactylum tricornutum* and *Thalassiosira weissflogii* could be traced to a plant-like NOS gene present in the genome. Additionally, Di Dato et al. (2015) found transcripts of NOS enzymes in *Pseudo-nitzschia multistriata* which aligned to other NOS sequences found in cyanobacteria, centric and ancestral pennate diatoms. The analysis of the *F. cylindrus* genome herein (https://genome.jgi.doe.gov/Fracy1/Fracy1.home.html) failed to determine any sequence match for NOS or NOS-like enzymes; this result is consistent with that of Di Dato et al. (2015) who also found no evidence for NOS in *F. cylindrus*. Thus, the presence of NOS or a NOS-like activity does not appear to be homologous among marine diatoms. This is especially apparent in *F. cylindrus* whose genetic composition is highly differentiated and divergent from that of many other diatoms; a probable manifestation of environmental adaptation (Mock et al., 2017). It would be beneficial for future studies to conclusively establish the molecular drivers behind NO production in *F. cylindrus*, in particular identifying any alternative NO-production mechanisms.

NO can also be chemically formed in seawater through bacterial denitrification/ nitrification cycles or when exposed to short-wavelength (219 nm - 419 nm) of light which can induce the photolysis of nitrite to NO (Mack and Bolton, 1999). While possible, it is unlikely that this mechanism is significant here due the irradiance used (white LED's peak at 460nm) and the lack of free-nitrite in the media and the axenic state of the culture.

4.4.2 Photosynthetic coupling of NO and its physiological influence

Interestingly, it is further demonstrated here that nitrite-dependent NO production could be abolished upon illumination, a finding that is consistent with other studies on microalgae (Mallick et al., 1999; Sakihama et al., 2002; Yamasaki et al., 1999). Additionally, when the photosynthetic inhibitor DCMU was added to illuminated cells, NO was detected at a similar concentration to those in the dark. This suggests that cells cannot produce high concentrations of NO during normal photosynthetic electron flow and can instead be explained in the context of nitrate/nitrite

metabolism (Sanz-Luque et al., 2015). During optimal growth, NR catalyses the reduction of nitrate to nitrite using NADPH in the cytosol (Figure 4.16). The product, nitrite, is transported into the chloroplast where the enzyme nitrite reductase (NiR) reduces it to ammonia. Essential to this reduction of nitrite is the reduced form of ferredoxin, created when water is oxidised at photosystem II (PSII) to $NADP^+$ at photosystem I (PSI) during normal photosynthetic electron flow. Thus, when photosynthesis is operating at its optimal capacity, nitrite is rapidly assimilated and does not accumulate in the chloroplast. If the supply of reduced ferredoxin diminishes, such as in the dark or during conditions that disrupt normal photosynthetic electron flow, nitrite accumulates, causing NR to convert nitrite to NO (Figure 4.16).

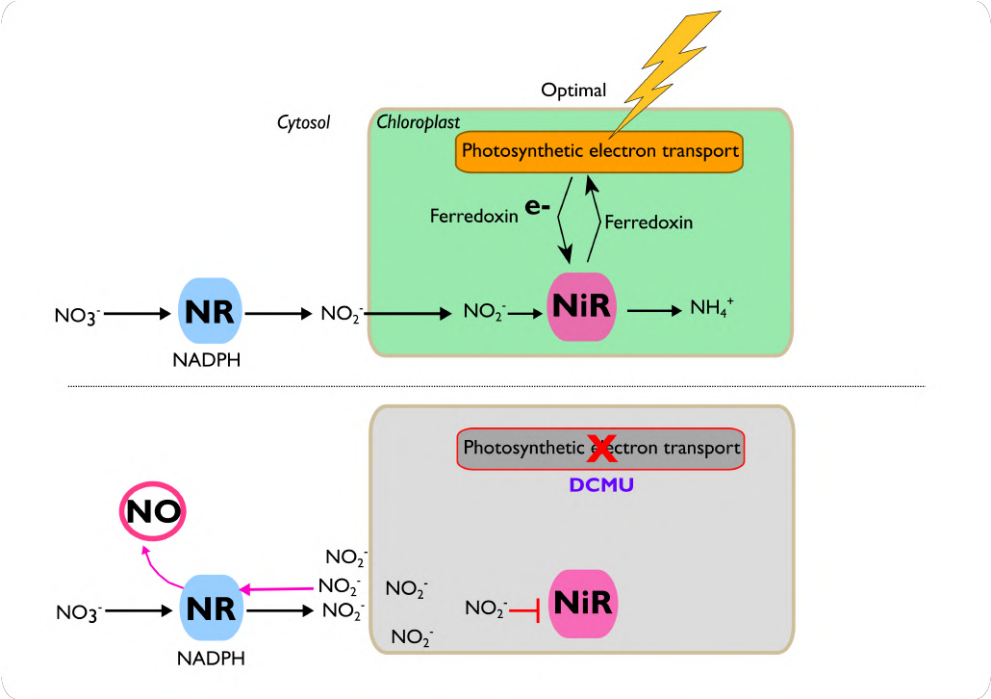

Figure 4.16: Schematic representing the linkage between NO production and nitrite accumulation. In the cytosol of photosynthetic organisms, nitrate (NO_3^-) is reduced to nitrite (NO_2^-) by nitrate reductase (NR). Under optimal photosynthetic electron transport, nitrite is rapidly assimilated by nitrite reductase (NiR) using reduced (e-) ferredoxin produced when water is oxidised at photosystem II. When the photosynthetic electron transport chain is disrupted (such as in the dark or when the photosynthetic inhibitor (DCMU) is added) ferredoxin can no longer be provided to NiR, thus nitrite accumulates and induces NR to convert NO_2- to NO.

The addition of exgoenous NO (from the NO donor SNAP) negatively influenced aspects of the electron transfer rate of PSII, the oxidation state of the primary electron acceptor Q_A (qP) and the

partitioning of energy into photochemical and non-photochemical pathways ($\Phi_{(loss)}$). Similar results have been observed in studies with higher plants. Recently, Wodala et al. (2008) demonstrated that NO limits the electron transfer between Q_A and Q_B and interrupts charge recombination with PSII. Furthermore, Takahashi and Yamasaki (2002) demonstrated that SNAP inhibited the electron transfer rate in isolated chloroplasts and limited the rate of ATP synthesis. In this study, NO did appear to inhibit the electron transfer rate but not cellular ATP concentration. This result was surprising as the NO-derived inhibition of electron transfer should be reflected in reduced ATP concentration, due to the loss of proton accumulation in the thylakoid lumen that is necessary to drive ATP formation via ATP synthase. It can only be speculated that either, a) the NO-derived inhibition was not sufficient to induce complete cessation of ATP synthesis, b) other ATP generating mechanisms were activated or c) the assay used was not sensitive enough for subtle variations in ATP. The observed NO-induced reduction in electron transport is consistent with that of other studies in higher plants (Takahashi and Yamasaki, 2002; Wodala et al., 2008) where it has been reported to slow down the transfer of electrons between Q_A and Q_B. The terminal electron acceptor of PSII consists of two plastoquinone molecules (Q_A and Q_B) separated by non-heme Fe^{2+}. NO is known to display a high affinity for ferric (Fe^{3+}) or ferrous forms of iron (Fe^{2+}), readily binding to heme and iron-sulphur protein complexes *in vivo* (Graziano and Lamattina, 2005). Thus the inhibition of electron transfer may be explained by the ability of NO to bind to Fe^{2+}, this essentially slows the transfer of electrons from Q_A to Q_B (Diner and Petrouleas, 1990; Graziano and Lamattina, 2005; Wodala et al., 2008). The interaction of NO with $Q_A{}^{Fe^{2+}}Q_B$ is further illustrated in this study by the reduction of the chlorophyll fluorescence parameter qP in response to increasing SNAP. The photochemical capacity of PSII can be described by the redox state of Q_A (Kramer et al., 2004; Oxborough and Baker, 1997); because qP describes the state of oxidation of Q_A, the observed decrease in qP may infer that the charge recombination reactions of Q_A is inhibited, causing a non-light induced closure of reaction centres. However, values of qP need to be interpreted with caution, as the model assumes non-connectivity of reaction centres (Kramer et al., 2004).

NO has also been reported to alter non-photochemical quenching of chlorophyll *a* fluorescence (Wodala et al., 2008). When exposed to increasing levels of SNAP, the division of excitation energy

into competing non-photochemical pathways was altered. Application of high levels of SNAP appeared to decrease the ability of cells to dissipate excess excitation energy via regulated non-photochemical pathways (ie xanthophyll cycling), and instead by dissipation process that are not regulated ($\Phi_{(NO)}$). Klughammer and Schreiber (2008) illustrated that an increase in the parameter $\Phi_{(NO)}$ and a subsequent decrease in $\Phi_{(NPQ)}$ can be traced to stress induced damage of the photosynthetic apparatus. The mechanisms behind these observations remain unclear and further work is needed to quantify and substantiate nitric oxides influence and interaction with the photosynthetic apparatus. It should be noted that the level of exogenous NO (from SNAP) used is an order of magnitude higher (mmol L^{-1}) than cells would be exposed to in the natural environment (nmol L^{-1}), nonetheless it clearly demonstrates the potential implications that high concentrations of NO can have on multiple aspects of photophysiology.

Previous studies have also found that NO can be produced during the normal growth cycle of some species of microalgae. Estevez and Puntarulo (2005) illustrated that cultures of Antarctic green algae *Chlorella sp.* produced NO during exponential growth. Kim et al. (2006) described the appearance of NO during growth of the toxic-forming flagellates *Chatonella marina* and *Heterosigma akashiwo*. Zhang et al. (2006a,b) demonstrated that low concentrations of NO (10^{-8} - 10^{-9} mol L^{-1}) were present in cultures of *Platymonas subcordiformis, Skeletonema costatum,* and *Gymnodinium sp.*. In this study, the growth of *F. cylindrus* could be stalled when increasing concentrations of NO (from the NO-donor SNAP) were added. This is consistent with other studies on microalgae upon NO addition (Chung et al., 2008; Sakihama et al., 2002; Zhang et al., 2003). The exact reason behind these observations remains unclear, although it may be similar to that of higher plants where NO is used in signal transduction pathways that regulate growth responses (Wilson et al., 2008). Additionally, in some microalgae NO can reach a high concentrations at the end of exponential growth (Estevez and Puntarulo, 2005; Zhang et al., 2006b), and this may have role in initiating programmed cell death (Chung et al., 2008). Vardi et al. (2006) initially proposed that NO could act as a population control agent in *Phaeodactylum tricornutum* upon exposure to the diatom-derived aldehyde 2E,4E/Z-decadienal (DD). Application of DD initiated a calcium transient that triggered a spike in NO which eventually lead to the promotion of caspase-dependent programmed cell death.

When DD was added to cells in this study, a significant increase in NO production was observed across all treatments. Diatom derived aldehydes (like DD) are the products of fatty-acid oxidation which are commonly released when populations are subjected to grazing and nutrient stress (Vardi, 2008). The observed spike after DD application may suggest NO could also be involved in stress based signalling as found in other diatoms. Although more work is need to substantiate this claim, future studies would benefit from examining potential mechanisms regulated by exposure to reactive aldehydes and intracellular NO signals.

4.4.3 Abiotic factor influencing NO production

Antarctic sea-ice diatoms are continually exposed to rapid and extreme variations in environmental parameters. The ability of a photosynthetic organism to adapt and thrive in this ephemeral habitat relies on efficient molecular machinery that can rapidly alter metabolic and physiological functions. Imperative to these adaptive processes is a system that effectively senses changing abiotic conditions. Various chemical signal molecular have been identified and recently NO has been proposed as another chemical messenger. Nitric oxide production in higher plants and microalgae appears to be heavily influenced by environmental variables such as light, salinity and nutrients (Bouchard and Yamasaki, 2008; Fancy et al., 2017; Kumar et al., 2015; Qiao and Fan, 2008). In this study, it has been shown that NO production in *F. cylindrus* is heavily dependent on the environmental nitrogen status, a scenario that appears to be consistent with other studies on microalgae (Bouchard and Yamasaki, 2008; Dolch et al., 2017; Mallick et al., 1999; Zhang et al., 2006b). Information regarding other abiotic influences are limited and need to be considered in future studies. The adjustment of salinity in this study appeared to influence the production of NO, where NO increased in a linear fashion with salt concentration and then declined at 55 ppt. The role of NO in salt tolerance in higher plants has been reported to alleviate the damage of osmotic stress by acting as an antioxidant (Fancy et al., 2017). In the marine environment, NO has been shown to enhance the secretion and flux of sodium chloride ions in mangroves. In microalgae, Zhang et al. (2006b) illustrated that NO production could be influenced by changes in salinity and temperature, a finding consistent with this study. Surprisingly, I observed a significant increase in NO when cells were exposed to a relatively high temperature (7.7°C); this also coincided with a decrease

in F_v/F_m. This suggests that NO was produced as a result of temperature induced stress, which may be used as a stress-signal molecule. A similar finding was also observed in the coral symbiont *Symbiodinium microadriaticum*, where exposure to acute heat stress induced the production of NO and caused a decline in F_v/F_m (Bouchard and Yamasaki, 2008). Bouchard and Yamasaki (2008), also found a positive correlation between NO production and capase activity, further indicating the role of NO as a cellular messenger. Therefore, thermally induced NO production may be a stress signal mechanism or it could indicate heightened enzymatic activity of NR. Although the degree of thermal exposure is not ecologically representative, it was selected to observe whether NO could be produced under extreme environmental pressure. Thus, it appears that production of NO in marine diatoms is tightly coupled to environmental forcing.

4.4.4 Implications

NO plays a key role in atmospheric chemistry via the photochemical destruction of ozone (O_3) and because anthropogenic sourced NO emissions are increasing their influence on biological activity needs to be evaluated. The transient nature of Antarctic sea-ice ecosystems ensures that ice-associated microbes are constantly exposed to variation in temperature, salinity, nutrients and light. The effect of NO in combination with the predicted changes on communities that inhibit the sea-ice matrix is unknown. In this study, I have illustrated that change in any one of these abiotic parameters can influence the production of NO in *F. cylindrus*. While speculative, it suggests that during periods of environmental stress NO could be produced in *F. cylindrus* as a "stress signal" molecule (Dolch et al., 2017; Vardi, 2008; Vardi et al., 2006). If NO can significantly impact cellular growth and impair aspects of photosynthetic electron transport, as demonstrated in this study, further investigation is warranted. In particular, examining the molecular mechanism behind NO production and whether it is an important extracellular signal transducer that facilitates a response to multiple environmental stressors.

Chapter 5

Rapid transition in snow thickness causes physiological stress in fast-ice algae communities in McMurdo Sound, Antarctica

---

5.1 Introduction

Light is the primary driver of ice-associated phototrophic organisms in polar ecosystems and variation in the quantity and quality of irradiance significantly influences the primary production (Arrigo et al., 2008; Petrou et al., 2016). When light penetrates sea-ice it interacts with the crystal lattice structure causing significant refraction and exponential attenuation of photosynthetically active radiation (PAR: 400 -700nm) with depth. Due to its higher albedo and light scattering properties, it is often the thickness of overlying snow that limits irradiance reaching ice-associated taxa. In land-fast ice, the majority of photosynthetic organisms are concentrated within a few centimetres of the ice-water interface (McMinn et al., 2010; Ryan et al., 2009) and bottom-ice microalgae are among the most shade-adapted organisms known to exist (Lizotte and Sullivan, 1991). Active growth has been recorded at < 5 μmol photon m^{-2} s^{-1} and photoinhibition/saturation can occur at < 20 μmol photon m^{-2} s^{-1} (McMinn et al., 1999a; Palmisano et al., 1987). However, the mechanisms underlying efficient shade-adaptation can also limit the capacity for photosynthetic adjustment

when sudden changes in irradiance occur (Raven, 2011; Raven and Beardall, 2011).

The timing and magnitude of changes in irradiance is critical in determining the capacity of algal adaptation (Juhl and Krembs, 2010). On the scale of hours to days, bottom-ice algae can efficiently photoacclimate to increased irradiance by modifying their light harvesting pigments and reaction centres (Katayama et al., 2011; Kuczynska et al., 2015). Adaptation on the scale of minutes to hours is limited by their photophysiological state (Juhl and Krembs, 2010; Petrou et al., 2010). The failure to quickly acclimate can rapidly lead to photoinhibition and photodamage if available photo-protection mechanisms cannot efficiently dissipate excess excitation energy (Ruban et al., 2004). Photoinhibition alone is not necessarily damaging under normal circumstances and can function as a repair mechanism by triggering the photo-inactivation of light harvesting proteins (Murata et al., 2007; Ryan et al., 2009). However, under conditions of saturating irradiance, the rate of inactivation can exceed the rate of repair and prolonged photoinhibition can lead to photo-damage (Nishiyama et al., 2006). In these circumstances the absorbed energy exceeds the capacity for utilisation and electrons leak onto O_2, generating harmful reactive oxygen species (ROS) (Diaz et al., 2018; Huang et al., 2018; Juhl and Krembs, 2010; Mallick and Mohn, 2000). When electrons leak on to O_2, superoxide (O_2^-) free-radicals form which can be converted into H_2O_2 and hydroxyl radicals (OH^-). Under normal photosynthetic conditions, the level of these radicals is reduced to sustainable levels by efficient antioxidation mechanisms that limit damage. However when exposed to excessive light, ROS detoxification mechanisms can be insufficient which leads to cellular damage.

A non-destructive method that aims to sense the *in situ* physiological status of under-ice algae communities is needed, particularly during events that trigger environmental flux. Snow thickness is highly influenced by wind-forced displacement during storm events, which climate model predict will increase over the next century. During these storm events, the rapid removal and placement of snow will become more frequent, creating immediate changes in under-ice PAR that will influence algal biology (Juhl and Krembs, 2010; McMinn et al., 1999b). The objective of this study was to determine if microelectrodes could be used as a proxy to define the physiological

status of a bottom-ice algae community during rapid variations in light. Specifically, I aim to determine a) what influence variation in snow thickness has on algal biomass and community structure and, b) examine the influence of rapid shifts in snow, and thus irradiance, on algal photophysiology.

5.2 Materials and methods

5.2.1 Study site and experimental design

Sea-ice algae concentrated in the bottom 300 mm of 1.8 m thick fast-ice at Cape Evans, McMurdo Sound, Antarctica (77°38S, 166°24E) was collected between November 11 and December 7, 2018. An area measuring ~20 m x 20 m was selected in which nine 5 m x 5 m quadrats were established (Figure 5.1). The size of the quadrats was selected so that the algal communities at the centre of each quadrat would be unaffected by the light conditions outside each plot. Each quadrat was randomly assigned a treatment (Table 5.2); snow was collected from adjacent difts and placed evenly to the required depth. Quadrats with no snow were cleared once a day to ensure maximum light penetration. The treatments were left for 10 days to acclimate the under-ice algal mat before ice cores were extracted to observe the community response prior to changes in snow thickness. The snow was then rapidly removed ("transitioned") from quadrats with thick snow (TS - 30 cm) and placed on those treatments with no snow (NS - 0 cm). Quadrats containing thin snow (10 cm) were not transitioned and remained at the required depth for the duration of the experiment as a control. Ice cores were extracted from the centre of each quadrat, one core was used for microsensor experimentation, the other for species identification. Cores were obtained by drilling to within 300 mm of the ice-water interface with a powered Jiffy ice auger; cores 300-500 mm long were then extracted using a Mark V ice corer (Kovaks). To minimise light shock all cores were extracted under a black curtain and transferred to a field laboratory wrapped in black plastic (Ryan and Beaglehole, 1994). For I-PAM and microsensor analysis, the bottom 30 mm of each extracted core was cut into a 50 mm x 50 mm x 30 mm block, placed into a clear plastic container and immersed in pre-chilled filtered seawater (-1.8°C); containers were partially submerged in a re-circulating glycol-filled water-bath maintained at -1.8°C (Figure 5.2).

(a)

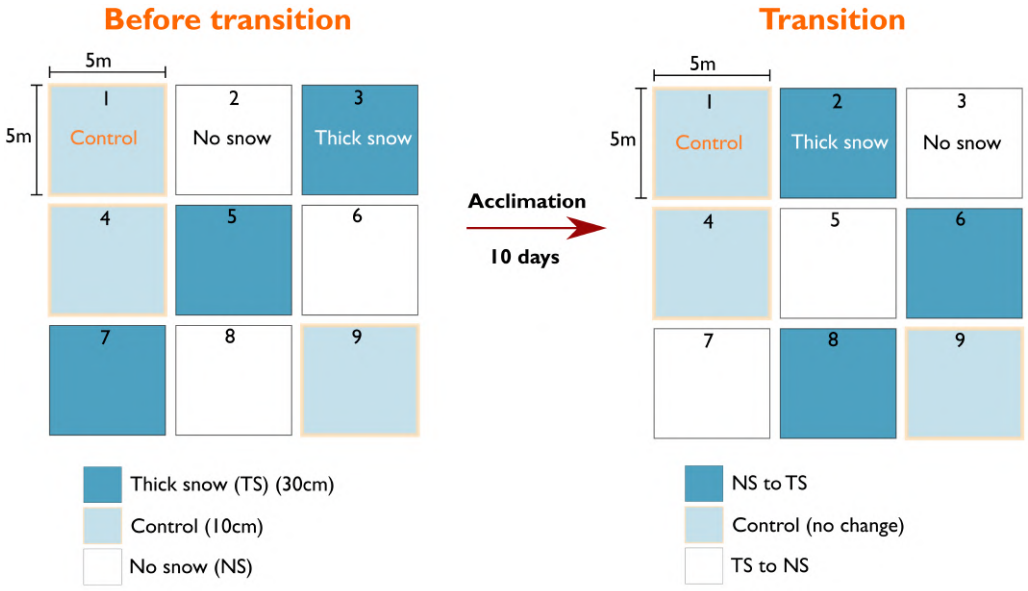

(b)

Figure 5.1: **a)** An *in situ* view of the nine 5 m x 5 m snow quadrats before snow transition. **b)** schematic representation of the random allocation of snow treatments. Quadrats ("before transition") were acclimated to their respective snow thickness for 10 days before snow was removed or added ("transitioned").

5.2.2 Microelectrodes

The pre-cut ice cores from each quadrat were inverted so that the algal mat faced upwards when placed in a clear plastic container filled with filtered seawater from the sample site. The temperature of the ice-core was maintained at -1.8°C ± 0.5°C by floating the plastic containers in a refrigerated recirculating water-bath containing ethylene glycol at -3.0°C ± 0.5°C. To ensure ice cores did not float and damage the microsensors, cores were kept submerged by two spring-loaded

Table 5.1: Illustration of the changes in snow thickness during the experiment. Snow was placed on the respective quadrats to the required depth: 1) thick - 30 cm, 2) control - 10 cm and 3) no snow. The treatments were left for 10 days to acclimate the under-ice algal mat prior to snow removal or addition ("transitioned"). Controls quadrats (10 cm snow thickness) were not transitioned and remained at the required depth for the duration of the experiment. Samples were extracted 24 and 72 hours after the transition.

Before transition	**Acclimation**	**Time after snow transition**	
	10 days	*24 hours*	*72 hours*
Thick (30cm)	⟶	No Snow	No Snow
Control (10cm)	⟶	Control (10cm)	Control (10cm)
No snow	⟶	Thick (30cm)	Thick (30cm)

metal pins (Figure 5.2a). A clear plastic cylinder measuring 1 cm x 1 cm was placed in the centre of each ice-core, this was conducted to ensure the measurement of extracellular metabolites was isolated to discreet patches. The microsensors were manoeuvred inside the cylinder to within 50 μm of the algal biofilm by a motorised micro-manipulator (Figure 5.2b). The under-ice irradiance of each treatment was simulated in the laboratory using a Lumitronics P1 LED light (GND solutions, Germany); this light has a fixed spectrum that simulates natural sunlight (Figure 5.2c). To ensure that illumination was consistent across the samples, light intensity was controlled with a variable resistor and neutral density filters. The resulting irradiance was calibrated with a Spectrosense 2+ light meter (Skye instruments) to correspond with the *in situ* under-ice irradiance (Table 5.2).

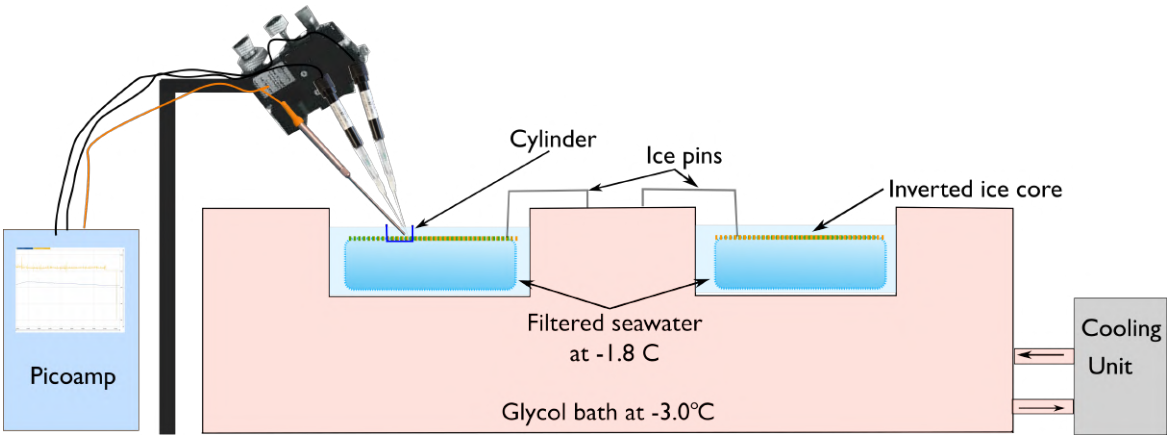

(a)

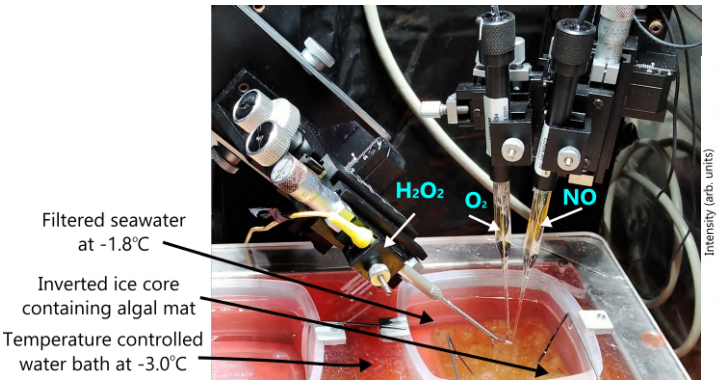

(b)

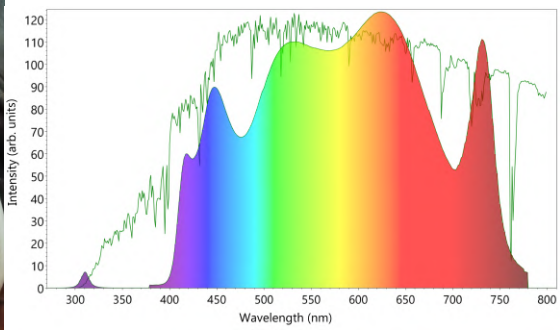

(c)

Figure 5.2: **a)** Graphical representation of the experimental design. Ice cores were inverted and placed within individual chambers then submerged in filtered seawater at a temperature of -1.8°C ± 0.5°C. **b)** Three microsensors (H_2O_2, O_2 and NO) in place above the inverted ice core containing the algal mat. **c)** Spectral profile of the Lumitronics P1 (GND solutions, Germany) growth light used in the microsensor experiments. Figure reproduced from GND solutions.

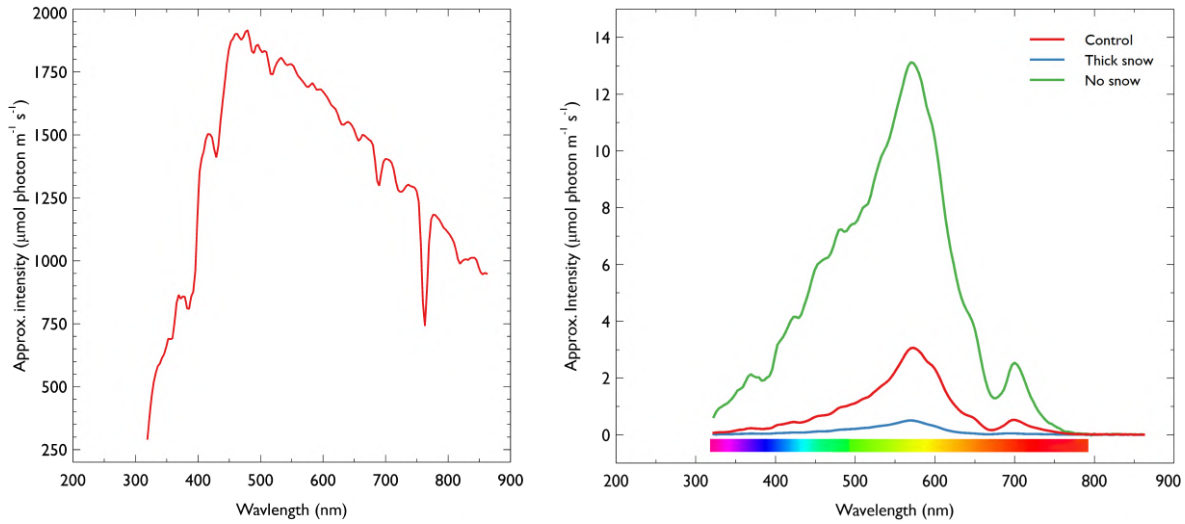

(a) **(b)**

Figure 5.3: **a)** Midday surface irradiance above the snow treatment quadrats and **b)** irradiance at the ice-water interface of control (10 cm), thick (30 cm) and no snow treatments. Values are approximate intensities in μmol photon m^{-2} s^{-1}. Both surface and under-ice measurements were performed using a RAMSES radiometer (TriOS optical systems, Germany).

Table 5.2: Nine 5 m x 5m quadrats were assigned, at random, to one of three snow treatments: 1) thick snow (30 cm), 2) control (10 cm) or 3) no snow (0 cm). The resulting under-ice irradiance were measured by manoeuvring a radiometer attached to an articulating arm (McMinn and Ashworth, 2007) to the middle of one quadrant representing each treatment.

Snow thickness	**Under-ice irradiance**
1. Thick (30 cm)	0.5 μmol photon m^{-2} s^{-1}
2. Control (10 cm)	5 μmol photon m^{-2} s^{-1}
3. No snow (0 cm)	13 μmol photon m^{-2} s^{-1}

Ice cores were extracted from the quadrats sequentially to minimise the delay in collecting microsensor data. Cut cores were left to equilibrate in the water bath in the dark for ~3 minutes. Samples were then exposed to their respective light regime for 5 minutes before oxygen (O_2), hydrogen peroxide (H_2O_2) and nitric oxide (NO) production was measured. Microsensors were aligned to within 100 μm of each other and inserted to within 50 μm of the algal biofilm using a motorised micro-manipulator (Figure 5.2b). Each microsensor was calibrated before use in filtered (0.45 μm), pre-chilled (~-1.7°C) seawater as per the manufactures instructions. The sensors were

left to equilibrate for 1 minute before logging the electrochemical trace over 5 minutes. O_2 (μmol), H_2O_2 (μmol) and NO production (nmol) were determined by extracting the last 30 seconds of each electrochemical trace and calculating the mean; the results were then normalised to the chlorophyll *a* concentration of each sample (mg chl*a* L^{-1}).

Oxygen

Oxygen production was measured electrochemically with a Clarke-type O_2 electrode (O_2, tip diameter - 50μm; Unisense, A/S, Aarhus, Denmark), connected to a field multimeter (Unisense). Sensors were calibrated before each use in filtered (0.45 μm) pre-chilled seawater (-1.7°C), using a two-point calibration as described in the manufacturers instructions.

Hydrogen peroxide

H_2O_2 (HPO, tip diameter - 2 mm) microsensors were obtained from World Precision Instruments (WPI, USA), these were connected to WPI free radical analyser. Sensors were calibrated before each use in filtered (0.45 μm) pre-chilled seawater (-1.7°C), using a multipoint calibration as described in the manufacturers instructions.

Nitric Oxide

Nitric oxide (NO) was measured electrochemically with a Clarke-type NO electrode (NO, tip diameter - 100μm; Unisense, A/S, Aarhus, Denmark), connected to a picoammeter (Unisense). Sensors were calibrated before each use in filtered (0.45 μm) pre-chilled seawater (-1.7°C), using a multipoint calibration as described in the manufacturers instructions.

5.2.3 Chlorophyll a, photophysiology and species composition

Chlorophyll *a* fluorescence was measured using a maxi imaging pulse amplitude modulated fluorometer (I-PAM, Walz Germany) using the methods described by Castrisios et al. (2018). Briefly, extracted ice-cores were cut into 50 mm x 50 mm x 30 mm blocks, placed in black plastic containers and carefully aligned into position on the I-PAM stage. The saturation pulse method was then used to determine the maximum quantum yield by measuring the minimum (F_o) and maximum (F_m) fluorescence of the inverted algae biofilm in a dark adapted state (Kennedy et al., 2012). F_v/F_m is a sensitive indicator of photosystem potential and a proxy for cellular health in photosynthetic organisms. The area-of-interest (AOI) function was used to determine F_v/F_m of discreet locations

on the ice core. Three semi-random AOI's were selected in areas where the minimum fluorescence (F_o) was >0.15; the intensity of F_o values are proportional to the amount of chl*a* and can therefore be attributed to the amount of biomass present. The process of fluorescence imagery was conducted within 30 seconds. Following imaging, samples were placed in a water-bath containing vessels of pre-chilled (-1.7°C) filtered seawater and left to equilibrate for 3 minutes in the dark before microsensor analysis.

Chlorophyll *a* (chl*a*) concentration was determined in triplicate using the acidification protocol as described by Evans et al. (1987). Briefly, algal cells were collected from within the cylinder embedded on the ice-surface (Figure 5.2a). Sub-samples were then filtered onto 25 mm GF/F filters and extracted in 10 ml of methanol in the dark at 4°C for 12 hours. chl*a* extracts were subsequently measured on a Turner fluorometer (10AU Turner designs, USA).Measurements were recorded in mg chl*a* L^{-1}.

5.2.4 Species composition

A 2 mL sample was taken from the bottom of each ice core and fixed in 0.5% gluteraldehyde. A 0.5 mL aliquot from each sample was prepared using a settling chamber and cells were examined using a Zeiss microscope. Microalgae were counted from 10 randomly selected fields of view and taxonomically identified using the descriptions found in Scott and Marchant (2005). The relative abundance was calculated as a percentage.

5.2.5 Statistical analysis

Where appropriate, data was analysed using two-way Analysis of Variance (ANOVA) to determine the variation among treatments over time. If significant differences were detected, post-hoc Tukey tests were used to compare the experimental groups to the control. Pearson correlations were performed to observe the relationship between production of extracellular metabolites. The final 60 seconds of each electrochemical trace was used for this analysis. Averages of the traces were used to determine the significance of correlations. The software package R (R core team 2019) and tests therein were used for all statistical analyses.

5.3 Results

The annual fast-ice at Cape Evans in 2019 was 1.8 m thick and comprised a community dominated by diatoms at the ice-water interface (Table 5.3). Fast-ice algal communities were exposed to one of three snow levels for ten days: 1) thick (30 cm), 2) thin (10 cm - control) or, 3) no snow (0 cm). Thereafter, snow was either removed or added depending on the treatment (Table 5.1). The change in snow thickness resulted in a shift in the under-ice irradiance from ~0.5 μmol photon m^{-2} s^{-1} under thick snow to ~13 μmol photon m^{-2} s^{-1} with no snow. The rapid transition in snow thickness had a profound influence on the under-ice algal community, resulting in dynamic changes in species composition, heightened photo-physiological stress and the release of extracellular metabolites.

5.4 Microelectrodes - extracellular metabolites

Hydrogen peroxide

H_2O_2 production was successfully measured for the first time in sea-ice cores. While there was no statistically significant difference in the production of H_2O_2 among treatments before the snow transition ($p>0.05$) (Figure 5.4a), 24 hours following the removal of thick snow (TS - NS) a significant ($p<0.05$) increase in H_2O_2 production was observed (384.9 μmol H_2O_2 mg chl*a* L^{-1}). After 72 hours, H_2O_2 production in TS - NS plots reduced to a mean of 45.68 μmol H_2O_2 mg chl*a* L^{-1} which was not significantly different compared to the treatments (Figure 5.4a). There was also no significant difference in H_2O_2 production when transitioning from no snow to thick snow (NS - TS) compared to the control.

Nitric oxide

The reactive oxygen metabolite nitric oxide was measured for the first time in a fast-ice community. There was no statistically significant difference in NO production during the transition NS - TS when compared to the control ($p>0.05$) (Figure 5.4b). In contrast TS - NS plots displayed a significant increase (10.32 nmol mg chl*a* L^{-1} ± 3.66 nmol mg chl*a* L^{-1}) in the production of NO

($p< 0.05$) 24 hours after the removal of thick snow (Figure 5.4b). After 72 hours, NO production in TS -NS had decreased to a non-significant level (3.874 nmol mg chl*a* L^{-1} ± 3.09 nmol mg chl*a* L^{-1}) compared to the other treatments.

Oxygen

There was no statistically significant difference in O_2 production when comparing the control and NS - TS treatment ($p>0.05$). A statistically significant increase in O_2 production was observed (113.39 μmol mg chl*a* L^{-1} ± 43.94 μmol mg chl*a* L^{-1}) in plots transitioning from thick snow to no snow ($p<0.05$) (Figure 5.4c). Following 72 hours, O_2 decreased (of 32.18 μmol mg chl*a* L^{-1} ± 28.54 μmol mg chl*a* L^{-1}) to a level that was not significantly different to that of the other treatments ($p>0.05$). Primary production could not be measured due to the difficultly in measuring the diffusion boundary layer without flow velocity (McMinn and Ashworth, 2007).

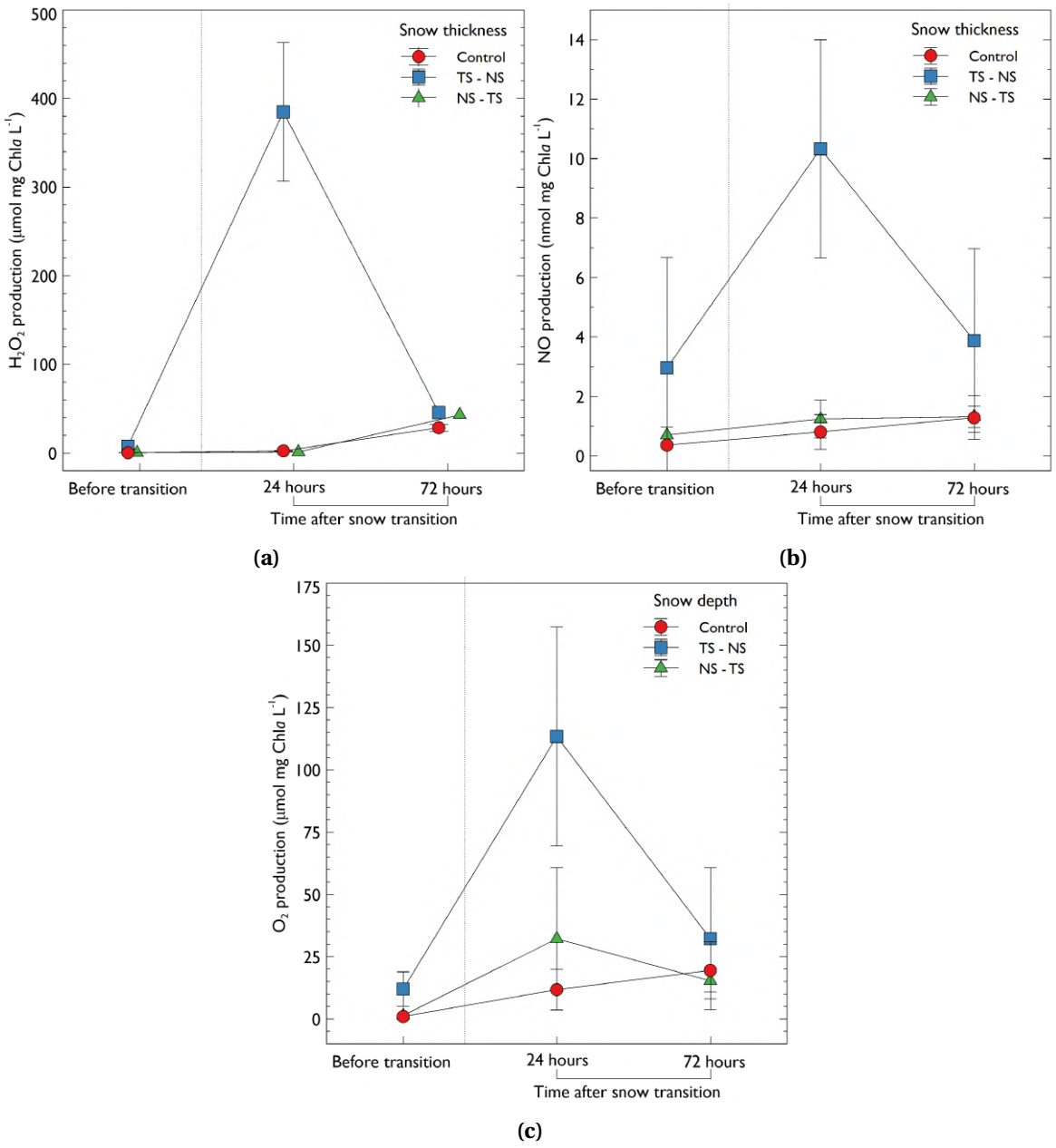

Figure 5.4: *In vivo* production of extracellular metabolites determined by microsensors of under-ice algal communities treated with three different snow depths 1) TS - thick snow (30 cm), 2) control (10 cm) and, 3) NS - no snow (0 cm). Sea-ice algal communities were acclimated to their respective snow treatment for 10 days prior to sampling. After 10 days, an initial sample was collected, denoted "before transition"; following this the snow was transitioned as previously described. Sampled were then collected at 24 and 72 hours after the transition. **a)** Production of H_2O_2 (μmol mg chl*a* L^{-1}). **b)** Nitric oxide (NO) production (nmol mg chl*a* L^{-1}). **c)** Oxygen production (μmol mg chl*a* L^{-1}).

To determine if the increases in H_2O_2 observed in the TS - NS treatment could be related to O_2 production, values were correlated using the Pearson correlation coefficient (Figure 5.5). There was no relationship between H_2O_2 and O_2 before the snow transition (R^2 = 0.002, p= 0.81) (Figure 5.5a), and 72 hours after (R^2 = 0.012, p = 0.58) (Figure 5.5c). However, a significant relationship between the amount of O_2 and H_2O_2 production was observed 24 hours after the transition from TS -NS (Pearson correlation coefficient of 0.79; R^2 = 0.62, p < 0.001 (Figure 5.5b). There was no significant correlation between NO and the production of both H_2O_2 and O_2. Additionally no significant correlation in the production of metabolites was observed in the control and NS - TS treatments.

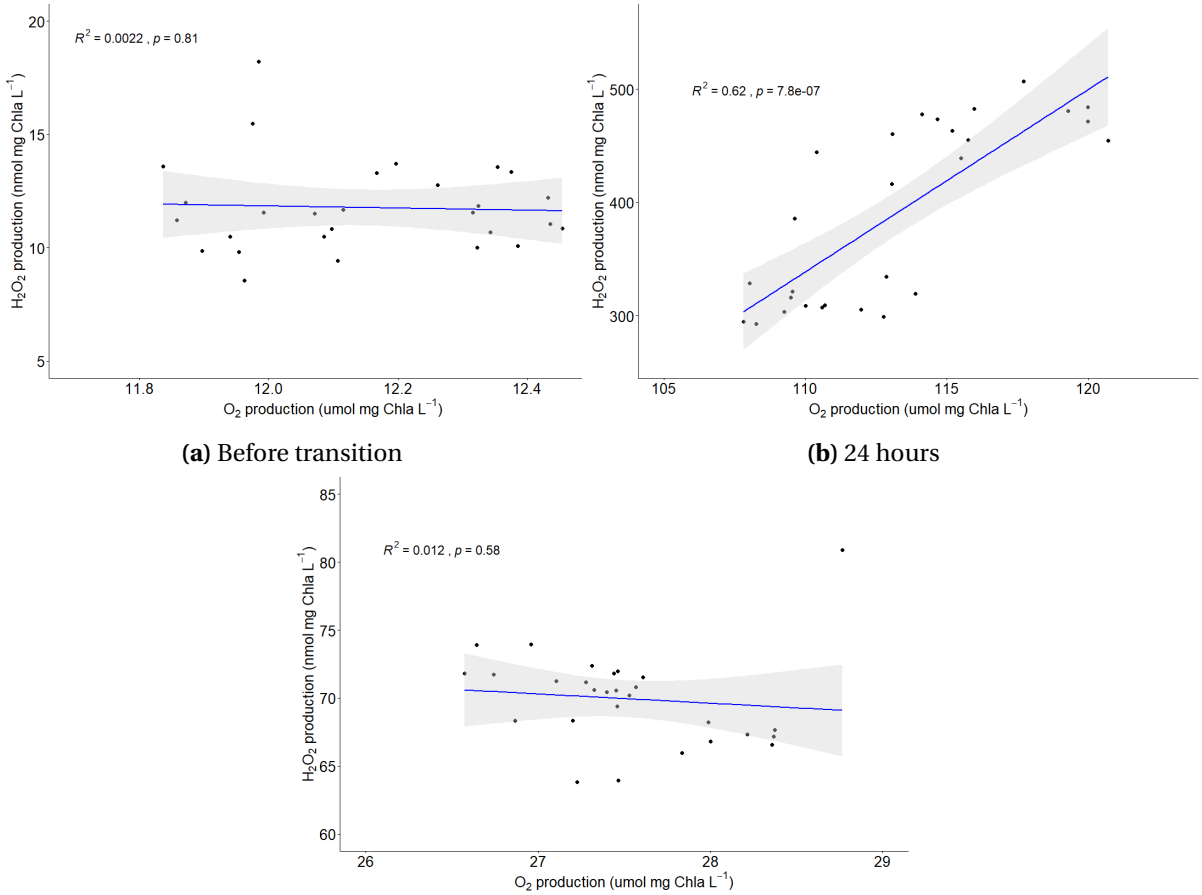

(a) Before transition

(b) 24 hours

(c) 72 hours

Figure 5.5: Correlation between hydrogen peroxide (nmol mg chl*a* L^{-1}) and oxygen production nmol mg chl*a* L^{-1}) in snow plots that were transitioned from thick to no snow (TS -NS). **a)** (0 hours) corresponds the relationship between H_2O_2 and O_2 before snow transition (thick (30 cm) snow for ten days prior to removal. **b)** 24 hours after transition from thick snow to no snow. **c)** 72 hours after transition from thick snow to no snow (TS -NS).

Table 5.3: The relative species composition (percentage) of bottom-ice alga at Cape Evans subjected to three snow depths: 1) control - 10 cm, 2) thick - 30 cm and 3) no snow - 0 cm. Before transition represents that the respective snow treatment was acclimated for 10 days prior to measurement. Following the acclimation period the snow was 'transitioned" as previously described (Table 5.1; 24 and 72 hours represent the time after the transition. Percentages in red highlight the dominant species of the community.

	Before transition			**24 hours**			**72 hours**		
Species	**Control**	**Thick (TS)**	**No snow (NS)**	**Control**	**TS - NS**	**NS- TS**	**Control**	**TS - NS**	**NS- TS**
Nitzschia stellata	40.1	38.8	29.3	47.3	38.3	59.5	54.0	14.3	51.1
Berkeleya adeliensis	34.4	20.3	45.9	35.3	32.0	25.1	34.3	55.0	23.6
Entomoneis kjellmannii	4.0	8.7	5.0	3.3	7.8	1.9	0.2	2.4	7.2
Fragilariopsis. sp	6.8	12.0	5.0	4.1	4.2	4.9	2.3	9.4	8.2
Nitzschia sp.	5.7	8.0	4.1	3.5	1.4	2.4	4.6	6.9	3.5
Navicula sp.	3.1	-	0.5	0.9	1.4	3.3	3.6	4.6	3.4
Nitzschia lecontei	2.8	7.6	5.0	2.7	1.9	0.9	0.9	3.0	2.4
Navicula glaceii	0.9	0.4	1.7	0.1	0.9	-	-	3.3	-
Pleurosigma sp.	-	-	-	-	0.1	0.1	0.0	0.1	0.1
Pinnnularia sp.	0.6	-	0.2	0.1	-	-	-	0.2	0.2
Fragilariospsis islandica	5.7	8.0	4.1	3.5	1.4	2.4	4.6	6.9	3.5
Nitzschia longissima	0.6	2.2	2.4	0.9	0.2	0.6	0.2	0.2	0.4
Thalassiosira antarctica	-	-	-	-	0.2	-	-	-	-

5.5 Chlorophyll, photophysiology and species composition

5.5.1 Species composition

Before the transition, the colonial pennate diatom *Nitzschia stellata* dominated the community under thick snow and control quadrats. In plots with no snow the tube dwelling diatom, *Berkeleya adeliensis*, was more abundant. Following the transition (24 hours), *N. stellata* was more abundant in all plots. *B. adeliensis* was more abundant in plots with no snow 72 hours after the transition, whereas *N. stellata* dominated the thick snow and control plots.

5.5.2 Chlorophyll *a* and photophysiology

After the 10 day acclimation period, chlorophyll *a* (chl*a*) concentration was significantly lower under thick snow (30 cm) (4.44 ± 4.10 mg chl*a* L^{-1}) compared to both the control (24.86 ± 4.27 mg chl*a* L^{-1}) and quadrats with no snow (20.32 ± 8.64 mg chl*a* L^{-1}) (Figure 2.6). Following removal of thick snow chl*a* concentration did not increase significantly (72 hours; 5.22 ± 2.50 mg chl*a* L^{-1}). In comparison, when thick snow (30 cm) was applied to quadrats which previously contained

no snow (NS - TS), chl*a* decreased by 38% after 72 hours (Figure 5.6a). There was no statistical difference in chl*a* between the quadrats that were transitioned from no snow to thick snow (NS - TS) and the control. Further analysis was performed to examine if chl*a* was correlated with snow depth (Figure 5.7); the results indicate a negative correlation (Pearson correlation coefficient -0.7, p= 0.035) between chl*a* and snow depth in quadrats before the snow transition. There was no significant correlation between snow depth and chl*a* following the transition.

The transition from thick snow to no snow (TS - NS) resulted in considerable photophysiological stress, as illustrated by the statistically significant reduction in maximum quantum yield (F_v/F_m) obtained using the I-PAM (Figure 5.6b). This rapid transition from low to high light, resulted in the reduction F_v/F_m from a mean of 0.444 ± 0.02 to 0.095 ± 0.027 after 72 hours. It is interesting to note that while F_v/F_m declined, the concentration of chl*a* did not change (Figure 5.6a). In contrast, photosynthetic performance improved when thick snow was applied to plots with no snow (NS - TS); F_v/F_m increased from a mean of 0.235 ± 0.139 to 0.337 ± 0.03, however this was not statistically significant (Figure5.6b). F_v/F_m in the control treatment declined slightly (Figure 5.6b) but this was not statistically significant ($p>0.05$).

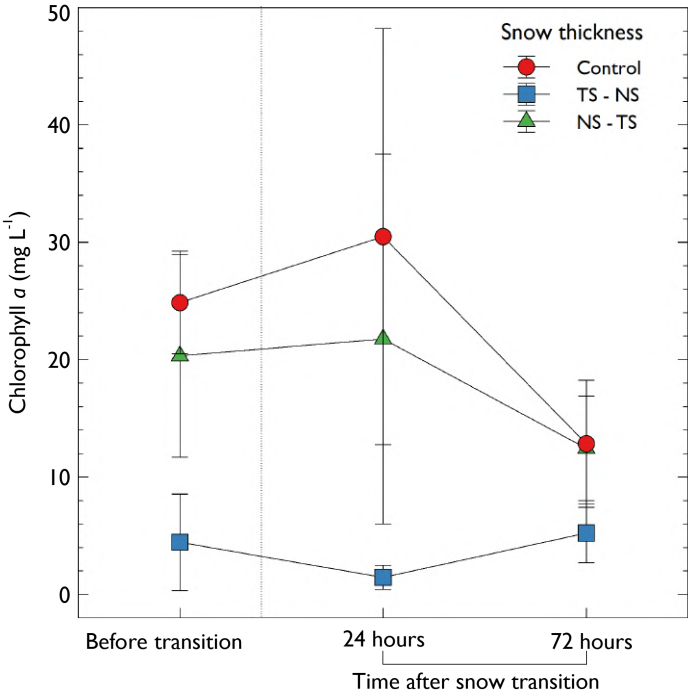

(a)

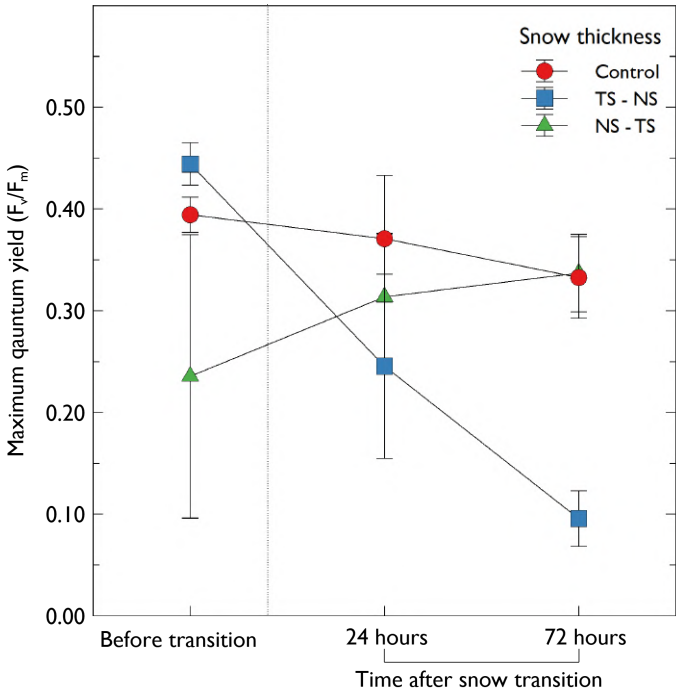

(b)

Figure 5.6: **a)** The chlorophyll *a* concentration and **b)** the maximum quantum yield (F_v/F_m) of under-ice algal communities treated with three different snow depths: 1) TS - thick snow (30 cm), 2) control (10 cm) and, 3) NS - no snow (0 cm). Sea-ice algal communities were acclimated to their respective snow treatment for 10 days prior to sampling. After 10 days an initial sample was collected, denoted "before transition"; following this the snow was transitioned as previously described. Sampled were then collected at 24 and 72 hours after the transition.

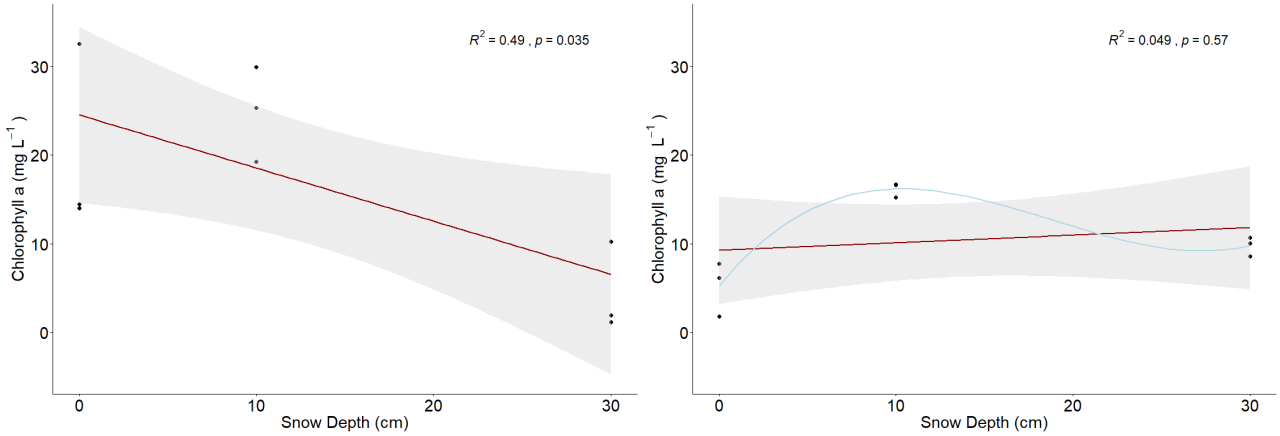

(a) Before transition **(b)** 72 hours

Figure 5.7: Correlation between chlorophyll *a* and snow depth **a)** before the snow transition (at snow depth for 10 days prior to removal) and **b)** 72 hours after the snow transition.

The I-PAM can provide distinct 2D images of the distribution of chl*a* florescence and physiological activity of photosystem II. A clear difference in the distribution of algal cells was observed after 72 hours (Figure 5.8). Under-ice algal communities exposed to thick snow prior to the transition displayed a distinctly patchy distribution (as indicated by the variation in Ft) and a significant reduction in photosynthetic performance (F_v/F_m) was observed (Figure 5.6). Interesting, 24 hours after the snow was removed (TS - NS), the patchy distribution changed to become more homogeneous across the base of the ice cores. In contrast, in NS - TS quadrats, the relatively homogeneous algal communities observed before the transition evolved to form a patchy distribution as observed under thick snow (Figure 5.8). This re-emergence of a patchy distribution under thick snow may indicate that the under-ice algal community underwent a shift in species dominance as a result of the rapid change in irradiance.

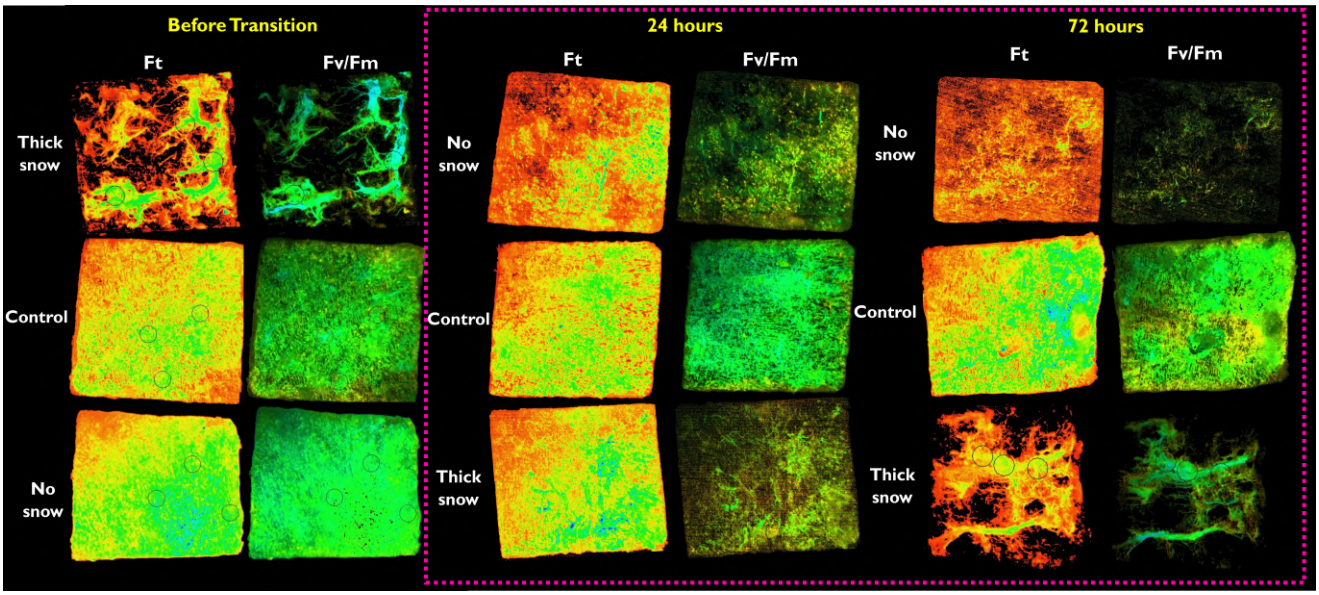

Figure 5.8: Representation of the fluorescent parameters obtained from an imaging-PAM (Walz, Germany). The figure shows a representative ice core cut to 50 mm x 50 mm extracted from the ice-water interface of each snow treatment; thick, control or no snow. The ice cores are shown inverted, so that the algal mat from the ice-water interface is facing up. Images are grouped by the amount of time after snow transition (before transition, 24 hours or 72 hours). The parameter Ft shows the distribution of the algal mat, the colour green/blue represents areas of increased biomass. Black circles (visible in some images) within the images are area-of-interest (AOI) functions used to determine F_v/F_m (Figure 5.6).

5.6 Discussion

Rapid oscillations in snow thickness can trigger large variation in the degree of under-algal biomass in polar habitats (Ackley and Sullivan, 1994; Campbell et al., 2015; Leu et al., 2015; Palmisano et al., 1985; Wongpan et al., 2018). The timing and magnitude of snow loading is critical in determining the extent of change and the severity of *in situ* physiological stress (Juhl and Krembs, 2010; Mundy et al., 2005; Vermuelen, 2013). Recent studies have shown that rapid removal of thick snow (>30 cm) can cause photoinhibition and stall algal growth of shade-adapted taxa (Campbell et al., 2015; Leu et al., 2015). In contrast, a cover of thin snow (<10 cm) can improve photosynthetic performance (Lund-Hansen et al., 2014) and increase algal standing stocks (Wongpan et al., 2018). Importantly, the net response of bottom-ice algae to rapid changes in snow depth is thought to be dependent on the ability to photoadapt photoadpative index of the population coupled with the initial snow

thickness before removal (Juhl and Krembs, 2010). The results presented in this study appear to confirm this relationship, whereby an inverse correlation between snow depth and chl*a* was present but only if the algal mat had sufficient time for acclimation (10 days). Furthermore, the community composition differed with respect to snow thickness; *B. adeliensis* dominated under no snow plots, whereas *N. stellata* communities were prominent under both thin (10 cm, control) and thick snow (30 cm). Interestingly, the rapid removal of thick snow (30 cm) significantly impacted the under-ice algal photophysiology, influenced community structure and induced the production of extracellular 'stress' metabolites.

Diatoms dominate the ice-water interface of land-fast ice and are known to be highly shade-adapted. Active growth has been recorded at very low radiances (<5 μmol photon m^{-2} s^{-1}) in both the Antarctic (McMinn et al., 2010) and the Arctic (Hancke et al., 2018). In this study, the presence of snow caused considerable narrowing of the spectral band and reduced the incident irradiance of PAR reaching the ice-water interface. The extent of snow cover had a significant effect on the community structure of bottom-ice microalgae taxa. In plots with no snow the tube-forming *B. adeliensis* was highly abundant, whereas the colonial pennate diatom *N. stellata* was the dominant species under thick (30 cm) and thin (10 cm) snow. This pattern of community change in response to variation in light has been noted previously in land-fast ice in McMurdo Sound (Grossi and Sullivan, 1985; McMinn, 1997; Ryan et al., 2006; Vermuelen, 2013). Ryan et al. (2009, 2006) illustrated the species succession of *B. adeliensis* in communities exposed to higher light and McMinn (1997) observed the dominance of *N. stellata* under thick snow cover. More recently, Vermuelen (2013) also showed a change in the ratio of *N. stellata* to *B. adeliensis* with snow depth and concluded that *B. adeliensis* preferred higher light than *N. stellata*. Before the snow transition, a higher level of biomass was present under plots with a thin layer of snow (control) and less under thick snow. Conversely, the maximum quantum yield of PS_{II} (F_v/F_m) was higher under thick snow and considerable less in quadrats with no snow. This suggests that the community (dominated by *B. adelienis*) exposed to a higher irradiance was either photophysiologically stressed or that photosynthetic capacity was reduced as a mechanism to limit photodamage (Kirst and Wiencke, 1995). Upon application of thick snow (NS - TS), F_v/F_m increased and the concentration of chl*a* declined. It

must be noted that the use of chl*a* (F_o) as a measure of biomass is viewed with caution because ice-associated taxa have the ability to rapidly modulate their pigment composition in response to irradiance. Thus, the decrease in chl*a* may be partially explained by the ability of diatoms to reduce the ratio of chl*a* to carotenoid pigments in response to the narrowing of the light spectrum (Campbell et al., 2015; Massom and Stammerjohn, 2010; Mundy et al., 2005). Chlorophyll *a* has light absorption peaks at 430 and 662 nm and the application of thick snow ensured significant attenuation of these spectral bands. Under this scenario, ice-algae are known to increase the production of higher wavelength absorbing carotenoid pigments as a mechanism to enhance the probability of photon capture (Lizotte, 2001; Lizotte and Sullivan, 1991; Lyon and Mock, 2014; McMinn et al., 1999b).

Following the removal of thick snow, there was a rapid decline in F_v/F_m suggesting that cells were undergoing photophysiological stress as a result of the increase in irradiance. Most records of the light saturation of photosynthesis of bottom-ice associated algae are <10 μmol photon m^{-2} s^{-1} (McMinn et al., 2003; Palmisano and Sullivan, 1983; Ryan et al., 2009), with reports of photoinhibition occurring at levels below 20 μmol photon m^{-2} s^{-1} (Kirst and Wiencke, 1995; Palmisano et al., 1985). During the course of this experiment, the under-ice irradiance did not exceed 14 μmol photon m^{-2} s^{-1}, but rapid exposure to this irradiance appeared to negatively influence the photosynthetic capacity of the low-light adapted community. Furthermore, the decline in F_v/F_m (24 hours) was correlated with an increase in the production of H_2O_2 and NO, suggesting significant photo-oxidative stress was evident which may have contributed to the decline of the dominate species. The uncharged nature of H_2O_2 ensures easy diffusion across cell membranes, which under saturating conditions can result in extracellular overflow. High concentration of H_2O_2 have been reported within Antarctic sea-ice, particularity in the upper sections where exposure to high irradiance is common (Cooper and Zika, 1983; King et al., 2005; Neftel et al., 1984). Interestingly, the half-life of H_2O_2 in seawater has been shown to be prolonged, with reports showing it can remain for up to 15 days in polar waters. This may have a considerable influence on the under-ice biology as toxicity of H_2O_2 has been shown to be variable among taxa. Florence and Stauber (1986) showed that species of *Nitszchia* remain highly susceptible to the presence of H_2O_2 in the immediate

environment. In contrast, Drábková et al. (2007) showed that the diatom *Navicula* could tolerate relatively high levels of H_2O_2. This is the first study to observe a real-time response of H_2O_2 and NO as a function of irradiance in an Antarctic fast-ice microbial community. The production of up to ~ 0.4 μmol mg $^{-1}$ chl*a* L^{-1} of H_2O_2 was reported following snow removal, and this reduced to below 0.1 μmol mg^{-1} chl*a* L^{-1} after 72 hours. The reason for the reduction remains unclear, but may indicate that cells had photo-acclimated to the irradiance or illustrate that the species succession had shifted to a high light favourable taxon (*B. adeliensis*). Furthermore, a pulse of NO was observed following the removal of thick snow (24 hours). This correlated with the increase in H_2O_2 and may also be explained in terms of photoinhibition. As previously described in Chapter 4, the production of NO in the sea-ice diatom *F. cylindrus* was only apparent under illuminating conditions when the photosynthetic chain was inhibited. Thus, the heightened production of NO observed here may further indicate that the shift in irradiance was sufficient to cause oxidative stress and inhibition of normal photosynthetic electron flow in shade-adapted algae. Extreme levels of ROS are highly damaging to phototrophic organisms and have been shown to damage the photosynthetic apparatus, prolong photoinhibition, inhibit the Calvin-Benson cycle, cause DNA damage and stall active growth (Janknegt et al., 2008; Murata et al., 2007; Nishiyama et al., 2006; Rijstenbil, 2002). It is surmised here that the rapid increase in irradiance caused significant production of ROS, whereby it affected the physiology of the algal community through photodamage and photoinhibition.

Microalgal species inhabiting the ice-water interface are diverse and the level at which photoinhibition occurs is different among taxa (McMinn et al., 2010). Rapid changes in light can negatively influence the under-ice algal biomass in populations that lack time and the ability to acclimate (Juhl and Krembs, 2010). The results presented in this study illustrate that these rapid changes in transmitted irradiance can impose a strong selective pressure on various sea-ice taxa. The presence of a thin layer of snow (< 10 cm) can positively influence under-ice algal biomass and increase primary productivity, as observed in the Arctic (Mundy et al., 2005, 2007). However, a rapid shift from low (thick snow) to high light (no snow) can cause significant oxidative stress. It is shown here, for the first time, that extracellular 'stress' metabolites can be measured *in situ* and

directly attributed to the physiological state of the cell. Further studies would benefit by calibrating extracellular measurements of ROS to the intracellular processes behind their production, particularly under the scenarios of future climatic change. A long-term priority should be developing bio-platforms that enable long-term monitoring of bottom-ice taxa during key transition events. The results presented here, indicate that the use of microsensors, in particular H_2O_2 and NO are beneficial in gaining an understanding of real-time physiological status of ice-associated microbes during environmental flux.

Chapter 6

Summary of findings

Light is the most influential driver of ice-associated microalgal community dynamics, but due to variation in ice and snow thickness, light is both transient and inconstant. The ability of photoautotrophs to adapt to this ephemeral habitat requires highly efficient metabolic machinery that can adapt to periods of high irradiance and extended darkness. Future predictions of high inter-annual variability and the increased occurrence of extreme climatic events in the Southern Ocean will have considerable impacts on both the timing and magnitude of light transmission (Petrou et al., 2016; Turner et al., 2008). Current climate models predict that increases in water temperature will lead to less ice formation in winter and speed up the melt process in spring/summer. Furthermore, these models anticipate an enhanced poleward shift in storm events that will result in higher winds, wave magnitude and increased precipitation (Bracegirdle et al., 2008; Massom and Stammerjohn, 2010). Increased wind and wave action will intensify the fragmentation of existing sea-ice floes, accelerate ice melt, and influence primary production. Heightened precipitation in the form of rain will enhance light transmission, whereas precipitation in the form of snow will decrease the quantity of irradiance reaching bottom-ice communities (Massom et al., 2001; Meiners et al., 2017). It is unknown whether these changes will have a positive or negative influence on ice-associated primary production. A non-destructive method that aims to sense *in situ* physiological status of under-ice algal communities is needed, particularly during events that trigger rapid alterations in light and spectral flux. In this thesis, I examined how the three main seasonal changes in incident

irradiance (darkness, sub-saturating and saturating) influence diatom physiology with an emphasis on how microelectrodes can be used to sense light-induced stress.

The overarching aims of this thesis were as follows:

1. To determine how Antarctic sea-ice diatoms are able to survive extended periods of darkness and recover upon illumination;
2. Investigate if exposure to variation in the magnitude and spectral quality of light upon illumination causes photophysiological stress;
3. Determine if light-induced photophysiological stress can be measured extracellularly using microsensors;
4. Investigate if ice-associated phototrophic stress can be measured *in vivo* with microsensors when exposed to rapid changes in irradiance.

The key findings of the thesis chapters were:

6.1 Chapter 2: Surviving the darkness

This was the first study to examine the proteome of a prominent sea-ice diatom in response to extended darkness. I showed that *F. cylindrus* utilises an ancient alternative metabolic mechanism that facilitate dark survival. The proteomic analysis of *F. cylindrus* during extended darkness indicated that cells rapidly decrease their light harvesting complexes and photosystems, while maintaining their photosynthetic capacity. This appeared to be mediated through mitochondrial respiratory processes of the Entner-doudorff pathway, lower glycolysis and the tricarboxylic acid cycle, ensuring rapid recovery upon illumination. Within the plastid, carbon fixation halted while the upper sections of the glycolysis, gluconeogenesis and pentose phosphate pathways became less active. Maintenance metabolism (or the ability to live in the dark), may be one of the fundamental reasons why diatoms dominate Antarctic sea-ice ecosystems.

6.2 Chapter 3: Rapid changes in light and its spectral composition influences extracellular metabolite production.

When cells of *F. cylindrus* emerged from long-term darkness, their photophysiological response differed depending on both the quantity and spectral quality of light on re-illumination. This may become pivotal under future scenarios which predict that sea-ice algal will experience large variations in the timing, composition and magnitude of irradiance. The results indicated that rapid exposure to light and alteration in its spectral composition can cause significant stress that was measurable using H_2O_2, NO and glucose microsensors. This metabolic overflow was related to the direct disruption of normal photosynthetic electron flow and it is proposed that extracellular production of certain metabolites can be attributed to the physiological state of the cell.

6.3 Chapter 4: Nitric oxide production

In chapter 4, I examined how and why nitric oxide was produced in response to saturating irradiance. By using a combination of microsensors, microfluidic chambers and artificial sea-ice tanks, a basic mechanistic insight into NO's dynamics within the Antarctic sea-ice diatom *F. cylindrus* was obtained. Results suggest that NO production in *F. cylindrus* is nitrite-dependent via a nitrate reductase enzyme. Furthermore, NO production was abolished upon exposure to light, but could be induced in the light when normal photosynthetic electron flow was disrupted. The addition of exogenous NO to cellular suspensions of *F. cylindrus* resulted in decreased cellular growth, disruption of photosynthetic electron transport and non-photochemical dissipation mechanisms. NO production was also observed when cells were exposed to salinity and temperature regimes that caused heightened cellular stress. It was speculated that during periods of environmental stress NO could be produced in *F. cylindrus* as a "stress signal" molecule.

6.4 Chapter 5: Rapid transition in snow thickness causes photophysiology stress and stalls primary production in fast-ice algae communities.

The results presented in this chapter illustrated that rapid changes in transmitted irradiance can impose a strong selective pressure on various sea-ice taxa. The presence of a thin layer of snow (< 10 cm) positively influenced under-ice algal biomass and increased primary productivity. However, a rapid shift from low (thick snow) to high light (no snow) caused increased production of NO and H_2O_2, indicating that the shift in irradiance was sufficient to cause oxidative stress and inhibition of normal photosynthetic electron flow in the shade-adapted microbial community. This was the first study to observe a real-time response of H_2O_2 and NO as a function of irradiance in an Antarctic fast-ice microbial community. It is surmised that rapid increases in irradiance can cause significant production of ROS, whereby it influenced the physiology of the algal community through photodamage and photoinhibition. It was illustrated, for the first time, that extracellular 'stress' metabolites can be detected with microsensors that reflect the physiological status of the phototrophic community.

6.5 Summary

Environment perturbation can influence multiple aspects of phototrophic metabolism and cause significant stress that manifests first in the photosynthetic apparatus. While photosynthesis primarily serves to capture and convert light into cellular energy, it can also function as an efficient monitoring system for environmental change. During events of ecosystem flux, alteration in the photosynthetic redox status and balance of photon capture to assimilation all act as molecular messengers that activate metabolic and photosynthetic adjustment. By measuring fluctuations in both the rate of, and products relating to photosynthesis, a real-time indication of microalgal health can be obtained that mirrors the *in situ* status of ice-associated microbes. The results presented provide a unique insight into plasticity of ice-associated diatoms with respect their capacity to survive long periods of darkness and to adapt to changes in irradiance. Throughout this thesis, it has been demonstrated that during rapid shifts in both the magnitude and spectral

quality of light, the production of photosynthetically related metabolites was observed. Detection of these molecules indicated that under conditions of saturating irradiance that cause stress or disrupt normal photosynthetic electron flow, the increased production of H_2O_2, NO and glucose can be attributed to metabolic processes taking place within the cell. The ability to measure *in vivo* overflow metabolism may provide an effective tool for real-time measurement of under-ice phototrophic health. The production of extracellular metabolites was successfully measured using microelectrodes in both the laboratory and the field. Deployable bio-platforms that encompass measurement of these metabolites *in situ* would be useful future addition for the assessment of ice-associated microbial communities during periods of environmental change.

References

Ackley, S. F. and Sullivan, C. W. (1994). Physical controls on the development and characteristics of Antarctic sea ice biological communities- a review and synthesis. *Deep-Sea Research Part I*, 41(10):1583–1604.

Allen, A. E., Dupont, C. L., Oborník, M., Horák, A., Nunes-Nesi, A., McCrow, J. P., Zheng, H., Johnson, D. a., Hu, H., Fernie, A. R., and Bowler, C. (2011). Evolution and metabolic significance of the urea cycle in photosynthetic diatoms. *Nature*, 473(7346):203–207.

Antia, N. J. (1976). Effects of temperature on the darkness survival of marine microplanktonic algae. *Microbial Ecology*, 3(1):41–54.

Arrigo, K. R. (2014). Sea Ice Ecosystems. *Annual Review of Marine Science*, 6(1):439–467.

Arrigo, K. R., van Dijken, G. L., and Bushinsky, S. (2008). Primary production in the Southern Ocean, 1997-2006. *Journal of Geophysical Research: Oceans*, 113(8):1997–2006.

Asada, K. (2006). Production and Scavenging of Reactive Oxygen Species in Chloroplasts and Their Functions. *Plant Physiology*, 141(2):391–396.

Bai, X., Song, H., Lavoie, M., Zhu, K., Su, Y., Ye, H., Chen, S., Fu, Z., and Qian, H. (2016). Proteomic analyses bring new insights into the effect of a dark stress on lipid biosynthesis in *Phaeodactylum tricornutum*. *Scientific Reports*, 6(1):25494.

Baldisserotto, C., Ferroni, L., Andreoli, C., Fasulo, M. P., Bonora, A., and Pancaldi, S. (2005). Dark-acclimation of the Chloroplast in *Koliella antarctica* Exposed to a Simulated Austral Night Condition. *Arctic, Antarctic and Alpine Research*, 37(2):146–156.

Beauchamp, C. and Fridovich, I. (1971). Superoxide dismutase: improved assays and an assay applicable to acrylamide gels. *Analytical biochemistry*, 44(1):276–287.

Bertrand, M. (2010). Carotenoid biosynthesis in diatoms. *Photosynthesis research*, 106(1-2):89–102.

Bottomley, P. J. and Stewart, W. D. (1976). ATP pools and transients in the blue-green alga, *Anabaena cylindrica*. *Archives of Microbiology*, 108(3):249–258.

Bouchard, J. N. and Yamasaki, H. (2008). Heat stress stimulates nitric oxide production in *Symbiodinium microadriaticum*: A possible linkage between nitric oxide and the coral bleaching phenomenon. *Plant and Cell Physiology*, 49(4):641–652.

Bowler, C., Allen, A. E., Badger, J. H., Grimwood, J., Jabbari, K., Kuo, A., Maheswari, U., Martens, C., Maumus, F., Otillar, R. P., Rayko, E., Salamov, A., Vandepoele, K., Beszteri, B., Gruber, A., Heijde, M., Katinka, M., Mock, T., Valentin, K., Verret, F., Berges, J. A., Brownlee, C., Cadoret, J. P.,

Chiovitti, A., Choi, C. J., Coesel, S., De Martino, A., Detter, J. C., Durkin, C., Falciatore, A., Fournet, J., Haruta, M., Huysman, M. J. J., Jenkins, B. D., Jiroutova, K., Jorgensen, R. E., Joubert, Y., Kaplan, A., Kröger, N., Kroth, P. G., La Roche, J., Lindquist, E., Lommer, M., Martin-Jézéquel, V., Lopez, P. J., Lucas, S., Mangogna, M., McGinnis, K., Medlin, L. K., Montsant, A., Secq, M. P. O. L., Napoli, C., Obornik, M., Parker, M. S., Petit, J. L., Porcel, B. M., Poulsen, N., Robison, M., Rychlewski, L., Rynearson, T. A., Schmutz, J., Shapiro, H., Siaut, M., Stanley, M., Sussman, M. R., Taylor, A. R., Vardi, A., Von Dassow, P., Vyverman, W., Willis, A., Wyrwicz, L. S., Rokhsar, D. S., Weissenbach, J., Armbrust, E. V., Green, B. R., Van De Peer, Y., and Grigoriev, I. V. (2008). The *Phaeodactylum* genome reveals the evolutionary history of diatom genomes. *Nature*, 456(7219):239–244.

Boyd, P. W. (2019). Physiology and iron modulate diverse responses of diatoms to a warming Southern Ocean. *Nature Climate Change*, 9(2):148–152.

Bracegirdle, T. J., Connolley, W. M., and Turner, J. (2008). Antarctic climate change over the twenty first century. *Journal of Geophysical Research Atmospheres*, 113(3).

Büchel, C. (2003). Fucoxanthin-Chlorophyll Proteins in Diatoms: 18 and 19 kDa Subunits Assemble into Different Oligomeric States. *Biochemistry*, 42(44):13027–13034.

Bunt, J. and Lee, C. (1972). Data on the Composition and Dark Survival of Four Sea-Ice Microalgae. *Limnology and Oceanography*, 17(3):458–461.

Campbell, K., Mundy, C. J., Barber, D. G., and Gosselin, M. (2015). Characterizing the sea ice algae chlorophyll a-snow depth relationship over Arctic spring melt using transmitted irradiance. *Journal of Marine Systems*, 147:76–84.

Castrisios, K., Martin, A., Müller, M. N., Kennedy, F., McMinn, A., and Ryan, K. G. (2018). Response of Antarctic sea-ice algae to an experimental decrease in pH: a preliminary analysis from chlorophyll fluorescence imaging of melting ice. *Polar Research*, 37(1):1438696.

Catalanotti, C., Yang, W., Posewitz, M. C., and Grossman, A. R. (2013). Fermentation metabolism and its evolution in algae. *Frontiers in Plant Science*, 4(May):1–17.

Chen, X., Schreiber, K., Appel, J., Makowka, A., Fähnrich, B., Roettger, M., Hajirezaei, M. R., Sönnichsen, F. D., Schönheit, P., Martin, W. F., and Gutekunst, K. (2016). The Entner–Doudoroff pathway is an overlooked glycolytic route in cyanobacteria and plants. *Proceedings of the National Academy of Sciences*, 113(19):5441–5446.

Cheng, Z. (2003). Highly Divergent Methyltransferases Catalyze a Conserved Reaction in Tocopherol and Plastoquinone Synthesis in Cyanobacteria and Photosynthetic Eukaryotes. *the Plant Cell Online*, 15(10):2343–2356.

Chung, C.-C. C., Hwang, S.-P. L., and Chang, J. (2008). Nitric oxide as a signalling factor to upregulate the death-specific protein in a marine diatom, *Skeletonema costatum*, during blockage of electron flow in photosynthesis. *Applied and Environmental Microbiology*, 74(21):6521–6527.

Cimoli, E., Lucieer, A., Meiners, K. M., Lund-Hansen, L. C., Kennedy, F., Martin, A., McMinn, A., and Lucieer, V. (2017). Towards improved estimates of sea-ice algal biomass: experimental assessment of hyperspectral imaging cameras for under-ice studies. *Annals of Glaciology*, 58(75pt1):68–77.

Comiso, J., Parkinson, C., Markus, T., Cavalieri, D., and Gersten, R. (2019). Current State of the Sea Ice Cover. *NASA - crysosphere*.

Cooksey, K. E. (1995). Adhesion of bacteria and diatoms to surfaces in the sea: a review. *Aquatic Microbial Ecology*, 9:87–96.

Cooper, W. and Zika, R. (1983). Photochemical Formation of Hydrogen Peroxide in Surface and Ground Waters Exposed to Sunlight. *Science*, 220(4598):711 LP – 712.

Cox, J., Hein, M. Y., Luber, C. A., Paron, I., Nagaraj, N., and Mann, M. (2014). Accurate proteome-wide label-free quantification by delayed normalization and maximal peptide ratio extraction, termed MaxLFQ. *Molecular & Cellular Proteomics*, 13(9):2513–2526.

Daloso, D. M., Müller, K., Obata, T., Florian, A., Tohge, T., Bottcher, A., Riondet, C., Bariat, L., Carrari, F., Nunes-Nesi, A., Buchanan, B. B., Reichheld, J.-P., Araújo, W. L., and Fernie, A. R. (2015). Thioredoxin, a master regulator of the tricarboxylic acid cycle in plant mitochondria. *Proceedings of the National Academy of Sciences*, 112(11):1392–1400.

Deppeler, S. L. and Davidson, A. T. (2017). Southern Ocean Phytoplankton in a Changing Climate. *Frontiers in Marine Science*, 4:40.

Di Dato, V., Musacchia, F., Petrosino, G., Patil, S., Montresor, M., Sanges, R., and Ferrante, M. I. (2015). Transcriptome sequencing of three *Pseudo-nitzschia* species reveals comparable gene sets and the presence of Nitric Oxide Synthase genes in diatoms. *Scientific Reports*, 5(June):1–14.

Diaz, J. M. and Plummer, S. (2018). Production of extracellular reactive oxygen species by phytoplankton: past and future directions. *Journal of Plankton Research*, 40:655–666.

Diaz, J. M., Plummer, S., Tomas, C., and Alves-De-Souza, C. (2018). Production of extracellular superoxide and hydrogen peroxide by five marine species of harmful bloom-forming algae. *Journal of Plankton Research*, 40(6):667–677.

Diner, B. A. and Petrouleas, V. (1990). Formation by NO of nitrosyl adducts of redox components of the Photosystem II reaction center. II. Evidence that HCO-3/CO2 binds to the acceptor-side non-heme iron. *BBA - Bioenergetics*, 1015(1):141–149.

Dolch, L. J., Lupette, J., Tourcier, G., Bedhomme, M., Collin, S., Magneschi, L., Conte, M., Seddiki, K., Richard, C., Corre, E., Fourage, L., Laeuffer, F., Richards, R., Reith, M., Rébeillé, F., Jouhet, J., McGinn, P., and Marechal, E. (2017). NO mediates nitrite-sensing and adaptation and triggers a remodeling of lipids. *Plant Physiology*, 175(November):pp.01042.2017.

Domingues, N., Matos, A. R., da Silva, J. M., and Cartaxana, P. (2012). Response of the Diatom *Phaeodactylum tricornutum* to photooxidative stress resulting from high light exposure. *PLoS ONE*, 7(6):1–6.

Drábková, M., Admiraal, W., and Maršálek, B. (2007). Combined exposure to hydrogen peroxide and light-selective effects on cyanobacteria, green algae, and diatoms. *Environmental Science and Technology*, 41(1):309–314.

Estevez, M. S. M. S. and Puntarulo, S. (2005). Nitric oxide generation upon growth of Antarctic *Chlorella sp.* cells. *Physiologia Plantarum*, 125(2):192–201.

Evans, C., O'Reilly, J., and Thomas, J. (1987). *A handbook for the measurement of chlorophyll-a and primary productivity*. College Station, Texas A&M University.

Fabris, M., Matthijs, M., Rombauts, S., Vyverman, W., Goossens, A., and Baart, G. J. E. E. (2012). The metabolic blueprint of *Phaeodactylum tricornutum* reveals a eukaryotic Entner-Doudoroff glycolytic pathway. *Plant Journal*, 70(6):1004–1014.

Falciatore, A. and Bowler, C. (2002). Revealing the molecular secrets of marine diatoms. *Annual Review of Plant Biology*, 53(29):109–130.

Falkowski, P. G. and LaRoche, J. (1991). Acclimation to spectral irradiance in algae. *Journal of Phycology*, 27(1):8–14.

Fancy, N. N., Bahlmann, A.-K., and Loake, G. J. (2017). Nitric oxide function in plant abiotic stress. *Plant, Cell & Environment*, 40(4):462–472.

Feild, T. S., Nedbal, L., and Ort, D. R. (1998). Nonphotochemical reduction of the plastoquinone pool in sunflower leaves originates from chlororespiration. *Plant Physiology*, 116(4):1209–1218.

Fernie, A. R., Carrari, F., and Sweetlove, L. J. (2004). Respiratory metabolism: Glycolysis, the TCA cycle and mitochondrial electron transport. *Current Opinion in Plant Biology*, 7(3):254–261.

Figueroa, F. L., Aguilera, J., Jimenez, C., Vergara, J. J., Robles, M. D., and Niell, F. X. (1995). Growth, pigment synthesis and nitrogen assimilation in the red alga Porphyra sp. (Bangiales, Rhodophyta) under blue and red light. *Scientia Marina*, 59:9–20.

Florence, T. M. and Stauber, J. L. (1986). Toxicity of copper complexes to the marine diatom Nitzschia closterium. *Aquatic Toxicology*, 8(1):11–26.

Ginger, M. L., McFadden, G. I., and Michels, P. (2010). Rewiring and regulation of cross-compartmentalized metabolism in protists. *Philosophical Transactions of the Royal Society B: Biological Sciences*, 365(1541):831–845.

Giovagnetti, V. and Ruban, A. V. (2017). Detachment of the fucoxanthin chlorophyll a/c binding protein (FCP) antenna is not involved in the acclimative regulation of photoprotection in the pennate diatom *Phaeodactylum tricornutum*. *Biochimica et Biophysica Acta - Bioenergetics*, 1858(3):218–230.

Goessling, J. W., Cartaxana, P., and Kühl, M. (2016). Photo-Protection in the Centric Diatom Coscinodiscus granii is Not Controlled by Chloroplast High-Light Avoidance Movement. *Frontiers in Marine Science*, 2(January):1–10.

Goessling, J. W., Frankenbach, S., Ribeiro, L., Serôdio, J., and Kühl, M. (2018). Modulation of the light field related to valve optical properties of raphid diatoms: Implications for niche differentiation in the microphytobenthos. *Marine Ecology Progress Series*, 588:29–42.

Gosselin, M., Legendre, L., Therriault, J. C., and Demers, S. (1990). Light and Nutrient Limitation of Sea-Ice Microalgae (Hudson Bay, Canadian Arctic).

Graff van Creveld, S., Rosenwasser, S., Levin, Y., and Vardi, A. (2016). Chronic Iron Limitation Confers Transient Resistance to Oxidative Stress in Marine Diatoms. *Plant Physiology*, 172(2):968–979.

Graziano, M. and Lamattina, L. (2005). Nitric oxide and iron in plants: An emerging and converging story. *Trends in Plant Science*, 10(1):4–8.

Grossi, S. M. G. and Sullivan, C. W. (1985). Sea ice microbial communities. V. The vertical zonation of diatoms in an Antarctic fast ice community. *Journal of Phycology*, 21(3):401–409.

Guillard, R. R. L. and Hargraves, P. E. (1993). *Stichochrysis immobilis* is a diatom, not a chrysophyte. *Phycologia*, 32(3):234–236.

Gundermann, K., Schmidt, M., Weisheit, W., Mittag, M., and Büchel, C. (2013). Identification of several sub-populations in the pool of light harvesting proteins in the pennate diatom *Phaeodactylum tricornutum*. *Biochimica et Biophysica Acta - Bioenergetics*, 1827(3):303–310.

Hama, T. (2001). Production and neutral aldose composition of dissolved carbohydrates excreted by natural marine phytoplankton populations. *Limnology and Oceanography*, 46(8):1945–1955.

Hancke, K., Lund-Hansen, L. C., Lamare, M. L., Højlund Pedersen, S., King, M. D., Andersen, P., and Sorrell, B. K. (2018). Extreme Low Light Requirement for Algae Growth Underneath Sea Ice: A Case Study From Station Nord, NE Greenland. *Journal of Geophysical Research: Oceans*, 123(2):985–1000.

Holdsworth, E. S. (1985). Effect of growth factors and light quality on the growth, pigmentation and photosynthesis of two diatoms, *Thalassiosira gravida* and *Phaeodactylum tricornutum*. *Marine Biology*, 86(3):253–262.

Hoober, J. K. and Eggink, L. L. (2001). A potential role of chlorophylls b and c in assembly of light-harvesting complexes. *FEBS Lett*, 489(1):1–3.

Hoober, J. K., Eggink, L. L., and Chen, M. (2007). Chlorophylls, ligands and assembly of light-harvesting complexes in chloroplasts. *Photosynthesis Research*, 94(2-3):387–400.

Horner, R. and Alexander, V. (1972). Algal populations in arctic sea ice: an investigation of heterotrophy. *Limnol.Oceanogr.*, 17(3):454–458.

Huang, W., Zhang, S.-B., and Liu, T. (2018). Moderate Photoinhibition of Photosystem II Significantly Affects Linear Electron Flow in the Shade-Demanding Plant Panax notoginseng. *Frontiers in plant science*, 9:637.

Ishihara, T., Ifuku, K., Yamashita, E., Fukunaga, Y., Nishino, Y., Miyazawa, A., Kashino, Y., and Inoue-Kashino, N. (2015). Utilization of light by fucoxanthin-chlorophyll-binding protein in a marine centric diatom, Chaetoceros gracilis. *Photosynthesis Research*, 126(2-3):437–447.

Jakob, T., Goss, R., and Wilhelm, C. (1999). Activation of diadinoxanthin de-epoxidase due to a chlororespiratory proton gradient in the dark in the diatom *Phaeodactylum tricornutum*. *Plant Biology*, 1(1):76–82.

Jakob, T., Goss, R., and Wilhelm, C. (2001). Unusual pH-dependence of diadinoxanthin de-epoxidase activation causes chlororespiratory induced accumulation of diatoxanthin in the diatom *Phaeodactylum tricornutum*. *Journal of Plant Physiology*, 158(3):383–390.

Janknegt, P. J., Van De Poll, W. H., Visser, R. J. W., Rijstenbil, J. W., and Buma, A. G. J. (2008). Oxidative stress responses in the marine antarctic diatom Chaetoceros brevis (Bacillariophyceae) during photoacclimation. *Journal of Phycology*, 44(4):957–966.

Joshi, A. S., Zhou, J., Gohil, V. M., Chen, S., and Greenberg, M. L. (2009). Cellular functions of cardiolipin in yeast. *Biochimica et Biophysica Acta (BBA) - Molecular Cell Research*, 1793(1):212–218.

Juhl, A. R. and Krembs, C. (2010). Effects of snow removal and algal photoacclimation on growth and export of ice algae. *Polar Biology*, 33(8):1057–1065.

Kamp, A., Høgslund, S., Risgaard-Petersen, N., and Stief, P. (2015). Nitrate storage and dissimilatory nitrate reduction by eukaryotic microbes.

Kamp, A., Stief, P., Knappe, J., and De Beer, D. (2013). Response of the ubiquitous pelagic diatom *Thalassiosira weissflogii* to darkness and anoxia. *PLoS ONE*, 8(12):1–11.

Katayama, T., Murata, A., and Taguchi, S. (2011). Responses of pigment composition of the marine diatom *Thalassiosira weissflogii* to silicate availability during. *Plankton and Benthos Research*, 6(1):1–11.

Kennedy, F., Martin, A., Bowman, J. P., Wilson, R., and McMinn, A. (2019). Dark metabolism: a molecular insight into how the Antarctic sea-ice diatom *Fragilariopsis cylindrus* survives long-term darkness. *New Phytologist*, 0(ja):nph.15843.

Kennedy, F., McMinn, A., and Martin, A. (2012). Effect of temperature on the photosynthetic efficiency and morphotype of *Phaeocystis antarctica*. *Journal of Experimental Marine Biology and Ecology*, 429:7–14.

Kim, D., Yamaguchi, K., and Oda, T. (2006). Nitric oxide synthase-like enzyme mediated nitric oxide generation by harmful red tide phytoplankton, *Chattonella marina*. *Journal of Plankton Research*, 28(6):613–620.

King, M. D., France, J. L., Fisher, F. N., and Beine, H. J. (2005). Measurement and modelling of UV radiation penetration and photolysis rates of nitrate and hydrogen peroxide in Antarctic sea ice: An estimate of the production rate of hydroxyl radicals in first-year sea ice. *Journal of Photochemistry and Photobiology A: Chemistry*, 176(1-3 SPEC. ISS.):39–49.

Kirst, G. and Wiencke, C. (1995). Ecophysiology of polar algae. *Journal of Phycology*, Volume 31(Issue 2):181–199.

Klughammer, C. and Schreiber, U. (2008). Complementary PS II quantum yields calculated from simple fluorescence parameters measured by PAM fluorometry and the Saturation Pulse method. *PAM Application Notes*, 1(1):27–35.

Kramer, D. M. and Evans, J. R. (2011). The Importance of Energy Balance in Improving Photosynthetic Productivity. *Plant Physiology*, 155(1):70–78.

Kramer, D. M., Johnson, G., Kiirats, O., and Edwards, G. E. (2004). New fluorescence parameters for the determination of QA redox state and excitation energy fluxes. *Photosynthesis Research*, 79(2):209–218.

Krieger-Liszkay, A. and Trebst, A. (2006). Tocopherol is the scavenger of singlet oxygen produced by the triplet states of chlorophyll in the PSII reaction centre. *Journal of Experimental Botany*, 57(8):1677–1684.

Kroth, P. G., Chiovitti, A., Gruber, A., Martin-Jezequel, V., Mock, T., Parker, M. S., Stanley, M. S., Kaplan, A., Caron, L., Weber, T., Maheswari, U., Armbrust, E. V., and Bowler, C. (2008). A model for carbohydrate metabolism in the diatom *Phaeodactylum tricornutum* deduced from comparative whole genome analysis. *PLoS One*, 3(1):e1426.

Kuczynska, P., Jemiola-Rzeminska, M., and Strzalka, K. (2015). Photosynthetic Pigments in Diatoms. *Marine Drugs*, 13(9):5847–5881.

Kumar, A., Castellano, I., Patti, F. P., Palumbo, A., and Buia, M. C. (2015). Nitric oxide in marine photosynthetic organisms. *Nitric Oxide - Biology and Chemistry*, 47:34–39.

Lavaud, J., Materna, A. C., Sturm, S., Vugrinec, S., and Kroth, P. G. (2012). Silencing of the Violaxanthin De-Epoxidase Gene in the Diatom Phaeodactylum tricornutum Reduces Diatoxanthin Synthesis and Non-Photochemical Quenching. *PLoS ONE*, 7(5):e36806.

Lavaud, J., Rousseau, B., and Etienne, A. L. (2002). In diatoms, a transthylakoid proton gradient alone is not sufficient to induce a non-photochemical fluorescence quenching. *FEBS Letters*, 523(1-3):163–166.

Laybourn-Parry, J., Marshall, W. A., and Marchant, H. J. (2005). Flagellate nutritional versatility as a key to survival in two contrasting Antarctic saline lakes. *Freshwater Biology*, 50(5):830–838.

Lepetit, B., Goss, R., Jakob, T., and Wilhelm, C. (2012). Molecular dynamics of the diatom thylakoid membrane under different light conditions. *Photosynthesis Research*, 111(1-2):245–257.

Lepetit, B., Volke, D., Gilbert, M., Wilhelm, C., and Goss, R. (2010). Evidence for the existence of one antenna-associated, lipid-dissolved and two protein-bound pools of diadinoxanthin cycle pigments in diatoms. *Plant physiology*, 154(4):1905–1920.

Leu, E., Mundy, C., Assmy, P., Campbell, K., Gabrielsen, T., Gosselin, M., Juul-Pedersen, T., and Gradinger, R. (2015). Arctic spring awakening – Steering principles behind the phenology of vernal ice algal blooms. *Progress in Oceanography*, 139:151–170.

Liu, J., Gerken, H., and Li, Y. (2014). Single-tube colony PCR for DNA amplification and transformant screening of oleaginous microalgae. *Journal of Applied Phycology*, 26(4):1719–1726.

Lizotte, M. P. (2001). The Contributions of Sea Ice Algae to Antarctic Marine Primary Production1. *American Zoologist*, 41(1):57–73.

Lizotte, M. P. and Sullivan, C. W. (1991). Rates of photoadaptation in sea ice diatoms from McMurdo Sound, Antarctica. *Journal of Phycology*, 27(3):367–373.

Lund-Hansen, L. C., Hawes, I., Sorrell, B. K., and Nielsen, M. H. (2014). Removal of snow cover inhibits spring growth of Arctic ice algae through physiological and behavioral effects. *Polar Biology*, 37(4):471–481.

Lyon, B. and Mock, T. (2014). Polar Microalgae: New Approaches towards Understanding Adaptations to an Extreme and Changing Environment. *Biology*, 3(1):56–80.

Lyon, B. R., Lee, P. A., Bennett, J. M., DiTullio, G. R., and Janech, M. G. (2011). Proteomic Analysis of a Sea-Ice Diatom: Salinity Acclimation Provides New Insight into the Dimethylsulfoniopropionate Production Pathway. *Reactive species and antioxidants. Redox biology is a fundamental theme of aerobic life.*, 157(4):1926–1941.

Mack, J. and Bolton, J. R. (1999). Photochemistry of nitrite and nitrate in aqueous solution: a review. *Journal of Photochemistry and Photobiology A: Chemistry*, 128(1-3):1–13.

Mallick, N. and Mohn, F. H. (2000). Reactive oxygen species: Response of algal cells. *Journal of Plant Physiology*, 157(2):183–193.

Mallick, N., Rai, L. C., Mohn, F. H., and Soeder, C. J. (1999). Studies on nitric oxide (NO) formation by the green alga *Scenedesmus obliquus* and the diazotrophic cyanobacterium *Anabaena doliolum*. *Chemosphere*, 39(10):1601–1610.

Marchetti, J., Bougaran, G., Jauffrais, T., Lefebvre, S., Rouxel, C., Saint-Jean, B., Lukomska, E., Robert, R., and Cadoret, J. P. (2013). Effects of blue light on the biochemical composition and photosynthetic activity of *Isochrysis sp. Journal of Applied Phycology*, 25(1):109–119.

Martin, A., Anderson, M. J., Thorn, C., Davy, S. K., and Ryan, K. G. (2011). Response of sea-ice microbial communities to environmental disturbance: An *in situ* transplant experiment in the Antarctic. *Marine Ecology Progress Series*, 424:25–37.

Martin, A., McMinn, A., Heath, M., Hegseth, E. N., and Ryan, K. G. (2012). The physiological response to increased temperature in over-wintering sea ice algae and phytoplankton in McMurdo Sound, Antarctica and Tromsø Sound, Norway. *Journal of Experimental Marine Biology and Ecology*, 428(C):57–66.

Masojídek, J., Torzillo, G., and Koblížek, M. (2013). Photosynthesis in Microalgae In. Handbook of Microalgal Culture: Applied Phycology and Biotechnology . (November 2017).

Massom, R. A., Eicken, H., Haas, C., Jeffries, M. O., Drinkwater, M. R., Sturm, M., Worby, A. P., Wu, X., Lytle, V. I., Ushio, S., Morris, K., Reid, P. A., Warren, S. G., and Allison, I. (2001). Snow on Antarctic sea ice. *Reviews of Geophysics*, 39(3):413–445.

Massom, R. A. and Stammerjohn, S. E. (2010). Antarctic sea ice change and variability - Physical and ecological implications. *Polar Science*, 4(2):149–186.

McMinn, A. (1997). Species Succession in Fast Ice Algal Communities. *Korea Journal Of Polar Research (1990 -2000)*, 8(1/2):47–52.

McMinn, A. and Ashworth, C. (2007). The use of oxygen microelectrodes to determine the net production by an Antarctic sea ice algal community. *Antarctic Science*, 10(01):39–44.

McMinn, A., Ashworth, C., and Ryan, K. (1999a). Growth and productivity of Antarctic sea ice algae under PAR and UV irradiances. *Botanica Marina*, 42(4):401–407.

McMinn, A., Ashworth, C., and Ryan, K. (1999b). Growth and productivity of Antarctic sea ice algae under PAR and UV irradiances. *Botanica Marina*, 42(4):401–407.

McMinn, A. and Lee, S. (2018). Use of glucose biosensors to measure extracellular glucose exudation by intertidal microphytobenthos in southern Tasmania. *Journal of Phycology*, 54(3):410–418.

McMinn, A. and Martin, A. (2013). Dark survival in a warming world. *Proceedings of the Royal Society B: Biological Sciences*, 280(1755).

McMinn, A., Martin, A., and Ryan, K. (2010). Phytoplankton and sea ice algal biomass and physiology during the transition between winter and spring (McMurdo Sound, Antarctica). *Polar Biology*, 33(11):1547–1556.

McMinn, A., Ryan, K., and Gademann, R. (2003). Diurnal changes in photosynthesis of Antarctic fast ice algal communities determined by pulse amplitude modulation fluorometry. *Marine Biology*, 143(2):359–367.

Medlin, L. K. (2016). Evolution of the diatoms: major steps in their evolution and a review of the supporting molecular and morphological evidence. *Phycologia*, 55(1):79–103.

Meiners, K. M., Arndt, S., Bestley, S., Krumpen, T., Ricker, R., Milnes, M., Newbery, K., Freier, U., Jarman, S., King, R., Proud, R., Kawaguchi, S., and Meyer, B. (2017). Antarctic pack ice algal distribution: Floe-scale spatial variability and predictability from physical parameters. *Geophysical Research Letters*, 44(14):7382–7390.

Mock, T., Otillar, R. P., Strauss, J., McMullan, M., Paajanen, P., Schmutz, J., Salamov, A., Sanges, R., Toseland, A., Ward, B. J., Allen, A. E., Dupont, C. L., Frickenhaus, S., Maumus, F., Veluchamy, A., Wu, T., Barry, K. W., Falciatore, A., Ferrante, M. I., Fortunato, A. E., Glöckner, G., Gruber, A., Hipkin, R., Janech, M. G., Kroth, P. G., Leese, F., Lindquist, E. A., Lyon, B. R., Martin, J., Mayer, C., Parker, M., Quesneville, H., Raymond, J. A., Uhlig, C., Valas, R. E., Valentin, K. U., Worden, A. Z., Armbrust, E. V., Clark, M. D., Bowler, C., Green, B. R., Moulton, V., van Oosterhout, C., and Grigoriev, I. V. (2017). Evolutionary genomics of the cold-adapted diatom *Fragilariopsis cylindrus*. *Nature*, 541(7638):536–540.

Mokrosnop, V. M. (2014). Functions of tocopherols in the cells of plants and other photosynthetic organisms. *Ukrainian biochemical journal*, 86(5):26–36.

Morgan-Kiss, R. M., Lizotte, M. P., Kong, W., and Priscu, J. C. (2016). Photoadaptation to the polar night by phytoplankton in a permanently ice-covered Antarctic lake. *Limnology and Oceanography*, 61(1):3–13.

Mundy, C. J., Barber, D. G., and Michel, C. (2005). Variability of snow and ice thermal, physical and optical properties pertinent to sea ice algae biomass during spring. *Journal of Marine Systems*, 58(3-4):107–120.

Mundy, C. J., Ehn, J. K., Barber, D. G., and Michel, C. (2007). Influence of snow cover and algae on the spectral dependence of transmitted irradiance through Arctic landfast first-year sea ice. *Journal of Geophysical Research: Oceans*, 112(3):1–10.

Mur, L. A., Mandon, J., Persijn, S., Cristescu, S. M., Moshkov, I. E., Novikova, G. V., Hall, M. A., Harren, F. J., Hebelstrup, K. H., and Gupta, K. J. (2013). Nitric oxide in plants: An assessment of the current state of knowledge. *AoB PLANTS*, 5:1–17.

Murata, N., Takahashi, S., Nishiyama, Y., and Allakhverdiev, S. I. (2007). Photoinhibition of photosystem II under environmental stress. *Biochimica et Biophysica Acta - Bioenergetics*, 1767(6):414–421.

Nagao, R., Tomo, T., Narikawa, R., Enami, I., and Ikeuchi, M. (2013). Light-independent biosynthesis and assembly of the photosystem II complex in the diatom *Chaetoceros gracilis*. *FEBS Letters*, 587(9):1340–1345.

Neftel, A., Jacob, P., and Klockow, D. (1984). Measurements of hydrogen peroxide in polar ice samples. *Enhanced biological carbon consumption in a high CO2 ocean.*, 311(5981):43–45.

Nguyen-Deroche, T. L. N., Caruso, A., Le, T. T., Bui, T. V., Schoefs, B., Tremblin, G., and Morant-Manceau, A. (2012). Zinc affects differently growth, photosynthesis, antioxidant enzyme activities and phytochelatin synthase expression of four marine diatoms. *The Scientific World Journal*, 2012.

Nishiyama, Y., Allakhverdiev, S. I., and Murata, N. (2006). A new paradigm for the action of reactive oxygen species in the photoinhibition of photosystem II.

Nixon, P. J. (2000). Chlororespiration. *Philosophical Transactions of the Royal Society B: Biological Sciences*, 355(1402):1541–1547.

Nymark, M., Valle, K. C., Brembu, T., Hancke, K., Winge, P., Andresen, K., Johnsen, G., and Bones, A. M. (2009). An Integrated Analysis of Molecular Acclimation to High Light in the Marine Diatom *Phaeodactylum tricornutum*. *PloS one*, 4(11):e7743.

Nymark, M., Valle, K. C., Hancke, K., Winge, P., Andresen, K., Johnsen, G., Bones, A. M., and Brembu, T. (2013). Molecular and Photosynthetic Responses to Prolonged Darkness and Subsequent Acclimation to Re-Illumination in the Diatom Phaeodactylum tricornutum. *PLoS ONE*, 8(3):e58722.

Oxborough, K. and Baker, N. R. (1997). Resolving chlorophyll a fluorescence images of photosynthetic efficiency into photochemical and non-photochemical components - Calculation of qP and Fv'/Fm' without measuring Fo'. *Photosynthesis Research*, 54(2):135–142.

Palenik, B., Zafiriou, O. C., and Morel, F. M. M. (1987). Hydrogen Peroxide Production by a Marine Phytoplankter. *Limnol. Oceanogr.*, 32(6):1365–1369.

Palmisano, a. C., Beeler SooHoo, J., and Sullivan, C. W. (1987). Effects of four environmental variables on photosynthesis-irradiance relationships in Antarctic sea-ice microalgae. *Marine Biology*, 94(2):299–306.

Palmisano, A. C., SooHoo, J. B., and Sullivan, C. W. (1985). Photosyntheis-irradiance relationships in sea ice microalgae from McMurdo Sound, Antarctica. *Journal of Phycology*, 21(3):341–346.

Palmisano, A. C. and Sullivan, C. W. (1982). Physiology of sea ice daitoms. I. Response of three polar daitoms to a simulated summer-winter transition. *Journal of Phycology*, 18(4):489–498.

Palmisano, A. C. and Sullivan, C. W. (1983). Physiology of sea ice diatoms. II. Dark survival of three polar diatoms. *Canadian Journal of Microbiology*, 29(Carlucci 1973):157–160.

Pamatmat, M. M. (1968). Ecology and Metabolism of a Benthic Community on an Intertidal Sandflat. *Internationale Revue der gesamten Hydrobiologie und Hydrographie*, 53(2):211–298.

Perkins, R., Underwood, G., Brotas, V., Snow, G., Jesus, B., and Ribeiro, L. (2001). Responses of microphytobenthos to light: Primary production and carbohydrate allocation over an emersion period. *Marine Ecology Progress Series*, 223:101–112.

Peters, E. and Thomas, D. (1996). Prolonged darkness and diatom mortality I: Marine Antarctic species. *Journal of Experimental Marine Biology and Ecology*, 207(1-2):25–41.

Petrou, K., Hill, R., Brown, C. M., Campbell, D. A., Doblin, M. A., and Ralph, P. J. (2010). Rapid photoprotection in sea-ice diatoms from the East Antarctic pack ice. *Limnology and Oceanography*, 55(3):1400–1407.

Petrou, K., Kranz, S. A., Trimborn, S., Hassler, C. S., Ameijeiras, S. B., Sackett, O., Ralph, P. J., and Davidson, A. T. (2016). Southern Ocean phytoplankton physiology in a changing climate. *Journal of Plant Physiology*, 203:135–150.

Pick, U., Weiss, M., Gounaris, K., and Barber, J. (1987). The role of different thylakoid glycolipids in the function of reconstituted chloroplast ATP synthase. *Biochimica et Biophysica Acta (BBA) - Bioenergetics*, 891(1):28–39.

Platt, T. and Jassby, A. D. (1976). The relationship between photosynthesis and light for natural assemblages of coastal marine phytoplankton. *Journal of Phycology*, 12(4):421–430.

Popels, L. C., MacIntyre, H. L., Warner, M. E., Zhang, Y., and Hutchins, D. A. (2007). Physiological responses during dark survival and recovery in *Aureococcus anophagefferens* (Pelagophyceae). *Journal of Phycology*, 43(1):32–42.

Prihoda, J., Tanaka, A., De Paula, W. B. M., Allen, J. F., Tirichine, L., and Bowler, C. (2012). Chloroplast-mitochondria cross-talk in diatoms. *Journal of Experimental Botany*, 63(4):1543–1557.

Pyszniak, A. M. and Gibbs, S. P. (1992). Immunocytochemical localization of photosystem I and the fucoxanthin-chlorophyll a/c light-harvesting complex in the diatom *Phaeodactylum tricornutum*. *Protoplasma*, 166(3):208–217.

Qiao, W. and Fan, L. M. (2008). Nitric oxide signaling in plant responses to abiotic stresses. *Journal of Integrative Plant Biology*, 50(10):1238–1246.

Raven, J. A. (2011). The cost of photoinhibition. *Physiologia Plantarum*, 142(1):87–104.

Raven, J. A. and Beardall, J. (2011). Carbohydrate Metabolism and Respiration in Algae. In Larkum, A. W. D., Douglas, S. E., and Raven, J. A., editors, *Photosynthesis in Algae: Advances in Photosynthesis and Respiration*, volume 14, pages 205–224. Springer Netherlands, Dordrecht.

Reeves, S., McMinn, A., and Martin, A. (2011). The effect of prolonged darkness on the growth, recovery and survival of Antarctic sea ice diatoms. *Polar Biology*, 34(7):1019–1032.

Revsbecht, N. P. and Ward, D. M. (1983). Oxygen Microelectrode That Is Insensitive to Medium Chemical Composition: Use in an Acid Microbial Mat Dominated by *Cyanidium caldarium*. *Microbiology*, (1):755–759.

Rijstenbil, J. W. (2002). Assessment of oxidative stress in the planktonic diatom *Thalassiosira pseudonana* in response to UVA and UVB radiation. *Journal of Plankton Research*, 24(12):1277–1288.

Rivkin, R. B. and Putt, M. (1987). Heterotrophy and photoheterotrophy by Antarctic microalgae: Light dependant incorporation of amino acids and glucose. *Journal of Phycology*, 23:442–452.

Ruban, A., Lavaud, J., Rousseau, B., Guglielmi, G., Horton, P., and Etienne, A. L. (2004). The super-excess energy dissipation in diatom algae: Comparative analysis with higher plants. *Photosynthesis Research*, 82(2):165–175.

Ryan, K. G. and Beaglehole, D. (1994). Ultraviolet radiation and bottom-ice algae: laboratory and field studies from McMurdo Sound, Antarctica. In Weiler, C. and Penahle, P., editors, *Ultraviolet Radiation in Antarctica: Measurement and Biological Effects*. American Geophysical Union, Washington, 62 edition.

Ryan, K. G., Cowie, R. O., Liggins, E., McNaughtan, D., Martin, A., and Davy, S. K. (2009). The short-term effect of irradiance on the photosynthetic properties of Antarctic fast-ice microalgal communities. *Journal of Phycology*, 45(6):1290–1298.

Ryan, K. G., Hegseth, E. N., Martin, A., Davy, S. K., O'Toole, R., Ralph, P. J., McMinn, A., and Thorn, C. J. (2006). Comparison of the microalgal community within fast ice at two sites along the Ross Sea coast, Antarctica. *Antarctic Science*, 18(4):583–594.

Sakihama, Y., Nakamura, S., and Yamasaki, H. (2002). Nitric oxide production mediated by nitrate reductase in the green alga *Chlamydomonas reinhardtii*: an alternative NO production pathway in photosynthetic organisms. *Plant & cell physiology*, 43(3):290–7.

Sanz-Luque, E., Chamizo-Ampudia, A., Llamas, A., Galvan, A., and Fernandez, E. (2015). Understanding nitrate assimilation and its regulation in microalgae. *Frontiers in plant science*, 6(October):899.

Schaub, I., Wagner, H., Graeve, M., and Karsten, U. (2017). Effects of prolonged darkness and temperature on the lipid metabolism in the benthic diatom *Navicula perminuta* from the Arctic Adventfjorden, Svalbard. *Polar Biology*, 40(7):0.

Schmitt, F. J., Renger, G., Friedrich, T., Kreslavski, V. D., Zharmukhamedov, S. K., Los, D. A., Kuznetsov, V. V., and Allakhverdiev, S. I. (2014). Reactive oxygen species: Re-evaluation of generation, monitoring and role in stress-signaling in phototrophic organisms. *Biochimica et Biophysica Acta - Bioenergetics*, 1837(6):835–848.

Schneider, R. J., Roe, K. L., Hansel, C. M., and Voelker, B. M. (2016). Species-Level Variability in Extracellular Production Rates of Reactive Oxygen Species by Diatoms. *Frontiers in Chemistry*, 4(March).

Schuetz, R., Kuepfer, L., and Sauer, U. (2007). Systematic evaluation of objective functions for predicting intracellular fluxes in *Escherichia coli*. *Molecular Systems Biology*, 3:119.

Scott, F. and Marchant, H. J. (2005). *Antarctic Marine Protists*. Australian Biological Resources Study and Australian Antarctic Division., Kingston.

Sims, P. A., Mann, D. G., and Medlin, L. K. (2006). Evolution of the diatoms: insights from fossil, biological and molecular data. *Phycologia*, 45(4):361–402.

Smayda, T. J. and Mitchell-Innes, B. (1974). Dark survival of autotrophic, planktonic marine diatoms. *Marine Biology*, 25(3):195–202.

Smith, S. R., Abbriano, R. M., and Hildebrand, M. (2012). Comparative analysis of diatom genomes reveals substantial differences in the organization of carbon partitioning pathways. *Algal Research*, 1(1):2–16.

Smith, S. R., Gillard, J. T. F., Kustka, A. B., McCrow, J. P., Badger, J. H., Zheng, H., New, A. M., Dupont, C. L., Obata, T., Fernie, A. R., and Allen, A. E. (2016). Transcriptional orchestration of the global cellular response of a model pennate diatom to diel light cycling under iron limitation. *PLoS Genetics*, 12(12):1–39.

Taddei, L., Stella, G. R., Rogato, A., Bailleul, B., Fortunato, A. E., Annunziata, R., Sanges, R., Thaler, M., Lepetit, B., Lavaud, J., Jaubert, M., Finazzi, G., Bouly, J. P., and Falciatore, A. (2016). Multisignal control of expression of the LHCX protein family in the marine diatom *Phaeodactylum tricornutum*. *Journal of Experimental Botany*, 67(13):3939–3951.

Takahashi, S. and Yamasaki, H. (2002). Reversible inhibition of phosphorylation in chloroplasts by nitric oxide. *FEBS Letters*, 512:145–148.

Tanaka, R., Oster, U., Kruse, E., Rüdiger, W., and Grimm, B. (1999). Reduced Activity of Geranylgeranyl Reductase Leads to Loss of Chlorophyll and Tocopherol and to Partially Geranylgeranylated Chlorophyll in Transgenic Tobacco Plants Expressing Antisense RNA for Geranylgeranyl Reductase1. *Plant physiology*, 120(3):695–704.

Taylor, F. and McMinn, A. (2002). Late Quaternary diatom assemblages from Prydz Bay, Eastern Antarctica. *Quaternary Research*, 57(1):151–161.

Tirichine, L. and Bowler, C. (2011). Decoding algal genomes: tracing back the history of photosynthetic life on Earth. *The Plant Journal*, 66(1):45–57.

Tovar-Méndez, A., Miernyk, J., and Randall, D. D. (2003). Regulation of pyruvate dehydrogenase complex activity in plant cells. *European Journal of Biochemistry*, 270(6):1043–1049.

Turner, J., Bindschadler, R., Convey, P., di Prisco, G., Fahrbach, E., Gutt, J., Hodgson, D., and Mayewski, P. Summerhayes, C. (2008). Antarctic Climate Change and the Environment. In *Scientific Committee on Antarctic Research*, volume 3, pages 9–22.

Underwood, G. J. C. and Paterson, D. M. (2003). The importance of extracellular carbohydrate production by marine epipelic diatoms. *Advances in Botanical Research*, 40:183–240.

Vardi, A. (2008). Cell signaling in marine diatoms. *Communicative & Integrative Biology*, 1(2):134–136.

Vardi, A., Formiggini, F., Casotti, R., De Martino, A., Ribalet, F., Miralto, A., and Bowler, C. (2006). A Stress Surveillance System Based on Calcium and Nitric Oxide in Marine Diatoms. *PLoS Biology*, 4(3):e60–9.

Vermuelen, F. (2013). *The influences of nutrients and snow on the spatial and temporal variability of sea ice algae*. Phd thesis, Victoria University of Wellington.

Vernotte, C., Picaud, M., Kirilovsky, D., Olive, J., Ajlani, G., and Astier, C. (1992). Changes in the photosynthetic apparatus in the cyanobacterium *Synechocystis sp.* PCC 6714 following light-to-dark and dark-to-light transitions. *Photosynthesis Research*, 32(1):45–57.

Vizcaíno, J. A., Csordas, A., Del-Toro, N., Dianes, J. A., Griss, J., Lavidas, I., Mayer, G., Perez-Riverol, Y., Reisinger, F., Ternent, T., Xu, Q.-W., Wang, R., and Hermjakob, H. (2016). 2016 update of the PRIDE database and its related tools. *Nucleic Acids Research*, 44(D1):D447–D456.

Vogel, H. and Sager, J. C. (1982). Photosynthetic response of *Prorocentrum mariae-lebouriae* (Dinophyceae) to different spectral qualities, irradiances, and temperatures. *Journal of Phycology*, 18.

von Wettstein, D., Gough, S., and Kannangara, C. G. (1995). Chlorophyll Biosynthesis. *The Plant Cell*, 7(7):1039.

Voskresenskaya, N. P. (2003). Blue Light and Carbon Metabolism. *Annual Review of Plant Physiology*, 23(1):219–234.

Waring, J., Klenell, M., Bechtold, U., Underwood, G. J. C., and Baker, N. R. (2010). Light-induced responses of oxygen photoreduction, reactive oxygen species production and scavenging in two diatom species. *Journal of Phycology*, 46(6):1206–1217.

Wessely, F., Bartl, M., Guthke, R., Li, P., Schuster, S., and Kaleta, C. (2011). Optimal regulatory strategies for metabolic pathways in *Escherichia coli* depending on protein costs. *Molecular Systems Biology*, 7:515.

Wilhelm, C., Büchel, C., Fisahn, J., Goss, R., Jakob, T., LaRoche, J., Lavaud, J., Lohr, M., Riebesell, U., Stehfest, K., Valentin, K., and Kroth, P. G. (2006). The Regulation of Carbon and Nutrient Assimilation in Diatoms is Significantly Different from Green Algae. *Protist*, 157(2):91–124.

Wilhelm, C., Jungandreas, A., Jakob, T., and Goss, R. (2014). Light acclimation in diatoms: From phenomenology to mechanisms. *Marine Genomics*, 16(1):5–15.

Wilson, I. D., Neill, S. J., and Hancock, J. T. (2008). Nitric oxide synthesis and signalling in plants. *Plant, Cell and Environment*, 31(5):622–631.

Wilson, R., Diseberg, A. F., Gordon, L., Zivkovic, S., Tatarczuch, L., Mackie, E. J., Gorman, J. J., and Bateman, J. F. (2010). Comprehensive profiling of cartilage extracellular matrix formation and maturation using sequential extraction and label-free quantitative proteomics. *Molecular & cellular proteomics : MCP*, 9(6):1296–1313.

Wilson, R., Golub, S. B., Rowley, L., Angelucci, C., Karpievitch, Y. V., Bateman, J. F., and Fosang, A. J. (2016). Novel elements of the chondrocyte stress response identified using an in vitro model of mouse cartilage degradation. *Journal of proteome research*, 15(3):1033–1050.

Wodala, B., Deak, Z., Vass, I., Erdei, L., Altorjay, I., and Horvath, F. (2008). In Vivo Target Sites of Nitric Oxide in Photosynthetic Electron Transport as Studied by Chlorophyll Fluorescence in Pea Leaves. *Plant Physiology*, 146(4):1920–1927.

Wolfe-Simon, F., Starovoytov, V., Reinfelder, J. R., Schofield, O., and Falkowski, P. G. (2006). Localization and Role of Manganese Superoxide Dismutase in a Marine Diatom. *Plant Physiology*, 142(4):1701–1709.

Wongpan, P., Meiners, K. M., Langhorne, P. J., Heil, P., Smith, I. J., Leonard, G. H., Massom, R. A., Clementson, L. A., and Haskell, T. G. (2018). Estimation of Antarctic Land-Fast Sea Ice Algal Biomass and Snow Thickness From Under-Ice Radiance Spectra in Two Contrasting Areas. *Journal of Geophysical Research: Oceans*, 123(3):1907–1923.

Wulff, A., Roleda, M. Y., Zacher, K., and Wiencke, C. (2008). Exposure to sudden light burst after prolonged darkness—a case study on benthic diatoms in Antarctica. *Diatom Research*, 23(2):519–532.

Yamanaka, S., Yano, R., Usami, H., Hayashida, N., Ohguchi, M., Takeda, H., and Yoshino, K. (2008). Optical properties of diatom silica frustule with special reference to blue light. *Journal of Applied Physics*, 103(7).

Yamasaki, H., Sakihama, Y., and Takahashi, S. (1999). An alternative pathway for nitric oxide production in plants: new features of an old enzyme. *Trends in plant science*, 4(4):128–129.

Yang, W., Catalanotti, C., Wittkopp, T. M., Posewitz, M. C., and Grossman, A. R. (2015). Algae after dark: Mechanisms to cope with anoxic/hypoxic conditions. *Plant Journal*, 82(3):481–503.

Zapata, M., Garrido, J., and Jeffery, S. (2006). Chlorophyll c Pigments: Current Status. In Grimm, B., Porra, R., Rudiger, W., and Scheer, H., editors, *Chlorophylls and Bacteriochlorophylls*, chapter 3, pages 39–53. Springer.

Zhang, Q., Gradinger, R., and Spindler, M. (1995). Dark Survival of Marine Microalgae in the High Arctic (Greenland Sea). *Polarforschung*, 65(3):111–116.

Zhang, S. and Bryant, D. A. (2014). Learning new tricks from an old cycle: the TCA cycle in cyanobacteria, algae and plants. *Perspectives in Phycology*, 1(2):73–86.

Zhang, Z., Lin, C., Liu, C., Sun, M., and Ding, H. (2003). The Effect of Nitric Oxide on the Growth of Marine Phytoplankton. *October*, 2(2):185–188.

Zhang, Z., Wu, Z., Liu, C., and Xing, L. (2006a). The study on the effect of NO on the growth of *Chaetoceros curvisetus*. *Chinese Journal of Oceanology and Limnology*, 24(4):413–420.

Zhang, Z.-B., Liu, C.-Y., Wu, Z.-Z., Xing, L., and Li, P.-F. (2006b). Detection of nitric oxide in culture media and studies on nitric oxide formationby marine microalgae. *Medical science monitor*, 12(2):BR75–BR85.

Appendices

Chapter A

Fragilariopsis sequence match 18s rRNA

A.1 DNA Extraction

DNA was extracted using the boiling method developed by Liu et al. (2014). Firstly, the sample was heated to 95°C for 10 min in sterile 10 mM Tris pH 8.1 using 0.5 cm^2 of *F.cylindrus* embedded on filter. Filter material was vortexed 1 min to free as much cells from the filter. After heating, the extract was cooled on ice and spun for 1 min on a microfuge. The PCR reaction was set up using MyTaq (Bioline Australia), 1 μL of template DNA, 1 μM of each primer (18S rRNA) Euk 4F 5' CTG GTT GAT CCT GCC AG 3' and Euk 516R 5' ACC AGA CTT GCC CTC C 3' The thermocycling conditions used were initial denaturation at 98°C for 30 seconds and 32 cycles of: 95 °C for 30 s, 59°C for 30 seconds, and 72°C for 45 seconds, followed by a final extension of 10 min at 72 °C. Thermocycler model used was a Peltier PTC200. Sequencing used the ABI BigDye cycle terminator kit 3.1 and ABI 3730 xl automated sequencer (done at Macrogen, Seoul, South Korea). Sequences were manually checked, ambiguous nucleotide positions near the primer regions removed, and sequence was compared to the NCBI database with closest sequences downloaded.

A.2 Sequence

Fragilariopsis cylindrus1 Euk4F 18rRNA

AGCCATGCATGTCTAAGTATAAATATTTTACTTTGAAACTGCGAACGGCTCATTATATCAGTTATA
GTTTATTTGATAGTCCCTTACTACTTGGATACCCGTAGTAATTCTAGAGCTAATCATGCGTCAATA
CCCTTCTGGGGTAGTATTTATTAGATTGAAACCAACCCCTTCGGGGTGATGTGGTGATTCATAAT
AAGCTTGCGGATCGCATGCCTTTGGCGGKGATGGATCATTCAAGTTTCTGCCCTATCAGCTTTG
GATGGTAGGGTATTGGCCTACCATGGCTTTAACGGGTAACGGGAAATTAGGGTTTGATTCCGGA
GAGGGAGCCTGAGAGACGGCTACCACATCCaAGGAAGGCAGCAGGCGCGTAAATTACCCAATCC
TGACACAGGGAGGTAGTGACAATAAATAACAATGCCGGGCCTTCTTAGGTCTGGCAATTGGAAT
GAGAACAATTTAAACCCCTTATCGAGTATCAATTGGAGGGCAAGTCTGGT

MH843675.1 Fragilariopsis sp. strain RCC4604 small subunit ribosomal RNA gene, partial sequence

AGCCATGCATGTCTAAGTATAAATATTTTACTTTGAAACTGCGAACGGCTCATTATATCAGTTATA
GTTTATTTGATAGTCCCTTACTACTTGGATACCCGTAGTAATTCTAGAGCTAATACATGCGTCAAT
ACCCTTCTGGGGTAGTATTTATTAGATTGAAACCAACCCCTTCGGGGTGATGTGGTGATTCATAA
TAAGCTTGCGGATCGCATGCCTTTGGCGGCGATGGATCATTCAAGTTTCTGCCCTATCAGCTTTG
GATGGTAGGGTATTGGCCTACCATGGCTTTAACGGGTAACGGGAAATTAGGGTTTGATTCCGGA
GAGGGAGCCTGAGAGACGGCTACCACATCCAAGGAAGGCAGCAGGCGCGTAAATTACCCAATCC
TGACACAGGGAGGTAGTGACAATAAATAACAATGCCGGGCCTTCTTAGGTCTGGCAATTGGAAT
GAGAACAATTTAAACCCCTTATCGAGTATCAATTGGAGGGCAAGTCTGGTGCCAGCAGCCGCGG
TAATTCCAGCTCCAATAGCGTATATTAAAGTTGTTGCAGTTAAAAAGCTCGTAGTTGGATTTGTG
GTGTGTCCAGTTGGCCTTTGCTCTTTGAGTGATAGTGCT-TTACTGGTCTGCCATGTTTGGGTGG
AATCTGTGTGGCATTAAGTTGTCGTGCAGGGGATGCCCATCGTTTACTGTGAAAAAATTAAAGTG
TTCAAAGCAGGCTTATGCCTCTGAATATATTAGCATGGAATAATGATATAGGACCTTGGTACTATT
TTGTTGGTTTGCGCACTGAGGTAATGATTAAAAGGGACAGTTGGGGGTATTTGTCTTCCATTGTC
CAAGGTGAAATTCTTGGAATTTTTGAAAAAAA

MG022765.1 Fragilariopsis cylindrus isolate CCAP 1023/1 small subunit ribosomal RNA gene, partial sequence

AGCCATGCATGTCTAAGTATAAATATTTTACTTTGAAACTGCGAACGGCTCATTATATCAGTTATA
GTTTATTTGATAGTCCCTTACTACTTGGATACCCGTAGTAATTCTAGAGCTAATACATGCGTCAAT
ACCCTTCTGGGGTAGTATTTATTAGATTGAAACCAACCCCTTCGGGGTGATGTGGTGATTCATAA
TAAGCTTGCGGATCGCATGCCTTTGGCGGCGATGGATCATTCAAGTTTCTGCCCTATCAGCTTTG
GATGGTAGGGTATTGGCCTACCATGGCTTTAACGGGTAACGGGAAATTAGGGTTTGATTCCGGA
GAGGGAGCCTGAGAGACGGCTACCACATCCAAGGAAGGCAGCAGGCGCGTAAATTACCCAATCC
TGACACAGGGAGGTAGTGACAATAAATAACAATGCCGGGCCTTCTTAGGTCTGGCAATTGGAAT
GAGAACAATTTAAACCCCTTATCGAGTATCAATTGGAGGGCAAGTCTGGTGCCAGCAGCCGCGG
TAATTCCAGCTCCAATAGCGTATATTAAAGTTGTTGCAGTTAAAAAGCTCGTAGTTGGATTTGTG
GTGTGTCCAGTTGGCCTTTGCTCTTTGAGTGATAGTGCT-TTACTGGTCTGCCATGTTTGGGTGG
AATCTGTGTGGCATTAAGTTGTCGTGCAGGGGATGCCCATCGTTTACTGTGAAAAAATTAGAGTG
TTCAAAGCAGGCTTATGCCTCTGAATATATTAGCATGGAATAATGATATAGGACCTTGGTACTATT
TTGTTGGTTTGCGCACTGAGGTAATGATTAAGAGGGACAGTTGGGGGTATTTGTATTCCATTGTC

AGAGGTGAAATTCTTGGATTTTTGGAAGACAAACTA

LC189084.1 Fragilariopsis cylindrus gene for 18S ribosomal RNA, partial sequence, strain: NIES-3966

AGCCATGCATGTCTAAGTATAAATATTTTACTTTGAAACTGCGAACGGCTCATTATATCAGTTATA
GTTTATTTGATAGTCCCTTACTACTTGGATACCCGTAGTAATTCTAGAGCTAATACATGCGTCAAT
ACCCTTCTGGGGTAGTATTTATTAGATTGAAACCAACCCCTTCGGGGGTGATGTGGTGATTCATAA
TAAGCTTGCGGATCGCATGCCTTTGGCGGCGATGGATCATTCAAGTTTCTGCCCTATCAGCTTTG
GATGGTAGGGTATTGGCCTACCATGGCTTTAACGGGTAACGGGAAATTAGGGTTTGATTCCGGA
GAGGGAGCCTGAGAGACGGCTACCACATCCAAGGAAGGCAGCAGGCGCGTAAATTACCCAATCC
TGACACAGGGAGGTAGTGACAATAAATAACAATGCCGGGCCTTCTTAGGTCTGGCAATTGGAAT
GAGAACAATTTAAACCCCTTATCGAGTATCAATTGGAGGGCAAGTCTGGTGCCAGCAGCCGCGG
TAATTCCAGCTCCAATAGCGTATATTAAAGTTGTTGCAGTTAAAAAGCTCGTAGTTGGATTTGTG
GTGTGTCCAGTTGGCCTTTGCTCTTTGAGTGATAGTGCT-TTACTGGTCTGCCATGTTTGGGTGG
AATCTGTGTGGCATTAAGTTGTCGTGCAGGGGATGCCCATCGTTTACTGTGAAAAAATTAGAGTG
TTCAAAGCAGGCTTATGCCTCTGAATATATTAGCATGGAATAATGATATAGGACCTTGGTACTATT
TTGTTGGTTTGCGCACTGAGGTAATGATTAAGAGGGACAGTTGGGGGTATTTGTATTCCATTGTC
AGAGGTGAAATTCTTGGATTTTTGGAAGACAAACTACTGCGAAAGCATTTACCAAGGATGTTTTC
ATTAATCAAGAACGAAAGTTAGGGGATCGAAGATGATTAGATACCATCGTAGTCTTAACCATAAAC
TATGCCGACAAGGGATTGGTGGAGTTTCGTTTCGTCTCCATCAGCACCTTGTGAGAAATCATAAG
TCTTTGGGTTCCGGGGGGGAGTATGGTCGCAAGGCTGAAACTTAAAGAAATTGACGGAAGGGCAC
CACCAGGAGTGGAGCCTGCGGCTTAATTTGACTCAACACGGGAAAACTTACCAGGTCCAGACAT
AGTGAGGATTGACAGATTGAGAGCTCTTTCTTGATTCTATGGGTGGTGGTGCATGGCCGTTCTTA
GTTGGTGGAGTGATTTGTCTGGTTAATTCCGTTAACGAACGAGACCCCTGCCTGCTAAATAGCAC
GTGTAGTGTTTATCACTGCATTTGTGCTTCTTAGAGGGACGTGCGTTCTATTAGACGCAGGAAGA
TAGGGGCAATAACAGGTCTGTGATGCCCTTAGATGTTCTGGGCCGCACGCGCGCTACACTGATG
CATTCAACGAGTTCTTACCTTGGCCGAGAGGCCTGGGCAATCTTTTGAACTTGCATCGTGATAGG
GATAGATTATTGCAATTATTAATCTTGAACGAGGAATTCCTAGTAAACGCAGATCATCAATCTGCA
TTGATTACGTCCCTGCCCTTTGTACACACCGCCCGTCGCACCTACCGATTGAATGGTCCGGTGA
GGCCTCGGGATTGTGGTTAGTTTCCTTTATTGGAAGTTAGTCGCGAGAACTTGTCCAAACCTTAT
CATTTAGAGGAAGGTGAAGTCGTAACAAGGTTTCC

EF140624.1 Fragilariopsis cylindrus 18S small subunit ribosomal RNA gene, partial sequence

AGCCATGCATGTCTAAGTATAAATATTTTACTTTGAAACTGCGAACGGCTCATTATATCAGTTATA
GTTTATTTGATAGTCCCTTACTACTTGGATACCCGTAGTAATTCTAGAGCTAATACATGCGTCAAT
ACCCTTCTGGGGTAGTATTTATTAGATTGAAACCAACCCCTTCGGGGGTGATGTGGTGATTCATAA
TAAGCTTGCGGATCGCATGCCTTTGGCGGCGATGGATCATTCAAGTTTCTGCCCTATCAGCTTTG
GATGGTAGGGTATTGGCCTACCATGGCTTTAACGGGTAACGGGAAATTAGGGTTTGATTCCGGA
GAGGGAGCCTGAGAGACGGCTACCACATCCAAGGAAGGCAGCAGGCGCGTAAATTACCCAATCC
TGACACAGGGAGGTAGTGACAATAAATAACAATGCCGGGCCTTCTTAGGTCTGGCAATTGGAAT
GAGAACAATTTAAACCCCTTATCGAGTATCAATTGGAGGGCAAGTCTGGTGCCAGCAGCCGCGG
TAATTCCAGCTCCAATAGCGTATATTAAAGTTGTTGCAGTTAAAAAGCTCGTAGTTGGATTTGTG
GTGTGTCCAGTTGGCCTTTGCTCTTTGAGTGATAGTGCT-TTACTGGTCTGCCATGTTTGGGTGG
AATCTGTGTGGCATTAAGTTGTCGTGCAGGGGATGCCCATCGTTTACTGTGAAAAAATTAGAGTG
TTCAAAGCAGGCTTATGCCTCTGAATATATTAGCATGGAATAATGATATAGGACCTTGGTACTATT
TTGTTGGTTTGCGCACTGAGGTAATGATTAAGAGGGACAGTTGGGGGTATTTGTATTCCATTGTC

AGAGGTGAAATTCTTGGATTTTTGGAAGACAAACTACTGCGAAAGCATTTACCAAGGATGTTTTC
ATTAATCAAGAACGAAAGTTAGGGGATCGAAGATGATTAGATACCATCGTAGTCTTAACCATAAAC
TATGCCGACAAGGGATTGGTGGAGTTTCGTTTCGTCTCCATCAGCACCTTGTGAGAAATCATAAG
TCTTTGGGTTCCGGGGGGGAGTATGGTCGCAAGGCTGAAACTTAAAGAAATTGACGGAAGGGCAC
CACCAGGAGTGGAGCCTGCGGCTTAATTTGACTCAACACGGGAAAACTTACCAGGTCCAGACAT
AGTGAGGATTGACAGATTGAGAGCTCTTTCTTGATTCTATGGGTGGTGGTGCATGGCCGTTCTTA
GTTGGTGGAGTGATTTGTCTGGTTAATTCCGTTAACGAACGAGACCCCTGCCTGCTAAATAGCAC
GTGTAGTGTTTATCACTGCATTTGTGCTTCTTAGAGGGACGTGCGTTCTATTAGACGCAGGAAGA
TAGGGGCAATAACAGGTCTGTGATGCCCTTAGATGTTCTGGGCCGCACGCGCGCTACACTGATG
CATTCAACGAGTTCTTACCTTGGCCGAGAGGCCTGGGCAATCTTTTGAACTTGCATCGTGATAGG
GATAGATTATTGCAATTATTAATCTTGAACGAGGAATTCCTAGTAAACGCAGATCATCAATCTGCA
TTGATTACGTCCCTGCCCTTTGTACACACCGCCCGTCGCACCTACCGATTGAATGGTCCGGTGA
GGCCTCGGGATTGTGGTTAGTTTCCTTTATTGGAAGTTAGTCGCGAGAACTTGTCCAAACCTTAT
CATTTAGAGGAAGGTGAAGTCGTAACAAGGTTTCCGTGGTGAACCTGCAG-

EF140623.1 Fragilariopsis curta 18S small subunit ribosomal RNA gene, partial sequence
AGCCATGCATGTCTAAGTATAAATATTTTACTTTGAAACTGCGAACGGCTCATTATATCAGTTATA
GTTTATTTGATAGTCCCTTACTACTTGGATACCCGTAGTAATTCTAGAGCTAATACATGCGTCAAT
ACCCTTCTGGGGTAGTATTTATTAGATTGAAACCAACCCCTTCGGGGTGATGTGGTGATTCATAA
TAAGCTTGCGGATCGCATGCCTTTGGCGGCGATGGATCATTCAAGTTTCTGCCCTATCAGCTTTG
GATGGTAGGGTATTGGCCTACCATGGCTTTAACGGGTAACGGGAAATTAGGGTTTGATTCCGGA
GAGGGAGCCTGAGAGACGGCTACCACATCCAAGGAAGGCAGCAGGCGCGTAAATTACCCAATCC
TGACACAGGGAGGTAGTGACAATAAATAACAATGCCGGGCCTTCTTAGGTCTGGCAATTGGAAT
GAGAACAATTTAAACCCCTTATCGAGTATCAATTGGAGGGCAAGTCTGGTGCCAGCAGCCGCGG
TAATTCCAGCTCCAATAGCGTATATTAAAGTTGTTGCAGTTAAAAAGCTCGTAGTTGGATTTGTG
GTGTGTCCAGTCGGCCTTTGCTCTTTGAGTGATAGTGCTGTTACTGGTCTGCCATGTTTGGGTG
GAATCTGTGTGGCATTAAGTTGTCGTGCAGGGGATGCCCATCGTTTACTGTGAAAAAATTAGAGT
GTTCAAAGCAGGCTTATGCCTCTGAATATATTAGCATGGAATAATGATATAGGACCTTGGTACTA
TTTTGTTGGTTTGCGCACTGAGGTAATGATTAAGAGGGACAGTTGGGGGTATTTGTATTCCATTG
TCAGAGGTGAAATTCTTGGATTTTTGGAAGACAAACTACTGCGAAAGCATTTACCAAGGATGTTT
TCATTAATCAAGAACGAAAGTTAGGGGATCGAAGATGATTAGATACCATCGTAGTCTTAACCATAA
ACTATGCCGACAAGGGATTGGCGGAGTTTCGTTTCGTCTCCGTCAGCACCTTGTGAGAAATCATA
AGTCTTTGGGTTCCGGGGGGGAGTATGGTCGCAAGGCTGAA-CTTAAAGAAATTGACGGAAGGGC
ACCACCAGGAGTGGAGCCTGCGGCTTAATTTGACTCAACACGGGAAA-CTTACCAGGTCCAGACA
TAGTGAGGATTGACAGATTGAGAGCTCTTTCTTGATTCTATGGGTGGTGGTGCATGGCCGTTCTT
AGTTGGTGGAGTGATTTGTCTGGTTAATTCCGTTAACGAACGAGACCCCTGCCTGCTAAATAGCA
CGTGTAGTGTTTATCACTGCATTTGTGCTTCTTAGAGGGACGTGCGTTCTATTAGACGCAGGAAG
ATAGGGGCAATAACAGGTCTGTGATGCCCTTAGATGTTCTGGGCCGCACGCGCGCTACACTGAT
GCATTCAACGAGTTCTTACCTTGGCCGAGAGGCCTGGGCAATCTTTTGAACTTGCATCGTGATAG
GGATAGATTATTGCAATTATTAATCTTGAACGAGGAATTCCTAGTAAACGCAGATCATCAATCTGC
ATTGATTACGTCCCTGCCCTTTGTACACACCGCCCGTCGCACCTACCGATTGAATGGTCCGGTGA
AGCCTCGGGATTGTGGTTAGTTTCCTTTATTGGAAGTTAGTCGCGAGAACTTGTCTAAACCTTAT
CATTTAGAGGAAGGTGAAGTCGTAACAAGGTTTCCGTAGGTGAACCTGCAG

AY672802.1 Fragilariopsis cylindrus small subunit ribosomal RNA gene, partial sequence
AGCCATGCATGTCTAAGTATAAATATTTTACTTTGAAACTGCGAACGGCTCATTATATCAGTTATA

GTTTATTTGATAGTCCCTTACTACTTGGATACCCGTAGTAATTCTAGAGCTAATACATGCGTCAAT
ACCCTTCTGGGGTAGTATTTATTAGATTGAAACCAACCCCTTCGGGGTGATGTGGTGATTCATAA
TAAGCTTGCGGATCGCATGCCTTTGGCGGCGATGGATCATTCAAGTTTCTGCCCTATCAGCTTTG
GATGGTAGGGTATTGGCCTACCATGGCTTTAACGGGTAACGGGAAATTAGGGTTTGATTCCGGA
GAGGGAGCCTGAGAGACGGCTACCACATCCAAGGAAGGCAGCAGGCGCGTAAATTACCCAATCC
TGACACAGGGAGGTAGTGACAATAAATAACAATGCCGGGCCTTCTTAGGTCTGGCAATTGGAAT
GAGAACAATTTAAACCCCTTATCGAGTATCAATTGGAGGGCAAGTCTGGTGCCAGCAGCCGCGG
TAATTCCAGCTCCAATAGCGTATATTAAAGTTGTTGCAGTTAAAAAGCTCGTAGTTGGATTTGTG
GTGTGTCCAGTTGGCCTTTGCTCTTTGAGTGATAGTGCT-TTACTGGTCTGCCATGTTTGGGTGG
AATCTGTGTGGCATTAAGTTGTCGTGCAGGGGATGCCCATCGTTTACTGTGAAAAAATTAGAGTG
TTCAAAGCAGGCTTATGCCTCTGAATATATTAGCATGGAATAATGATATAGGACCTTGGTACTATT
TTGTTGGTTTGCGCACTGAGGTAATGATTAAGAGGGACAGTTGGGGGTATTTGTATTCCATTGTC
AGAGGTGAAATTCTTGGATTTTTGGAAGACAAACTACTGCGAAAGCATTTACCAAGGATGTTTTC
ATTAATCAAGAACGAAAGTTAGGGGATCGAAGATGATTAGATACCATCGTAGTCTTAACCATAAAC
TATGCCGACAAGGGATTGGTGGAGTTTCGTTTCGTCTCCATCAGCACCTTGTGAGAAATCATAAG
TCTTTGGGTTCCGGGGGGAGTATGGTCGCAAGGCTGAAACTTAAAGAAATTGACGGAAGGGCAC
CACCAGGAGTGGAGCCTGCGGCTTAATTTGACTCAACACGGGAAAACTTACCAGGTCCAGACAT
AGTGAGGATTGACAGATTGAGAGCTCTTTCTTGATTCTATGGGTGGTGGTGCATGGCCGTTCTTA
GTTGGTGGAGTGATTTGTCTGGTTAATTCCGTTAACGAACGAGACCCCTGCCTGCTAAATAGCAC
GTGTAGTGTTTATCACTGCATTTGTGCTTCTTAGAGGGACGTGCGTTCTATTAGACGCAGGAAGA
TAGGGGCAATAACAGGTCTGTGATGCCCTTAGATGTTCTGGGCCGCACGCGCGCTACACTGATG
CATTCAACGAGTTTTTACCTTGGCCGAGAGGCCTGGGCAATCTTTTGAACTTGCATCGTGATAGG
GATAGATTATTGCAATTATTAATCTTGAACGAGGAATTCCTAGTAAACGCAGATCATCAATCTGCA
TTGATTACGTCCCTGCCCTTTGTACACACCGCCCGTCGCACCTACCGATTGAATGGTCCGGTGA
GGCCTCGGGATTGTGGTTAGTTTCCTTTATTGGAAGTTAGTCGCGAGAACTTGTCCAAACCTTAT
CATTTAGAGGAAGGTGAAGTCGTAACAAGGTTT

Chapter B

Photosynthesis-associated proteins and abbreviations

JGI ID	Protein Name	Gene
LHC		
271330	chlorophyll a/b-binding protein	LHC1
169285	chlorophyll a/b-binding protein	LHC2
206215	fucoxanthin chlorophyll a/c protein	LHC4
209305	fucoxanthin chlorophyll a/c protein	LHC5
267995	fucoxanthin chlorophyll a/c protein	LHC6
268940	fucoxanthin chlorophyll a/c protein	LHC7
269616	fucoxanthin chlorophyll a/c protein	LHC8
166511	fucoxanthin chlorophyll a/c protein	LHC9
LHCF		
193422	Lhcf type I	LHCF T1
267324	chlorophyll a/b-binding protein	LHCF1
170453	chlorophyll a/b-binding protein	LHCF3
271208	chlorophyll a/b-binding protein	LHCF4
170761	Chloroa_b-bind-domain-containing protein	LHCF5
267329	fucoxanthin chlorophyll a/c binding protein	LHCF6

271435	chlorophyll a/b-binding protein	LHCF8
271557	fucoxanthin chlorophyll a/c protein	LHCF9
271561	fucoxanthin chlorophyll a/c protein, lhcf type	LHCF10
205888	chlorophyll a/b-binding protein	LHCF11
271931	fucoxanthin chlorophyl a/c protein	LHCF12
267837	fucoxanthin chlorophyl a/c protein	LHCF14
174589	fucoxanthin chlorophyll a/c protein	LHCF15
269868	fucoxanthin-chlorophyll a-c binding protein	LHCF16
267702	fucoxanthin-chlorophyll a-c binding protein	LHCF17
268624	fucoxanthin-chlorophyll a-c binding protein	LHCF18
268626	fucoxanthin chlorophyll a/c protein	LHCF19
269543	fucoxanthin chlorophyll a/c protein	LHCF20
269567	fucoxanthin-chlorophyll a-c binding protein	LHCF21
273255	fucoxanthin chlorophyll a/c protein	LHCF22
143190	fucoxanthin chlorophyll a/c protein, partial	LHCF23
LHCR		
273003	fucoxanthin chl a/c protein	LHCR4
270606	fucoxanthin chlorophyll a/c protein	LHCR5
209926	chlorophyll a/b-binding protein	LHCR6
274939	fucoxanthin chlorophyll a/c protein	LHCR8
261294	chlorophyll a/b-binding protein	LHCR10
269925	fucoxanthin chlorophyll a/c protein	LHCR11
269918	fucoxanthin chlorophyll a/c protein (BLASt - 99.8 - fcy) LHCR 12	LHCR12
208340	fucoxanthin chlorophyll a/c protein	LHCR13
260998	fucoxanthin chlorophyll a/c protein	LHCR14
LHCx		
218498	fucoxanthin chlorophyll a/c binding protein	LHCx2
209887	chlorophyll a/b-binding protein	LHCx3
271962	fucoxanthin chlorophyll a/c binding protein	LHCx5
188478	Chloroa_b-bind-domain-containing protein	LHCx6
267951	fucoxanthin chlorophyll a/c binding protein	LHCx7
244998	Chloroa_b-bind-domain-containing protein	LHCx8

Other		
205285	chloroplast ferredoxin dependent NADH oxireductase	FNR1
275587	chloroplast ferredoxin dependent NADH oxireductase	FNR3
193119	ferredoxin NADP reductase	FNR*
271986	ferredoxin reductase-like protein	FNR**
141473	ferredoxin reductase-like protein, partial	FNR***
143628	Flavodoxin, partial	FLD
167955	oxygen-evolving enhancer protein 1 precursor	OEE1
272258	plastocyanin	PC-1
271949	precursor cytochrome c6	PET
272228	rieske iron-sulfur protein of cytochrome B6/F complex	PET*
211201	chlorophyll a/b-binding protein	Fc17531
223513	chlorophyll a/b-binding protein	LHC *
268240	ATP synthase F1 gamma	ATP F1
210953	ATP synthase subunit A	ATP subA
268077	photosystem II 12 kDa extrinsic protein, chloroplastic	PSII-U
272316	extrinsic protein in photosystem II	PSII *
259589	photosystem II stability/assembly factor	PSII **

Chapter C

Publications and contributions

New Phytologist

Research

Dark metabolism: a molecular insight into how the Antarctic sea-ice diatom *Fragilariopsis cylindrus* survives long-term darkness

Fraser Kennedy[1], Andrew Martin[1], John P. Bowman[2], Richard Wilson[3] and Andrew McMinn[1]

[1]Institute for Marine and Antarctic Studies, University of Tasmania, Hobart, 7000 Tasmania, Australia; [2]Centre for Food Safety and Innovation, Tasmanian Institute of Agriculture, Hobart, 7000 Tasmania, Australia; [3]Central Science Laboratory, University of Tasmania, Hobart, 7000 Tasmania, Australia

Author for correspondence:
Fraser Kennedy
Tel: +3 6226 6379
Email: f.c.kennedy@utas.edu.au

Received: *14 February 2019*
Accepted: *2 April 2019*

New Phytologist (2019)
doi: 10.1111/nph.15843

Key words: Antarctic, dark survival, *Fragilariopsis cylindrus*, metabolism, proteomics, sea-ice algae.

Summary

- Light underneath Antarctic sea-ice is below detectable limits for up to 4 months of the year. The ability of Antarctic sea-ice diatoms to survive this prolonged darkness relies on their metabolic capability. This study is the first to examine the proteome of a prominent sea-ice diatom in response to extended darkness, focusing on the protein-level mechanisms of dark survival.
- The Antarctic diatom *Fragilariopsis cylindrus* was grown under continuous light or darkness for 120 d. The whole cell proteome was quantitatively analysed by nano-LC–MS/MS to investigate metabolic changes that occur during sustained darkness and during recovery under illumination.
- Enzymes of metabolic pathways, particularly those involved in respiratory processes, tricarboxylic acid cycle, glycolysis, the Entner–Doudoroff pathway, the urea cycle and the mitochondrial electron transport chain became more abundant in the dark. Within the plastid, carbon fixation halted while the upper sections of the glycolysis, gluconeogenesis and pentose phosphate pathways became less active.
- We have discovered how *F. cylindrus* utilises an ancient alternative metabolic mechanism that enables its capacity for long-term dark survival. By sustaining essential metabolic processes in the dark, *F. cylindrus* retains the functionality of the photosynthetic apparatus, ensuring rapid recovery upon re-illumination.

Introduction

Primary production within Antarctic sea-ice is spatially and temporally variable, largely due to strong physiochemical gradients within the ice and seasonal variation in solar irradiance. The light required for photosynthesis is the single most influential driver of ice-associated microbial communities (Peters & Thomas, 1996; Arrigo, 2014), however ice typically attenuates surface irradiance from *c.* 1500 to *c.* 5 μmol photon^{-1} m^{-2} s^{-1} during the summer months (McMinn *et al.*, 2010a,b). Ecological success of phototrophs relies on metabolic plasticity with respect to the pigment-protein complexes of the photosynthetic apparatus. Ice-associated algae must minimise damage from excess light or increase photon capture in low light by modifying the specific ratio of these complex types.

The light-harvesting antenna in diatoms is large and, although it shares a high homology with the light-harvesting complexes of higher plants and green algae, it differs with respect to pigment composition and excitation absorption properties (Wilhelm *et al.*, 2014; Ishihara *et al.*, 2015; Taddei *et al.*, 2016; Giovagnetti & Ruban, 2017). It is comprised largely of the pigments chlorophyll *a* (Chl*a*) Chl*c*, and fucoxanthin, which are bound to fucoxanthin Chl*a*/*c*-binding proteins (FCPs). The addition of fucoxanthin allows diatoms to absorb more of the electromagnetic spectrum, particularly the blue-green wavelengths that dominate aquatic environments (Bertrand, 2010) Diatom genomes encode three variations of FCP, each with its own evolutionary origin and differing with respect to functionality and thylakoid interaction (Büchel, 2003; Lepetit *et al.*, 2012; Nymark *et al.*, 2013; Ishihara *et al.*, 2015). The three clades of FCP are LHCF (those associated with all Chl*c*-containing algae that fulfils the primary role in light harvesting), LHCR (those of distinct red-algal origin, tightly associated with the photosystem I (PSI) antenna) and LHCx (those related to the ancient Li818 light inducible proteins of green algae that are mainly ultilised during stress (Gundermann *et al.*, 2013; Wilhelm *et al.*, 2014)). Variation in the type of FCP accompanying the photosystem is biologically relevant because irradiance directly influences clade expression (Lepetit *et al.*, 2010; Wilhelm *et al.*, 2014). Collectively, the FCPs have led to the success of diatoms in ecosystems characterised by variable irradiance, especially low-light conditions (Nagao *et al.*, 2013; Kuczynska *et al.*, 2015; Morgan-Kiss *et al.*, 2016).

With the onset of the polar winter, light drops to below detectable limits for up to 4 months (Palmisano & Sullivan, 1983; Peters & Thomas, 1996; McMinn & Martin, 2013). To

retain viability, polar phototrophs use strategies that modify physiology and metabolic output to maintain DNA integrity. Some taxa form cysts or resting stages, while others are facultatively heterotrophic and/or survive on stored energy reserves. Cyst and spore formation is relatively common in the Arctic, but does not appear to be a mainstream strategy among Antarctic taxa (Taylor & McMinn, 2002; McMinn & Martin, 2013). Heterotrophic uptake of organic substrates has been previously reported as a potential mechanism to supplement energy requirements (Palmisano & Sullivan, 1983; Rivkin & Putt, 1987; Laybourn-Parry *et al.*, 2005), however the energy obtained is unlikely to be sufficient to enable long-term dark survival. Studies have also shown that the uptake and metabolism of exogenous supplied organic substrates is irregular or ineffective (Bunt & Lee, 1972; Horner & Alexander, 1972). Sea-ice diatoms may exploit currently unknown metabolic pathways that sustain essential metabolic processes and the components required to maintain viability. The ability to rapidly regulate metabolic output in response to any given light regime would confer a competitive advantage and ensure rapid recovery of the photosynthetic machinery upon re-illumination. Maintenance metabolism may help to explain why many sea-ice diatoms are able to rapidly resume photosynthesis and grow rapidly after extended darkness (Peters & Thomas, 1996; Wulff *et al.*, 2008; McMinn *et al.*, 2010a,b; Reeves *et al.*, 2011; Nymark *et al.*, 2013). Despite studies indicating strong downregulation of photophysiological processes during prolonged darkness (Peters, 1996; Peters & Thomas, 1996; Popels *et al.*, 2007; Wulff *et al.*, 2008; Reeves *et al.*, 2011; Martin *et al.*, 2012), a certain level of functionality and structural arrangement must be retained in the dark. This situation infers that cells are actively maintaining some degree of photosynthetic capacity and sustaining constituents of the photosynthetic apparatus in the dark. The question remains how cells are able to sustain metabolism in the absence of a primary energy source. It is widely known that diatoms are able to use stored energy reserves in the form of lipids and carbohydrates during periods of low cellular energetics (Bunt & Lee, 1972; Smayda & Mitchell-Innes, 1974; Antia, 1976; Peters & Thomas, 1996; Zhang *et al.* 1995; Raven and Beardall 2011; Martin *et al.*, 2012; Mock *et al.*, 2017) and that the rate of consumption is low. Cells might also switch to alternative unconventional metabolic pathways, or amplify the regulatory flexibility of existing pathways to enhance metabolic possibilities (Allen *et al.*, 2011). For example, some marine algae use alternative electron donors and utilise fermentative metabolism under dark anoxic conditions (Fernie *et al.*, 2004; Catalanotti *et al.*, 2013; Kamp *et al.*, 2013, 2015; Yang *et al.*, 2015). Considering the complex genomic origins of sea-ice diatoms in which alternative metabolic routes may have been acquired by the procurement of genes via horizontal gene transfer, endosymbiosis and duplication events, adjustment of metabolism via alternative routes is possible (Sims *et al.*, 2006; Tirichine & Bowler, 2011; Medlin, 2016). Evidence of diatoms acquiring genes from various sources is illustrated in the functional differentiation of genes encoding isozymes of conserved metabolic functions (Falciatore & Bowler, 2002; Bowler *et al.*, 2008; Smith *et al.*, 2012; Mock *et al.*, 2017). Smith *et al.* (2012), showed that 31% of the genes in diatoms are unique to that particular species, an observation attributed to the complex evolutionary adjustments of the genome. Some species have retargeted select nuclear encoded genes to discrete organelles, resulting in isozymes that target multiple subcellular locations (Kroth *et al.*, 2008; Smith *et al.*, 2012). For example, diatoms have approximately twice as many enzymes involved in glycolysis than green algae. A high number of isozymes can amplify regulatory flexibility and enhance the functional possibilities of metabolic processes.

The psychrophilic pennate diatom *Fragilariopsis cylindrus* is prominently ice-associated and, as a result, has evolved specialised survival mechanisms. Therefore, it is a useful indicator species for investigations into adaptation and acclimation to the polar sea-ice habitat (Mock *et al.*, 2017). Several studies have described the effect of darkness on the survivability of Antarctic phytoplankton and sea-ice algae (Bunt & Lee, 1972; Palmisano & Sullivan, 1983; Peters & Thomas, 1996; Baldisserotto *et al.*, 2005; Reeves *et al.*, 2011), but most research has focused on physiological adaptation rather than the biochemical and molecular drivers behind dark-induced metabolism. Recent advances in functional genomics has made it possible to examine the molecular processes enabling dark survival (Nymark *et al.*, 2013; Bai *et al.*, 2016; Mock *et al.*, 2017). In this study we aim to gain a comprehensive insight into how *F. cylindrus* can survive extended periods of darkness by examining the expression profile of the proteome. Although proteomics is still some way removed from real proof of physiological function, it does provide a unique profile of metabolic function and our results provide the first insight into the molecular basis for long-term dark survival.

Materials and Methods

Algal culture

A monoculture of *F. cylindrus* was isolated from Antarctic pack ice in 2015 (Davis station, East Antarctica). This culture was taxonomically identified using the descriptions found in Scott & Marchant (2005) and confirmed by 18S rRNA sequencing (Supporting Information Notes S1). The culture was maintained in exponential growth phase in L_1 media (Guillard & Hargraves, 1993) under cool white fluorescent light (50 µmol photon m^{-2} s^{-1}, 12 h : 12 h, light : cycle) at 2°C ± 1°C in a batch system and bubbled with filtered air. Cultures were then divided into six Erlenmeyer flasks (and amended with double-concentrated L_1 medium; Table S1). Flasks were divided into two treatments: continuous light (50 µmol photon^{-1} m^{-2} s^{-1}), $n = 3$ and continuous dark, $n = 3$. Cells were kept in their respective treatment for 120 d, with subsampling on days 0, 0.5 (12 h), 1, 3, 7, 21, 30, 60, 120. Following 120 d, dark cells were re-exposed to 50 µmol photon^{-1} m^{-2} s^{-1} of white light for 24 h to examine cell recovery.

DNA extraction

DNA was extracted using the boiling method developed by Liu *et al.*, 2014. Firstly, the sample was heated to 95°C for 10 min in

sterile 10 mM Tris pH 8.1 using 0.5 cm^2 of *F. cylindrus* embedded on filter. Filter material was vortexed 1 min to free the maximum number of cells from the filter. After heating, the extract was cooled on ice and spun for 1 min in a microfuge. The polymerase chain reaction (PCR) was set up using MyTaq enzyme (Bioline Australia), 1 µl of template DNA, 1 µM of each primer (18S rRNA) Euk 4F 5′-CTGGTTGATCCTGCCAG-3′ and Euk 516R 5′-ACCAGACTTGCCCTCC-3′.

The thermocycling conditions used were initial denaturation at 98°C for 30 s and 32 cycles of: 95°C for 30 s, 59°C for 30 s, and 72°C for 45 s, followed by a final extension of 10 min at 72°C. The thermocycler model used was a Peltier PTC200.

Sequencing used the ABI BigDye cycle terminator kit 3.1 and an ABI 3730 xl automated sequencer (carried out at Macrogen, Seoul, South Korea). Sequences were manually checked, ambiguous nucleotide positions near the primer regions were removed, and sequence was compared with the National Center for Biotechnology Information (NCBI) database with closest sequences downloaded (SI 1).

Proteomic sample preparation, lysis and digestion

Subsamples (100 ml) were withdrawn from each replicate and centrifuged at 10 000 ***g*** for 2 min at 2°C. The supernatant was then removed, and the resulting pellets were placed in 1 ml centrifuge tubes and spun again at 2°C for 1 min at 10 000 ***g***. The supernatant was discarded, and the resulting pellets were washed with 1 ml of ice-cold phosphate-buffered saline (pH 7.3) and spun at 2°C for 10 min. This step was repeated twice. The pellets were finally plunged into liquid nitrogen and stored at −80°C for *c.* 1 month before analysis.

The algal cell extracts were thawed on ice followed by the addition of 500 µl of ice-cold high-pressure liquid chromatography (HPLC) grade water. Extracts were then sonicated on ice for 2 min in a 100 W, 20 kHz sonicator with a titanium microtip, then plunged into liquid nitrogen. The extracts were then thawed on ice before 0.1 g of combusted quartz glass beads were added. Sample were crushed for 2 min at 2°C, and then plunged into liquid nitrogen. This step was repeated twice. Nonlysed cells and debris were subsequently collected by centrifugation at 15 000 ***g*** for 30 min at 2°C. The resulting whole cell lysates were removed and spun again at 15 000 ***g*** for 15 min to isolate any insoluble components. The supernatant was aspirated, and protein concentrations were calculated using a Pierce Coomassie Protein Assay Kit (ThermoFisher Scientific, Melbourne, Australia). Samples were normalised by taking approximately equal amounts of protein (100 µg) for each trypsin digest and analysing the same amount of each digest by LC/MS. Any remaining variation in overall signal was compensated for by the normalisation of peptide intensities across samples.

Protein solutions were added to −20°C absolute ethanol at a ratio of 1 : 9, mixed and kept at −20°C for 60 min. Samples were then centrifuged at 18 000 ***g*** for 10 min to concentrate precipitated protein. The supernatant was removed, and the resulting pellets washed with −20°C absolute ethanol. This step was then repeated. Samples were spun again at 18 000 ***g*** for 10 min; the supernatant was aspirated and the remaining pellet was left to air dry to remove any ethanol residue.

Protein samples were digested with trypsin using standard procedures (Wilson *et al.*, 2010) and analysed by nanoLC-MS/MS using an LTQ-Orbitrap XL and Ultimate 3000 nanoHPLC system (ThermoFisher Scientific, Waltham, MA, USA). Tryptic peptides (*c.* 1 µg) were loaded onto a 20 mm × 75 mm PepMap 100 trapping column (3 mm C_{18}) at 5 ml min^{-1}, using 98% water, 2% acetonitrile and 0.05% TFA. Peptides were separated at 0.3 ml min^{-1} on a 250 mm × 75 mm PepMap 100 RSLC column (2 mm C_{18}) at 40°C from 97% mobile phase A (0.1% formic acid in water) to 50% mobile phase B (0.08% formic acid in 80% acetonitrile and 20% water) by elution with 3–10% B over 10 min, 10–40% B over 120 min, 40–50% B over 10 min, holding at 95% B for 10 min then re-equilibration in 3% B for 15 min. Solid phase peptide extracts were injected once and dissolved phase extracts were injected twice to achieve equivalent analysis time. The LTQ-Orbitrap was controlled using XCALIBUR 2.1 software in data-dependent mode as described in Wilson *et al.* (2016).

MS/MS spectra were searched against the *F. cylindrus* database (Joint Genome Institute, *F. cylindrus* CCMP 1102; https://genome.jgi.doe.gov/Fracy1/Fracy1.home.html) using the Andromeda search engine in MAXQUANT, v.1.5.1.2 (http://maxquant.org/). Default settings for protein identification by LTQ-Orbitrap MS/MS and label-free quantitation (LFQ) included a maximum of two missed cleavages, mass error tolerances of 20 ppm then 4.5 ppm for initial and main peptide searches, respectively; 0.5 Da tolerance for fragment ions, variable methionine oxidation and fixed cysteine carbamidomethylation. The false discovery rate (FDR) for both peptide-spectrum matching and protein identification was set to 0.01. MaxQuant peptides.txt and proteinGroups.txt output files are provided (Tables S2, S3, respectively). Proteins only identified by site, reverse sequences, contaminants and proteins identified on the basis of a single matching peptide were excluded. Peptide LFQ values, normalised according to the MaxLFQ algorithm using a minimum peptide ratio count of two (Cox *et al.*, 2014), were first $\log_2$-transformed and proteins identified in fewer than two biological replicates and five time points were excluded. After imputation of remaining missing values with random intensity values for low-abundance proteins, mean LFQ values (dark vs light) were compared using a moderated *t*-test. Protein abundance changes are expressed throughout on a $\log_2$ scale, in which positive values represent increased abundance in dark-induced cells, and negative values indicate reduced abundance. Proteins with an FDR of < 2% and mean $\log_2$ LFQ differences >/< 0.5 (*c.* 1.5-fold on the linear scale) were considered to be significant.

The mass spectrometry proteomics data were deposited to the ProteomeXchange Consortium via the PRIDE (Vizcaíno *et al.*, 2016) partner repository with the dataset identifier PXD007098.

Pulse-amplitude-modulated fluorometry (PAM)

Chl*a* fluorescence was measured using a pulse-amplitude-modulated fluorometer (Water-PAM, Walz, Effeltrich, Germany)

and the method described in Kennedy *et al.* (2012). Measurements were taken on days 0, 0.5, 1, 3, 7, 14, 21, 30, 60, 90 and 120 and recovery was assessed at 1, 2, 4, 8 and 24 h.

Nonphotochemical fluorescence quenching (NPQ) was calculated using the Stern–Volmer quenching parameter described in Kramer *et al.* (2004).

Adenosine 5′-triphosphate (ATP)

Determination of ATP concentration in cell extracts was performed through the bioluminescence of ATP with recombinant firefly luciferase and D-luciferin (Molecular Probes, ThermoFisher Scientific) as per the manufacturer's instructions. Luminescence of samples and standards was read on a microplate reader (BMG FLUOstar Optima, BMG Labtech, Melbourne, Australia). Standard curves were conducted with each assay and the concentration of cellular ATP was normalised to cell concentration.

Chlorophyll *a* analysis

Chl*a* concentration was determined in triplicate using the acidification protocol as described by Evans *et al.* (1987). Briefly, 20 ml subsamples were filtered onto 25 mm GF/F filters and extracted in 10 ml of methanol in the dark at 4°C for 12 h. Chl*a* extracts were subsequently measured on a Turner fluorometer (10AU Turner Designs, San Jose, CA, USA).

Results

One of two treatments were assigned to cultures of *Fragilariopsis cylindrus*, either continuous light or continuous dark. Cells were kept in these respective treatments for 120 d, with subsampling on days 0, 0.5 (12 h), 1, 3, 7, 21, 30, 60 and 120. After 120 d, dark cells were re-exposed to white light for 24 h to examine cell recovery. The proteomic profiles of dark cells were compared with those in constant light, this comparison revealed two key functional differences: first, widespread downregulation of proteins associated with photosynthesis and carbon fixation; and second, upregulation of respiratory processes of glycolysis, the Entner–Doudoroff pathway and the tricarboxylic acid cycle.

Cell numbers and chlorophyll concentration

Cell concentration decreased in both treatments up to day 21, when stabilisation in cell numbers was observed (Fig. 1a). Numbers of cells in the constant light increased from day 30, which may indicate a degree of active growth. While proteomic samples were normalised for any changes in biomass, some minor variations in protein expressions may be present.

Following 3 d of darkness, Chl*a* concentration declined from a mean of 18.63 $\mu g\,l^{-1}$ down to 12.74 $\mu g\,l^{-1}$ (Fig. 1b). This concentration increased to 17.34 $\mu g\,l^{-1}$ on day 7 and remained relatively unchanged until day 60. After which, Chl*a* decreased from 17.58 $\mu g\,l^{-1}$ to 14.72 $\mu g\,l^{-1}$ by day 120 of darkness. Chl*a* concentration did not differ significantly between light and dark for the first 21 d, after which Chl*a* concentration in the light increased from 19.03 $\mu g\,l^{-1}$ on day 21 to 28.71 $\mu g\,l^{-1}$ on day 60. Re-exposure of dark-treated cells to light failed to alter the Chl*a* concentration.

Light harvesting and the photosynthetic pathway

Proteins from the three-major light-harvesting complex (LHC) clades (LHCF, LHCR and LHCx) were mostly downregulated within the initial 12 h of darkness (Fig. 2). Following this, there was limited change in the expression of these proteins in the dark when compared with the light during the first 21 d. After 30 d, downregulation of most LHC proteins across all clades was observed. In addition, oxygen evolving complex 1, photosystem II 12 kDa protein and Chl*a*/*b* binding protein Fc17531 were also downregulated. There was no change in the expression of ATP synthase subunits following 12 h. Widespread upregulation of light-harvesting proteins after 120 d of dark exposure compared with continuous light was observed except for those classified in the photoprotective clade (LHCx), which remained downregulated. This was also reflected in proteins involved in the photosynthetic chain: ferredoxin (log_2 +1.1-fold), flavodoxin (+1.91-fold), plastocyanin (log_2 +1.3-fold) and photosystem II 12 kDa protein (log_2 +0.5-fold). These were all highly expressed in the dark at 120 d. Re-illumination of dark cells for 24 h induced significant expression of proteins in the primary light-harvesting clades LHC and LHCF, as well as the red-algal-like LHCR clade. By contrast, proteins of the photoprotective LHCx clade were either downregulated or remained unchanged.

The maximum quantum yield (F_v/F_m) of photosystem II (PSII) was similar in both dark and light-treated cells over 120 d (Fig. 3a). In the light, F_v/F_m declined from a preincubation mean of 0.585 to a mean of 0.388 on day 120. A similar pattern was observed in the dark, F_v/F_m declined from a mean of 0.577–0.461 on day 120. The maximum electron transfer rate ($rETR_{max}$) was significantly higher ($P < 0.05$) in the light than the dark at all time points except day 14. Within 1 h of dark cells being re-illuminated, the $rETR_{max}$ and F_v/F_m rapidly increased and continued to increase until the final assessment at 24 h, when it was well above the preincubation levels.

Non-photochemical quenching (NPQ), which is important to dissipate adverse effects of high light intensities, was considerably lower in the dark (Fig. 3b). However, after an initial sharp decline, NPQ in the dark-treatment group increased from 0.14 on day 1 to 0.41 on day 120. Following re-illumination, NPQ of dark cells continued to increase with increasing light exposure. The photosynthetic parameter alpha (α) was significantly higher in the dark than the light over the course of the experiment (Fig. S1), indicating that structural breakdown between the antenna and photosystem II did not occur in the dark. Upon re-illumination of dark-treated cells with 50 $\mu mol\ m^{-2}\ s^{-1}$ of white light, α was reduced to preincubation levels.

Cellular ATP concentration decreased to undetectable levels after 21 d of dark exposure (Fig. 2c) and remained at low levels until re-illumination occurred. As ATP concentration is highly unlikely to be zero, the observed concentration may not be attributed to the cells current physiology but is more likely to be a limitation of the assay when ATP concentration is below the

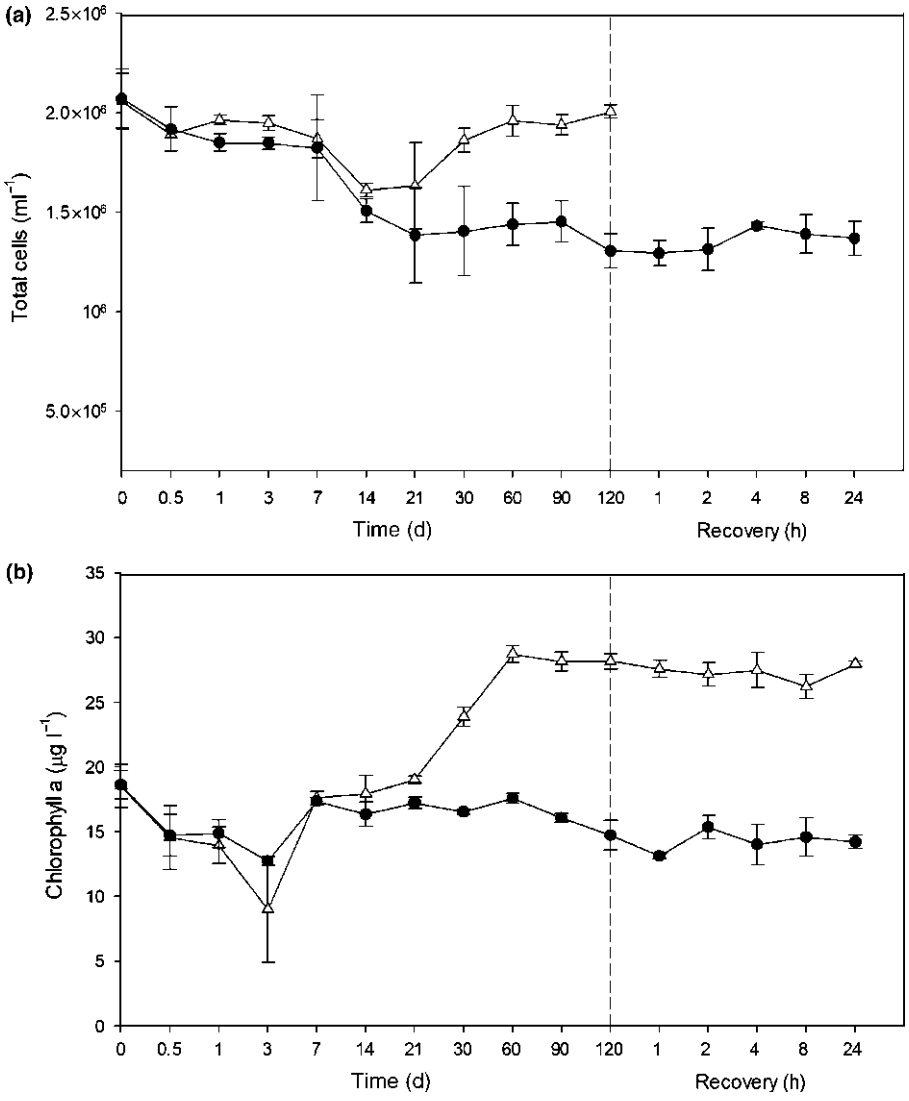

Fig. 1 (a) Growth curves of *Fragilariopsis cylindrus* (cells ml^{-1}) and (b) chlorophyll *a* concentration ($\mu g\ l^{-1}$) of dark-treated (closed circles) and light-treated (open triangles) cells. Points after the dashed line represent the re-illumination of dark-treated cells for 24 h at 50 µmol photon^{-1} m^{-2} s^{-1}. Error bars represents the standard deviation of the mean.

detection limit. Within 1 h of re-illumination, cellular ATP concentrations returned to preincubation levels. ATP in light-treated cell increased from a low of 0.018 pmol cell^{-1} after 12 h to a high of 0.080 pmol cell^{-1} after 14 d and remained at that level until day 120.

Pigments While a number of proteins of the tetrapyrrole/chlorophyll biosynthetic pathway were significantly affected in dark-treated cells, their expression changes were not coordinated. The degree of expression changes and the specific roles of components in the pathway are shown in Fig. S2. Here, 3 d of darkness resulted in the sporadic upregulation of a number of proteins in the pathway, appearing to coincide with a decline in Chl*a* concentration (Fig. 1b). Limited change in expression was observed between days 7 and 21 of dark exposure. Subsequently, four out of nine enzymes in the pathway were significantly upregulated from day 30 to 120 compared with in the light. Two proteins in the pathway remained either unchanged or downregulated throughout the entire experimental period (porphobilinogen synthase (JGI|187290) and Mg-protoporphyrin IX methyltransferase (JGI|268444)). Chl*a* increased in light-treated cells from day 30, as a result, the protein expression in this pathway may be underestimated. The exact reason for the contrasting expression of this pathway in the dark when compared with in the light remains unclear.

Proteins of the carotenoid biosynthetic pathway were not coordinately expressed in the dark when compared with in the light (Fig. S3). Phytoene desaturase (JGI|213515, JGI|270748) and ς-carotene desaturase (JGI|229199) were predominately downregulated, whereas two violaxanthin de-epoxidases, which are important in the generation of nonphotochemical quenching (also called diadinoxanthin de-epoxidase) were upregulated, but at different times.

Calvin–Benson cycle Most proteins involved in the Calvin cycle were downregulated in response to extended darkness when compared with in the light (Fig. 4). This was not surprising as the three main functional proteins involved: ribulose-1,5 bisphosphate carboxylase/oxygenase (RUBISCO, JGI|274497), fructose-1,6- bisphosphatase (FBPase, JGI|1739843, JGI|158118,

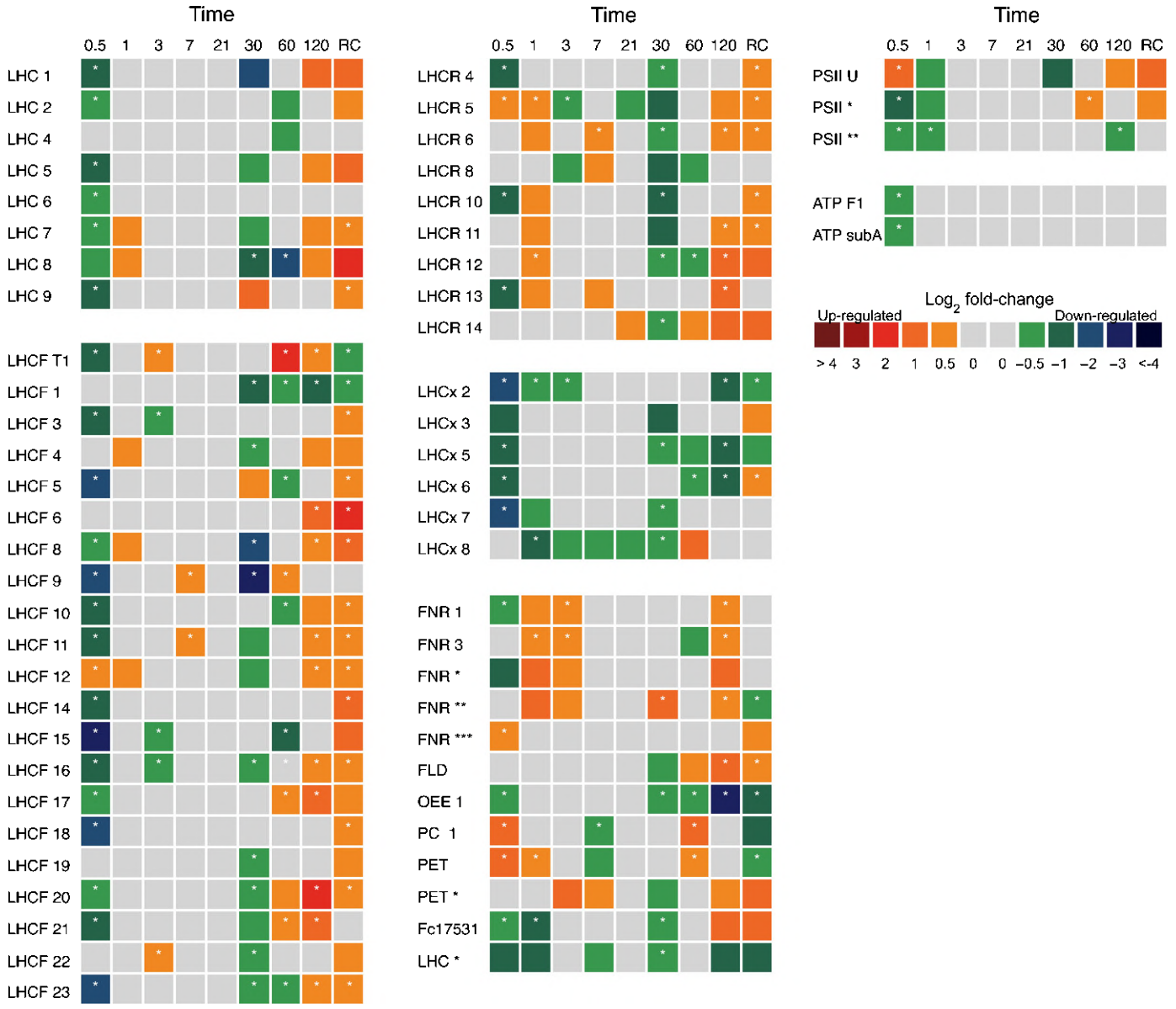

Fig. 2 Matrix of photosynthesis-associated *Fragilariopsis cylindrus* proteins in dark-treated cells when compared with continuous light. Proteins are grouped by relative function and to the corresponding clade; antenna proteins (LHCF, major light harvesting; LHCR, red-algal linage; LHCx, photoprotective; or LHC, clade unknown) or those involved in oxygenic photosynthesis. Each box represents the relative expression of the proteins indicated, after the duration of dark exposure in days, with the exception of RC, which denotes the dark recovery phase in which dark-treated cells were re-exposed to white light (50 μmol photon^{-1} m^{-2} s^{-1}) for 24 h. The colours represent the protein abundance change (difference in mean $\log_2$ LFQ values, dark vs light) the scale shown. White stars (*) inside boxes represent a significant expression (FDR < 2% and $\log_2$ LFQ difference >/< 0.5). All expressed proteins have been normalised to relative cell abundance. Abbreviations correspond to the proteins described in Supporting Information Table S4.

JGI|212570) and sedoheptulose 1,7-bisphophate (SBPase, JGI|271643) are activated by photosynthesis-associated reactions. All proteins of the Calvin cycle were observed; widespread downregulation occurred on days 7, 30, 60 and 120. Re-illumination for 24 h failed to alter the expression of most Calvin cycle proteins.

Respiratory metabolism

Glycolysis and the Entner–Doudoroff pathway Glycolysis occurs in two phases; the upper (preparatory) and lower (payoff) phases. Conventionally, the upper-phase begins in the chloroplast and completes in the cytosol. However, all chloroplast and cytosol-targeted glycolytic proteins were downregulated during prolonged darkness, particularly from day 30 (Fig. 5). After 30 d of darkness, some lower-phase glycolytic proteins, thought to be mitochondrial targeted, were upregulated (Fig. 4). This change coincided with the unexpected expression of proteins involved in the mitochondrial Entner–Doudoroff pathway (EDP; Fig. 5).

Some glycolysis proteins can also function in reverse for gluconeogenesis to form glucose from pyruvate. The use of this pathway during darkness seems unlikely as the specific enzymes of the

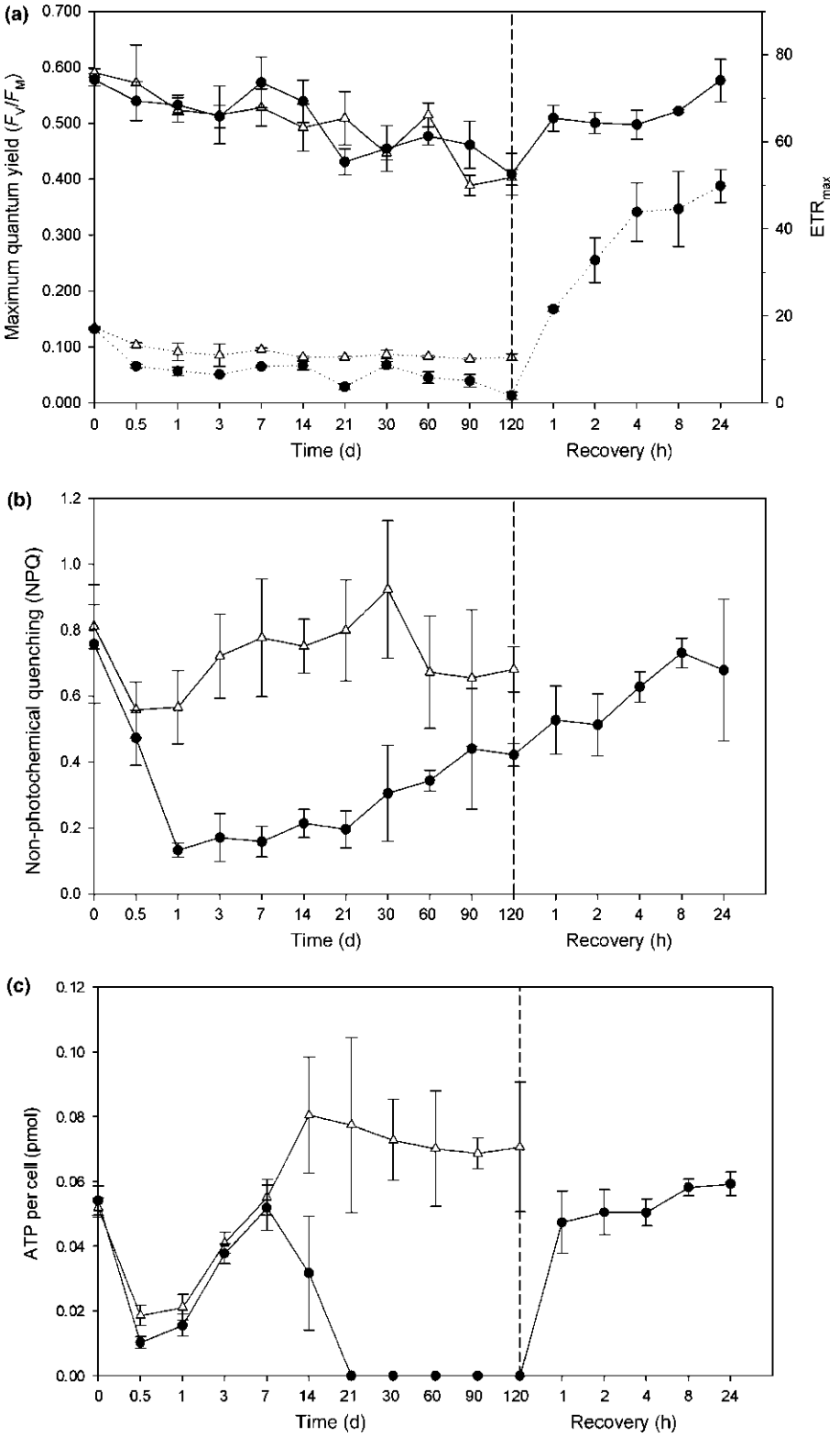

Fig. 3 (a) Maximum quantum yield (F_v/F_m) and maximum electron transfer rate (ETRmax) (dotted lines). (b) Nonphotochemical quenching (NPQ). (c) ATP concentration per cell (ρmol), of dark-treated (closed circles) and light-treated (open triangles) *Fragilariopsis cylindrus* cells. Points after the dashed line represent the re-illumination of dark-treated cells for 24 h at 50 μmol photon^{-1} m^{-2} s^{-1}. Error bars represent the standard deviation of the mean.

pathway were downregulated, specifically two pyruvate carboxylase (PEP) and three phosphoenolpyruvate carboxylase (PEPCK) isozymes.

The anabolic pentose phosphate pathway runs parallel to that of glycolysis. In response to dark exposure, the proteins involved in the pentose phosphate pathway were heavily downregulated compared with in the light (Fig. 5).

Tricarboxylic acid cycle (TCA), pyruvate and mitochondrial electron transport chain The TCA cycle is located in the

Step	JGI ID	Description	Time								
			0.5	1	3	7	21	30	60	120	RC
1	274497	Ribulose-1,5-bisphosphate carboxylase/oxygenase	*			*					
2	209502	Phosphoglycerate kinase	*								*
2	171765	Phosphoglycerate kinase	*			*		*	*	*	
3	173478	Glyceraldehyde 3-phosphate dehydrogenase (precursor)	*			*			*	*	
3	270428	Glyceraldehyde 3-phosphate dehydrogenase (precursor)	*					*	*	*	
3	269867	Glyceraldehyde 3-phosphate dehydrogenase				*		*	*	*	*
4	272546	Fructose 1,6-bisphosphate aldolase (precursor)									
4	270038	Fructose 1,6-bisphosphate aldolase (precursor)				*		*	*	*	
4	173934	Fructose 1,6-bisphosphate aldolase				*				*	
5	173983	Fructose 1,6-bisphosphatase	*						*	*	
5	158118	Fructose 1,6-bisphosphatase				*					
5	212570	Fructose 1,6-bisphosphatase	*					*	*	*	
6	206407	Transketolase		*		*		*	*	*	
6	259678	Transketolase						*	*		
7	271743	Sedheptulose 1,7-bisphosphatase	*							*	
8	272607	Ribose-5-phosphate isomerase	*	*							
9	193653	Phosphoribokinase				*		*	*	*	
10	274452	Triose phosphate isomerase	*	*							*
10	176563	Triose phosphate isomerase	*							*	*
10	269372	Triose phosphate isomerase	*								
11	261890	Glucose 6-phosphate isomerase (putative)								*	*
12	213392	UTP-glucose 1-phosphate uridylytransferase (^)	*					*	*	*	
13	276710	Phosphoglucomutase (putative)	*	*							
13	213392	Phosphoglucomutase (^)	*					*	*	*	
14	273154	Ribulose phosphate 3-epimerase	*					*			

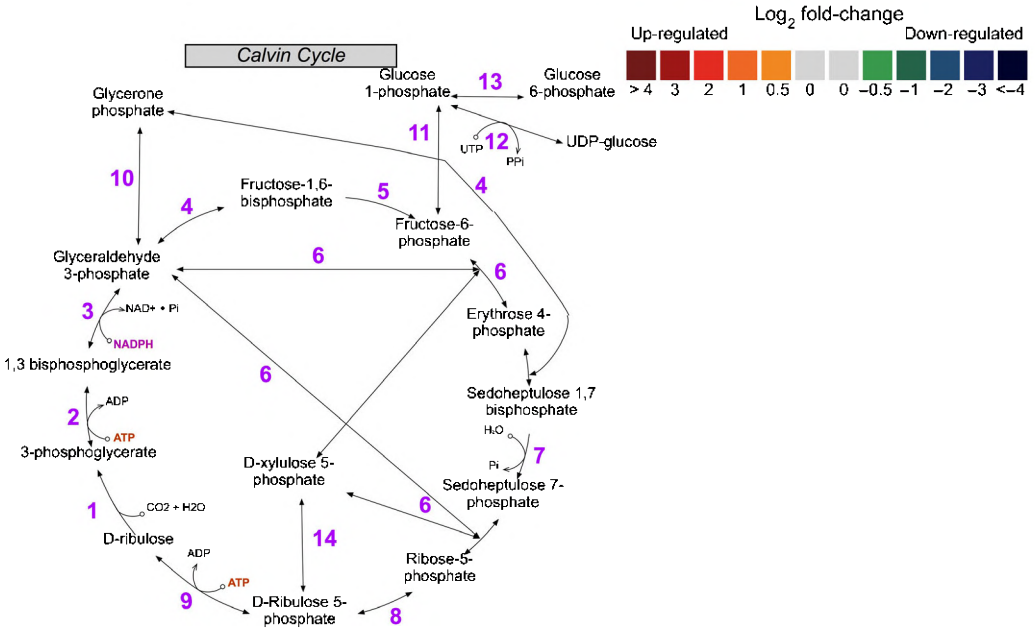

Fig. 4 Expression of *Fragilariopsis cylindrus* proteins involved in the Calvin cycle in the dark when compared with in the light. JGI ID corresponds to the Joint Genome Institute identification number of that particular protein. Each box represents the relative expression of the proteins indicated, after the duration of dark exposure in days, with the exception of RC which denotes the dark recovery phase in which dark-treated cells were re-exposed to white light (50 μmol photon^{-1} m^{-2} s^{-1}) for 24 h. The colours represent the protein abundance change (difference in mean $\log_2$ LFQ values, dark vs light) the scale shown. White stars (*) inside boxes represent a significant expression (FDR < 2% and $\log_2$ LFQ difference >/< 0.5). All expressed proteins have been normalised to relative cell abundance.

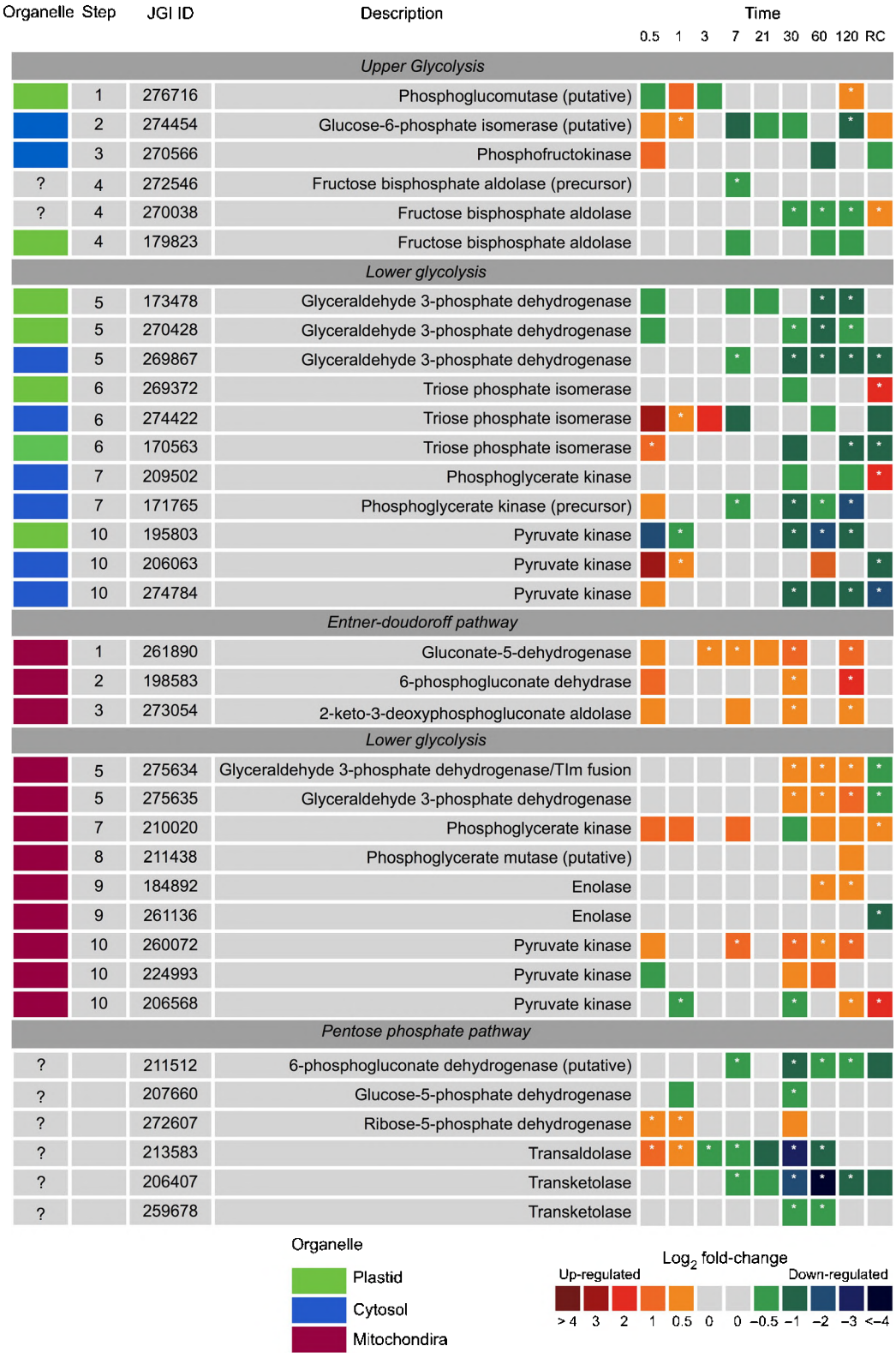

Fig. 5 Expression of *Fragilariopsis cylindrus* proteins involved in glycolysis, Entner–Doudoroff and pentose phosphate pathways in the dark when compared with in continuous light. JGI ID corresponds to the Joint Genome Institute identification number of that particular protein. Each box represents the relative expression of the proteins indicated, after the duration of dark exposure in days, with the exception of RC that denotes the dark recovery phase in which dark-treated cells were re-exposed to white light (50 μmol photon^{-1} m^{-2} s^{-1}) for 24 h. The colours represent the protein abundance change (difference in mean $\log_2$ LFQ values, dark vs light) the scale shown. White stars (*) inside boxes represent a significant expression (FDR < 2% and $\log_2$ LFQ difference >/< 0.5). Organelle indicates the protein suggested cellular location. All expressed proteins have been normalised to relative cell abundance.

mitochondrial matrix where it catalyses the complete aerobic oxidation of pyruvate to form CO_2, ATP, nicotinamide adenine dinucleotide (NADH), and carbon skeletons for biosynthetic processes. The TCA cycle was widely upregulated in the dark compared with the light, especially on days 30, 60 and 120. The eight main TCA cycle reactions are summarised in Fig. 6.

Imperative for TCA cycle function is a source of pyruvate. Proteins of the 2-oxoacid dehydrogenase multienzyme family involved in the production of pyruvate were upregulated in the dark (Fig. 6). These proteins comprise the pyruvate dehydrogenase complex (PDHC), oxoglutarate dehydrogenase complex (ODHC), and the branched-chain 2-oxoacid dehydrogenase (BCODH).

Although specifically unrelated to the TCA cycle, L-lactate dehydrogenase (JGI|274468) was also heavily upregulated in the dark from day 30 to day 120. This protein catalyses the reversible conversion of lactate into pyruvate. Similarly, malic enzyme (JGI|173391), which also forms pyruvate (from malate, reversible), was heavily upregulated in the dark from day 30 (Fig. 6).

Methylmalonyl-CoA mutase (JGI|273786) was highly upregulated throughout dark exposure (Fig. 6). This mitochondrial enzyme forms succinyl-CoA for use in the TCA cycle via the breakdown of odd-chain fatty acids, or branched-chain amino acids.

Utilising precursors of the TCA cycle to generate energy across the mitochondrial membrane are the series of enzyme complexes of the electron transport chain (mETC). Complexes I, II and V, but not III and IV were observed. These enzyme complexes were primarily upregulated towards the latter half of dark exposure when compared with in the light (Fig. 7a).

Urea cycle and nitrogen metabolism

Proteins of the urea cycle were significantly upregulated in the dark when compared with the light, but were not all coordinately expressed. Argininosuccinate synthase (JGI|207847 and JGI|213508) and argininosuccinate lyase (JGI|215156) were the only proteins in the cycle to be significantly downregulated from day 30 of dark exposure (Fig. 8). All other proteins were predominately upregulated, primarily on day 0.5 and from day 30 to day 120.

The glutamate cycle (or GS/GOGAT cycle) plays a central role in the recycling and assimilation of nitrogenous compounds (Fig. 7b). Two glutamine synthase proteins were observed in the experiments; a plastid located glutamine synthase II (GSII) (JGI|158325) and glutamine synthase (GS) (JGI|277211). The former was consistently downregulated under dark conditions, while the latter was heavily upregulated from day 30. GS expression coincided with significant upregulation of a glutamate synthase (GOGAT) on day 30 (JGI|225787) and a cytoplasmic aspartate aminotransferase (AST) (JGI|170472); both are involved in the primary assimilation of ammonium. Nitrate reductase (JGI|206583), which assimilates nitrate, was downregulated from day 21 (dark).

Fatty acid biosynthesis and β-oxidation

Proteins involved in the synthesis of fatty acids were predominantly downregulated in the dark compared with in the light (Fig. S4). UDP-sulfoquinovose synthase (putative: JGI|268690), which forms the important thylakoid lipid sulfoquinovosl diacylglycerol (SQDG), was upregulated in the dark from 12 h. The hydrophobic molecule carrier protein lipocalin (JGI|268796) was also upregulated in the dark from day 3. Some proteins involved in fatty acid β-oxidation were upregulated towards the latter part of the dark incubation (Fig. S4).

Transcription, translation and proteolysis

Ribosomal proteins were largely downregulated following 12 h of darkness (Fig. S5). After day 1, these ribosomal proteins were strongly upregulated compared with continuous light. Subsequently, there was limited change in the expression of these proteins until day 60 when a number of ribosomal 40S subunit proteins were significantly upregulated. By contrast, following 120 d of dark exposure, most ribosomal proteins were downregulated. Re-illumination of dark cells for 24 h failed to alter the expression of many ribosomal proteins.

The downregulation of most ribosomal proteins on day 120 of dark exposure coincided with the upregulation of some serine and cysteine proteases, in addition to ubiquitin-containing proteins and proteasome subunits (Fig. S6). Dark proteolytic subunits that are ATP dependent were predominately downregulated.

Discussion

This study is the first to examine the proteome of a prominent sea-ice diatom in response to extended darkness. It has been successful in illustrating the capacity of *F. cylindrus* to survive 4 months of darkness and retain photosynthetic viability. Examination of the proteome demonstrated the ability of the species to utilise cellular resources to sustain dark metabolism.

This study should be viewed with an understanding of the likely effect of constant light, which may influence protein comparisons. Cells grown in constant light are likely to have experienced oxidative stress, which can affect consumption of photosystem products via the Calvin–Benson cycle. As a result, some protein expressions may be over- or underestimated. Despite this caveat, this study is the first to examine the proteome of a sea-ice diatom over an extended period of darkness and a comparison with cells in constant light was a necessary limitation. This study is intended to provide a foundation for future studies on the long-term dark metabolism of sea-ice diatoms.

Light harvesting and photosynthetic pathway

Some proteins involved in light harvesting identified in this study were significantly altered in abundance during extended darkness. Within 12 h, proteins from all clades of the light-harvesting apparatus were downregulated, with the LHCx photoprotective

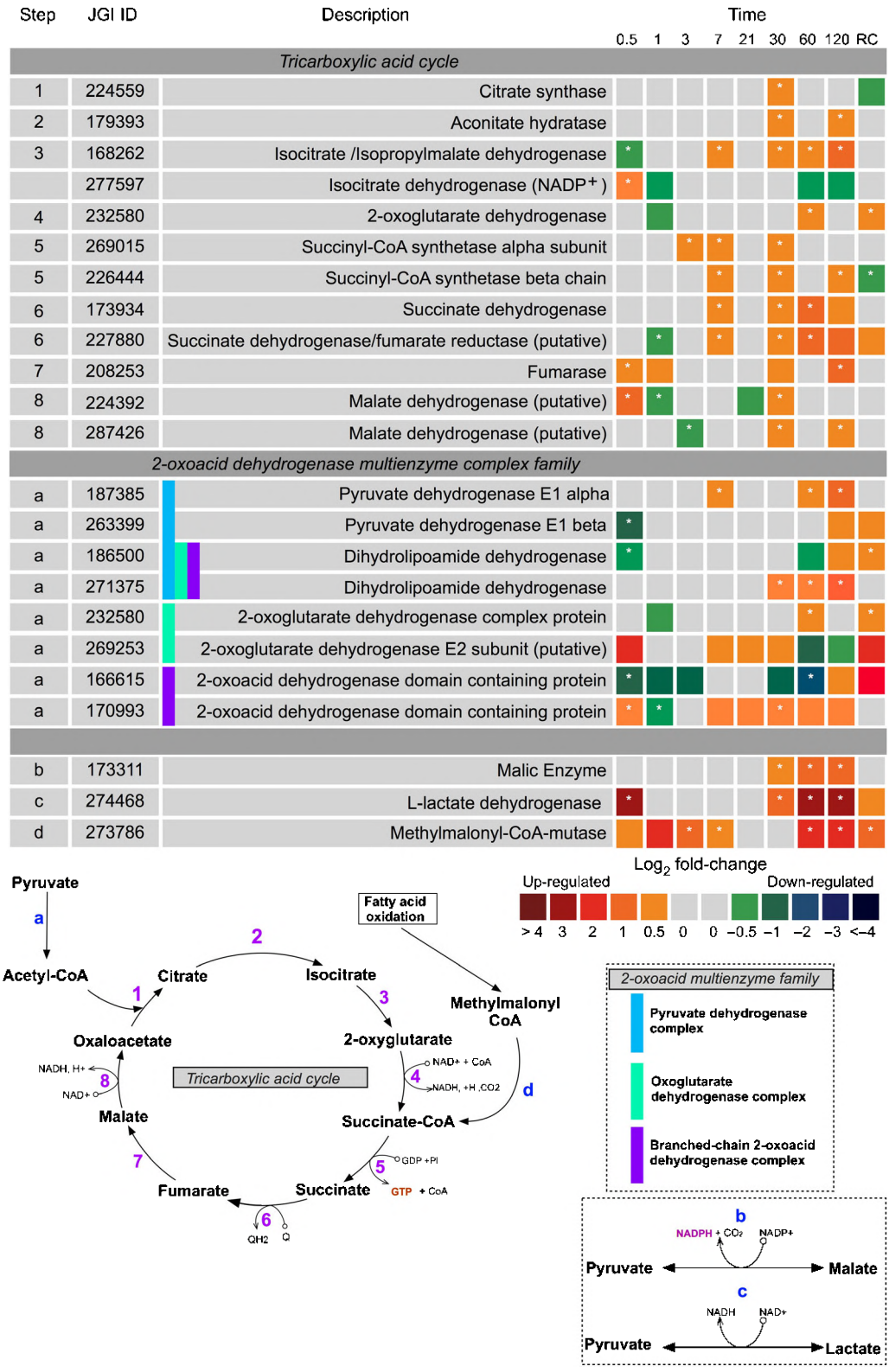

Fig. 6 Expression of *Fragilariopsis cylindrus* proteins involved tricarboxylic acid pathway and pyruvate metabolism in the dark when compared with in the light. Steps corresponds to the stage in which a protein appears in the biosynthetic pathway. JGI ID corresponds to the Joint Genome Institute identification number of that particular protein. Each box represents the relative expression of the proteins indicated, after the duration of dark exposure in days as indicated, with the exception of RC that denotes the dark recovery phase in which dark-treated cells were re-exposed to white light (50 μmol photon^{-1} m^{-2} s^{-1}) for 24 h. The colours represent the protein abundance change (difference in mean $\log_2$ LFQ values, dark vs light) the scale shown. White stars (*) inside boxes represent a significant expression (FDR < 2% and $\log_2$ LFQ difference >/< 0.5). All expressed proteins have been normalised to relative cell abundance.

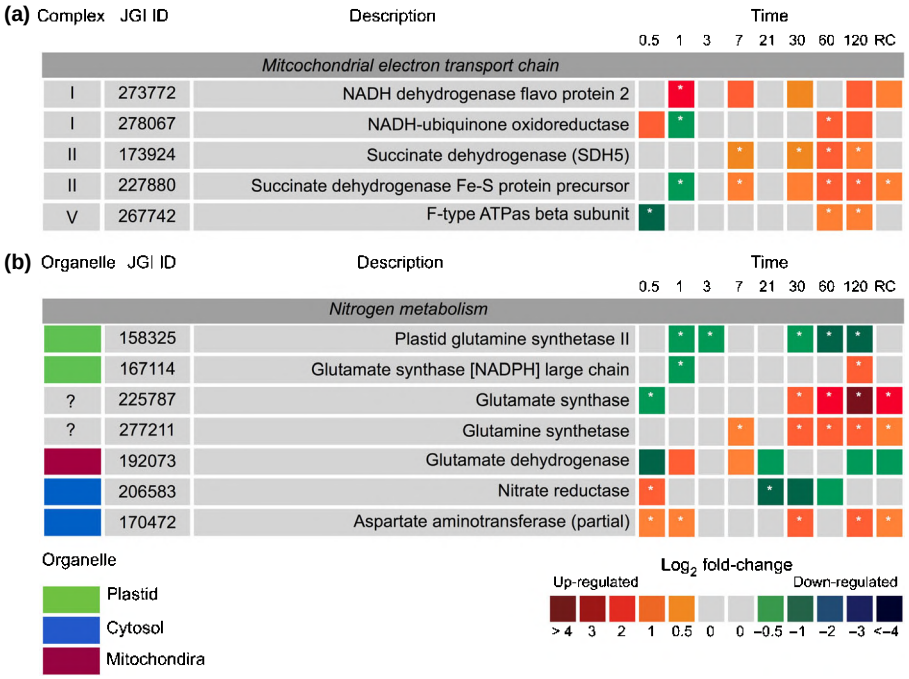

Fig. 7 Expression of *Fragilariopsis cylindrus* proteins involved in (a) the mitochondrial electron transport chain and (b) nitrogen metabolism in the dark when compared with in the light. Complex refers to the denoted protein complex number of the transport chain, whereas organelle indicates the protein suggested cellular location. JGI ID corresponds to the Joint Genome Institute identification number of that particular protein. Each box represents the relative expression of the proteins indicated, after the duration of dark exposure in days as indicated, with the exception of RC that denotes the dark recovery phase in which dark-treated cells were re-exposed to white light (50 μmol photon^{-1} m^{-2} s^{-1}) for 24 h. The colours represent the protein abundance change (difference in mean $\log_2$ LFQ values, dark vs light) the scale shown. White stars (*) inside boxes represent a significant expression (FDR < 2% and $\log_2$ LFQ difference >/< 0.5). All expressed proteins have been normalised to relative cell abundance.

clade being heavily downregulated. This finding is similar to that of Mock *et al.* (2017), who also observed widespread reduction in the regulation of photosystem genes in the dark. Interestingly, these authors only observed this trend after 7 d; it remains unclear why photosynthetic proteins in this study were so rapidly downregulated. Calvin–Benson cycle proteins also exhibited a similar trend to that of photosystem proteins (dark), indicating that cells had completely abolished the photosynthetic processes in the dark. Within 1 h of light re-exposure after 120 d of darkness, ETR_{max} exhibited higher levels following dark exposure than the pretreatment, indicating that cells regained and even improved their photosynthetic performance upon re-illumination. A similar response in ETR_{max} following re-illumination was observed by Nymark *et al.* (2013) and this may illustrate that the photosynthetic apparatus of *F. cylindrus* was not degraded during extended darkness. This adaptive response has been noted in previous studies with polar diatoms, in which the photosynthetic apparatus is maintained so that photosynthesis can resume rapidly upon return to favourable light conditions (Bunt & Lee, 1972; Palmisano & Sullivan, 1982; Peters & Thomas, 1996; McMinn & Martin, 2013; Schaub et al., 2017). Furthermore, if degradation of light-harvesting antenna complexes was occurring, a gradual reduction in the photosynthetic parameter α would be apparent, as resonance energy transfer between the antenna and photosystem II would become inefficient due to physical breakdown (Falkowski & LaRoche, 1991; Vernotte *et al.*, 1992; Nymark *et al.*, 2013). This appears unlikely as α was maintained. Additionally, the widespread upregulation of LHCF and LHCR proteins at day 120 of dark exposure implies that cells were actively regulating and maintaining photosystem proteins.

To ensure photosystem functionality, continuous transport across multiple membranes needs to be protected and maintained. Any depletion in macromolecule transporters in thylakoid membranes would result in the degradation of the LHC. Diatom thylakoids are enriched with the anionic lipid SQDG, which accounts for over 40% of the total lipid content (Schaub et al., 2017). In this study, while speculative, the increased expression of plastid UDP-sulfoquinovose synthase, which is essential for the production of SQDG, was observed in the dark. The potential function of SQDG in thylakoid membranes may be similar to that of higher plants and green algae in which negatively charged lipids associate and interact with plastidic ATP synthase (Pick *et al.*, 1987; Joshi *et al.*, 2009). In addition, the outer lamellae of low-light-adapted diatoms have been shown to be enriched in SQDG, ATP synthase and photosystem I (PSI) complexes (Pyszniak & Gibbs, 1992). This finding supports the concept that SQDG may act to help maintain thylakoid membrane integrity and protect the functionality of ATP synthase, although more work needs to be conducted to support this statement. Additionally, maintenance of chloroplasts in the dark may also involve the energisation of thylakoid membrane via chlororespiration. Chlororespiration has been shown to facilitate the maintenance of ATP synthase during prolonged darkness, enabling

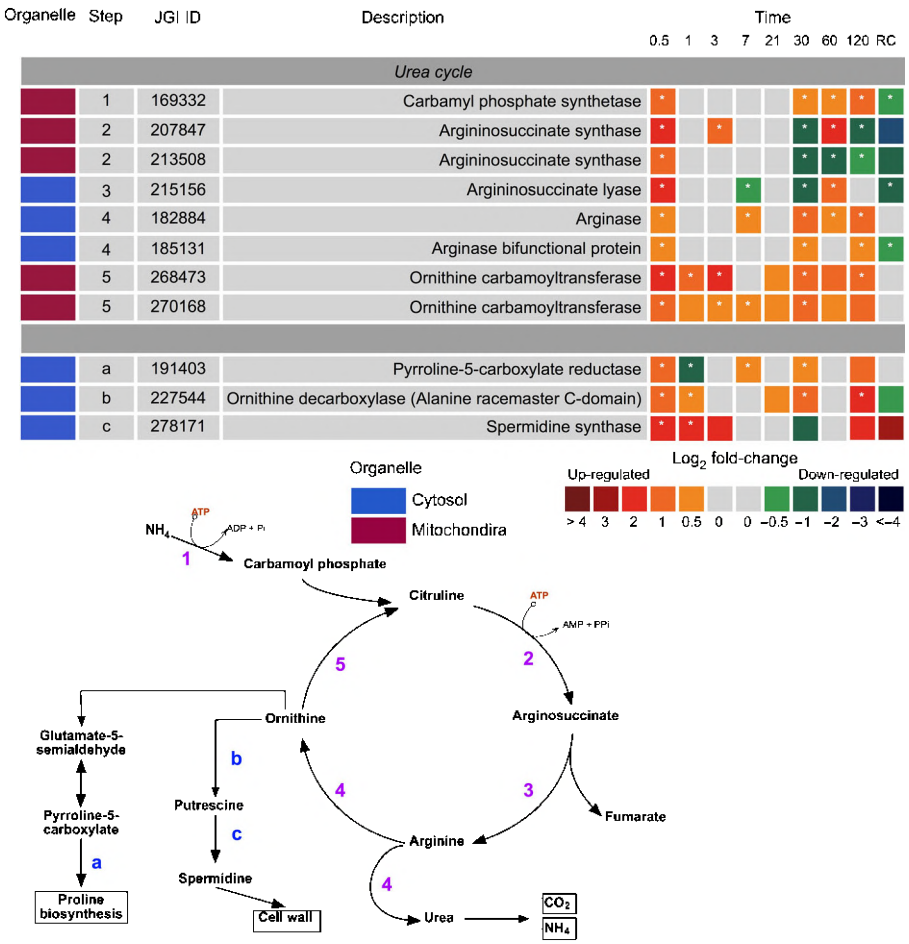

Fig. 8 Expression of *Fragilariopsis cylindrus* proteins involved in the urea cycle and auxillaries in the dark when compared with in the light. JGI ID corresponds to the Joint Genome Institute identification number of that particular protein. Each box represents the relative expression of the proteins indicated, after the duration of dark exposure in days as indicated, with the exception of RC that denotes the dark recovery phase in which dark-treated cells were re-exposed to white light (50 μmol photon^{-1} m^{-2} s^{-1}) for 24 h. The colours represent the protein abundance change (difference in mean $\log_2$ LFQ values, dark vs light) the scale shown. White stars (*) inside boxes represent a significant expression (FDR < 2% and $\log_2$ LFQ difference >/< 0.5). Organelle indicates the proteins suggested cellular location. All expressed proteins have been normalised to relative cell abundance.

rapid ATP production upon re-illumination (Feild *et al.*, 1998; Jakob *et al.*, 1999; Nixon, 2000; Lavaud et al., 2002, 2012; Wilhelm et al., 2006). The de-epoxidation of diadinoxanthin is correlated with increased nonphotochemical quenching (NPQ) of photosystem II fluorescence. NPQ increased from day 30 (dark); this finding is consistent with the results of Jakob *et al.* (2001), who showed that de-epoxidation of the xanthophyll cycle and subsequent increase in NPQ were highest during long-term dark exposure in *Phaeodactylum tricornatum*. Upon re-illumination, ATP concentration in dark exposed cells rapidly returned to pre-treatment levels within 1 h and continued to increase over the next 24 h. This change not only infers active ATP synthase maintenance in the dark, but also indicates that cells may retain a fully functional LHC.

Respiratory metabolism

Diatoms are unique in that they are the only photosynthetic organism with a mitochondrial-targeted glycolytic pathway (Kroth *et al.*, 2008; Smith *et al.*, 2012). It is unknown if this is an ancient trait or one that has been recently acquired via gene transfer (Ginger *et al.*, 2010). The observed downregulation of plastid/cytosolic-targeted glycolytic proteins in the dark and the upregulation of mitochondrial lower-phase proteins suggested significant metabolic plasticity. The physical association of glycolysis with the mitochondria negated the need to transport pyruvate and NADH into the organelle to supply the TCA cycle in the dark. Additionally, the recently discovered mitochondrial Entner–Doudoroff pathway (EDP) in diatoms can provide the necessary glyceraldehyde 3-phosphate for the lower phase and supplement pyruvate for the TCA (Fabris *et al.*, 2012). The EDP is considered to be an ancient form of glycolysis that is predominately restricted to prokaryotic lineages. EDP gene sets have are also been found in *Thalassiosira pseudonana* and *Phaeodactylum tricornutum*, seemingly obtained via horizontal gene transfer (Fabris *et al.*, 2012; Chen *et al.*, 2016). Regulation of the EDP has been hypothesised, as in glycolysis, to be associated with the cellular energy status with pathway flux dependent on ATP concentration (Schuetz *et al.*, 2007). Cellular ATP concentration declined to undetectable levels in the dark from day 21. While speculative, this low level of ATP may have triggered the cell to initiate glycolysis and the EDP. A similar observation was noted by Fabris *et al.* (2012) in *Phaeodactylum tricornutum*, in which gene transcripts for EDP increased in the dark. Although the EDP provides less energy per molecule of glucose than the conventional glycolytic route (with net yield of 1 ATP, 1 NADH and 1 NADPH and 2 pyruvate. Glycolysis: 2 ATP, 2 NADH and 1 pyruvate), it requires less resources to synthesise the necessary enzymes (Wessely *et al.*, 2011; Fabris *et al.*, 2012). Coordination of several metabolic routes is derived from the necessity to

conserve energy, and the move to energetic inefficiency is essentially a trade-off between the high operational costs of alternate catabolic processes and the low investment of enzyme synthesis. Exactly why the ATP pool in the dark did not increase following activation of respiratory pathways remains unclear. This situation may imply that the rate of consumption required to maintain essential metabolic processes is equal to, or exceeds, that of production. This is highly likely if substrate level phosphorylation is the main ATP generating mechanism, as it produces less ATP than oxidative phosphorylation and is generally unable to replenish the ATP pool (Bottomley and Stewart, 1976a,b).

The tricarboxylic acid cycle, pyruvate and the mitochondrial electron transport chain

TCA cycle proteins were co-ordinately expressed in the dark and predominantly upregulated from day 30. This delayed upregulation appears to correspond with the expression of the EDP and lower-phase mitochondrial glycolytic proteins. The cycle is also likely to be sustained in the dark through the action of multiple anaplerotic enzymes that act to replenish TCA cycle intermediates. These are, for example, malic enzyme to pyruvate, aspartate aminotransferase to 2-oxoglutarate and β-oxidation of fatty acids via succinyl-CoA. The TCA cycle is a series of catabolic reactions that supports energy transduction, but it is also entangled in a broader network that augments multiple features of metabolism. For example, the TCA cycle has been shown to be tightly regulated with the urea cycle in diatoms (Allen *et al.*, 2011). The urea cycle in this study did indeed appear to be co-ordinated with the TCA cycle and may serve as a centre for the connection metabolism critical in balancing the demand for cellular processes when carbon fixation is abolished. A key regulatory point for TCA cycle flux, and crucial to its linkage with glycolysis, is likely to be the PDHC of the 2-oxoacid dehydrogenase multienzyme complex family (Alejandro *et al.*, 2003), but may also be regulated by thioredoxin (Daloso *et al.*, 2015). While it remains unclear in this study, it is probable that thioredoxin is not a major regulator (Table S5). It is possible that the collective upregulation of the PDHC may indicate amplified acetyl-CoA flux into the TCA cycle.

Coupled with the TCA cycle, the mitochondrial electron transport chain generates ATP in the absence of photosynthesis. The upregulation of complexes I, II and V in the dark and the corresponding expression of proteins involved in both the TCA cycle and glycolysis may indicate increased oxidative phosphorylation. This is especially apparent from day 30 of dark exposure and may highlight a specific threshold in the capacity of cells to survive in the absence of photosynthesis without mobilising reserves or inducing catabolism of nonessential metabolic components. Although when considering the observed ATP levels from day 21, any increase in abundance of oxidative phosphorylation processes must be viewed with caution, as the protein abundance of oxidative phosphorylation process in cells exposed to constant light is not regulated when photophosphorylation is the primary energy generator. This situation may result in an overestimation of the abundance of dark oxidative phosphorylation proteins, exacerbating the expression of this pathway in the dark. Metabolic flux measurements would be useful to further explore dark respiratory processes.

Urea cycle and nitrogen metabolism

The main route of nitrogen assimilation in diatoms is via the reduction of nitrate by nitrate reductase (NR) in the cytosol. In this study, active uptake of nitrate in the dark is unlikely due to the energy requirements for assimilation and downregulation of a NR enzyme. Instead, utilisation of other nitrogenous forms may be occurring. The use of NH_3/NH_4^+ formed through the catabolism of proteins and amino acids, is likely to be reassimilated through GS/GOGAT enzymes. Significant expression of enzymes involved in the catabolism of proteins and amino acids suggests heightened NH_3/NH_4^+ formation. In addition, the downregulation of a plastid GSII and NADPH-GOGAT and upregulation of GS/GOGAT with evidence for mitochondrial export, may infer heightened NH_3/NH_4^+ assimilation. Tight association between the mitochondria and GS/GOGAT is essential, as it is dependent on the input of carbon skeletons in the form of 2-oxoglutarate derived from the TCA cycle.

Similarly, associated with both pathways is the urea cycle, which in diatoms serves as a hub for recycling nitrogenous compounds (Allen *et al.*, 2011; Prihoda *et al.*, 2012). It is not clear why the cycle was not co-ordinately expressed in the dark, but this finding is consistent with other studies in which alternative nitrogenous sources are available (Allen *et al.*, 2011; Smith *et al.*, 2016). The catabolism of proteins into their amino acid constituents provides NH_4^+ and monomers for TCA oxidation.

Conclusions

The capacity for a phototroph to modify its metabolic activity to an obligatory light regime enhances its survival and success in a transient environment. Sustaining essential metabolic processes in the dark is imperative so that photosynthesis can occur rapidly upon re-illumination. Maintenance metabolism (or the ability to live in the dark), may be one of the fundamental reasons why diatoms dominate Antarctic sea-ice ecosystems. Our proteomic analysis of *F. cylindrus* during extended darkness has indicated that cells rapidly decrease their LHC and photosystems, while maintaining their photosynthetic capacity. This appears to be mediated through mitochondrial respiratory processes of the Entner–Doudoroff pathway, glycolysis and TCA cycle, ensuring rapid recovery upon illumination. These results align with field studies in which the ability sea-ice diatoms to rapidly recover upon the return of light is well known. While analysis of the proteome alone is still some way removed from real proof of physiological function, it nonetheless provides a metabolic blueprint that establishes a valuable scaffold for future work to expand upon. Caveats of this study are acknowledged and, in considering these, future work requires a mechanistic understanding of the processes that are primarily responsible for dark ATP generation and ATP synthase maintenance. This would benefit from a quantitative assessment of respiration and metabolic flux, along with

the molecular and environmental drivers that enable activation of the Entner–Doudoroff and mitochondrial glycolysis pathways.

Acknowledgements

This research was supported under Australian Research Council's Special Research Initiative for Antarctic Gateway Partnership (Project ID SR140300001). FK was supported by a PhD Scholarship under the Australian Government Research Training Programme.

Author contributions

FK designed and performed the experiments, analysed the data, wrote the manuscript. FK, AM, AMcM and JPB planned and designed the research. RW analysed the samples.

ORCID

John P. Bowman https://orcid.org/0000-0002-4528-9333
Fraser Kennedy https://orcid.org/0000-0003-1796-0764
Andrew Martin https://orcid.org/0000-0001-8260-5529
Andrew McMinn https://orcid.org/0000-0002-2133-3854
Richard Wilson https://orcid.org/0000-0003-0152-4394

References

Alejandro T, Miernyk J, Randal D. 2003. Regulation of pyruvate dehydrogenase complex activity in plant cells. *European Journal of Biochemistry* **270**: 1043–1049.

Allen AE, Dupont CL, Oborník M, Horák A, Nunes-Nesi A, McCrow JP, Zheng H, Johnson DA, Hu H, Fernie AR *et al.* 2011. Evolution and metabolic significance of the urea cycle in photosynthetic diatoms. *Nature* **473**: 203–207.

Antia NJ. 1976. Effects of temperature on the darkness survival of marine microplanktonic algae. *Microbial Ecology* **3**: 41–54.

Arrigo KR. 2014. Sea ice ecosystems. *Annual Review of Marine Science* **6**: 439–467.

Bai X, Song H, Lavoie M, Zhu K, Su Y, Ye H, Chen S, Fu Z, Qian H. 2016. Proteomic analyses bring new insights into the effect of a dark stress on lipid biosynthesis in *Phaeodactylum tricornutum*. *Scientific Reports* **6**: 25494.

Baldisserotto C, Ferroni L, Andreoli C, Fasulo MP, Bonora A, Pancaldi S. 2005. Dark-acclimation of the chloroplast in *Koliella antarctica* exposed to a simulated austral night condition. *Arctic, Antarctic and Alpine Research* **37**: 146–156.

Bertrand M. 2010. Carotenoid biosynthesis in diatoms. *Photosynthesis Research* **106**: 89–102.

Bottomley PJ, Stewart WDP. 1976a. ATP pools and transients in the blue-green alga, *Anabaena cylindrica*. *Archives of Microbiology* **258**: 249–258.

Bottomley PJ, Stewart WDP. 1976b. The measurement and significance of ATP pools in filamentous blue-green algae. *British Phycological Journal* **11**: 69–82.

Bowler C, Allen AE, Badger JH, Grimwood J, Jabbari K, Kuo A, Maheswari U, Martens C, Maumus F, Otillar RP *et al.* 2008. The *Phaeodactylum* genome reveals the evolutionary history of diatom genomes. *Nature* **456**: 239–244.

Büchel C. 2003. Fucoxanthin-chlorophyll proteins in diatoms: 18 and 19 kDa subunits assemble into different oligomeric states. *Biochemistry* **42**: 13027–13034.

Bunt JS, Lee CC. 1972. Data on the composition and dark survival of four sea-ice microalgae. *Limnology and Oceanography* **17**: 458–461.

Catalanotti C, Yang W, Posewitz MC, Grossman AR. 2013. Fermentation metabolism and its evolution in algae. *Frontiers in Plant Science* **4**: 1–17.

Chen X, Schreiber K, Appel J, Makowka A, Fähnrich B, Roettger M, Hajirezaei MR, Sönnichsen FD, Schönheit P, Martin WF *et al.* 2016. The Entner–Doudoroff pathway is an overlooked glycolytic route in cyanobacteria and plants. *Proceedings of the National Academy of Sciences, USA* **113**: 5441–5446.

Cox J, Hein MY, Luber CA, Paron I, Nagaraj N, Mann M. 2014. Accurate proteome-wide label-free quantification by delayed normalization and maximal peptide ratio extraction, termed MaxLFQ. *Molecular & Cellular Proteomics : MCP* **13**: 2513–2526.

Daloso DM, Müller K, Obata T, Florian A, Tohge T, Bottcher A, Riondet C, Bariat L, Carrari F, Nunes-Nesi A *et al.* 2015. Thioredoxin, a master regulator of the tricarboxylic acid cycle in plant mitochondria. *Proceedings of the National Academy of Sciences, USA* **112**: 1392–1400.

Evans CA, O'Reilly JE, Thomas J. 1987. *A handbook for the measurement of chlorophyll-a and primary productivity*. College Station, Texas, USA: Texas A&M University.

Fabris M, Matthijs M, Rombauts S, Vyverman W, Goossens A, Baart GJEEE. 2012. The metabolic blueprint of *Phaeodactylum tricornutum* reveals a eukaryotic Entner–Doudoroff glycolytic pathway. *The Plant Journal* **70**: 1004–1014.

Falciatore A, Bowler C. 2002. Revealing the molecular secrets of marine diatoms. *Annual Review of Plant Biology* **53**: 109–130.

Falkowski PG, LaRoche J. 1991. Acclimation to spectral irradiance in algae. *Journal of Phycology* **27**: 8–14.

Feild TS, Nedbal L, Ort DR. 1998. Nonphotochemical reduction of the plastoquinone pool in sunflower leaves originates from chlororespiration. *Plant Physiology* **116**: 1209–1218.

Fernie AR, Carrari F, Sweetlove LJ. 2004. Respiratory metabolism: glycolysis, the TCA cycle and mitochondrial electron transport. *Current Opinion in Plant Biology* **7**: 254–261.

Ginger ML, McFadden GI, Michels P. 2010. Rewiring and regulation of cross-compartmentalized metabolism in protists. *Philosophical Transactions of the Royal Society of London. Series B: Biological Sciences* **365**: 831–845.

Giovagnetti V, Ruban AV. 2017. Detachment of the fucoxanthin chlorophyll *a/c* binding protein (FCP) antenna is not involved in the acclimative regulation of photoprotection in the pennate diatom *Phaeodactylum tricornutum*. *Biochimica et Biophysica Acta (BBA) – Bioenergetics* **1858**: 218–230.

Guillard RRL, Hargraves PE. 1993. *Stichochrysis immobilis* is a diatom, not a chrysophyte. *Phycologia* **32**: 234–236.

Gundermann K, Schmidt M, Weisheit W, Mittag M, Büchel C. 2013. Identification of several sub-populations in the pool of light harvesting proteins in the pennate diatom *Phaeodactylum tricornutum*. *Biochimica et Biophysica Acta (BBA) – Bioenergetics* **1827**: 303–310.

Horner R, Alexander V. 1972. Algal populations in Arctic sea ice: an investigation of heterotrophy. *Limnology Oceanography* **17**: 454–458.

Ishihara T, Ifuku K, Yamashita E, Fukunaga Y, Nishino Y, Miyazawa A, Kashino Y, Inoue-Kashino N. 2015. Utilization of light by fucoxanthin-chlorophyll-binding protein in a marine centric diatom, *Chaetoceros gracilis*. *Photosynthesis Research* **126**: 437–447.

Jakob T, Goss R, Wilhelm C. 1999. Activation of diadinoxanthin de-epoxidase due to a chiororespiratory proton gradient in the dark in the diatom *Phaeodactylum tricornutum*. *Plant Biology* **1**: 76–82.

Jakob T, Goss R, Wilhelm C. 2001. Unusual pH-dependence of diadinoxanthin de-epoxidase activation causes chlororespiratory induced accumulation of diatoxanthin in the diatom *Phaeodactylum tricornutum*. *Journal of Plant Physiology* **158**: 383–390.

Joshi AS, Zhou J, Gohil VM, Chen S, Greenberg ML. 2009. Cellular functions of cardiolipin in yeast. *Biochimica et Biophysica Acta (BBA) – Molecular Cell Research* **1793**: 212–218.

Kamp A, Høgslund S, Risgaard-Petersen N, Stief P. 2015. Nitrate storage and dissimilatory nitrate reduction by eukaryotic microbes. *Frontiers in Microbiology* **6**: 1–15.

Kamp A, Stief P, Knappe J, De Beer D. 2013. Response of the ubiquitous pelagic diatom *Thalassiosira weissflogii* to darkness and anoxia. *PLoS ONE* **8**: 1–11.

Kennedy F, McMinn A, Martin A. 2012. Effect of temperature on the photosynthetic efficiency and morphotype of *Phaeocystis antarctica*. *Journal of Experimental Marine Biology and Ecology* **429**: 7–14.

Kramer DM, Johnson G, Kiirats O, Edwards GE. 2004. New fluorescence parameters for the determination of QA redox state and excitation energy fluxes. *Photosynthesis Research* **79**: 209–218.

Kroth PG, Chiovitti A, Gruber A, Martin-Jezequel V, Mock T, Parker MS, Stanley MS, Kaplan A, Caron L, Weber T *et al.* 2008. A model for carbohydrate metabolism in the diatom *Phaeodactylum tricornutum* deduced from comparative whole genome analysis (J Kroymann, Ed.). *PLoS ONE* **3**: e1426.

Kuczynska P, Jemiola-Rzeminska M, Strzalka K. 2015. Photosynthetic pigments in diatoms. *Marine Drugs* **13**: 5847–5881.

Lavaud J, Materna AC, Sturm S, Vugrinec S, Kroth PG. 2012. Silencing of the violaxanthin de-epoxidase gene in the diatom *Phaeodactylum tricornutum* reduces diatoxanthin synthesis and non-photochemical quenching (D Bhattacharya, Ed.). *PLoS ONE* **7**: e36806.

Lavaud J, van Gorkom H, Etienne A-L. 2002. Photosystem II electron transfer cycle and chlorespiration in planktonic diatoms. *Photosynthesis Research* **74**: 51–59.

Laybourn-Parry J, Marshall WA, Marchant HJ. 2005. Flagellate nutritional versatility as a key to survival in two contrasting Antarctic saline lakes. *Freshwater Biology* **50**: 830–838.

Lepetit B, Goss R, Jakob T, Wilhelm C. 2012. Molecular dynamics of the diatom thylakoid membrane under different light conditions. *Photosynthesis Research* **111**: 245–257.

Lepetit B, Volke D, Gilbert M, Wilhelm C, Goss R. 2010. Evidence for the existence of one antenna-associated, lipid-dissolved and two protein-bound pools of diadinoxanthin cycle pigments in diatoms. *Plant Physiology* **154**: 1905–1920.

Liu J, Gerken H, Li Y. 2014. Single-tube colony PCR for DNA amplification and transformant screening of oleaginous microalgae. *Journal of Applied Phycology* **26**: 1719–1726.

Martin A, McMinn A, Heath M, Hegseth EN, Ryan KG. 2012. The physiological response to increased temperature in over-wintering sea ice algae and phytoplankton in McMurdo Sound, Antarctica and Tromsø Sound, Norway. *Journal of Experimental Marine Biology and Ecology* **428**: 57–66.

McMinn A, Martin A. 2013. Dark survival in a warming world. *Proceedings of the Royal Society of London. Series B: Biological Sciences* **280**: 20122909.

McMinn A, Martin A, Ryan K. 2010a. Phytoplankton and sea ice algal biomass and physiology during the transition between winter and spring (McMurdo Sound, Antarctica). *Polar Biology* **33**: 1547–1556.

McMinn A, Pankowskii A, Ashworth C, Bhagooli R, Ralph P, Ryan K. 2010b. *In situ* net primary productivity and photosynthesis of Antarctic sea ice algal, phytoplankton and benthic algal communities. *Marine Biology* **157**: 1345–1356.

Medlin LK. 2016. Evolution of the diatoms: major steps in their evolution and a review of the supporting molecular and morphological evidence. *Phycologia* **55**: 79–103.

Mock T, Otillar RP, Strauss J, McMullan M, Paajanen P, Schmutz J, Salamov A, Sanges R, Toseland A, Ward BJ *et al.* 2017. Evolutionary genomics of the cold-adapted diatom *Fragilariopsis cylindrus*. *Nature* **541**: 536–540.

Morgan-Kiss RM, Lizotte MP, Kong W, Priscu JC. 2016. Photoadaptation to the polar night by phytoplankton in a permanently ice-covered Antarctic lake. *Limnology and Oceanography* **61**: 3–13.

Nagao R, Tomo T, Narikawa R, Enami I, Ikeuchi M. 2013. Light-independent biosynthesis and assembly of the photosystem II complex in the diatom *Chaetoceros gracilis*. *FEBS Letters* **587**: 1340–1345.

Nixon PJ. 2000. Chlororespiration. *Philosophical Transactions of the Royal Society of London. Series B: Biological Sciences* **355**: 1541–1547.

Nymark M, Valle KC, Hancke K, Winge P, Andresen K, Johnsen G, Bones AM, Brembu T. 2013. Molecular and photosynthetic responses to prolonged darkness and subsequent acclimation to re-illumination in the diatom *Phaeodactylum tricornutum* (R Subramanyam, Ed.). *PLoS ONE* **8**: e58722.

Palmisano AC, Sullivan CW. 1982. Physiology of sea ice diatoms. I. Response of three polar diatoms to a simulated summer-winter transition. *Journal of Phycology* **18**: 489–498.

Palmisano AC, Sullivan CW. 1983. Physiology of sea ice diatoms. II. Dark survival of three polar diatoms. *Canadian Journal of Microbiology* **29**: 157–160.

Peters E. 1996. Prolonged darkness and diatom mortality: II. Marine temperate species. *Journal of Experimental Marine Biology and Ecology* **207**: 43–58.

Peters E, Thomas DN. 1996. Prolonged darkness and diatom mortality I: marine Antarctic species. *Journal of Experimental Marine Biology and Ecology* **207**: 25–41.

Pick U, Weiss M, Gounaris K, Barber J. 1987. The role of different thylakoid glycolipids in the function of reconstituted chloroplast ATP synthase. *Biochimica et Biophysica Acta (BBA) – Bioenergetics* **891**: 28–39.

Popels LC, MacIntyre HL, Warner ME, Zhang Y, Hutchins DA. 2007. Physiological responses during dark survival and recovery in *Aureococcus anophagefferens* (Pelagophyceae). *Journal of Phycology* **43**: 32–42.

Prihoda J, Tanaka A, De Paula WBM, Allen JF, Tirichine L, Bowler C. 2012. Chloroplast-mitochondria cross-talk in diatoms. *Journal of Experimental Botany* **63**: 1543–1557.

Pyszniak AM, Gibbs SP. 1992. Immunocytochemical localization of photosystem I and the fucoxanthin-chlorophyll *a/c* light-harvesting complex in the diatom *Phaeodactylum tricornutum*. *Protoplasma* **166**: 208–217.

Raven JA, Beardall J. 2011. Carbohydrate metabolism and respiration in algae. In: Larkum AWD, Douglas SE, Raven JA, eds. *Photosynthesis in algae: advances in photosynthesis and respiration*. Dordrecht, the Netherlands: Springer Netherlands, 205–224.

Reeves S, McMinn A, Martin A. 2011. The effect of prolonged darkness on the growth, recovery and survival of Antarctic sea ice diatoms. *Polar Biology* **34**: 1019–1032.

Rivkin RB, Putt M. 1987. Heterotrophy and photoheterotrophy by Antarctic microalgae: light dependant incorporation of amino acids and glucose. *Journal of Phycology* **23**: 442–452.

Schaub I, Wagner H, Graeve M, Karsten U. 2017. Effects of prolonged darkness and temperature on the lipid metabolism in the benthic diatom *Navicula perminuta* from the Arctic Adventfjorden, Svalbard. *Polar Biology* **40**: 1425–1439.

Schuetz R, Kuepfer L, Sauer U. 2007. Systematic evaluation of objective functions for predicting intracellular fluxes in *Escherichia coli*. *Molecular Systems Biology* **3**: 119.

Scott F, Marchant HJ. 2005. *Antarctic marine protists*. Kingston, Tasmania, Australia: Australia Biological Resources Study and Australian Antarctic Division.

Sims PA, Mann DG, Medlin LK. 2006. Evolution of the diatoms: insights from fossil, biological and molecular data. *Phycologia* **45**: 361–402.

Smayda TJ, Mitchell-Innes B. 1974. Dark survival of autotrophic, planktonic marine diatoms. *Marine Biology* **25**: 195–202.

Smith SR, Abbriano RM, Hildebrand M. 2012. Comparative analysis of diatom genomes reveals substantial differences in the organization of carbon partitioning pathways. *Algal Research* **1**: 2–16.

Smith SR, Gillard JTF, Kustka AB, McCrow JP, Badger JH, Zheng H, New AM, Dupont CL, Obata T, Fernie AR *et al.* 2016. Transcriptional orchestration of the global cellular response of a model pennate diatom to diel light cycling under iron limitation. *PLoS Genetics* **12**: 1–39.

Taddei L, Stella GR, Rogato A, Bailleul B, Fortunato AE, Annunziata R, Sanges R, Thaler M, Lepetit B, Lavaud J *et al.* 2016. Multisignal control of expression of the LHCX protein family in the marine diatom *Phaeodactylum tricornutum*. *Journal of Experimental Botany* **67**: 3939–3951.

Taylor F, McMinn A. 2002. Late Quaternary diatom assemblages from Prydz Bay, Eastern Antarctica. *Quaternary Research* **57**: 151–161.

Tirichine L, Bowler C. 2011. Decoding algal genomes: tracing back the history of photosynthetic life on Earth. *The Plant Journal* **66**: 45–57.

Vernotte C, Picaud M, Kirilovsky D, Olive J, Ajlani G, Astier C. 1992. Changes in the photosynthetic apparatus in the cyanobacterium *Synechocystis* sp. PCC 6714 following light-to-dark and dark-to-light transitions. *Photosynthesis Research* **32**: 45–57.

Vizcaíno JA, Csordas A, Del-Toro N, Dianes JA, Griss J, Lavidas I, Mayer G, Perez-Riverol Y, Reisinger F, Ternent T *et al.* 2016. 2016 update of the PRIDE database and its related tools. *Nucleic Acids Research* **44**: D447–D456.

Wessely F, Bartl M, Guthke R, Li P, Schuster S, Kaleta C. 2011. Optimal regulatory strategies for metabolic pathways in *Escherichia coli* depending on protein costs. *Molecular Systems Biology* **7**: 515.

Wilhelm C, Büchel C, Fisahn J, Goss R, Jakob T, LaRoche J, Lavaud J, Lohr M, Riebesell U, Stehfest K *et al.* 2006. The regulation of carbon and nutrient assimilation in diatoms is significantly different from green algae. *Protist* **157**: 91–124.

Wilhelm C, Jungandreas A, Jakob T, Goss R. 2014. Light acclimation in diatoms: from phenomenology to mechanisms. *Marine Genomics* **16**: 5–15.

Wilson R, Diseberg AF, Gordon L, Zivkovic S, Tatarczuch L, Mackie EJ, Gorman JJ, Bateman JF. 2010. Comprehensive profiling of cartilage extracellular matrix formation and maturation using sequential extraction and label-free quantitative proteomics. *Molecular & Cellular Proteomics : MCP* **9**: 1296–1313.

Wilson R, Golub SB, Rowley L, Angelucci C, Karpievitch YV, Bateman JF, Fosang AJ. 2016. Novel elements of the chondrocyte stress response identified using an *in vitro* model of mouse cartilage degradation. *Journal of Proteome Research* **15**: 1033–1050.

Wulff A, Roleda MY, Zacher K, Wiencke C. 2008. Exposure to sudden light burst after prolonged darkness—a case study on benthic diatoms in Antarctica. *Diatom Research* **23**: 519–532.

Yang W, Catalanotti C, Wittkopp TM, Posewitz MC, Grossman AR. 2015. Algae after dark: mechanisms to cope with anoxic/hypoxic conditions. *The Plant Journal* **82**: 481–503.

Zhang Q, Gradinger R, Spindler M. 1995. Dark survival of marine microalgae in the high Arctic (Greenland Sea). *Polarforschung* **65**: 111–116.

Supporting Information

Additional Supporting Information may be found online in the Supporting Information section at the end of the article.

Fig. S1 Photosynthetic parameter alpha.

Fig. S2 Proteins involved in the tetrapyrrole/chlorophyll biosynthetic pathway.

Fig. S3 Proteins involved in carotenoid biosynthesis.

Fig. S4 Proteins involved in fatty acid biosynthesis and β-oxidation.

Fig. S5 Proteins involved in transcription and translation.

Fig. S6 Proteins involved in proteolysis.

Notes S1 18s rRNA – *Fragilariopsis*_ID.

Table S1 Medium nutrient concentrations.

Table S2 Peptide-spectrum matches.

Table S3 Raw protein identifications.

Table S4 Photosynthetic protein abbreviations.

Table S5 Thioredoxin protein expression.

Please note: Wiley Blackwell are not responsible for the content or functionality of any Supporting Information supplied by the authors. Any queries (other than missing material) should be directed to the *New Phytologist* Central Office.

POLAR RESEARCH, 2018
VOL. 37, 1438696
https://doi.org/10.1080/17518369.2018.1438696

RESEARCH NOTE

OPEN ACCESS Check for updates

Response of Antarctic sea-ice algae to an experimental decrease in pH: a preliminary analysis from chlorophyll fluorescence imaging of melting ice

Katerina Castrisios [a], Andrew Martin [a], Marius N. Müller[b], Fraser Kennedy [a], Andrew McMinn[a] & Ken G. Ryan[c]

[a]Institute for Marine and Antarctic Studies, University of Tasmania, Hobart, Australia; [b]Department of Oceanography, Federal University of Recife, Cidade Universitária, Recife, Brazil; [c]School of Biological Sciences, Victoria University of Wellington, Wellington, New Zealand

ABSTRACT

Microorganisms confined to annual sea ice in the Southern Ocean are exposed to highly variable oxygen and carbonate chemistry dynamics because of the seasonal increase in biomass and limited exchange with the underlying water column. For sea-ice algae, physiological stress is likely to be exacerbated when the ice melts; however, variation in carbonate speciation has rarely been monitored during this important state-transition. Using pulse amplitude modulated fluorometry (Imaging-PAM, Walz), we documented in situ changes in the maximum quantum yield of photosystem II (F_v/F_m) of sea-ice algae melting out into seawater with initial pH values ranging from 7.66 to 6.39. Although the process of ice-melt elevated seawater pH by 0.2–0.55 units, we observed a decrease in F_v/F_m between 0.02 and 0.06 for each unit drop in pH during real-time fluorescence imaging. These results are considered preliminary but provide context for including carbonate chemistry monitoring in the design of future sea ice state-transition experiments. Imaging-PAM is a reliable technology for determining F_v/F_m, but is of limited use for obtaining additional photosynthetic parameters when imaging melting ice.

KEYWORDS

Antarctica; imaging-PAM; photophysiology; carbonate chemistry

ABBREVIATIONS

I-PAM: imaging pulse amplitude modulated fluorometry; PAR: photosynthetically active radiation; UV-B: ultraviolet radiation

Introduction

High-latitude waters of the Southern Ocean will be among the first places on Earth to experience the effects of anthropogenic-induced climate change, including ocean warming and acidification (Fabry et al. 2008; Doney 2010). In the McMurdo Sound region of Antarctica, the mean seawater pH is currently 8.05, with a seasonal range of 0.42 units. By 2100 pH is predicted to drop below 7.9 and exhibit greater annual variability (Kapsenberg et al. 2015). The associated change in seawater carbonate speciation (increased CO_2, HCO_3^-, H^+; decreased CO_3^{2-}) and its effect on polar ocean primary production are not fully resolved. Shelf waters surrounding Antarctica are effective sinks for anthropogenic carbon emissions, and increased oceanic CO_2 availability could facilitate faster rates of photosynthesis and growth in marine photoautotrophs (Riebesell et al. 1993). However, dissolved inorganic carbon is rarely in short supply in planktonic ecosystems and many taxa, including diatoms, possess carbon-concentrating-mechanisms that are highly efficient at elevating CO_2 at the site of RuBisCO (Reinfelder 2011; Kranz et al. 2015). To date, incubation experiments with Southern Ocean phytoplankton have demonstrated a variable response to elevated CO_2 (Müller et al. 2015). Some phytoplankton down-regulate carbon-concentrating mechanisms, a response that potentially liberates energy that can be reallocated to other functions (Raven et al. 2011), but this does not always equate to increased growth rates and primary production (Torstensson et al. 2012; Trimborn et al. 2013; McMinn et al. 2014; Young et al. 2015).

For microbes confined to annual sea ice in the Southern Ocean the situation is significantly different. Because of the seasonal increase in biomass and limited exchange with the underlying water column, there are a number of dramatic chemical changes that take place within the ice matrix, specifically variable CO_2, O_2 and pH dynamics (Thomas & Dieckmann 2002; Thomas & Papadimitriou 2003). Efficient physiological acclimation that sustains photosynthesis within the ice is therefore critically important (Arrigo & Thomas 2004; McMinn et al. 2005), but the influence of pH on algal physiology is not clearly understood. Experimental work with cells growing near the upper surface of the ice demonstrates that increased CO_2 enhances growth by approximately 20%, provided that cells are incubated at a constant pH of ca. 8.0 (McMinn et al. 2014). If microbes are exposed to decreasing pH (< ca. 7.2), then the increase in H^+ ions has been shown to reduce growth rates by almost 50% (McMinn et al. 2014).

CONTACT Andrew Martin Andrew.Martin@utas.edu.au Institute for Marine and Antarctic Studies, University of Tasmania, Hobart, Private Bag 129, Hobart, Tasmania 7001, Australia

A general understanding of how sea ice impacts the carbon cycle and ocean–atmosphere CO_2 exchange in polar regions is now emerging (see Rysgaard et al. 2011; Fransson et al. 2015), but the associated changes in carbonate chemistry due to melting ice remain poorly characterized (Bates et al. 2014). The bottom-ice algae that dominate the biological assemblages in Antarctic fast-ice undergo considerable physiological stress during the melt process. This ecological state-transition has been well studied with respect to UV-B and PAR (e.g., Palmisano & Sullivan 1983; Mock & Kroon 2002; McMinn et al. 2010; Ryan et al. 2012), temperature (e.g., Arrigo & Thomas 2004; Mock & Thomas 2005; Ralph et al. 2005) and salinity (e.g., Arrigo & Sullivan 1992; Ralph et al. 2007; Ryan et al. 2011; Ugalde et al. 2014), but not to associated changes in pH. The evolution of distinct pH environments within sea ice has only recently been described by utilizing an experimental outdoor facility (Hare et al. 2013). Analysis of vertical pH profiles revealed a consistent C-shaped pattern with highest pH values (>9) in both top and bottom sections of the ice and lowest pH (ca. 7) in interior ice sections, albeit in the absence of biological activity. In spring and summer, microbial photosynthetic activity depletes dissolved CO_2 and pH rises. However, it is not known how variation in pH influences algal photophysiology with respect to freeze–thaw dynamics.

A particularly useful tool for correlating algal photophysiology with changing environmental conditions has been pulse amplitude modulated fluorometry. This technique is based on measuring variable chlorophyll *a* fluorescence, which provides a unique indicator of intracellular activity in photoautotrophs (Schreiber 2004; Ralph & Gademan 2005; Baker 2008). McMinn et al. (2003) pioneered the use of pulse amplitude modulated fluorometry in Antarctica, and various configurations of the technology have now been employed for the in vitro analysis of ice shavings, extracted brines and melted ice cores (e.g., Ryan et al. 2004; Ralph et al. 2007; Kennedy et al. 2012; Martin et al. 2012). I-PAM (Walz, Germany) provides unprecedented two-dimensional in situ imagery which allows physiological stress to be measured with significantly less disruption of the physical habitat (Ryan et al. 2011; Hawes et al. 2012; Lund-Hansen et al. 2014). This technology has only been employed once in Antarctica and with mixed success (Ryan et al. 2011), but the capacity to generate in situ data warrants further investigation. In this preliminary study, our objectives were to expose sea-ice algae to changes in pH to determine whether short-term (8-h) exposure to reduced pH influences algal photophysiology (Experiment 1) and to quantify changes in pH that occur during the melt process (Experiment 2). We also determine whether imaging fluorescence is a viable technology to resolve changes in algal photophysiology during state-transition experiments.

Materials and methods

Study area

Bottom-ice algae were collected from 1.8 m thick annual fast-ice at Cape Evans, McMurdo Sound, Antarctica (77°38′S, 166°24′E), between 27 November and 1 December 2013 (Fig. 1). Limited incubation space in the field laboratory required that the experiment be carried out over four days; one day per pH treatment and one day for the control. The order of the treatments and control was selected at random to minimize any effect of in situ change in the microbial community. Two ice cores were required each day and these were obtained by drilling to within 300 mm of the ice/water interface using a powered ice auger (Jiffy), and then using a

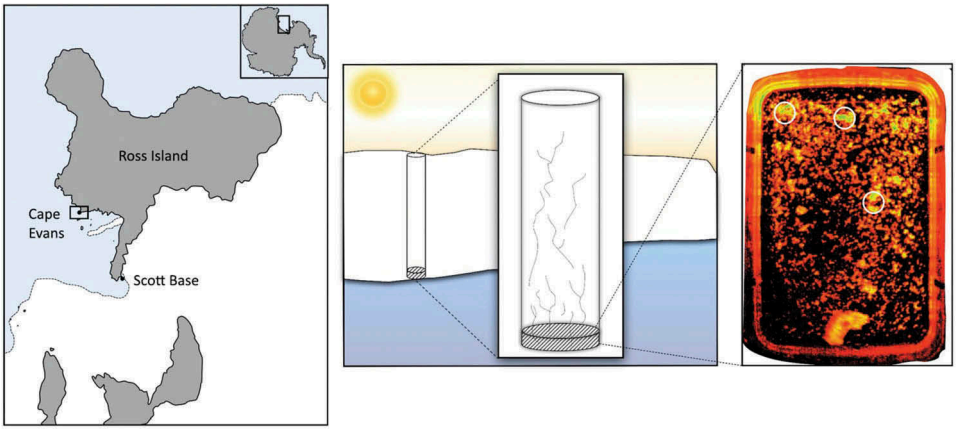

Figure 1. Location and schematic representation of sampling site at Cape Evans, McMurdo Sound, Antarctica. The image on the right shows a typical ice sample melting into manipulated seawater. The ice has been imaged using minimal fluorescence, F_o, with an I-PAM. The circles represent regions of relatively high algal biomass.

Mark V corer (Kovacs) to extract the last section of ice from the bottom of each hole. Once clear of the ice, each core was immediately transferred to a black polythene bag to protect the algae from light shock and transported a short distance to the field laboratory inside a cool box.

Experimental set-up

Each day, the two extracted ice cores were cut, under minimal light, into three pieces 40 mm × 40 mm × 20 mm thick to include bottom-ice algae. The six blocks of ice were then dark-adapted for 30 min in a cool box maintained at about 0°C before being placed into individual airtight plastic containers with clear plastic covers containing 112 ml of seawater (filtered to 0.7 µm, −1.8°C). The seawater had previously been collected from a local dive hole. Seawater pH was reduced by adding HCl which changed the total alkalinity (A_T) while keeping the dissolved inorganic carbon (C_T) concentration relatively constant. Untreated seawater was used as a control treatment (pH 7.66, pCO_2 1651 µatm). The three pH treatments ranged from 7.32 to 6.39 (free scale). During the daily incubation, the six plastic containers containing ice core samples were placed in a temperature controlled water bath at 0.5°C ± 0.2°C for 480 min. An artificial light source comprising a 3 × 4 array of LED lamps suspended 800 mm above the water bath was used to provide an incubation irradiance of 40 µmol photons m^{-2} s^{-1}. Three of the plastic containers were periodically opened in order to assess algal photophysiology (Experiment 1). Constant agitation of the seawater inside the containers (generated by circulation of the liquid in the water bath) ensured that the ice was bathed in seawater and prevented stratification as the ice melted. The other three containers, also exposed to light, remained closed for the duration of the experiment to examine the change in carbonate chemistry due to the melt process and biological activity (Experiment 2).

Experiment 1: photophysiology

Variable chlorophyll fluorescence was measured using the Maxi version of the I-PAM instrument (Walz). The I-PAM Maxi can resolve the distribution of chlorophyll *a* and activity of photosystem II in two dimensions over an area of 130 mm × 100 mm and the user has the option of employing pulse-modulated excitation for the generation of rapid light curves, actinic light and saturation pulses. The blue excitation light supplied by the I-PAM is centred on 450 nm, which is a wavelength that is characteristic of the blue-green spectra at the bottom of the ice (Lund-Hansen et al. 2014). The saturation pulse method was used to determine minimum (F_o) and maximum (F_m) fluorescent yields (F_v/F_m) of the dark-adapted ice samples. The I-PAM operational software includes an area-of-interest function that was used to select three specific locations on each block of ice to obtain F_v/F_m measurements. Selecting locations on each block of ice was a semi-random process; data were only acquired from areas-of-interest where F_o was >0.15. F_o is a measure of minimum fluorescence intensity of algae in the dark-adapted state where intensity is proportional to biomass. Fluorescent measurements of the blocks of ice were made by first removing the lid and then carefully aligning each plastic container on the stage of the I-PAM by using the live near-infrared imaging feature. After obtaining fluorescence measurements the lid was placed back on the container and immediately returned to the water bath. This process was performed in the dark in a field laboratory maintained at ca. 4°C and took no more than 30 s per sample. An initial assessment of F_v/F_m was made before the ice was added to the containers and then at 30-min intervals up to 120 min. Thereafter, fluorescence imaging was carried out at 240, 360 and 480 min. Samples were dark-adapted in the water bath for 10 min prior to fluorescence analysis (10–15 min is typical for dark-adapting sea ice algae (Ralph et al. 2007; McMinn et al. 2010)) by turning off the overhead light array. The generation of rapid light curves was attempted, but like Ryan et al. (2011), we could not achieve the required saturation to derive the necessary parameters.

Experiment 2: carbonate chemistry

Samples for C_T and A_T were taken from replicates of the melted ice at the end of each experimental run. C_T samples were filtered through 0.2 µm sterile filters into 12.5 ml Exetainers (Labco), poisoned with $HgCl_2$ and sealed air tight. A_T samples were filtered through GF/F filters, poisoned with $HgCl_2$ and stored in 250 ml polythene flasks. The programme CO_2SYS version 1.05 (Lewis & Wallace 1998) was used to calculate the carbonate system using the dissociation constants for carbonic acid (Roy et al. 1993). C_T and A_T samples were analysed as the mean of triplicate measurements with the infrared detection method using a dissolved inorganic carbon analyser (Apollo SciTech, model AS-C3) and the potentiometric titration method for A_T. Data were corrected to Certified Reference Materials (Scripps Institution of Oceanography, USA). Consecutive measurements of the Dickson standard resulted in an average precision of >98% for both C_T and A_T.

Ice algal species composition

A 10 ml sample of three randomly selected core sections was fixed in 0.5% gluteraldehyde. A 0.5 ml

aliquot from each sample was prepared using a special settling chamber and cells were examined using a Zeiss compound microscope with standard optics. Microalgae were counted from 10 randomly selected fields of view.

Data analysis

To examine potential changes in maximum quantum yield (F_v/F_m) relative to pH and incubation period, a linear third-order polynomial model was fitted to the data using the statistical package RStudio (version 0.98.939; RStudio Team).

Results and discussion

This is the first study to employ chlorophyll imaging fluorometry to examine the effect of decreased pH on algal photophysiology. Experiments were conducted in a remote Antarctic field camp with limited facilities to replicate a precisely controlled laboratory environment. A broad initial pH regime was chosen (6.39–7.66) to allow for shifts in carbonate chemistry induced by outgassing and experimental handling procedures, specifically the removal of plastic lids to perform I-PAM measurements, which exposed ice samples to the atmosphere (3.5 min during the 8-h incubation, Experiment 1).

The sea ice at Cape Evans in McMurdo Sound was 1.8 m thick in November–December 2013, with no snow cover. The bottom-ice community was dominated by the pennate diatom *Nitzschia stellata*, which accounted for >90% of the observed cells. Other taxa present within the ice included *Fragilariopsis* spp., *Gyrosigma* sp., *Navicula directa* and *N. glaciei*.

Photophysiology

The ratio F_v/F_m derived using the saturation pulse method is a sensitive indicator of photosynthetic potential in photoautotrophs. Prior to incubation, F_v/F_m of the sea-ice algae ranged from 0.37 to 0.52, which is indicative of a relatively healthy community that was well-acclimated to the light climate within the ice matrix (Table 1). At the incubation temperature of 0.5°C, it took approximately two hours for the ice to completely melt, during which time the ice was imaged four times. The post-melt F_v/F_m values obtained at 240, 360 and 480 min were derived from algae that were suspended in seawater (Fig. 1). The maximum quantum yield of photosystem II declined in all treatments and the control during the period of ice-melt (Table 1). This response is indicative of the physiological stress associated with both the transition from semi-solid ice to liquid water and exposure to light. A similar response was documented by Ryan et al. (2011) when sea-ice algae were first examined using imaging fluorescence. These authors also identified salinity to be a significant co-stressor, particularly at concentrations <24. To prevent saline shock in the current study, we used smaller blocks of ice. As a result, the salinity only decreased from 34 to ca. 28 by the end of the experiment (Table 2) and any effect on F_v/F_m is considered to be minimal. To determine whether pH also influenced the photosynthetic yield measurements, we fitted a linear third-order polynomial model to the fluorescence data. This model accounted for the variation in initial F_v/F_m that was evident in the pH 7.66 treatment (Table 2). By retaining only the first order term in the model, the analysis revealed that for each unit drop in pH, the change in yield of photosystem II decreased over time by between 0.02 and 0.06 ($t(10) = 4.06$, $r^2 = 0.623$, $p < 0.01$; Fig. 2).

Table 1. Response of sea-ice algae exposed to variable pH during ice-melt. Maximum quantum yield (F_v/F_m) was determined using imaging fluorescence (I-PAM). Each value is the mean with standard error in parentheses, $n = 3$.

	Initial pH_{free}			
Time (min)	6.39	6.84	7.32	Control (7.66)
0	0.52 (0.01)	0.49 (0.01)	0.49 (0.02)	0.37 (0.02)
30	0.50 (0.02)	0.45 (0.02)	0.46 (0.03)	0.36 (0.02)
60	0.50 (0.02)	0.47 (0.01)	0.44 (0.02)	0.37 (0.02)
90	0.51 (0.03)	0.47 (0.01)	0.43 (0.02)	0.37 (0.02)
120	0.50 (0.02)	0.42 (0.01)	0.41 (0.01)	0.35 (0.04)
240	0.46 (0.02)	0.45 (0.01)	0.45 (0.01)	0.35 (0.03)
360	0.45 (0.01)	0.43 (0.01)	0.41 (0.02)	0.35 (0.04)
480	0.44 (0.02)	0.42 (0.02)	0.43 (0.02)	0.34 (0.02)

Experimental manipulation of pH has two main effects on marine photoautotrophs, specifically acidification (increased H^+) and carbonation (elevated CO_2). Relative to ambient oceanic conditions, the former generally has a negative effect on algal physiology, the latter a positive effect. This results in an optimum curve with respect to the physiological response in marine microbes (see Bach et al. 2015). McMinn et al. (2014) were the first to examine how algae released from the ice matrix respond to manipulated carbonate chemistry, and while a decline in F_v/F_m was observed in brine algae exposed to a pH regime that varied from 8.66 to 7.19, the trend was not significant. More recently, Coad et al. (2016) melted algae from the snow/ice interface region of annual pack-ice into a pH regime that varied from 7.82 to 7.0, but only modest impacts on photophysiology were documented after seven days. Because of this non-response in photosynthetic parameters, McMinn et al. (2017) have questioned the use of pulse amplitude modulated fluorometry to measure stress response in pH/CO_2 experiments. In this study, we adopted a more acidic regime and did observe a significant response to reduced pH. However, the relationship between H^+ concentration and F_v/F_m has yet to be substantiated. Previous studies that have included growth rates (e.g., McMinn et al. 2014; McMinn et al. 2017) have shown

Table 2. Carbonate chemistry of CO_2 manipulation experiment utilizing bottom-ice algae at Cape Evan, 2013. The end of experiment data (8-h incubation) illustrates the changes in carbonate chemistry associated with ice-melt. The unit for C_T, A_T and CO_2 is µmol kg^{-1}. The unit for pCO_2 is µatm.

Initial seawater chemistry									
pH_{free}	Salinity			C_T	SD	A_T	SD	pCO_2	CO_2
Control 7.66	34.67			2303	9	2396	40	1651	44
Start of experiment		End of experiment							
pH_{free}	Salinity	pH_{free}	Salinity	C_T	SD	A_T	SD	pCO_2	CO_2
Control 7.66	34.67	Control 8.15	28.07	2175	220	2493	50	593	16
7.32	34.73	7.52	27.33	2230	260	2282	114	4335	120
6.84	34.70	7.14	30.00	1983	175	1860	19	6547	174
6.39	34.80	6.94	28.67	1879	101	1879	180	10,177	273

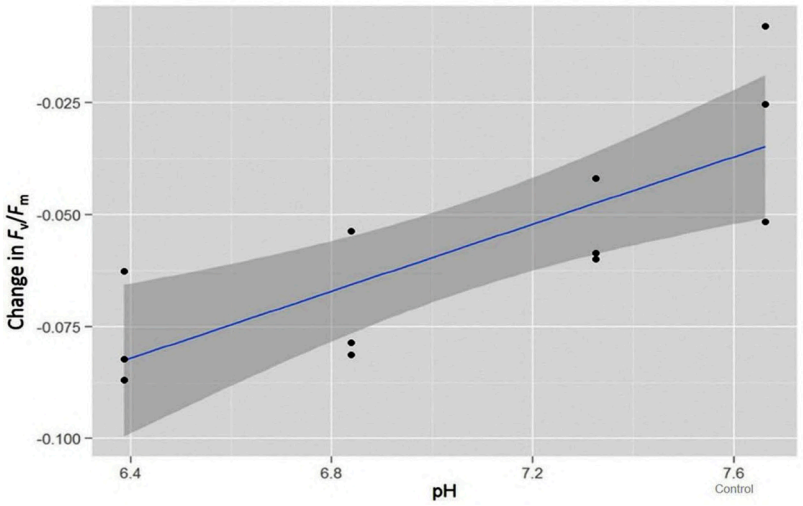

Figure 2. Linear third-order polynomial model of maximum quantum yield (F_v/F_m) for each pH treatment and the control contrasting the difference between start and end-point measurements. The error variance is represented by the dark grey band.

that a decline in growth is attributed to high H+ concentration rather than high CO_2. This suggests that H+ concentration can influence intracellular pH and/or changes in membrane potential, energy partitioning and enzyme activity (Beardall & Raven 2004; Suffrian et al. 2011), and this has a subsequent effect on photosynthetic performance. Although the decline in photosynthetic potential observed during ice-melt was most pronounced in cells exposed to the lowest pH (6.39), F_v/F_m was consistently higher compared to the less acidic treatments and the control (Table 2). This highlights the fact that a significant increase in H+ ions has a minimal short-term effect on F_v/F_m, as assessed using an I-PAM. The relative change in F_v/F_m described by the model must be considered a subtle trend, but it is potentially indicative of a more significant stress response had the experiment been conducted over a longer time period. Importantly, we did not observe a threshold at which point algal photophysiology is compromised to the extent observed when other stressors such as light (Ralph et al. 2007; Ryan et al. 2009; Ryan et al. 2011), temperature (Ralph et al. 2005; Rajanahally et al. 2014) or salinity (Ryan et al. 2004; Ralph et al. 2007; Ryan et al. 2011) are manipulated.

Carbonate chemistry

The aim of Experiment 2 was to provide a rudimentary insight into the changes in pH that occur as the sea ice melts. The post-incubation carbon chemistry data (Table 2) was obtained from plastic containers that were not opened during the incubation period and for that reason the data are not directly comparable with the photophysiology experiment. By the end of the incubation period, ice-melt and the biological activity of liberated microbes had increased the seawater pH in all treatments and the control, from 0.2 to 0.55 units. This provides a very basic illustration of the dynamic that occurs at the receding ice edge which has recently been described at an ecologically relevant scale in the Arctic Ocean as part of the NASA ICESCAPE project (Bates et al. 2014). The carbonate chemistry of below-ice interface melt waters at 19 ice stations was variable and difficult to predict, but generally exhibited higher pH and lower pCO_2 compared to the co-located mixed layer beneath. Although we collected ice cores from a discrete area of sea ice, there was significant variation in post-melt measurements of C_T and A_T, presumably due to variability in biomass and the ratio of ice to

brine volume in each block of ice. However, algal cellular physiology is not directly affected by variation in C_T and A_T; of significance is the change in the total concentration of ions (CO_2, HCO_3, CO_3 and H^+) that are made available.

In situ fluorescence imaging

The practice of actively releasing cells from the ice matrix is likely to modify or damage cellular physiology and ice-associated microbes should ideally be studied in situ. While this has been successfully achieved using oxygen electrodes (e.g., Kühl et al. 2001; Trenerry et al. 2002; McMinn et al. 2012) and habitat modification experiments (Martin et al. 2011), options for physiology experiments are limited. In situ fluorescence imaging is of significant interest because algal photophysiology can be assessed at a spatially relevant scale, specifically the assessment of cells inside the microscopic brine channels that characterise the ice matrix. Although our measurements are only indicative of ablation at the receding ice edge in the austral summer, real-time measurements are considered important because this state-transition, and exposure to physico-chemical stress, occurs relatively quickly. Like Ryan et al. (2011), we could not use the I-PAM to generate rapid light curves and obtain the additional photosynthetic parameters $rETR_{max}$, alpha, and Ek. The maximum rate of electron flow from photosystem II to photosystem I (ETR_{max}) is of particular interest because it describes photosynthetic capacity. The initial ice dimensions used by Ryan et al. (2011) were 70 mm × 60 mm × 15 mm and we reduced this to 40 mm × 40 mm × 20 mm (i.e., a 50% reduction in volume). However, the relative abundance of algae within the ice was still too high. The rapid light curves do not reach an asymptote because multiple layers of densely packed cells confound the required response to the increasing irradiance emitted by the fluorometer. To an extent, this problem has now been addressed by Hawes et al. (2012), who successfully generated rapid light curves RLCs during fluorescence imaging of newly forming Arctic sea ice with a relatively low biomass. These authors used the I-PAM Mini (Walz), which has a reduced imaging area of 30 × 23 mm, and integrated the fluorescence data obtained from a series of ice core sections that were 2 mm thick. Working with such thin sections is not a practical solution in state-transition experiments because of rapid ice-melt. For this reason we suggest the I-PAM Maxi is only relevant for collecting in situ measurements of maximum quantum yield (F_v/F_m).

Conclusion

This is the first study to document statistically significant photophysiological stress in sea-ice algae due to decreased pH. Future experiments will require greater experimental precision, but the data provide context for assessing the relative importance of carbonate chemistry to sea-ice ecophysiology. Importantly, the physiological stress associated with rapid exposure to high light and low salinity during ice-melt is significant and the compound stress associated with the projected decline in pH in Antarctic coastal waters has the potential to shift environmental conditions beyond physiologically tolerable levels (McMinn et al. 2014). A mechanistic understanding of how ice-associated microbes adapt to freeze–thaw dynamics requires a clearer insight into how pH influences algal physiology. For this reason, we suggest that carbonate chemistry monitoring should be included in the design of future multi-stressor state-transition experiments.

Acknowledgements

We thank Antarctica New Zealand for logistic support and the staff at Scott Base for their help in preparation and deployment to the field.

Disclosure statement

No potential conflict of interest was reported by the authors.

Funding

We acknowledge Victoria University of Wellington grant 100241 for financial support.

ORCID

Katerina Castrisios http://orcid.org/0000-0001-6085-9077
Andrew Martin http://orcid.org/0000-0001-8260-5529
Fraser Kennedy http://orcid.org/0000-0003-1796-0764

References

Arrigo K.R. & Sullivan C.W. 1992. The influence of salinity and temperature covariation on the photophysiological characteristics of Antarctic sea ice microalgae. *Journal of Phycology 28*, 746–756.

Arrigo K.R. & Thomas D.N. 2004. Large scale importance of sea ice biology in the Southern Ocean. *Antarctic Science 16*, 471–486.

Bach L.T., Riebesell U., Gutowska M.A., Federwisch L. & Schulz K.G. 2015. A unifying concept of coccolithophore sensitivity to changing carbonate chemistry embedded in an ecological framework. *Progress in Oceanography 135*, 125–138.

Baker N.R. 2008. Chlorophyll fluorescence: a probe of photosynthesis in vivo. *Annual Review of Plant Biology 59*, 89–113.

Bates N.R., Garley R., Frey K.E., Shake K.L. & Mathis J.T. 2014. Sea–ice melt CO_2-carbonate chemistry in the western Arctic Ocean: meltwater contributions to air–sea CO_2 gas exchange, mixed-layer properties and rates of net community production under sea ice. *Biogeosciences 11*, 6769–6789.

Beardall J. & Raven J.A. 2004. The potential effects of global climate change on microalgal photosynthesis, growth and ecology. *Phycologia 43*, 26–40.

Coad T., Nomura D., McMinn A. & Martin A. 2016. Effect of elevated CO_2 concentration on the photophysiology and growth of microalgae in Antarctic pack ice communities. *Deep-Sea Research Part II Topical Studies in Oceanography 131*, 160–169.

Doney S.C. 2010. The growing human footprint on coastal and open-ocean biogeochemistry. *Science 328*, 1512–1516.

Fabry V.J., Seibel B.A., Feely R.A. & Orr J.C. 2008. Impacts of ocean acidification on marine fauna and ecosystem processes. *Journal of Marine Science 65*, 414–432.

Fransson A., Chierici M., Nomura D., Granskog M.A., Kristiansen S., Martma T. & Nehrke G. 2015. Effect of glacial drainage water on the CO_2 system and ocean acidification state in an Arctic tidewater-glacier fjord during two contrasting years. *Journal of Geophysical Research—Oceans 120*, 2413–2429.

Hare A.A., Wang F., Barber D., Geilfus N.-X., Galley R.J. & Rysgaard S. 2013. pH evolution in sea ice grown at an outdoor experimental facility. *Marine Chemistry 154*, 46–54.

Hawes I., Lund-Hansen L.C., Sorrell B.K., Nielson M.H., Borzák R. & Buss I. 2012. Photobiology of sea ice algae during initial spring growth in Kangerlussuaq, west Greenland: insights from imaging variable chlorophyll fluorescence of ice cores. *Photosynthesis Research 112*, 103–115.

Kapsenberg L., Kelley A.L., Shaw E.C., Martz T.R. & Hofmann G.E. 2015. Near-shore Antarctic pH variability has implications for the design of ocean acidification experiments. *Scientific Reports 5*, article no. 10497, doi: 10.1038/srep10497.

Kennedy F., McMinn A. & Martin A. 2012. Effect of temperature and sea ice on the photosynthetic efficiency and morphotype of *Phaeocystis antarctica*. *Journal of Experimental Marine Biology and Ecology 429*, 7–14.

Kranz S.A., Young J.N., Hopkinson B., Goldman J.A.L., Tortell P.D. & Morel F.M.M. 2015. Low temperature reduces the energetic requirement for the CO_2 concentrating mechanism in diatoms. *The New Phytologist 205*, 192–201.

Kühl M., Glud R.N., Borum J., Roberts R. & Rysgaard S. 2001. Photosynthetic performance of surface-associated algae below sea ice as measured with a pulse-amplitude-modulated (PAM) fluorometer and O_2 microsensors. *Marine Ecology Progress Series 223*, 1–14.

Lewis E. & Wallace D.W.R. 1998. *Program developed for CO_2 system calculations. ORNL/CDIAC-105*. Oak Ridge, TN: Carbon Dioxide Information Analysis Center, Oak Ridge National Laboratory, US Department of Energy.

Lund-Hansen L.C., Hawes I., Sorrell B.K. & Nielsen M.H. 2014. Removal of snow cover inhibits spring growth of Arctic ice algae through physiological and behavioural effects. *Polar Biology 37*, 471–481.

Martin A., Anderson M.J., Thorn C., Davy S.K. & Ryan K. G. 2011. Response of sea-ice microbial communities to environmental disturbance: an in situ transplant experiment in the Antarctic. *Marine Ecology Progress Series 424*, 25–37.

Martin A., McMinn A., Heath M., Hegseth E. & Ryan K.G. 2012. The physiological response to increased temperature in over-wintering sea ice algae and phytoplankton in McMurdo Sound, Antarctica and Tromsø Sound, Norway. *Journal of Experimental Marine Biology and Ecology 428*, 57–66.

McMinn A., Ashworth C., Bhagooli R., Martin A., Salleh S., Ralph P. & Ryan K.G. 2012. Antarctic coastal microalgal primary production and photosynthesis. *Marine Biology 159*, 2827–2837.

McMinn A., Martin A. & Ryan K.G. 2010. Phytoplankton and sea ice algal biomass and physiology during the transition between winter and spring (McMurdo Sound, Antarctica). *Polar Biology 33*, 1547–1556.

McMinn A., Müller M.N., Martin A. & Ryan K.G. 2014. The response of Antarctic sea ice algae to changes in pH and CO_2. *PLoS One 9*, e86984, doi: 10.1371/journal.pone.0086984.

McMinn A., Müller M.N., Martin A., Ugalde S.C., Lee S., Castrisios K. & Ryan K.G. 2017. Effects of CO_2 concentration on a late summer surface sea ice community. *Marine Biology 164*, article no. 87, doi: 10.1007/s00227-017-3102-4.

McMinn A., Pankowski A. & Delfatti T. 2005. Effect of hyperoxia on the growth and photosynthesis of polar sea ice microalgae. *Journal of Phycology 41*, 732–741.

McMinn A., Ryan K.G. & Gademann R. 2003. Diurnal changes in photosynthesis of Antarctic fast ice algal communities determined by pulse amplitude modulation fluorometry. *Marine Biology 143*, 359–367.

Mock T. & Kroon B.M. 2002. In situ primary production in young Antarctic sea ice. *Hydrobiology 470*, 127–132.

Mock T. & Thomas D.N. 2005. Recent advances in sea-ice microbiology. *Environmental Microbiology 7*, 605–619.

Müller M.N., Trull T.W. & Hallegraeff G.M. 2015. Differing response of three Southern Ocean *Emiliania huxleyi* ecotypes to changing seawater carbonate chemistry. *Marine Ecology Progress Series 531*, 81–90.

Palmisano A.C. & Sullivan C.W. 1983. Sea-ice microbial communities (SIMCO). I. *Polar Biology 2*, 171–177.

Rajanahally M.A., Sim D., Ryan K.G. & Convey P. 2014. Can bottom ice algae tolerate irradiance and temperature changes? *Journal of Experimental Marine Biology and Ecology 461*, 516–527.

Ralph P.J. & Gademan R. 2005. Rapid light curves: a powerful tool to assess photosynthetic activity. *Aquatic Botany 82*, 222–237.

Ralph P.J., McMinn A., Ryan K.G. & Ashworth C. 2005. Short-term effect of temperature on the photokinetics of microalgae from the surface layers of Antarctic pace ice. *Journal of Phycology 41*, 763–769.

Ralph P.J., Ryan K.G., Martin A. & Fenton G. 2007. Melting out of sea ice causes greater photosynthetic stress in sea ice algae than freezing in. *Journal of Phycology 43*, 948–956.

Raven J.A., Giordano M., Beardall J. & Maberly S.C. 2011. Algal and aquatic plant carbon concentrating mechanisms in relation to environmental change. *Photosynthesis Research 109*, 281–296.

Reinfelder J.R. 2011. Carbon concentrating mechanisms in eukaryotic marine phytoplankton. *Annual Review of Marine Science 3*, 291–315.

Riebesell U., Wolf-Gladrow D.A. & Smetacek V. 1993. Carbon dioxide limitation of marine phytoplankton growth rates. *Nature 361*, 249–251.

Roy R.N., Roy L.N., Vogel K.M., Porter-Moore C., Pearson T., Good C., Millero F.J. & Campbell D.M. 1993. The dissociation constants of carbonic acid in seawater at salinities 5 to 45 and temperatures 0 to 45°C. *Marine Chemistry 44*, 249–267.

Ryan K.G., Cowie R., Liggins E., McNaughtan D., Martin A. & Davy S.K. 2009. The short-term effect of irradiance on the photosynthetic properties of Antarctic fast-ice microalgal communities. *Journal of Phycology 45*, 1290–1298.

Ryan K.G., McMinn A., Hegseth E. & Davy S.K. 2012. The effects of ultraviolet-B radiation on Antarctic sea-ice algae. *Journal of Phycology 48*, 74–84.

Ryan K.G., Ralph P.J. & McMinn A. 2004. Photoacclimation of Antarctic bottom ice algal communities to lowered salinities during melting. *Polar Biology 27*, 679–686.

Ryan K.G., Tay M.L., Martin A., McMinn A. & Davy S.K. 2011. Chlorophyll fluorescence imaging analysis of the responses of Antarctic bottom-ice algae to light and salinity during melting. *Journal of Experimental Marine Biology and Ecology 399*, 156–161.

Rysgaard S., Bendtsen J., Delille B., Dieckmann G.S., Glud R., Kennedy H., Mortensen J., Papadimitriou S., Thomas D.N. & Tison J.-L. 2011. Sea ice contribution to the air-sea CO_2 exchange in the Arctic and Southern Oceans. *Tellus Series B Chemical and Physical Meteorology 63*, 823–830.

Schreiber U. 2004. Pulse-amplitude-modulated (PAM) fluorometry and saturation pulse method: an overview. In G.C. Papageorgiou & Govindjee (eds.): *Chlorophyll a fluorescence: a signature of photosynthesis*. Pp. 279–319. Dordrecht: Springer.

Suffrian K., Schulz K.G., Gutowska M.A., Riebesell U. & Bleich M. 2011. Cellular pH measurements in *Emiliania huxleyi* reveal pronounced membrane proton permeability. *New Phytologist 190*, 595–608.

Thomas D.N. & Dieckmann G.S. 2002. Biogeochemistry of Antarctic sea ice. In R.N. Gibson et al. (eds.): *Oceanography and marine biology: an annual review. Vol. 40*. Pp. 143–169. Boca Raton, FL: CRC Press.

Thomas D.N. & Papadimitriou S. 2003. Biogeochemistry of sea ice. In D.N. Thomas & G.S. Dieckmann (eds.): *Sea ice – an introduction to its physics, biology and geology*. Pp. 267–302. Oxford: Blackwell Publishing.

Torstensson A., Chierici M. & Wulff A. 2012. The influence of increased temperature and carbon dioxide levels on the benthic/sea ice diatom *Navicula directa*. *Polar Biology 35*, 205–214.

Trenerry L.J., McMinn A. & Ryan K.G. 2002. In situ oxygen microelectrode measurements of bottom-ice algal production in McMurdo Sound, Antarctica. *Polar Biology 25*, 72–80.

Trimborn S., Brenneis T., Sweet E. & Rost B. 2013. Sensitivity of Antarctic phytoplankton species to ocean acidification: growth, carbon acquisition, and species interaction. *Limnology and Oceanography 58*, 997–1007.

Ugalde S., Martin A., Meiners K.M., McMinn A. & Ryan K. G. 2014. Extracellular organic carbon dynamics during a bottom-ice algal bloom (Antarctica). *Aquatic Microbial Ecology 73*, 195–210.

Young J.N., Kranz S.A., Goldman J.A.L., Tortell P.D. & Morel F.M.M. 2015. Antarctic phytoplankton down-regulate their carbon-concentrating mechanisms under high CO_2 with no change in growth rates. *Marine Ecology Progress Series 532*, 13–28.

Annals of Glaciology 58(75pt1) 2017 doi: 10.1017/aog.2017.6

Towards improved estimates of sea-ice algal biomass: experimental assessment of hyperspectral imaging cameras for under-ice studies

Emiliano CIMOLI,[1] Arko LUCIEER,[2] Klaus M. MEINERS,[3,4] Lars Chresten LUND-HANSEN,[5,6] Fraser KENNEDY,[1] Andrew MARTIN,[1] Andrew McMINN,[1] Vanessa LUCIEER[1]

[1]*Institute for Marine and Antarctic Studies, University of Tasmania, Hobart, Tasmania 7001, Australia.*
E-mail: emiliano.cimoli@utas.edu.au
[2]*School of Land and Food, University of Tasmania, Hobart, Tasmania 7001, Australia*
[3]*Australian Antarctic Division, Department of the Environment and Energy, Kingston, Tasmania 7050, Australia*
[4]*Antarctic Climate & Ecosystems Cooperative Research Centre, University of Tasmania, Hobart, Tasmania 7001, Australia*
[5]*Aquatic Biology, Department of Bioscience, Aarhus University, DK-8000 Aarhus C, Denmark*
[6]*Arctic Research Centre, Aarhus University, DK-8000 Aarhus C, Denmark*

ABSTRACT. Ice algae are a key component in polar marine food webs and have an active role in large-scale biogeochemical cycles. They remain extremely under-sampled due to the coarse nature of traditional point sampling methods compounded by the general logistical limitations of surveying in polar regions. This study provides a first assessment of hyperspectral imaging as an under-ice remote-sensing method to capture sea-ice algae biomass spatial variability at the ice/water interface. Ice-algal cultures were inoculated in a unique inverted sea-ice simulation tank at increasing concentrations over designated cylinder enclosures and sparsely across the ice/water interface. Hyperspectral images of the sea ice were acquired with a pushbroom sensor attaining 0.9 mm square pixel spatial resolution for three different spectral resolutions (1.7, 3.4, 6.7 nm). Image analysis revealed biomass distribution matching the inoculated chlorophyll *a* concentrations within each cylinder. While spectral resolutions >6 nm hindered biomass differentiation, 1.7 and 3.4 nm were able to resolve spatial variation in ice algal biomass implying a coherent sensor selection. The inverted ice tank provided a suitable sea-ice analogue platform for testing key parameters of the methodology. The results highlight the potential of hyperspectral imaging to capture sea-ice algal biomass variability at unprecedented scales in a non-invasive way.

KEYWORDS: hyperspectral imaging, ice algae, ice tank, remote sensing, sea ice, under-ice environment

INTRODUCTION

Sea-ice algae are important contributors to primary production in the polar oceans (McMinn and others, 2012; Arrigo and others, 2014; Kohlbach and others, 2016) and play an active role in large-scale biogeochemical cycles determining rates of carbon export (Boetius and others, 2013) and ocean/atmosphere exchange (Vancoppenolle and others, 2013). During winter and spring, sea-ice algae are vital for polar marine ecosystems as they provide an essential food source for pelagic herbivores (Flores and others, 2012; Arrigo and others, 2014). During the melt season, ice algae can seed the spring phytoplankton bloom following ice ablation (Brugel and others, 2009; Søreide and others, 2010; Mundy and others, 2014).

Chlorophyll *a* (chl-a) concentrations in sea ice are considered a useful proxy for algal biomass abundance (Gradinger, 2009; Meiners and others, 2012). The highest algal standing stocks are usually found at the bottom of the ice cover near the ice/water interface (Arrigo and others, 2010). Using chl-a as proxy, several studies have reported high spatial variability in ice-algal biomass, for example changes across multiple orders of magnitude on spatial scales ranging from millimetres (Hawes and others, 2012) to the mesoscale (metres to kilometres) (Steffens and others, 2006; Gradinger, 2009).

Unlike phytoplankton and ocean colour, chl-a concentrations in sea ice cannot be monitored with aerial or satellite remote-sensing techniques. Current sea-ice chl-a sampling methods include ice core sampling (Miller and others, 2015), diver operated fluorometers (Rysgaard and others, 2001) or simple imagery data (such as video or still photographs) (Gutt, 1995; Katlein and others, 2015). These established methodologies are labour intensive, invasive or have a coarse resolution and are not appropriate for capturing the high spatial and temporal variability of ice-algae biomass. This has consequences for our understanding of ice-algal dynamics, with associated implications for estimating their overall contribution to marine production and how they respond to environmental changes (Meiners and others, 2012). Due to the high logistical costs involved in monitoring in the harsh polar environments, there is a need to develop new and efficient methodologies that can efficiently track ice-algal biomass across multiple spatial scales.

Recent studies have explored methods for quantifying chl-a (as proxy for biomass) within sea ice by measuring the spectral composition of downward transmitted visible light that is measured beneath the ice/water interface (Mundy and others, 2007; Campbell and others, 2014; Melbourne-Thomas and others, 2015). Transmitted light measurements

at the ice bottom can provide information on algal biomass due to the light absorption by algal pigments such as chl-a (Maykut and Grenfell, 1975; Perovich, 1996). Quantitative methods are usually performed by deploying upward looking spectral irradiance sensors below the ice (at 15–50 cm distance) using an L-arm. The measured spectrum of transmitted irradiance can then be statistically correlated to the amount of measured chl-a (determined from ice core samples) using empirical correlations methods and univariate models such as Normalized Difference Indices (NDI) or Empirical Orthogonal Functions (EOFs) (Mundy and others, 2007; Melbourne-Thomas and others, 2015; Lange and others, 2016). These novel methods are providing new opportunities for monitoring ice-algal biomass at an increased sampling rate in a non-invasive manner. For example, irradiance sensors can be mounted on Remotely Operated Vehicles (ROVs) for further enhancing the spatial extent of these surveys (Lange and others, 2016). The use of transmitted irradiance spectra, however, only determines the integrated (over the entire ice thickness) ice-algal biomass.

We are taking advantage of such considerations and for the first time we experimentally assess the possibility of employing hyperspectral imaging (HI) cameras in transmission mode (measuring transmitted instead of reflected light) to map sea-ice algae biomass distribution at the ice/water interface. In contrast to the wide and disconnected footprint of radiance and irradiance sensors, HI cameras are able to map spectral signatures across a target area at high spatial resolutions (Johnsen and others, 2013; Amigo and others, 2015). HI is usually employed in reflectance mode and these systems are gaining considerable momentum in the natural sciences and close-range remote-sensing domain as the technology becomes more accessible and portable (e.g. Lucieer and others, 2014; Malenovský and others, 2015; Holzinger and others, 2016). Recent applications in related disciplines include mapping of benthic algae distributions and biomass (Chennu and others, 2013), coral physiology (Perkins and others, 2016) and algae pigment composition (Nogami and others, 2014). Sea ice is an optically complex medium and there are many challenges in measuring transmitted radiance through the ice that need to be overcome through gradual testing and evaluation both in laboratory and in-situ studies. Aside from understanding the target spectral signature, we also need to understand the complexity associated with both under-ice HI deployment and data processing.

In the present study, a HI camera was used to image an inverted sea-ice simulation tank specifically designed for growing and monitoring sea-ice microbial consortia at the ice/water interface. The tank is termed 'inverted' due to its 'upside down' representation of the sea-ice environment, i.e. the light source is beneath the ice and a water layer is above it (Fig. 1). This configuration provides an ideal environment for testing different hyperspectral imaging scenarios in a controlled environment.

This first test is a proof of concept, aimed to developing a near remote-sensing method that can identify ice-algae patchiness at multiple spatial scales in a non-invasive manner. For this purpose, we inoculated the tank with ice-algal communities to establish six spatially variable algal patches at the tank's ice/water interface. This study starts by outlining our novel experimental set-up and the data acquisition methodologies. We then employ exploratory image analysis to assess the feasibility of HI to resolve ice-algal spatial variability. The study concludes by comparing our sea-ice tank to an in-situ scenario and discussing future possibilities and limitations of the method.

DATA AND METHODOLOGY

All experiments were conducted at the Algal Laboratories of the Institute of Marine and Antarctic Studies in Hobart, at the University of Tasmania, Australia. The experiment was divided into five sequential phases; (1) ice-tank preparation, (2) algae culturing, (3) hyperspectral imaging, (4) chl-a sampling and (5) data processing.

Inverted ice-tank design and preparation

The inverted ice tank was built as an 'upside down' representation of the sea-ice environment comprising, from the bottom to the top, a light source, air, glass, ice and water interfaces (Fig. 1).

The tank's area of frozen ice is 0.85 m × 0.85 m and ice growth is initiated using 30 litres of filtered deionized water frozen overnight (at −20 °C) followed by the addition of 70 litres of pre-chilled (−1.7 °C) 0.2 µm filtered seawater. The initial addition of fresh water is necessary to ensure that the freezing seawater adhered to the base of the tank and did not float to the surface by expulsion of the hypersaline brine. The filtered seawater layer (36 ppt) was left to freeze for 2 days followed by the removal of excess hypersaline brine resulting in an ice thickness of ~70 mm. Additional pre-chilled seawater (−1.7 °C, 36 ppt) was then added to achieve a 20–30 mm water layer above the ice, which remained unfrozen at a temperature of ~−1.8°C. Images of the ice surface before algae inoculation are shown in Figures 2a, b.

The upward directed light source is a Cree Xlamp XP-E High-Efficiency white LED and has a typical double bell spectral curve characteristic of white LED light sources (Fig. 1). It covers the Photosynthetically Active Radiation (PAR) (from 400 to 700 nm) range and provides moderate intensities in the regions of interest where ice algae show their main absorption peaks (e.g. Fritsen and others, 2011). The lighting system was deliberately installed to be consistent with measured under-ice PAR irradiance intensities. For example, using a Li-COR PAR sensor to measure light flux at the ice/water interface of the inverted ice tank, we measured light levels ranging from 31.4 to 58.6 µmol photon m^{-2} s^{-1} from the dark areas to bright areas. This is comparable with in-situ measurements beneath Arctic (e.g. Lund-Hansen and others, 2014) or Antarctic sea ice (e.g. SooHoo and others, 1987). The glass sheet between the light source, the ice and water layers is optically clear allowing transmission of >90% of light and having minimal influence on the optical properties of the transmitted light.

Ice algae culturing and inoculation

Algal cultures consisting of *Fragilariopsis cylindrus, Nitzschia stellata* and *Navicula glaciei* were extracted from Antarctic sea ice in 2015, and maintained semi-continuously in L_{10} media (Guillard and Ryther, 1962) under cool white fluorescent light (60 µmol photon m^{-2} s^{-1}, 12:12 light/dark cycle) at 2 ± 1°C. Each algal species was grown separately in a continuous batch system, bubbled with 0.2 um filtered air and

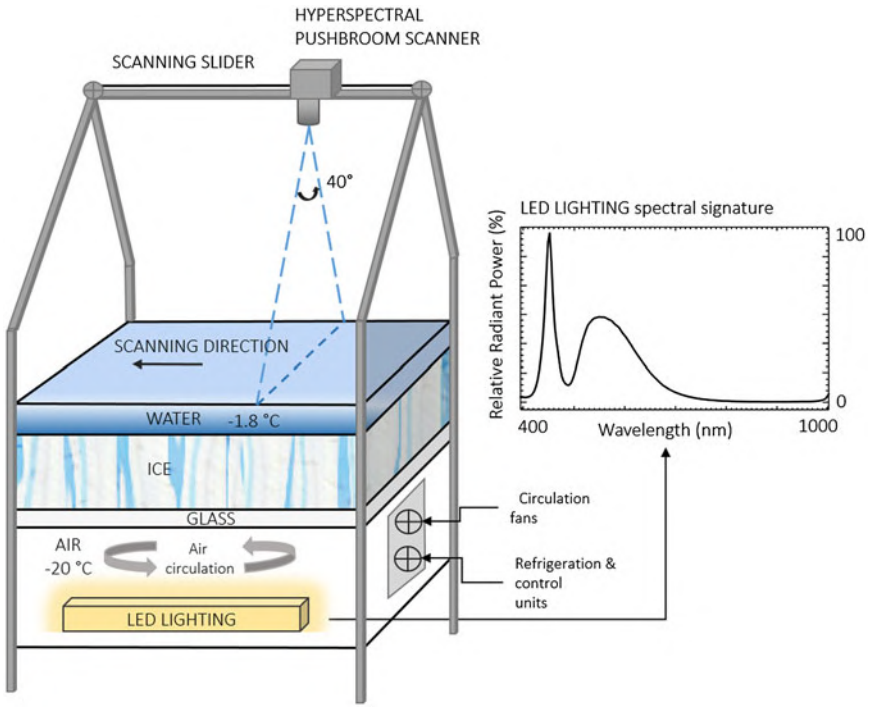

Fig. 1. Illustration of the inverted sea-ice simulation tank and spectral signature of the LED artificial light source. The hyperspectral pushbroom scanner was mounted onto a motorized sliding rail at 1.2 m distance above the ice/water interface. The layered surfaces (glass, ice, water) cover an area of 0.85 m × 0.85 m. The distance from the camera fore-optics to the ice layer is 1 m. The illustration is not to scale.

amended with L_1 nutrients (Guillard and Ryther, 1962). Before inoculation, cells were acclimated to −1°C over a 12-h period to limit any cold induced shock from the ice-tank environment. Once ready for inoculation, varying volumes were extracted from the parent cultures and added to a set of eight cylinders to spatially distribute algal biomass at increasing concentrations. This provided an increasing scale of biomass abundance intensities among the eight cylinders.

The cylinders were 80 mm in diameter and 50–60 mm high and were placed 20–30 mm deep in the ice layer and left emerging above the water surface layer (Fig. 2d). Two types of material were chosen for the cylinders; opaque PVC tubes and optically clear acrylic tubes. Based on the expected concentrations, the biomass abundance intensities inoculated in the eight cylinders were denominated as follows: two empty controls (C1 and C2) in PVC and acrylic, respectively; a Very Low (VL) in PVC; a Low (L) in acrylic; a Medium (M) in acrylic; a Medium High (MH) in PVC; a High (H) in acrylic; and a Very High (VH) in PVC. Figure 2d shows the VH PVC cylinder after inoculation.

Hyperspectral imaging

A pushbroom SPECIM AISA KESTREL 10 (AK10) hyperspectral line scanner was employed for imaging the algal distributions at the ice/water interface (Figs 2b, c). Imaging with the pushbroom sensor required a scan to be conducted in a forward motion across the target of interest in order to create the image (Fig. 1). Thus, the AK10 was integrated into a motorized slider with precise adjustable speeds for this purpose (Fig. 2b). The AK10 has a 40° Field of View (FOV) and comprises a total of 2048 pixels that can be binned into 1020 to improve the Signal to Noise Ratio

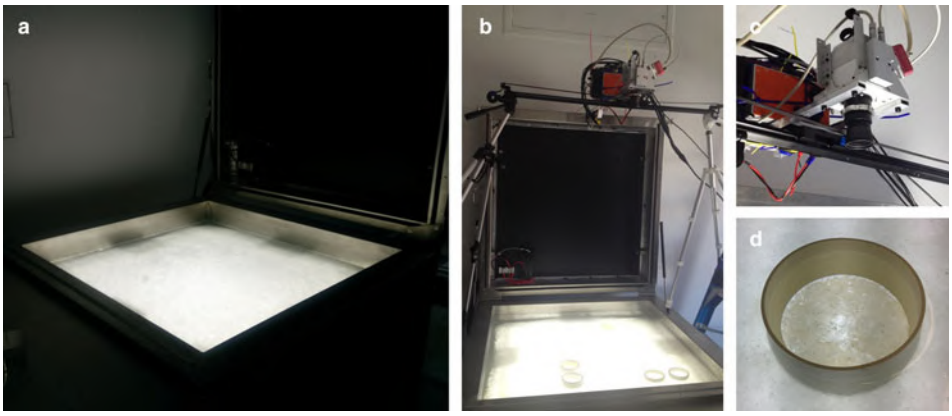

Fig. 2. (a) Image of the inverted sea-ice simulation tank in the dark room setting with all external light sources off. (b) Image of the inverted ice tank together with the motorized slider and the cylinder's set-up. (c) The SPECIM AISA Kestrel 10 hyperspectral imager. (d) High (H) algae abundance cylinder after two days of algae inoculation.

(SNR) per pixel. The sensor's spectral range goes from 400 to 1000 nm and allows for customized spectral resolution and integration times (frequency) to be set according to the survey scenario. The motorized slider was placed 1.2 m above the ice/water interface (1 m considering the camera fore-optics) allowing the camera to achieve a spatial across-track resolution of 0.9 mm, which covered a scan line width of 728 mm. The imaging frequency was set to 5 Hz and the sliding rail speed ~8–10 mm s^{-1} providing along-track resolution of 0.8–0.9 mm (thus 0.9 mm square pixels in the composed image). Hereafter, a spatial resolution of 0.9 mm will refer to the 0.9 mm × 0.9 mm squared nature of the image pixel size. We selected the slider speed and frequency to maximize the intensity of the acquired signal, or SNR. For this experiment, we repeated the scanning process at three different spectral resolutions of 1.7, 3.4 and 6.8 nm in order to assess the effect of spectral resolution. All three frames were binned to 1020 pixels. The hyperspectral imaging was performed in the dark with no influence from any other external light source except the tank's LED light source (Fig. 2a). HI on the tank was performed 3 days after inoculation of algae.

Chl-a sampling

In order to provide a semi-quantitative validation of the six cylinders' chl-a concentrations, the cylinders were sampled using a 10 mL lab-pipette by scratching the ice while simultaneously sucking up any content at the ice/water interface in five different 1 cm^2 random spots within each cylinder. 1 cm^2 sample sub-areas were roughly measured with a mm-scale ruler resting above the cylinders while operating the pipette. The 50 mL samples for each cylinder were immediately filtered onto Whatman GF/F filters, extracted for 24 h in ethanol and analyzed for chl-a content according to Holm-Hansen and Riemann (1978) using a Turner 10 AU fluorometer.

Data processing

The images were composed from the acquired line-scans using SPECIM Lumo Recorder software. All hyperspectral images were converted to radiance values (W m^{-2} sr^{-1} nm^{-1}) per pixel from the raw digital numbers (DN) using ENVI software and the provided calibration files. The images are then pre-processed using MATLAB. Pre-processing involved selecting a region of interest (ROI) and spectral filtering. Selecting an ROI was done manually and this process discarded the extra imaged areas that are not the ice/water interface such as the steel borders of the ice tank (Fig. 2b). Even though the images resulted in high SNR by measuring just below the saturation level, we performed a Savitzy-Golay filter with a third polynomial order and a filter width of five (Tsai and Philpot, 1998; Vidal and Amigo, 2012). The filter aimed to smooth out the high-frequency noise while preserving the relevant spectral features at low intensity wavelengths. In order to capture the differences between different algae abundances from light transmitted through the artificial sea ice, Principal Component Analysis (PCA) was performed on the three images taken at the three different spectral resolutions. The hyperspectral images consist of a three-dimensional (x, y, λ) data cubes where x and y represent the spatial dimension and λ the spectral dimension. PCA exploration method was applied in this case to track the most variable features across the spectral dimension of the hyperspectral images and to outline relevant spectral bands carrying the relevant information on ice-algal biomass (Rodarmel and Shan, 2002; Amigo and others, 2015).

Transmitted radiance measured with the AK10 was compared with publically available data from a series of Remotely Operated Vehicle (ROV) transects performed in the Arctic by Nicolaus and Katlein (2013) to provide a comparison with spectral data collected under in-situ conditions. Radiance along these transects, was measured using an ROV instrumented with a TRiOS RAMSES radiance sensor (of 3 nm spectral resolution). Operating depths ranged from 1 to 8 m, for different sea-ice types, which varied from snow-free to variable snow cover (from 2 to 10 cm thickness), from First Year Ice (FYI) to Multi Year Ice (MYI) (from 0.3 to 3.8 m thickness). Detailed information about each transect can be found in Nicolaus and Katlein (2013). The ROV dataset is available online under doi:10.1594/PANGAEA.78671.

RESULTS

The arrangement of the algal cylinders in the ice tank is shown in Figure 3a as an RGB composite image. The figure also displays the ice-algal biomass range from VL to VH as inoculated across the cylinders. The results of the PCA for the HI frame taken at 1.7 nm are shown in Figures 3b–d.

The first principal component (PC1) accounts for 99.8 % of the spectral variability (Fig. 3b) and represents variations in light intensity across the ice tank. This is confirmed by the loadings of PC1 that clearly match the spectral intensity of the LED light source (Figs 1, 3c). The light intensity is higher at the centre and decreases towards the edges of the ice tank. This difference in light intensity across the tank is mostly attributed to the non-diffuse (directional) light field emitted by the light source and the shadow structures in the image caused by the circulation fans and the presence of their sustaining structure between the light source and the ice. Another factor influencing light intensity variability was the different ice thickness observed from 7–9 cm at the centre to 5 cm at the edges (due to physical complications of achieving freezing conditions in those locations). PC1 does not contain any information regarding biomass variability but indicatively maps the light intensity distribution over the ice surface.

The second principal component (PC2) accounts for 0.09 % of the spectral variation in the hyperspectral image but displays a coherent relationship to the algal cylinder densities. High and low PC2 intensity areas match with low and high biomass values, respectively. Control cylinders (C1 and C2) stand out as high intensity areas opposing to H and VH cylinders (Fig. 3d). Results from the chl-a sampling are in agreement with the visual observations for VL (0.036 mg m^{-2}), L (0.164 mg m^{-2}), M (0.366 mg m^{-2}), MH (0.636 mg m^{-2}). Chl a sampling in cylinders H (2.712 mg m^{-2}) and VH (1.804 mg m^{-2}) did not match with the increasing inoculation scale with H cylinder having a higher chl-a concentration than VH. Loadings of PC2 in Figure 3c indicate that low PC2 intensity in Figure 3d is associated with increasing loading values at the peaks at ~450 and 680 nm (Fig. 3c). These peaks closely match with ice-algae absorption bands (Legendre and Gosselin, 1991; Fritsen and others, 2011) suggesting a strong association between PC2 and ice-algal biomass. Within cylinder patchiness is also observed as

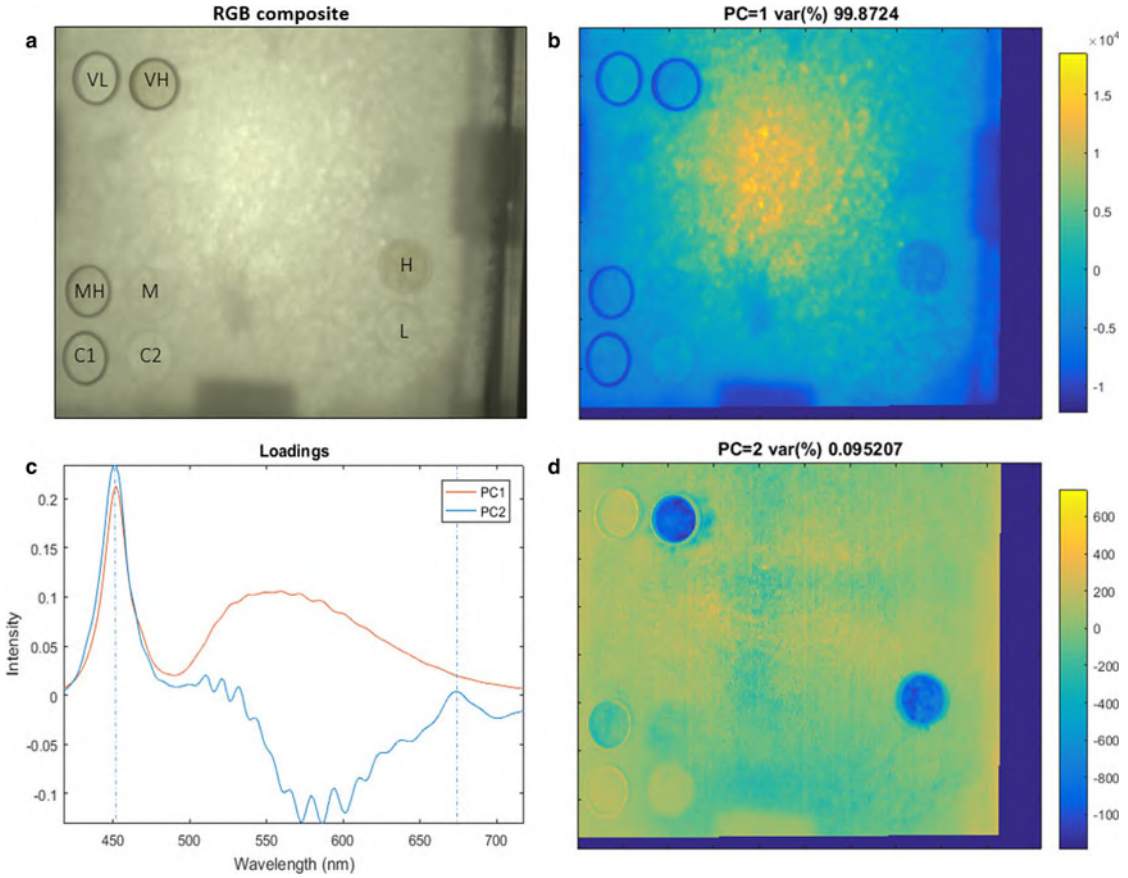

Fig. 3. Results of PCA applied to the 1.7 nm spectral resolution frame of the ice surface. (a) RGB composite of the hyperspectral image after algae inoculation displaying the performed biomass redistribution among cylinders. The RGB composite image is similar to what is observable by the human eye or normal imagery. (b) First principal component (PC1) representing light intensity variability within the image. (c) PCA loadings for each of the principal components. Algae absorption bands are clearly visible in PC2 at ~450 and 680 nm. (d) Second principal component (PC2) representing algae biomass abundance variability. The colour bar is unit-less as representing PC intensities.

darker spots of low PC2 intensity, particularly for cylinders MH, H and VH (Fig. 3d).

Loadings of PC2 are not purely representative of ice algae. Figure 3c shows that PC2 is also influenced by another element of variability affecting the spectral range between 500 and 650 nm. Opposite to ice algae, loadings on this component are low while algae related loading peaks (450 and 680 nm) are high. This high contrast can be observed at the edges of the PVC cylinders in Figure 3d thus suggesting that PC2 is influenced by variation caused by such cylinders and therefore slightly influencing the rest of the PC2 intensities across the image. This enhances PC2 intensity image features such as the shading of the circulation fans and the PVC cylinders themselves (Fig. 3d). Variability on the third principal component was also explored but did not show any relevant information.

The large disagreement between chl-a sampling in cylinder H and VH is attributed to leakage of algal-cells from cylinder VH to the surroundings as can be observed in Figure 3d at the top left. This leakage might have occurred during the hyperspectral image acquisition or later during chl-a sampling due to ice melting. Another cause might be the relatively poor efficacy of the chl-a sampling method compared with the within-cylinder variability for H and VH observed as dark spots spread across the 80 cm^2 cylinder area (Fig. 2c).

The analysis performed for the three different spectral resolutions (1.7, 3.4, 6.8 nm, respectively) demonstrates that while a spectral resolution of 3.4 nm is capable of performing the same differentiation as 1.7 nm, resolutions of >6 nm are not able to capture fine scale variability of biomass according to this first method exploration (Fig. 4). This is most likely related to the fine range of ice-algal spectral absorption features.

The AK10 measured radiance per pixel across the tank. It is observed that radiance intensities measured in the tank are in the same spectral radiance range compared with the measurements by Nicolaus and Katlein (2013) across different types of sea-ice conditions and ROV depths (Fig. 5). The ROV transects numbers are chosen as indexed in the original dataset (Nicolaus and Katlein, 2013).

DISCUSSION

In this study, we present the first results of a laboratory experiment employing an HI camera for differentiating ice-algae biomass distribution at the ice/water interface. Employing a sliding pushbroom hyperspectral sensor over an inverted sea-ice tank allows to test the ability of hyperspectral imaging for capturing the detailed spatial distribution of sea-ice algae and test a range of hyperspectral sensor configurations, such as spectral resolution and integration time.

Sea ice is a three phase medium (principally consisting of ice, brine and air bubbles) with high scattering properties and contains optically active substances in the PAR range such as Colored Dissolved Organic Matter (CDOM) but in particular

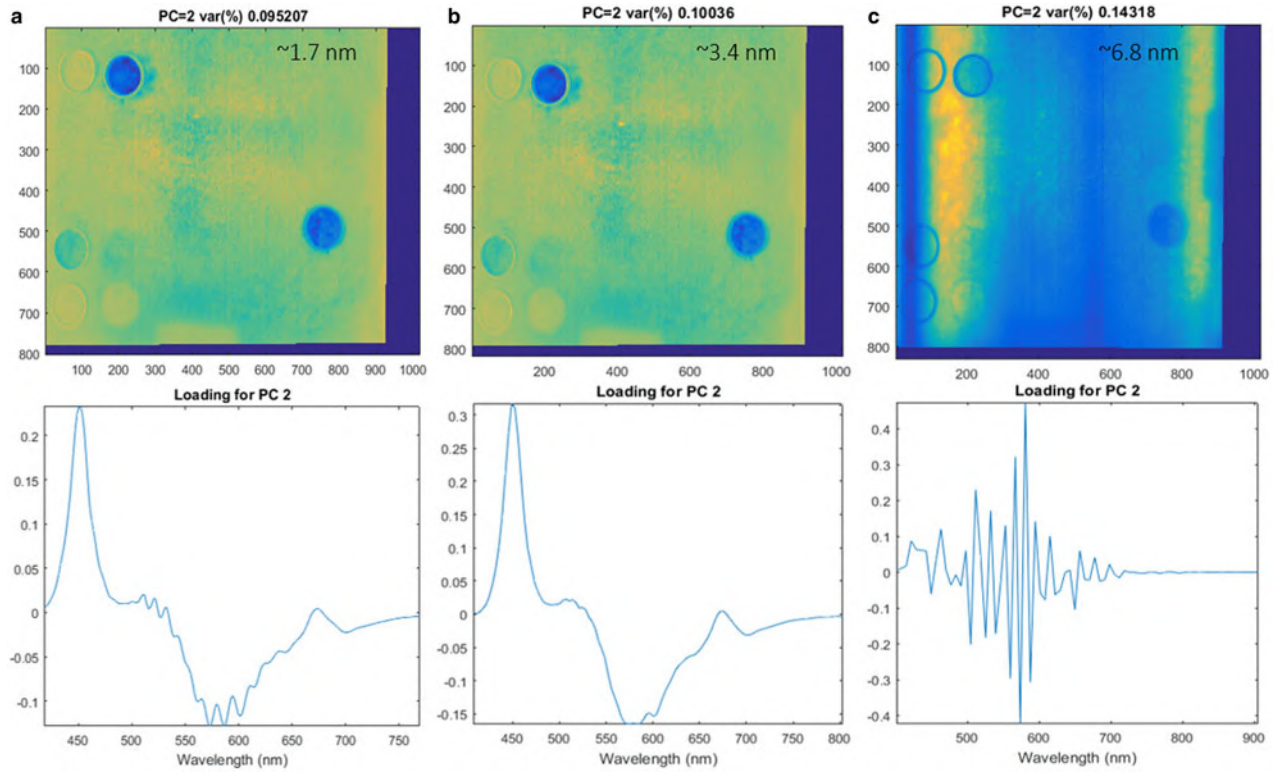

Fig. 4. Principal component 2 (PC2) representing algae biomass variability for different spectral resolutions 1.7 nm (a), 3.4 nm (b), 6.8 nm (c), respectively. The difference in biomass PC2 loadings between 1.7 and 3.4 nm is minimal. The figure outlines the working spectral resolution range for hyperspectral imaging aimed to capture algae biomass abundance. The test suggests that sensors with spectral resolution above 6.8 nm cannot be used for the purpose and for example discards the use of snapshot hyperspectral sensors compared to pushbroom scanners. The colour bar is omitted.

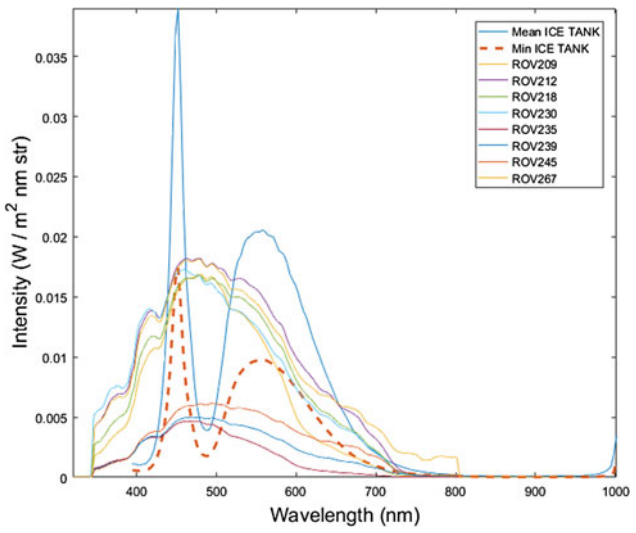

Fig. 5. Comparison of radiance levels measured in the inverted ice tank with a series of Arctic under-ice radiance transects measured in-situ with a Remotely Operated Vehicle (ROV) for different sea-ice conditions. The ice tank radiance is obtained from the hyperspectral frames. Mean ICE TANK is the mean between all pixels in the frame whereas Min ICE TANK is the pixel with minimum intensity (taken in a non-shadowed area). ROV transects data are publicly available from the study performed by Nicolaus and Katlein (2013) in Arctic sea ice. Sea-ice conditions varied from snow to no snow cover (from 2 to 10 cm thickness), from First Year Ice (FYI) to Multi Year Ice (MYI) (from 0.3 to 3.8 m thickness) and ROV water depth varied from 1 to 8 m.

microalgae (Perovich, 1996; Grenfell and others, 2006; Xie and others, 2014). Light reaching the ice sub-surface can be reduced to <1% of the incoming solar radiation depending on surface and ice properties (e.g. due to snow, presence of melt-ponds, ice thickness, ice structure, etc.) resulting in very low under-ice light levels (Petrich and others, 2012). Sea ice also affects the geometric properties of the light field exiting the medium due to its lamellar structure funnelling light in a downward direction and generating a forward peaked light field (Katlein and others, 2014).

We have presented a proof of concept study conducted under controlled laboratory conditions to test HI technology as a new remote-sensing technique to map ice algal distribution at the bottom of the sea ice. The hyperspectral frames acquired with a 0.9 mm square pixel spatial resolution and spectral resolutions of 1.7 and 3.4 nm were able to provide spectral differentiation between different algal concentrations at the ice/water interface in our experimental set-up. The results were validated by the pre-determined cylinder inoculation scale and chl-a sampling within the cylinders. It is noted that our chl-a measurements do not provide an exact determination of chl-a within the cylinders but serve as a semi-quantitative measure of the algal biomass to allow for between cylinder comparison.

Spectral resolutions >6 nm were not able to provide such discrimination due to the finer spectral scale of algae absorption features compared with the coarser transmitted light curve measured. This result has further importance in selecting appropriate sensors for this detection of ice algae. For example, snapshot hyperspectral sensors are easier to use (more portable and not constantly requiring six orientation

parameters) than pushbroom sensors, which require constant and accurate forward motion and are sensitive to drift. However, to attain adequate SNR and due to the finite number of pixels on a focal plane array, snapshot HI sensors necessarily make a trade-off in the resolution of the various dimensions of data of the hypercube sacrificing either spatial or spectral resolution. Considering the low-light of the under-ice environment, the high micro-scale spatial variability of ice algae and its fine-scale spectral features, snapshot HI would be very limited in this type of application.

Comparison of the experimental set-up with an in-situ scenario

It might be argued that light intensity measured in the ice tank is different from the typically low intensity transmitted solar radiation found under sea ice. Thus, the capability of a HI sensor to perform in low light conditions in a dynamic setting would be put into question. The effect of increasing distances from the sensor to the sea-ice bottom (water-column thickness) would further accentuate this issue. Our study compared measured radiance intensity levels with the AK10 to multiple in-situ situations showing consistent light levels even for the worst case scenarios around algae absorption bands (690 nm) (Fig. 5). Additionally, the measurements maximized the SNR by reaching near saturation light levels. We expect that with the same settings, lower light levels would affect SNR but would still yield accurate information on algae spatial distribution.

The different spectral signature of the LED light source compared with sunlight radiation is not expected to influence PCA results in an in-situ scenario. The spectral bands representing algae variability are quite narrow (as seen in PC2 loadings in Fig. 3c), and PCA was capable of decomposing between the spectral composition of the light source (with variability due to changes in overall intensity, as PC1) and algae related absorption bands (as PC2). Lange and others (2016) observed a similar behaviour in-situ when employing Empirical Orthogonal Functions (EOFs) (analogous to PCA) outlining how secondary modes (or PCs) are free of the dominant signal spectral variability and better represent chl-a absorption.

A similar ice structure to that found in the field, with lamellar ice crystals, brine and air pockets, was also observed within the ice tank (using macro photography). This caused the light to be in a diffuse and scattered form similar to in-situ observations (Petrich and others, 2012). The spatial variability of light intensity caused by the lamp and variations in the ice thickness is not considered disadvantageous. Snow is the most common and greatest attenuator of light in the snow – sea-ice layered matrix and produces a similar effect creating high variability in light intensities within very short distances (e.g. Nicolaus and others, 2013). Indeed, our experimental results suggest the method's indifference to light intensity variability (e.g. induced by spatially variable snow and ice thickness). This observation would need to be further investigated for a real sea-ice sampling scenario that comprises additional optically active elements. However, our results outline the potential of the technique to focus only on relevant spectral features associated with sea-ice algae presence and biomass variability. From an optical HI perspective, the experimental set-up therefore properly represented the four components of the layered structure of real sea ice (air, ice, water, algae). Whether it will be possible to control and mimic natural ice features including the skeletal layer and quantify columnar ice growth, are considerations for future experiments.

Ice algae were inoculated 3 days prior to the imaging in the ice tank and resided at the ice/water interface only (~5 mm deep in the ice structure). While measured chl-a concentrations are proportional to in-situ observations both in the Arctic (Arrigo and others, 2010) and the Antarctic (Meiners and others, 2012), depending on the region, in-situ ice-algae concentrations might be vertically variable (Meiners and others, 2012; Arrigo, 2014). Notwithstanding, higher concentrations of sea-ice algae are most frequently found in the bottom <10 cm of the ice, and can also be found exclusively attached at the ice/water interface (Arrigo, 2014; Lund-Hansen and others, 2016). Another consideration in interpreting the spectral data is the physiological status of the algal cultures. All three cultures were in an exponential growth phase prior to inoculation and acclimated to 60 µmol photon m^{-2} s^{-1}, which was a comparable irradiance with that provided by the ice tank. In natural conditions, sea-ice algae can be exposed to different levels of irradiance and can respond physiologically to these changes. For example, shade-adaptation requires that intracellular chlorophyll *a* is upregulated to maximize the capacity for growth and different compounds of accessory pigments can be produced under different irradiance conditions (SooHoo and others, 1987; Fritsen and others, 2011). In an in-situ scenario, this and other biological components of the within-ice community (dead algae cells and detritus) are likely to influence the spectral signatures observed with HI sensors by slightly shifting the spectral bands better representing algae variability in PCA analysis.

A new type of vision under the ice: possibilities, limitations and future work

The main advantage of the proposed application of HI is the ability to capture light at high spectral and spatial resolutions (in this case mm scales) in a non-invasive manner with great potential for studies aimed at investigating ice-algal spatial distribution, variability and environmental controls (Campbell and others, 2015; Lange and others, 2016; Lund-Hansen and others, 2016). Studies employing hyperspectral imaging for different types of underwater biomes have been performed on mycrophytobenthos (Chennu and others, 2013) and coral reef biota (Caras and Karnieli, 2015).

By establishing local in-situ correlations between chl-a and spectral indices such as NDIs (Melbourne-Thomas and others, 2015) or EOFs (Lange and others, 2016) the hyperspectral image processing workflow can then be theoretically extended to regression analysis and quantification of chl-a per pixel unit. Planned future work will investigate the possibility of applying different statistical approaches to the acquired imagery.

In the present tests, HI frames captured radiance at mm resolution but biomass differences were only validated among the cylinders. Variability in PC2 intensity was observed across the rest of the entire ice tank (outside of the cylinders) probably due to the random inoculation. Nevertheless, we cannot prove that these fine-scale intensity variations are associated with fine-scale (sub-millimetre) patterns in algal spatial distribution. Even though we visually observed a leakage pattern in PC2 at sub-millimetre

resolution from a cylinder (Fig. 3d), at this stage we are not able to quantitatively validate this due to the difficulty of sampling chl-a at such small scales.

Different scanning distances from the ice surface can yield different HI spatial resolutions ranging from sub-millimetre to the meter scale. Employing the sensor at increased distances from the ice sub-surface would allow to scan and map higher spatial extents at the cost of spatial resolution. However, influences caused by the anisotropic properties of the under-ice light field need to be carefully taken into consideration when measuring radiance from multiple angular directions such as the ones obtained from a large FOV HI sensor (Katlein and others, 2016, 2014). Water column correction would also need to be considered and corrected for, if greater surveying depths are to be considered (Johnsen and others, 2013).

The use of close-range hyperspectral imaging is an emerging area of study with technical challenges to overcome for marine applications. In the marine environment, technical challenges are often accentuated for spectral analysis and sensor deployment. In the under-ice environment we are faced with further limitations such as selecting an appropriate material for the camera housing that maintains its optical integrity and can operate under very low temperatures. To the authors knowledge, only a few published studies are currently available on deploying hyperspectral imaging cameras under water, but the technology certainly presents great potential from a marine remote-sensing perspective (Chennu and others, 2013; Johnsen and others, 2013).

HI systems could theoretically be deployed on Autonomous Underwater Vehicles or ROVs (Johnsen and others, 2013). In the present test, we employed a stable and relatively accurate motorized slider moving at slow speeds (8–10 mm s^{-1}) and relatively low frequency (5 Hz). Much more investigation is required for assessing HI systems performance on an underwater vehicle of any kind.

CONCLUSION

Current biomass sampling methodologies are not capable of capturing the abundance and distribution of sea-ice algae. Therefore, little is known of how changes in their environment will affect their existence with concomitant impacts on the whole marine polar food web and high latitude carbon cycles.

Through an experimental set-up consisting of an 'inverted' sea-ice simulation tank we were able to map transmitted light through an algal-colonized sea-ice layer at unprecedented spectral (1.7, 3.4 and 6.8 nm) and spatial resolutions (0.9 mm square pixel size). Decomposition of the hyperspectral data through PCA outlined two main components of variability in the images; the first (PC1) representing light intensity and the second (PC2) representing algae biomass across the tank. Light intensity variability is typically found in the field and is mostly attributed to variations in snow thickness. Biomass abundance in-situ is mostly concentrated at the bottom of the ice at the ice/water interface with algae presenting multiple degrees of 'patchiness'. Overall, the inverted sea-ice simulation tank presented an adequate optical set-up for investigating the application of hyperspectral imaging (HI) cameras for ice-algal studies.

In this preliminary experiment, HI was able to differentiate between low and high biomass abundances and was validated over a discrete scale of six cylinder units with increasing concentrations. Further observations, such as within-cylinder patchiness and algae leakage from a cylinder observed in the PCA analysis plots, suggested the ability to discriminate algae variability at cm to mm scale. Our assessment of three different spectral resolutions indicated that while bandwidths of 1.7 and 3.6 nm successfully captured algae biomass spatial variability, bandwidths over 6 nm were not provide such differentiation. This suggests that a sensible sensor configuration is required for ice-algal habitat mapping.

Planned future work will investigate several aspects aimed to move towards the deployment of the technology in-situ by assessing varying spatial resolutions, varying light intensity levels, varying camera settings (such as movement speed and imaging frequency) and applying regression models to correlate hyperspectral imagery data to sampled chl-a values among others. Further investigation in HI technology is also required for assessing the range of spatial resolutions achievable for capturing the multiple spatial scales of variability of ice-associated algae, and for the potential of characterizing under-ice light field properties, as seen in the PC1 light intensity distribution mapping (Katlein and others, 2016, 2014). The methodology proposed in this study is still in its infancy with several important caveats that need to be addressed. Nevertheless, this study demonstrates the potential of hyperspectral imaging as an improved and valid methodology capable of providing unprecedented datasets for estimating sea-ice algal biomass at the ice/water interface.

ACKNOWLEDGEMENTS

This research was supported under Australian Research Council's Special Research Initiative for Antarctic Gateway Partnership (Project ID SR140300001). We acknowledge the University of Tasmania Terraluma's group and Terraluma engineer Richard Ballard for advice and technical support. We gratefully acknowledge the collaboration with Petri Nygrén from SPECIM (Spectral Imaging Ltd) and Marc Fimeri (Adept Turnkey Pty Ltd) for assisting with the collection of the hyperspectral imagery and laboratory testing with the AISA KESTREL 10. Emiliano Cimoli is supported by the Antarctic Gateway Partnership and the University of Tasmania's PhD program.

REFERENCES

Amigo JM, Babamoradi H and Elcoroaristizabal S (2015) Hyperspectral image analysis. A tutorial. *Anal. Chim. Acta*, **896**, 34–51 (doi: 10.1016/j.aca.2015.09.030)

Arrigo KR (2014) Sea ice ecosystems. *Annu. Rev. Mar. Sci.*, **6**, 439–467 (doi: 10.1146/annurev-marine-010213-135103)

Arrigo KR, Mock T and Lizotte MP (2010) Primary producers and sea ice. In Thomas DN and Dieckmann GS eds. *Sea ice*. Oxford: Wiley-Blackwell, 283–325

Arrigo KR, Brown ZW and Mills MM (2014) Sea ice algal biomass and physiology in the Amundsen Sea, Antarctica. *Elem. Sci. Anthr.*, **2**, 28 (doi: 10.12952/journal.elementa.000028)

Boetius A and 16 others RV Polarstern ARK27-3-Shipboard Science Party (2013) Export of algal biomass from the melting Arctic sea ice. *Science*, **339**, 1430–1432 (doi: 10.1126/science.1231346)

Brugel S and 7 others (2009) Phytoplankton biomass and production in the southeastern Beaufort Sea in autumn 2002 and 2003. *Mar. Ecol. Prog. Ser.*, **377**, 63–77 (doi: 10.3354/meps07808)

Campbell K, Mundy CJ, Barber DG and Gosselin M (2014) Remote estimates of ice algae biomass and their response to

environmental conditions during spring melt. *ARCTIC*, **67**, 375 (doi: 10.14430/arctic4409)

Campbell K, Mundy CJ, Barber DG and Gosselin M (2015) Characterizing the sea ice algae chlorophyll a–snow depth relationship over Arctic spring melt using transmitted irradiance. *J. Mar. Syst.*, **147**, 76–84 (doi: 10.1016/j.jmarsys.2014.01.008)

Caras T and Karnieli A (2015) Ground-level classification of a coral reef using a hyperspectral camera. *Remote Sens.*, **7**, 7521–7544 (doi: 10.3390/rs70607521)

Chennu A and 6 others (2013) Hyperspectral imaging of the microscale distribution and dynamics of microphytobenthos in intertidal sediments: hyperspectral imaging of MPB biofilms. *Limnol. Oceanogr. Methods*, **11**, 511–528 (doi: 10.4319/lom.2013.11.511)

Flores H and 29 others (2012) Impact of climate change on Antarctic krill. *Mar. Ecol. Prog. Ser.*, **458**, 1–19 (doi: 10.3354/meps09831)

Fritsen CH, Wirthlin ED, Momberg DK, Lewis MJ and Ackley SF (2011) Bio-optical properties of Antarctic pack ice in the early austral spring. *Deep Sea Res. Part II Top. Stud. Oceanogr.*, **58**, 1052–1061 (doi: 10.1016/j.dsr2.2010.10.028)

Gradinger R (2009) Sea-ice algae: major contributors to primary production and algal biomass in the Chukchi and Beaufort Seas during May/June 2002. *Deep Sea Res. Part II Top. Stud. Oceanogr., Western Artic Shelf-Basin Interactions (SBI)Project*, **2**, 56, 1201–1212 (doi: 10.1016/j.dsr2.2008.10.016)

Grenfell TC, Light B and Perovich DK (2006) Spectral transmission and implications for the partitioning of shortwave radiation in arctic sea ice. *Ann. Glaciol.*, **44**, 1–6

Guillard RRL and Ryther JH (1962) Studies of marine planktonic diatoms: I. Cyclotella Nana Hustedt, and Detonula Confervacea (cleve) Gran. *Can. J. Microbiol.*, **8**, 229–239 (doi: 10.1139/m62-029)

Gutt J (1995) The occurrence of sub-ice algal aggregations off northeast Greenland. *Polar Biol.*, **15**, 247–252 (doi: 10.1007/BF00239844)

Hawes I and 5 others (2012) Photobiology of sea ice algae during initial spring growth in Kangerlussuaq, West Greenland: insights from imaging variable chlorophyll fluorescence of ice cores. *Photosynth. Res.*, **112**, 103–115 (doi: 10.1007/s11120-012-9736-7)

Holm-Hansen O and Riemann B (1978) Chlorophyll a determination: improvements in methodology. *Oikos*, **30**, 438–447 (doi: 10.2307/3543338)

Holzinger A, Allen MC and Deheyn DD (2016) Hyperspectral imaging of snow algae and green algae from aeroterrestrial habitats. *J. Photochem. Photobiol. B*, **162**, 412–420 (doi: 10.1016/j.jphotobiol.2016.07.001)

Johnsen G and 8 others (2013) Underwater hyperspectral imagery to create biogeochemical maps of seafloor properties. In *Subsea optics and imaging*. Cambridge: Elsevier, 508–540e

Katlein C, Nicolaus M and Petrich C (2014) The anisotropic scattering coefficient of sea ice. *J. Geophys. Res. Oceans*, **119**, 842–855 (doi: 10.1002/2013JC009502)

Katlein C, Fernández-Méndez M, Wenzhöfer F and Nicolaus M (2015) Distribution of algal aggregates under summer sea ice in the Central Arctic. *Polar Biol.*, **38**, 719–731 (doi: 10.1007/s00300-014-1634-3)

Katlein C, Perovich DK and Nicolaus M (2016) Geometric effects of an inhomogeneous sea ice cover on the under ice light field. *Front. Earth Sci.*, **4**, 1–10

Kohlbach D and 5 others (2016) The importance of ice algae-produced carbon in the central Arctic Ocean ecosystem: food web relationships revealed by lipid and stable isotope analyses. *Limnol. Oceanogr.*, **61**, 2027–2044 (doi: 10.1002/lno.10351)

Lange BA, Katlein C, Nicolaus M, Peeken I and Flores H (2016) Sea ice algae chlorophyll a concentrations derived from under-ice spectral radiation profiling platforms. *J. Geophys. Res. Oceans*, **121**, 8511–8534, (doi: 10.1002/2016JC011991)

Lange BA, Katlein C, Nicolaus M Peeken I and Flores H. () Sea ice algae chlorophyll a concentrations derived from under-ice spectral radiation profiling platforms,. *J. Geophys. Res. Oceans*, **121**, 8511–8534 (doi: 10.1002/2016JC011991)

Legendre L and Gosselin M (1991) In situ spectroradiometric estimation of microalgal biomass in first-year sea ice. *Polar Biol.*, **11**, 113–115 (doi: 10.1007/BF00234273)

Lucieer A, Malenovský Z, Veness T and Wallace L (2014) HyperUAS-imaging spectroscopy from a multirotor unmanned aircraft system. *J. Field Robot.*, **31**, 571–590 (doi: 10.1002/rob.21508)

Lund-Hansen LC, Hawes I, Sorrell BK and Nielsen MH (2014) Removal of snow cover inhibits spring growth of Arctic ice algae through physiological and behavioral effects. *Polar Biol.*, **37**, 471–481 (doi: 10.1007/s00300-013-1444-z)

Lund-Hansen LC, Hawes I, Nielsen MH and Sorrell BK (2016) Is colonization of sea ice by diatoms facilitated by increased surface roughness in growing ice crystals? *Polar Biol*. (doi: 10.1007/s00300-016-1981-3)

Malenovský Z, Turnbull JD, Lucieer A and Robinson SA (2015) Antarctic moss stress assessment based on chlorophyll content and leaf density retrieved from imaging spectroscopy data. *New Phytol.*, **208**, 608–624 (doi: 10.1111/nph.13524)

Maykut GA and Grenfell TC (1975) The spectral distribution of light beneath first-year sea ice in the Arctic Ocean. *Limnol. Oceanogr.*, **20**, 554–563 (doi: 10.4319/lo.1975.20.4.0554)

McMinn A and 6 others (2012) Antarctic coastal microalgal primary production and photosynthesis. *Mar. Biol.*, **159**, 2827–2837 (doi: 10.1007/s00227-012-2044-0)

Meiners KM and 14 others (2012) Chlorophyll a in Antarctic sea ice from historical ice core data. *Geophys. Res. Lett.*, **39**, n/a–n/a (doi: 10.1029/2012GL053478)

Melbourne-Thomas J and 5 others (2015) Algorithms to estimate Antarctic sea ice algal biomass from under-ice irradiance spectra at regional scales. *Mar. Ecol. Prog. Ser.*, **536**, 107–121

Miller LA and 22 others (2015) Methods for biogeochemical studies of sea ice: the state of the art, caveats, and recommendations. *Elem. Sci. Anthr.*, **3**, 38 (doi: 10.12952/journal.elementa.000038)

Mundy C and 9 others (2014) Role of environmental factors on phytoplankton bloom initiation under landfast sea ice in Resolute Passage, Canada. *Mar. Ecol. Prog. Ser.*, **497**, 39–49 (doi: 10.3354/meps10587)

Mundy CJ, Ehn JK, Barber DG and Michel C (2007) Influence of snow cover and algae on the spectral dependence of transmitted irradiance through Arctic landfast first-year sea ice. *J. Geophys. Res.*, **112** (doi: 10.1029/2006JC003683)

Nicolaus M and Katlein C (2013) Mapping radiation transfer through sea ice using a remotely operated vehicle (ROV). *Cryosphere*, **7**, 763–777 (doi: 10.5194/tc-7-763-2013)

Nicolaus M, Petrich C, Hudson SR and Granskog MA (2013) Variability of light transmission through Arctic land-fast sea ice during spring. *Cryosphere*, **7**, 977–986 (doi: 10.5194/tc-7-977-2013)

Nogami S, Ohnuki S and Ohya Y (2014) Hyperspectral imaging techniques for the characterization of *Haematococcus pluvialis* (Chlorophyceae). *J. Phycol.*, **50**, 939–947 (doi: 10.1111/jpy.12226)

Perkins RG and 7 others (2016) Microspatial variability in community structure and photophysiology of calcified macroalgal microbiomes revealed by coupling of hyperspectral and high-resolution fluorescence imaging. *Sci. Rep.*, **6**, 22343 (doi: 10.1038/srep22343)

Perovich DK (1996) The Optical Properties of Sea Ice. DTIC Document

Petrich C, Nicolaus M and Gradinger R (2012) Sensitivity of the light field under sea ice to spatially inhomogeneous optical properties and incident light assessed with three-dimensional Monte Carlo radiative transfer simulations. *Cold Reg. Sci. Technol.*, **73**, 1–11 (doi: 10.1016/j.coldregions.2011.12.004)

Rodarmel C and Shan J (2002) Principal component analysis for hyperspectral image classification. *Surv. Land Inf. Sci.*, **62**, 115

Rysgaard S, Kühl M, Glud RN and Hansen JW (2001) Biomass, production and horizontal patchiness of sea ice algae in a high-Arctic fjord (Young Sound, NE Greenland). *Mar. Ecol. Prog. Ser.*, **223**, 15–26

SooHoo JB and 5 others (1987) Spectral light absorption and quantum yield of photosynthesis in sea ice microalgae and a bloom of *Phaeocystis pouchetii* from McMurdo Sound, Antarctica. *Mar. Ecol.-Prog. Ser.*, **39**, 175–189

Søreide JE, Leu E, Berge J, Graeve M and Falk-Petersen S (2010) Timing of blooms, algal food quality and Calanus glacialis reproduction and growth in a changing Arctic. *Glob. Change Biol.*, **16**, 3154–3163 (doi: 10.1111/j.1365-2486.2010.02175.x)

Steffens M and 6 others (2006) Spatial variation of biogeochemical properties of landfast sea ice in the Gulf of Bothnia, Baltic Sea. *Ann. Glaciol.*, **44**, 80–87

Tsai F and Philpot W (1998) Derivative analysis of hyperspectral data. *Remote Sens. Environ.*, **66**, 41–51

Vancoppenolle M and 9 others (2013) Role of sea ice in global biogeochemical cycles: emerging views and challenges. *Quat. Sci. Rev.*, **79**, 207–230

Vidal M and Amigo JM (2012) Pre-processing of hyperspectral images. Essential steps before image analysis. *Chemom. Intell. Lab. Syst., Special Issue Section: Selected Papers from the 1st African-European Conference on Chemometrics, Rabat, Morocco, September 2010 Special Issue Section: Preprocessing methods Special Issue Section: Spectroscopic Imaging*, **117**, 138–148 (doi: 10.1016/j.chemolab.2012.05.009)

Xie H, Aubry C, Zhang Y and Song G (2014) Chromophoric dissolved organic matter (CDOM) in first-year sea ice in the western Canadian Arctic. *Mar. Chem.*, **165**, 25–35 (doi: 10.1016/j.marchem.2014.07.007)

A published article has been removed from appendix C for copyright or proprietary reasons.

It has been published as: Martin, A., McMinn, A., 2018. Sea ice, extremophiles and life on extra-terrestrial ocean worlds, International journal of astrobiology, 17(1), 1-16